Magnetization processes of magnetic modulated nanowires

Ester María Palmero Rodríguez

Supervisor: Prof. Manuel Vázquez Villalabeitia
co-Supervisor: Dr. Rafael Pérez del Real
co-Supervisor: Dr. Cristina Bran

Tutor: Prof. Manuel Hernández Vélez

Thesis submitted to the Faculty of Sciences of the
Autonomous University of Madrid in partial fulfillment
of the requirements for the degree of Doctor in Physics

Department of Applied Physics. Faculty of Physics
Autonomous University of Madrid
October 2016

Contents

Abstract

This Ph.D. thesis focuses on the study of magnetization reversal processes of modulated magnetic nanowires, in composition and in diameter, fabricated by electrodeposition into porous anodic alumina templates. The research work covers the fabrication of the different nanowire arrays, and the geometrical, structural and magnetic characterization of nanowire arrays and individual nanowires.

The modulated nanowire arrays were synthesized by different anodization and electrodeposition techniques. For nanowires with modulated composition, the templates were fabricated by two-step anodization and pulsed electrodeposition; and the modulated diameter nanowires were grown by potentiostatic electrodeposition into alumina templates made by hard pulsed anodization.

First, a study about the magnetic properties of FeCo alloy nanowire arrays was performed in the full range of composition, varying from pure Fe to pure Co, and for different nanowire diameters. Furthermore, to obtain magnetically harder FeCo nanowires, a small amount of Cu was added to the alloy and thermal treatments were performed. By Ferromagnetic Resonance (FMR) measurements the magnetic anisotropy of nanowire arrays and the influence of Cu doping and annealing was determined.

Compositionally modulated (multilayer) nanowires were studied. They were synthesized intercalating non-ferromagnetic Cu layers between ferromagnetic FeCoCu segments, with a constant nanowire diameter. The multilayer nanowires were fabricated with different Cu layer thicknesses and FeCoCu segment lengths in order to study the influence of their thickness/length on the magnetic properties of the nanowire array. It was determined that the magnetostatic interactions between magnetic segments strongly affect the magnetic properties of the system. This influence has been studied by the First-Order Reversal Curves (FORC) technique.

The magnetization reversal processes of individual FeCoCu nanowires with tailored geometrical modulations along the nanowire length have been studied by Magneto-Optical Kerr Effect (MOKE) measurements. The magnetization configuration of modulated diameter FeCoCu and Co nanowires was determined by X-Ray Magnetic Circular Dichroism combined with Photoemission Electron Microscopy (XMCD-PEEM). The modulations in diameter and the tailored magnetocrystalline anisotropy offer the possibility to control the domain wall propagation along the nanowire.

The applicability of magnetic nanowire arrays has been addressed by the development of two sensing devices prototypes: a position sensor and a tachometer. The electronic system was designed in order to easily and accurately detect the magnetic field generated by the nanowire array.

Finally, alumina templates were used to fabricate magnetically soft NiCu alloy nanowires, and the magnetic properties of the arrays were studied as function of the nanowire composition, diameter and length. Moreover, by template-assisted fabrication a *core-shell* magnetic (Ni)-polymeric (polystyrene) nanocomposite was successfully synthesized and magnetically characterized.

Resumen

Esta tesis doctoral tiene como objetivo principal el estudio de los procesos de inversión de la imanación en nanohilos magnéticos modulados, tanto en composición como en diámetro, fabricados mediante electrodeposición en plantillas de alúmina. Este trabajo de investigación comprende la fabricación de los distintos arrays de nanohilos, así como su caracterización geométrica, estructural y magnética, tanto de los arrays como de nanohilos individuales.

Los arrays de nanohilos fueron fabricados mediante distintas técnicas de anodización y electrodeposición. Para los nanohilos modulados en composición, se fabricaron las plantillas mediante anodización en dos pasos y electrodeposición pulsada; y los nanohilos con diámetro modulado mediante electrodeposición potenciostática en membranas producidas mediante anodización dura y pulsada.

En primer lugar, se realizó un estudio sobre las propiedades magnéticas de arrays de nanohilos de FeCo en aleación en un rango completo de composición, desde Fe puro hasta Co puro, y para diversos diámetros de nanohilo. Además, para endurecer magnéticamente los nanohilos de FeCo, se añadió una pequeña cantidad de Cu a la aleación, seguido de tratamientos térmicos de los arrays. Mediante medidas de Resonancia Ferromagnética (*Ferromagnetic Resonance*, FMR) se determinó la anisotropía magnética de los arrays de nanohilos y la influencia del dopado con Cu y el tratamiento térmico.

Se han estudiado nanohilos con composición modulada (multicapa). Estos nanohilos se fabricaron intercalando capas de Cu entre los segmentos de FeCoCu, con un diámetro de nanohilo constante. Los nanohilos multicapa se produjeron con diferente espesor de las capas de Cu y longitud de los segmentos de FeCoCu para estudiar la influencia del espesor/longitud en las propiedades magnéticas del array. Se ha

determinado que las interacciones magnetostáticas entre los segmentos magnéticos tienen una gran influencia sobre las propiedades magnéticas del sistema. Esta influencia se ha estudiado mediante las curvas de reversión de primer orden (*First-Order Reversal Curves*, FORC).

Los procesos de reversión de la imanación en nanohilos individuales de FeCoCu con diámetro modulado se han estudiado mediante medidas de Efecto Kerr Magneto-Óptico (*Magneto-Optic Kerr* Effect, MOKE). La configuración de la imanación en nanohilos modulados de FeCoCu y Co se determinó mediante Dicroísmo Circular Magnético de Rayos X combinado con un Microscopio Electrónico de Fotoemisión (*X-Ray Magnetic Circular Dichroism - Photoemission Electron Microscopy*, XMCD-PEEM). La modulación en diámetro y el ajuste de la anisotropía magnetocristalina ofrecen la posibilidad de controlar la propagación de la pared de dominio a lo largo del nanohilo.

La aplicación de los arrays de nanohilos ha sido demostrada mediante su empleo en dos dispositivos sensores: un sensor de posición y un tacómetro. El sistema electrónico fue diseñado de forma que el campo magnético generado por el array fuese fácilmente detectado y con precisión suficiente.

Finalmente, se utilizaron las plantillas de alúmina para fabricar nanohilos de NiCu, aleación magnéticamente blanda, y se estudiaron las propiedades magnéticas de los arrays en función de su composición, diámetro y longitud. Además, se utilizaron las plantillas para fabricar con éxito un nanocompuesto con estructura *core-shell* formado con un material magnético (Ni) y un polímero (poliestireno), para su posterior caracterización magnética.

Chapter 1

Introduction

1.1. Nanotechnology. Nanostructures

Nanoscaled magnetic materials have received considerable attention during the last years motivated by the broad spectrum of applications in advanced technologies. The applicability of nanoscaled materials has been widely exploded in fields as high density magnetic storage and microwave devices, semiconductors, sensors, logic circuits, biomedicine or thermo-magneto-electric devices [1-8], where their miniaturization is a necessity [9-11]. In this way, nanotechnology requires the optimization of the fabrication and the characteristics of the nanostructured materials to properly cover the needs in specific applications.

Nanomaterials are classified into three classes depending on their geometric parameters [12, 13]: 0D nanostructures, whose three dimensions are reduced to nanoscale (e.g. nanoparticles, particularly attractive for biomedical applications such as hyperthermia or drug delivery [14]) (Figure 1.1(a)); 1D nanostructures, which exhibit two dimensions reduced to the nanoscale (e.g. nanowires, nanotubes or nanorods, which one of their most interesting properties is the shape anisotropy) (Figure 1.1(b)); and 2D nanostructures, where only one of its three dimensions has been reduced to the nanoscale (e.g. magnetic thin films used in spin valves and magnetic tunnel junctions [15]) (Figure 1.1(c)).

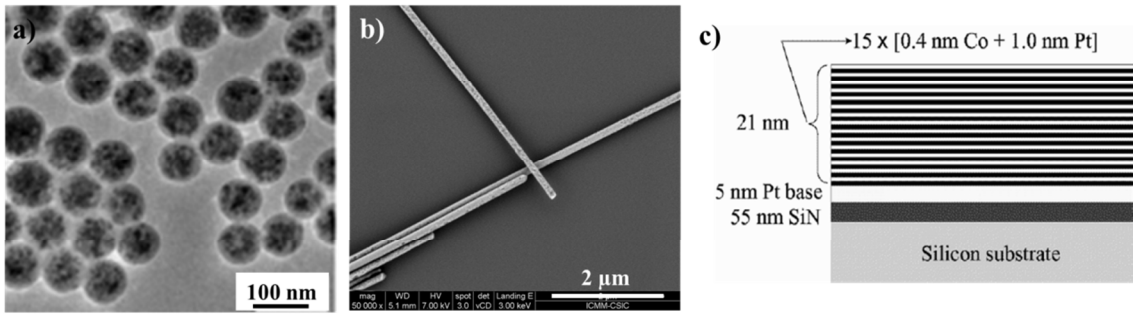

Figure 1.1 (a) TEM image of Fe_3O_4 nanoparticles embedded in a polystyrene matrix [16]; (b) SEM image of Co nanowires on Si substrate; and (c) scheme of layer structure used for Co/Pt thin films ([17]).

1.1.1. Nanofabrication techniques

There are different techniques for the fabrication of nanomaterials, which are usually categorized into two main groups: top-down and bottom-up techniques. The first one gathers the fabrication methods which are based in the reduction of the size of the material, starting from bulk, until the desired nanosize is reached. The most common top-down techniques are electron-beam, X-ray and focused ion beam lithographies. Bottom-up approaches are based in the constitution of a final material from atoms or molecules as building blocks, generally by self-assembly techniques. Examples of bottom-up approaches are the sol-gel and electrochemical growth methods, characterized by their low-cost fabrication and higher production efficiencies, allowing for their potential applicability in the industry [18-20].

1.1.1.1. Nanowires fabrication

Nanowires can be fabricated by a broad range of techniques [21], such as nano-lithography to carry out the deposition of nanostripes (nanowires with rectangular cross section) on top of a substrate [22, 23], hydrothermal growth starting from a seed [24], chemical vapor deposition [25], molecular self-assembly [26, 27] or template-assisted [20] techniques, among others. The templates most commonly used for nanowires fabrication are track-etched polycarbonate and porous alumina membranes. The polycarbonate templates have non-ordered pores and with non-homogeneous diameter. On the other hand, self-organized pores of alumina templates allow to easily obtaining close-packed nanowire arrays [28].

Between the different nanostructures and fabrication techniques, the template-assisted growth of single metallic or alloys nanowires into highly ordered alumina membranes has attracted much interest due to its low fabrication cost and possibility to tune easily the composition or geometry [20, 28-30].

1.2. Some basic concepts of magnetism

Magnetism fundamentally arises from the interaction between the orbital of neighboring electrons with overlapping wave functions, when their atoms are close enough. Considering the Pauli's exclusion principle, it is not possible to find two electrons with the same spin at the same point in the space and, consequently they should have opposite spin. If a given atom presents a certain magnetic moment direction, it will make the second atom highly dependent on that direction. The fundamental nature of the wave function tends to keep electrons with the same spin apart, which reduces their Coulomb energy. When the electrons have parallel spins, the system energy is then lower. The exchange energy is the difference in energy between the parallel and anti-parallel alignment of neighboring spin moments. For ferromagnetic exchange the exchange coupling is such that the parallel magnetization is the most stable configuration. On the other hand, for anti-ferromagnetic exchange the magnetic moments tend to be coupled in anti-parallel configuration. Considering two neighboring electrons with spins S_1 and S_2, the exchange interaction energy can be represented by:

$$E_{exch} = -2JS_1S_2 \tag{1.1}$$

where J is the exchange constant, being positive for parallel and negative for anti-parallel alignment.

In the case of ferromagnetic materials, in response to the exchange energy, the material should be fully magnetized, with all the individual atomic moments aligned with an applied field, originating a maximum value of magnetostatic energy for the material. However, magnetic materials tend to reduce this magnetostatic energy (i.e. tend to demagnetize) by the formation of magnetic domains inside the material [31, 32]. The magnetic domains are regions where all the magnetic moments are aligned along the same direction (Figure 1.2). The demagnetized state is possible when magnetic

moments of different domains lie along random directions, originating the overall macroscopic magnetization suppression. Between two magnetic domains, there is a gradual transition of the magnetic moment orientation, known as domain wall.

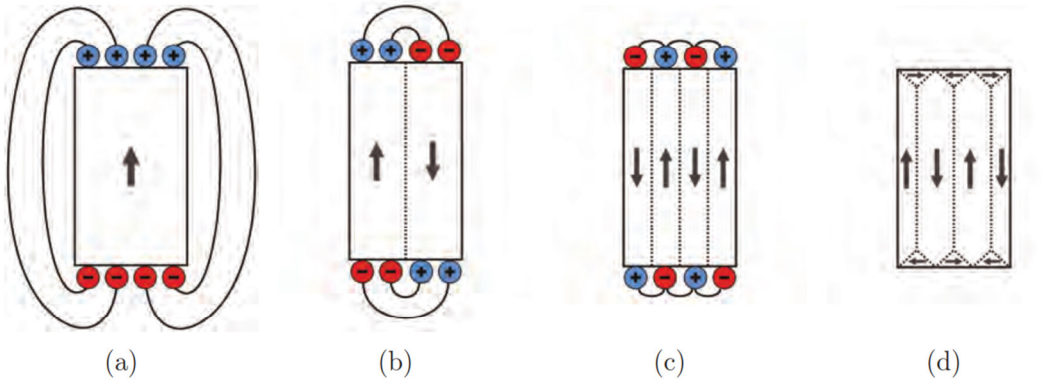

Figure 1.2 Domains formation in a ferromagnetic material and therefore the reduction in the magnetostatic energy [33].

When a magnetic field is applied to a magnetic material, the magnetization state can be determined by the eigenvalue of the magnetization vector configuration that minimizes the total system energy. The total free energy (E_T) can be expressed as follows:

$$E_T = E_{exch} + E_H + E_{elas} + E_{crys} + E_{sh} \tag{1.2}$$

where E_{exch} is the exchange energy, E_H is the Zeeman energy, E_{elas} is the magnetoelastic energy, E_{crys} is the magnetocrystalline energy, and E_{sh} is the shape anisotropy energy.

The Zeeman energy is the energy of the magnetization in an externally applied field, which is minimized when the magnetization is aligned with the applied field. This energy term is given by:

$$E_H = -\boldsymbol{M} \cdot \boldsymbol{H} \tag{1.3}$$

where $\boldsymbol{M}$ and $\boldsymbol{H}$ are the magnetization and external field vectors, respectively.

The magnetoelastic energy describes the effect of magnetostriction, which is related to the stress on the magnetization of a material. This effect is observed, for example when applying a magnetic field to Ni nanowires embedded into alumina template at low temperature [34, 35].

1.2.1. Magnetic anisotropy energy

Magnetic materials usually present preferential magnetization orientation in one particular direction of space, induced by the magnetic anisotropy. This fact originates magnetization easy (energetically favorable magnetization direction), intermediate and hard axis [36, 37]. There are different sources of magnetic anisotropy, being the magnetocrystalline (K_{crys}) and the shape (K_{sh}) anisotropies the most relevant for this work.

1.2.1.1. Shape anisotropy

The shape anisotropy contribution arises from the material shape. A magnetic material with a high aspect ratio (e.g. nanowires) presents an important shape anisotropy which originates a demagnetizing field (H_D) due to the magnetic charges at its surfaces. The demagnetizing field is opposite and proportional to the magnetization (M) within the material when an external field is applied:

$$H_D = -N_d M \tag{1.4}$$

where N_d is the demagnetizing factor, which depends on the material shape.

The magnetostatic energy originated by the shape anisotropy (E_{sh}) can be expressed as:

$$E_{sh} = \frac{1}{2}\mu_0 N_d M^2 \tag{1.5}$$

As example, the shape anisotropy energy for a specimen in the shape of a prolate spheroid (i.e. rod shape, being an approximation of nanowire shape) magnetized to a value M at an angle θ to c (Figure 1.3) is given by:

$$E_{sh} = \frac{1}{2}\mu_0 N_c M^2 + \frac{1}{2}\mu_0 (N_a - N_c) M^2 sin^2\theta \quad (1.6)$$

where N_a and N_c are the demagnetizing factors along the semi-minor axes a and semi-major axis c, respectively. As the long axis of the prolate spheroid plays an easy axis role, the shape anisotropy constant (K_{sh}) is then given by:

$$K_{sh} = \frac{1}{2}\mu_0 (N_a - N_c) M^2 \quad (1.7)$$

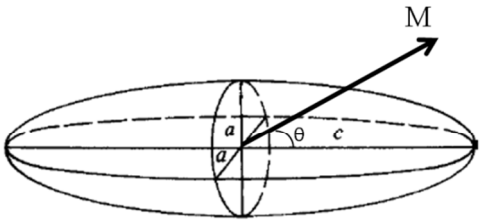

Figure 1.3 Prolate spheroid (adapted from [37]).

1.2.1.2. Magnetocrystalline anisotropy

The spin-orbit interaction between the atoms in a crystal depends on the spatial atom distribution, which can affect the magnetic coupling. Consequently, the magnetization along certain orientations in crystalline materials is energetically preferred. The magnetocrystalline anisotropy is directly related to the crystalline structure and symmetry of the material.

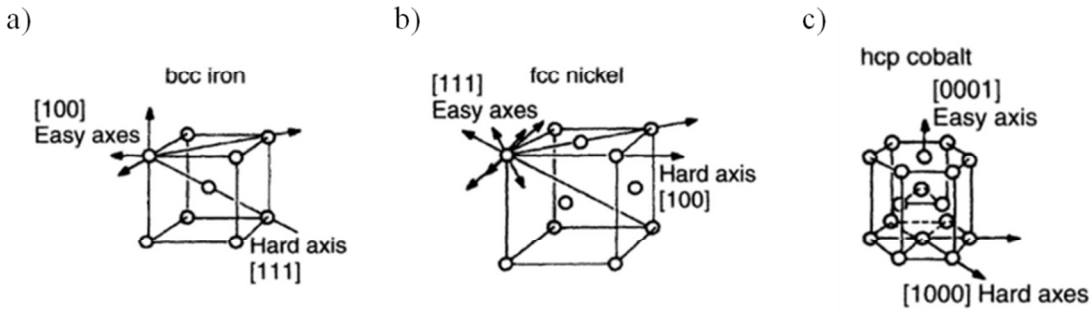

Figure 1.4 Lattice structures of (a) body-centered cubic (*bcc*) iron, (b) face-centered cubic (*fcc*) nickel, and (c) hexagonal close-packed (*hcp*) cobalt. Magnetization easy and hard axes are shown for each case [38].

For a cubic crystallographic structure, face-centered cubic (*fcc*) or body-centered cubic (*bcc*), the magnetic anisotropy energy can be expressed as:

$$E_{crys} = K_0 + K_1(cos^2\theta_1 cos^2\theta_2 + cos^2\theta_2 cos^2\theta_3 + cos^2\theta_3 cos^2\theta_1) + \cdots$$
$$\ldots + K_2(cos^2\theta_1 cos^2\theta_2 cos^2\theta_3) + \cdots \quad (1.8)$$

where K_0, K_1, and K_2 are the anisotropy constants and θ_1, θ_2, and θ_3 are the angles between the magnetization direction and the crystallographic axes.

For a hexagonal close-packed (*hcp*) crystallographic structure, considering an angle θ between the magnetization and the longitudinal axis (c-axis) of the crystalline lattice, the magneto-crystalline energy is given by:

$$E_{crys} = K_0 + K_1 sin^2\theta + K_2 sin^4\theta + \cdots \quad (1.9)$$

Table 1.1 collects the values of the anisotropy constant K_1 and K_2 for Fe, Co and Ni, which originate the easy and hard axes for each crystallographic structure shown in Figure 1.4.

Table 1.1 Anisotropy constants K_1 and K_2 for different elements at room temperature [38].

Element	Structure	$K_1 \cdot 10^{-4}$ (J/m^3)	$K_2 \cdot 10^{-4}$ (J/m^3)
Fe	*bcc*	4.8	-1.0
Ni	*fcc*	-0.45	-0.23
Co	*hcp*	41	15

1.3. Nanomagnetism

1.3.1. 0D Nanostructures: Nanoparticles

Nanoparticles are characterized by the reduction of their three dimensions to the nanoscale, showing a typical sized between 1 and few hundreds of nm. Nowadays, nanoparticle research is a scientific field which is attracting much interest due to their small size. They present interesting and different new properties compared to bulk materials, which could be useful in a wide variety of applications, such as biomedical, optics and electronics [14, 39].

In magnetic nanoparticles, the surface area becomes an important characteristic as the spins at the surface highly affect the magnetic properties of the nanoparticles. Particularly, when antiferromagnetic (AFM) materials are reduced to the nanoscale, they exhibit weak ferromagnetism (Figure 1.5(b) and (f)), differently as at the macroscale where they present zero magnetization values [40, 41].

Magnetic specimens with small sizes can present single-domain configuration, and they can exhibit superparamagnetic (SPM) behavior (Figure 1.5(d)) if the energy barrier, Δ, becomes comparable to the thermal energy k_BT, where k_B is the Boltzmann constant, and T the temperature [15, 42]. Considering the relaxation time (τ_0 with typical values between 10^{-9} and 10^{-10} s), the characteristic time for the spin to randomly flip (Néel relaxation time, τ_N) is given by:

$$\tau_N = \tau_0 exp\left(\frac{\Delta}{k_B T}\right) \tag{1.10}$$

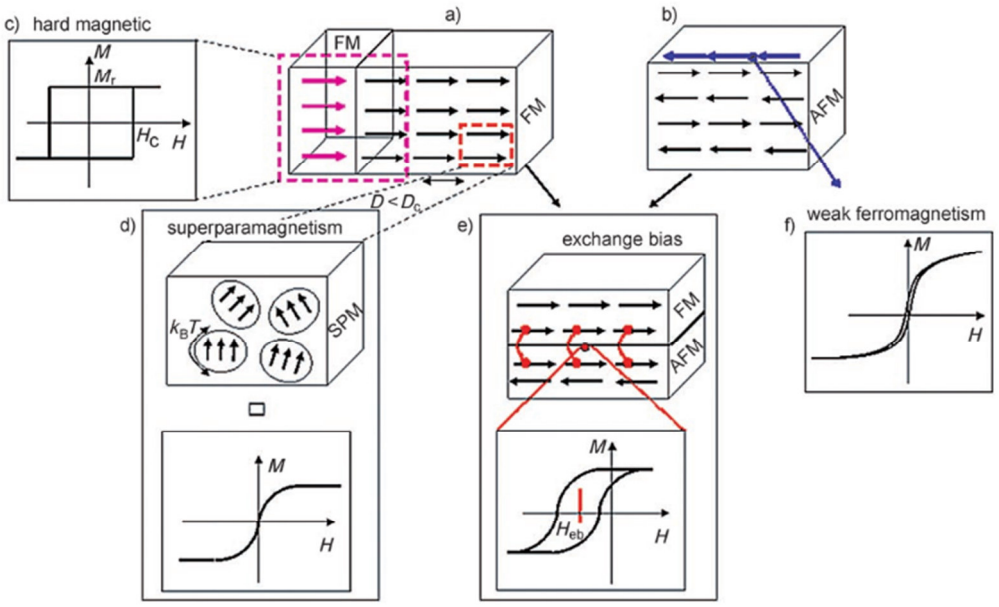

Figure 1.5 Schematic representation of the different effects occurring in magnetic nanomaterials: (a) ferromagnetic (FM) and (b) antiferromagnetic (AFM) spin arrangement; (c) typical hysteresis loop for permanent magnet material with high remanent magnetization (M_r) and coercive field (H_c); (d) magnetic moment arrangement for a material with superparamagnetic (SPM) behavior; (e) hysteresis loop showing exchange bias effect produced by the exchange coupling between FM and AFM materials; and (f) representation of the typical hysteresis loop obtained for pure AFM nanoparticles ([42]).

At temperature low enough that k_BT is not enough to influence the spins in a SPM nanoparticle, the spin become blocked along a particular direction [21]. This temperature is called the blocking temperature (T_B):

$$T_B = \frac{K_{eff} V_{NP}}{k_B ln\left(\frac{\tau_N}{\tau_0}\right)} \tag{1.11}$$

where K_{eff} is the effective magnetic anisotropy constant and V_{NP} is the nanoparticle volume.

1.3.2. 1D Nanostructures: Nanowires

Nanowires are considered potential candidates for applications, such as magnetic storage recording, sensing devices, biomedicine or drug delivery [20, 43-45]. What characterizes these nanostructures is their high aspect ratio, which potentially

increases their shape anisotropy, making them useful for specific applications where it is required. If the nanowires are fabricated with the proper composition, together with the high shape anisotropy, these nanostructures will exhibit high remanence and coercive field, which make them suitable candidates for permanent magnets applications [46, 47].

1.3.2.1. Magnetization reversal modes in cylindrical nanowires

The application of magnetic nanowires requires a thorough understanding of the magnetization reversal processes of those nanostructures. The magnetization reversal mechanism depends on the compositional and geometrical properties of the nanowires. According to experimental observations and micromagnetic simulations the reversal in nanowires takes place by the nucleation of domain walls (DWs) at the end of the nanowire followed by their subsequent depinning and propagation along the nanowire length [48-51]. It was determined that the domain wall structure is transverse or vortex (TDW or VDW, respectively), depending on the nanowire diameter [51], being TDW in nanowires with small diameter, and VDW for nanowires with larger diameter (Figure 1.6).

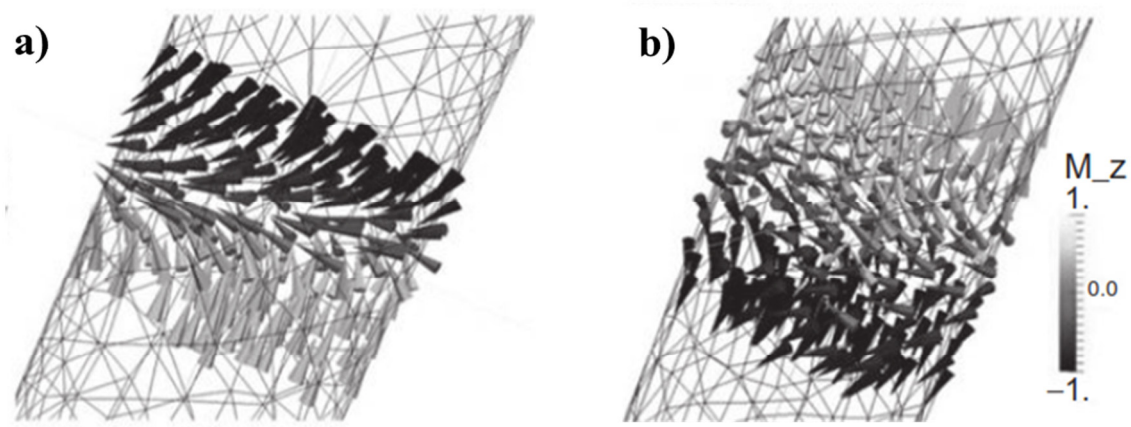

Figure 1.6 (a) Transverse and (b) vortex domain wall in a cylindrical nanowire [52].

The magnetization and magnetic anisotropy of nanowires are determined by the balance between shape, magnetocrystalline and magnetoelastic anisotropy terms. For nanowires with negligible or very small magnetocrystalline anisotropy (i.e. Fe, Ni or FeNi alloy nanowires, which grow into cubic phases) the magnetization reversal is mainly determined by the shape anisotropy, and is affected by the magnetostatic interactions between nanowires in the array [53-55]. For some materials (e.g. Ni) magnetoelastic anisotropy can play some relevant role due to the stresses induced by thermal strains arising from different expansion coefficients of metal nanowires and the surrounding alumina. For all the nanowires, the coercive field decreases with an increase in diameter, originated by a decrease in the shape anisotropy. Furthermore, in general, the coercive field for TDW mode is higher than for VDW mode [52].

For Co and Co-based nanowires, the magnetocrystalline anisotropy plays a decisive role. Co nanowires usually crystallize into *hcp* crystallographic structure with strong magnetocrystalline anisotropy energy constant whose magnetization easy direction is determined by the c-axis of hexagonal symmetry. Most commonly for these nanowires, the magnetization easy axis lies almost perpendicular to the nanowire axis [56-58]. The crystallographic structure of Co nanowires strongly depend on the electrodeposition parameters, which allow for the easy axis rotation out of the perpendicular direction [57].

The magnetic anisotropy of nanowires can be modified by the incorporation of different elements into the system [59-61]. After adding Ni to synthesize CoNi alloy nanowires, the magnetic properties of the alloy depend strongly on the amount of Co. For Co content below 50%, the shape anisotropy predominates and the coercivity can be adjusted by the composition. On the other hand, for more than 50% of Co in the alloy the magnetocrystalline anisotropy becomes predominant and the crystallographic structure determines the magnetic behavior [62-65]. CoFe alloys with high Fe content present relatively small magnetocrystalline anisotropy and magnetostriction which reduces the magnetic hardness (i.e., coercivity) and enhances magnetic susceptibility [66].

On the other hand, by micromagnetic simulations it was shown that the current induced motion of TDWs in cylindrical nanowires is different from that in magnetic nanostripes [67]. Walker breakdown effect limits the domain wall velocity in

nanostripes. At a critical external magnetic field, the transformation of the domain wall takes place (from TDW to VDW or vice versa), and this originate in a reduction of the domain wall propagation velocity. Micromagnetic simulations showed that the Walker limit does not exist in cylindrical nanowires [67].

1.3.3. 2D Nanostructures: Thin films.

If one of the three materials dimensions is reduced to the nanoscale, we obtain thin films. Magnetic thin films and multilayers are used in magnetic recording devices as read and write heads [68]. For magnetic storage data it is usual to employ multilayers of magnetic/non-magnetic materials [69, 70].

Thin films are fabricated by depositing atoms onto a substrate (Figure 1.1(c)) by different methods: chemical vapor deposition, electrodeposition from a liquid electrolyte, thermal evaporation, and sputtering. The last one is the most widely used method as it permits almost any combination of elements to be deposit and the obtained material is highly reproducible.

Directional structures can be produced in a thin film by arranging the deposition conditions. The directionality can be the result of crystallographic texture in materials with significant magnetocrystalline anisotropy. Furthermore, it is necessary to consider the magnetoelastic anisotropy originated by the difference in thermal expansion coefficients between the film and substrate. During the fabrication process, a uniaxial anisotropy can be induced in a magnetic thin film if the deposition is performed in the presence of an applied magnetic field [37].

Due to shape anisotropy, the magnetization in thin films tends to lie in the plane of the film, but the effect of perpendicular anisotropy has gained much interest in the last years for the applications in magnetic storage. The perpendicular anisotropy in thin films can be generated by choosing the appropriate film thickness or the material (e.g. CoCrPt, CoFeB or MnCoAl, among others [71-73]).

When the multilayer thin films are composed of a ferromagnetic (FM) and an anti-ferromagnetic (AFM) layer, the magnetic characteristics of the system are influenced by the exchange bias coupling between the two different magnetic layers.

Figure 1.5(e) shows that the exchange bias originates a shift of the hysteresis loops along the field axis, characterized by the exchange bias field (H_{eb}) and the increase in the coercive field [42]. The occurrence of the coupling between FM layers separated by non-magnetics or AFM layers has propelled the development of new devices for technological applications, such as in magnetic data storage, sensing devices and biomedicine [15, 74].

1.4. Objectives

The main objective of this research is to study the magnetization reversal processes of cylindrical and modulated nanowires within a broad range of compositions and geometries. The change in composition of the alloy enables the control of the effective anisotropy axis, which is determined by the balance between the magnetocrystalline and shape anisotropies. The study focus on two types of modulated nanowires: (i) nanowires modulated in composition, and (ii) modulated diameter nanowires. In order to achieve the main objective, different sub-objectives have been proposed:

- The study of magnetic properties of FeCo nanowire arrays in the full range of compositions from pure Fe to pure Co, for two nanowire diameters.
- To determine the effect of adding Cu into FeCo alloy nanowires and the influence of thermal treatments on the magnetic properties of nanowire arrays.
- Addition of Cu layers between FeCoCu segments to form multilayer nanowires arrays, and determine the influence of the layers/segments thickness/length on the magnetic behavior of the array.
- The study of magnetostatic interactions within the multilayer nanowire array.
- Determination of the magnetization reversal process of individual nanowires with modulated diameter. Study the influence of geometry and crystallographic structure.

- Development of two sensing devices prototypes: position sensor and tachometer, to demonstrate the applicability of magnetic nanowire arrays.
- Study of magnetic properties of NiCu nanowires as function of nanowire composition, diameter and length.
- Template-assisted fabrication of different nanocomposite structures.

1.5. Manuscript outline

The work is structured in seven chapter and two appendices, comprising an introduction, a description of the experimental techniques, the main results and discussions and the final conclusions and future perspectives. They are organized as follows:

- Chapter 2 gathers the techniques used for geometrical, compositional and structural characterization, as well as the techniques employed to perform the magnetic characterization of arrays or isolated nanowires.

- In Chapter 3, the influence of nanowire composition and diameter on the magnetic properties of FeCo cylindrical nanowire arrays has been studied in detail. Furthermore, the effect of adding a small amount of Cu into the alloy and the subsequent annealing on the structural and magnetic properties has been described.

- In Chapter 4, cylindrical multilayer nanowires have been studied. The magnetic properties have been determined as a function of the ferromagnetic/non-ferromagnetic segment/layer length/thickness. Also the intra-wire and inter-wires magnetostatic interactions in the system have been studied and the effect on the magnetic properties has been quantified.

- In Chapter 5, the magnetization configuration and reversal processes of nanowires with tailored diameter modulations along the nanowire length have been established. It has been determined that the shape and magnetocrystalline anisotropies play a determining role on the magnetization reversal processes.

- In Chapter 6 the applicability of magnetic nanowire arrays has been addressed by the description of two sensing devices implementation: a position sensor and a tachometer.

- The main conclusions and future perspectives are collected in Chapter 7.

- Appendix I contains the study of two magnetically soft systems: NiCu nanowire arrays and the nanocomposite formed by Ni nanowires embedded into polystyrene nanotubes. Appendix II describes the synthesis, using the alumina membranes as templates, and the magnetic characterization of multi-walled carbon nanotubes (MWCNTs) filled with magnetic nanoparticles (NPs).

The results included in the different chapters are based on the following publications:

Chapter 3:

- C. Bran, E.M. Palmero, Z-A. Li, R.P. del Real, M. Spasova, M. Farle, and M. Vázquez, "Correlation between structure and magnetic properties in Co_xFe_{100-x} nanowires: role of composition and wire diameter" *J. Phys. D: Appl. Phys*. 48, 145304 (2015).

- C. Bran, E.M. Palmero, R.P. del Real, and M. Vázquez, "CoFeCu electroplated nanowire arrays: Role of composition and annealing on structure and magnetic properties" *Phys. Status Solidi A* 211 (5), 1076–1082 (2014).

- E.M. Palmero, R. Salikhov, U. Wiedwald, C. Bran, M. Spasova, M. Vázquez, and M. Farle, "Enhanced magnetocrystalline anisotropy of $Fe_{30}Co_{70}$ nanowires by Cu additives and annealing" *Nanotechnology* 27, 365704 (2016).

Chapter 4:

- E.M. Palmero, C. Bran, R.P. del Real, C. Magén, and M. Vázquez, "Structural and Magnetic Characterization of FeCoCu/Cu Multilayer Nanowire Arrays" *IEEE Magn. Lett.* 5, 6700304 (2014).

- E.M. Palmero, F. Béron, C. Bran, R.P. del Real, and M. Vázquez, "Magnetic interactions in compositionally modulated nanowire arrays" *Nanotechnology* 27, 435705 (2016).

Chapter 5:

- E.M. Palmero, C. Bran, R.P. del Real, and M. Vázquez, "Vortex domain wall propagation in periodically modulated diameter FeCoCu nanowire as determined by the magneto-optical Kerr effect" *Nanotechnology* 26, 461001 (2015).
- C. Bran, E. Berganza, E.M. Palmero, J.A. Fernández-Roldán, R.P. del Real, L. Aballe, M. Foerster, A. Asenjo, A. Fraile Rodríguez, and M. Vázquez, "Spin configuration of cylindrical bamboo-like magnetic nanowires" *J. Mater. Chem. C* 4, 978–984 (2016).

Chapter 6:

- E.M. Palmero, C. Bran, M. Vázquez, and R.P. del Real, "Magnetic nanowires based sensors", *submitted.*

Appendix I:

- E.M. Palmero, C. Bran, R.P. del Real, C. Magén, and M. Vázquez, "Magnetic behavior of NiCu nanowire arrays: Compositional, geometry and temperature dependence" *J. Appl. Phys.* 116, 033908 (2014).
- B. Sanz, E.M. Palmero, R.P. del Real, M. Vázquez, and C. Mijangos, "Arrays of magnetic Ni nanowires grown inside polystyrene nanotubes" *Ind. Eng. Chem. Res.* 54 (51), 13005–13008 (2015).

Appendix II:

- K. Stojak Repa, D. Israel, J. Alonso, M.H. Phan, E.M. Palmero, M. Vázquez, and H. Srikanth, "Superparamagnetic properties of carbon nanotubes filled with $NiFe_2O_4$ nanoparticles" *J. Appl. Phys.* 117, 17C723 (2015).

This work reports the research made on the synthesis and characterization of FeCo-based nanowire arrays and single nanowires with modulated composition and geometry, fabricated by different anodization techniques and electroplating into the AAO templates. The work has been performed mainly at the Institute of Materials Science of Madrid (ICMM-CSIC), in the Group of Nanomagnetism and Magnetization

Processes. FMR measurements were performed at the University of Duisburg-Essen (Germany), during the research stay granted by the German Academic Exchange Service (DAAD) in the group led by Prof. Michael Farle. Furthermore, HRTEM characterization of FeCo nanowires was performed in collaboration with this group. HRTEM measurements on FeCoCu/Cu multilayer nanowires and NiCu alloy nanowires were carried out in collaboration with the team at the Institute of Materials Science of Aragón in Zaragoza (Dr. César Magén). The synthesis and characterization of Ni nanowires embedded into polystyrene nanotubes was performed in collaboration with the group led by Prof. Carmen Mijangos at the Institute of Polymers Science and Technology (ICTP-CSIC). The synthesis and characterization of multi-walled carbon nanotubes filled with magnetic nanoparticles was performed in collaboration with the research group led by Prof. Hari Srikanth at the University of South Florida (Tampa, USA).

Bibliography

[1] K. Terabe, T. Hasegawa, C. Liang, M. Aono, Control of local ion transport to create unique functional nanodevices based on ionic conductors, *Sci. Technol. Adv. Mat.*, 8 (2007) 536-542.

[2] E. Ferain, R. Legras, Templates for engineered nano-objects for use in microwave, electronic devices and biomedical sensing application, *Nucl. Instrum. Meth. B*, 267 (2009) 1028-1031.

[3] N. Gao, H. Wang, E.-H. Yang, An experimental study on ferromagnetic nickel nanowires functionalized with antibodies for cell separation, *Nanotechnology*, 21 (2010) 105107.

[4] X. Chen, C.K. Wong, C.A. Yuan, G. Zhang, Nanowire-based gas sensors, *Sensors Actuat. B-Chem.*, 177 (2013) 178-195.

[5] D.J. Lee, E. Kim, D. Kim, J. Park, S. Hong, Nano-Storage Wires, *ACS Nano*, 7 (2013) 6906-6913.

[6] R. Lavrijsen, J.-H. Lee, A. Fernández-Pacheco, D.C. Petit, R. Mansell, R.P. Cowburn, Magnetic ratchet for three-dimensional spintronic memory and logic, *Nature*, 493 (2013) 647-650.

[7] K. Gandha, K. Elkins, N. Poudyal, X. Liu, J.P. Liu, High energy product developed from cobalt nanowires, *Sci. Rep*., 4 (2014) 5345.

[8] A. Chałupniak, E. Morales-Narváez, A. Merkoçi, Micro and nanomotors in diagnostics, *Adv. Drug Deliver. Rev.*, 95 (2015) 104-106.

[9] M. Barbic, A. Scherer, Stray field magnetic resonance tomography using ferromagnetic spheres, *J. Magn. Res.*, 181 (2006) 223-228.

[10] T. Eichner, F. Grüner, S. Becker, M. Fuchs, D. Habs, R. Weingartner, U. Schramm, H. Backe, P. Kunz, W. Lauth, Miniature magnetic devices for laser-based, table-top free-electron lasers, *Phys. Rev. Spec Top.-Ac.*, 10 (2007) 082401.

[11] W.K. Peng, L. Chen, J. Han, Development of miniaturized, portable magnetic resonance relaxometry system for point-of-care medical diagnosis, *Rev. Sci. Instrum.*, 83 (2012) 095115.

[12] P.R. Sajanlal, T.S. Sreeprasad, A.K. Samal, T. Pradeep, Anisotropic nanomaterials: structure, growth, assembly, and functions*, Nano Reviews* 2 (2011) 5883.

[13] J. García-Calzón, M.E. Díaz-García, Synthesis and analytical potential of silica nanotubes, *TrAC-Trend. Anal. Chem.*, 35 (2012) 27-38.

[14] M. Colombo, S. Carregal-Romero, M.F. Casula, L. Gutierrez, M.P. Morales, I.B. Boehm, J.T. Heverhagen, D. Prosperi, W.J. Parak, Biological applications of magnetic nanoparticles, *Chem. Soc. Rev*., 41 (2012) 4306-4334.

[15] J.M.D. Coey, Magnetism and magnetic materials, Cambridge University Press, 2010.

[16] J. Zhou, C. Wang, P. Wang, P.B. Messersmith, H. Duan, Multifunctional magnetic nanochains: exploiting self-polymerization and versatile reactivity of mussel-inspired polydopamine, *Chem. Mater.*, 27 (2015) 3071-3076.

[17] S. Eriksson, F. Ramirez-Martinez, E. Curtis, B. Sauer, P. Nutter, E. Hill, E. Hinds, Micron-sized atom traps made from magneto-optical thin films, *Appl. Phys. B*, 79 (2004) 811-816.

[18] K.D. Sattler, Handbook of Nanophysics: Principles and Methods, CRC press, 2010.

[19] A. Biswas, I.S. Bayer, A.S. Biris, T. Wang, E. Dervishi, F. Faupel, Advances in top–down and bottom–up surface nanofabrication: Techniques, applications & future prospects, *Adv. Colloid. Interfac.*, 170 (2012) 2-27.

[20] C. Sousa, D. Leitao, M. Proenca, J. Ventura, A. Pereira, J. Araujo, Nanoporous alumina as templates for multifunctional applications, *Appl. Phys. Rev*., 1 (2014) 031102.

[21] Ph.D. thesis, M.J.P. Proença, Magnetism at the Nanoscale: Nanoparticles, Nanowires, Nanotubes and their Ordered Arrays, (2012).

[22] A. Colli, A. Fasoli, S. Pisana, Y. Fu, P. Beecher, W.I. Milne, A.C. Ferrari, Nanowire lithography on silicon, *Nano Lett*., 8 (2008) 1358-1362.

[23] M. Jaafar, L. Serrano-Ramón, O. Iglesias-Freire, A. Fernández-Pacheco, M.R. Ibarra, J.M. De Teresa, A. Asenjo, Hysteresis loops of individual Co nanostripes measured by magnetic force microscopy, *Nanoscale Res. Lett*., 6 (2011) 1.

[24] S.H. Ko, D. Lee, H.W. Kang, K.H. Nam, J.Y. Yeo, S.J. Hong, C.P. Grigoropoulos, H.J. Sung, Nanoforest of hydrothermally grown hierarchical ZnO nanowires for a high efficiency dye-sensitized solar cell, *Nano Lett.*, 11 (2011) 666-671.

[25] T. Kuykendall, P. Pauzauskie, S. Lee, Y. Zhang, J. Goldberger, P. Yang, Metalorganic chemical vapor deposition route to GaN nanowires with triangular cross sections, *Nano Lett*., 3 (2003) 1063-1066.

[26] P. Rahe, M. Nimmrich, A. Greuling, J. Schütte, I.G. Stará, J.i. Rybáček, G. Huerta-Angeles, I. Starý, M. Rohlfing, A. Kühnle, Toward molecular nanowires self-assembled on an insulating substrate: Heptahelicene-2-carboxylic acid on Calcite (1014), *J. Phys. Chem. C*, 114 (2009) 1547-1552.

[27] F. Chen, Y.-J. Zhu, K.-W. Wang, K.-L. Zhao, Surfactant-free solvothermal synthesis of hydroxyapatite nanowire/nanotube ordered arrays with biomimetic structures, *Cryst. Eng. Comm*., 13 (2011) 1858-1863.

[28] H. Masuda, K. Fukuda, Ordered metal nanohole arrays made by a two-step replication of honeycomb structures of anodic alumina, *Science*, 268 (1995) 1466-1468.

[29] K. Nielsch, J. Choi, K. Schwirn, R.B. Wehrspohn, U. Gösele, Self-ordering regimes of porous alumina: the 10 porosity rule, *Nano Lett.*, 2 (2002) 677-680.

[30] K. Pirota, M. Knobel, M. Hernández-Vélez, K. Nielsch, M. Vázquez, in Handbook of Nanoscience and Nanotechnology, A.V. Narlikar, Y.Y. Fu (eds.) Oxford University Press, USA, 2010.

[31] C. Binns, Nanomagnetism: fundamentals and applications, Newnes, 2014.

[32] D. Jiles, Introduction to magnetism and magnetic materials, CRC press, 2015.

[33] C. Kittel, Physical theory of ferromagnetic domains, *Rev. Mod. Phys*., 21 (1949) 541.

[34] H. Zeng, S. Michalski, R.D. Kirby, D.J. Sellmyer, L. Menon, S. Bandyopadhyay, Effects of surface morphology on magnetic properties of Ni nanowire arrays in self-ordered porous alumina, *J. Phys.-Condens. Mat.*, 14 (2002) 715.

[35] H. Schlörb, V. Haehnel, M.S. Khatri, A. Srivastav, A. Kumar, L. Schultz, S. Fähler, Magnetic nanowires by electrodeposition within templates, *Phys. Status Solidi B*, 247 (2010) 2364-2379.

[36] S. Chikazumi, C. Graham, Physics of Ferromagnetism (International Series of Monographs on Physics; 94), Oxford University Press, 1997.

[37] B.D. Cullity, C.D. Graham, Introduction to magnetic materials, John Wiley & Sons, 2011.

[38] R.C. O'handley, Modern magnetic materials, Wiley, 2000.

[39] Y. Pan, X. Du, F. Zhao, B. Xu, Magnetic nanoparticles for the manipulation of proteins and cells, *Chem. Soc. Rev.*, 41 (2012) 2912-2942.

[40] W. Schuele, V. Deetscreek, Appearance of a weak ferromagnetism in fine particles of antiferromagnetic materials*, J. Appl. Phys.,* 33 (1962) 1136-1137.

[41] H. Bi, S. Li, Y. Zhang, Y. Du, Ferromagnetic-like behavior of ultrafine NiO nanocrystallites, *J. Magn. Magn. Mater.*, 277 (2004) 363-367.

[42] A.H. Lu, E.e.L. Salabas, F. Schüth, Magnetic nanoparticles: synthesis, protection, functionalization, and application, *Angew. Chem. Int. Ed*., 46 (2007) 1222-1244.

[43] A. Prina-Mello, Z. Diao, J.M.D. Coey, Internalization of ferromagnetic nanowires by different living cells, *J. Nanobiotechnology*, 4 (2006) 1.

[44] X. Kou, X. Fan, R.K. Dumas, Q. Lu, Y. Zhang, H. Zhu, X. Zhang, K. Liu, J.Q. Xiao, Memory effect in magnetic nanowire arrays, *Adv. Mater.*, 23 (2011) 1393-1397.

[45] K.M. Pondman, N.D. Bunt, A.W. Maijenburg, R.J. van Wezel, U. Kishore, L. Abelmann, E. Johan, B. ten Haken, Magnetic drug delivery with FePd nanowires, *J. Magn. Magn. Mater.*, 380 (2015) 299-306.

[46] T. Maurer, F. Ott, G. Chaboussant, Y. Soumare, J.-Y. Piquemal, G. Viau, Magnetic nanowires as permanent magnet materials, *Appl. Phys. Lett.,* 91 (2007) 172501.

[47] D. Niarchos, G. Giannopoulos, M. Gjoka, C. Sarafidis, V. Psycharis, J. Rusz, A. Edström, O. Eriksson, P. Toson, J. Fidler, Toward Rare-Earth-Free Permanent Magnets: A Combinatorial Approach Exploiting the Possibilities of Modeling, Shape Anisotropy in Elongated Nanoparticles, and Combinatorial Thin-Film Approach, *JOM*, 67 (2015) 1318-1328.

[48] N. Usov, S. Peschany, Magnetization curling in a fine cylindrical particle, *J. Magn. Magn. Mater.*, 118 (1993) L290-L294.

[49] L. Belliard, J. Miltat, A. Thiaville, S. Dubois, J. Duvail, L. Piraux, Observing magnetic nanowires by means of magnetic force microscopy, *J. Magn. Magn. Mater.*, 190 (1998) 1-16.

[50] R. Hertel, Computational micromagnetism of magnetization processes in nickel nanowires, *J. Magn. Magn. Mater.*, 249 (2002) 251-256.

[51] R. Hertel, J. Kirschner, Magnetization reversal dynamics in nickel nanowires, *Physica B*, 343 (2004) 206-210.

[52] Y.P. Ivanov, O. Chubykalo-Fesenko, Micromagnetic simulations of cylindrical magnetic nanowires, in *Magnetic Nano-and Microwires,* M. Vázquez (ed.), (2015).

[53] X. Zhang, G. Wen, Y. Chan, R. Zheng, X. Zhang, N. Wang, Fabrication and magnetic properties of ultrathin Fe nanowire arrays, *Appl. Phys. Lett.*, 83 (2003) 3341-3343.

[54] M.A. Kashi, A. Ramazani, S. Doudafkan, A. Esmaeily, Microstructure and magnetic properties in arrays of ac electrodeposited Fe_xNi_{1-x} nanowires induced by the continuous and pulse electrodeposition, *Appl. Phys. A*, 102 (2011) 761-764.

[55] M.S. Salem, P. Sergelius, R. Zierold, J.M. Montero Moreno, D. Görlitz, K. Nielsch, Magnetic characterization of nickel-rich NiFe nanowires grown by pulsed electrodeposition, *J. Mater. Chem.,* 22 (2012) 8549-8557.

[56] K. Maaz, S. Karim, M. Usman, A. Mumtaz, J. Liu, J. Duan, M. Maqbool, Effect of crystallographic texture on magnetic characteristics of cobalt nanowires, *Nanoscale Res. Lett.,* 5 (2010) 1111.

[57] L. Vivas, J. Escrig, D. Trabada, G. Badini-Confalonieri, M. Vázquez, Magnetic anisotropy in ordered textured Co nanowires, *Appl. Phys. Lett.*, 100 (2012) 252405.

[58] L. Vivas, Y.P. Ivanov, D. Trabada, M. Proenca, O. Chubykalo-Fesenko, M. Vázquez, Magnetic properties of Co nanopillar arrays prepared from alumina templates, *Nanotechnology,* 24 (2013) 105703.

[59] H. Hu, H. Chen, S. Yu, L. Chen, J. Chen, G. Wu, Fabrication and magnetic properties of Co_xPd_{1-x} composite nanowire, *J. Magn. Magn. Mater*., 299 (2006) 170-175.

[60] S. Shamaila, R. Sharif, S. Riaz, M. Ma, M. Khaleeq-ur-Rahman, X. Han, Magnetic and magnetization properties of electrodeposited fcc CoPt nanowire arrays, *J. Magn. Magn. Mater.*, 320 (2008) 1803-1809.

[61] M. Zeng, H. Yang, J. Liu, R. Yu, Gradient magnetic binary alloy nanowire, *J. Appl. Phys*., 115 (2014) 17B514.

[62] S. Talapatra, X. Tang, M. Padi, T. Kim, R. Vajtai, G. Sastry, M. Shima, S. Deevi, P. Ajayan, Synthesis and characterization of cobalt–nickel alloy nanowires, *J. Mater. Sci.,* 44 (2009) 2271-2275.

[63] M. Vázquez, L.G. Vivas, Magnetization reversal in Co-base nanowire arrays, *Phys. Status Solidi B*, 248 (2011) 2368-2381.

[64] L. Vivas, M. Vazquez, J. Escrig, S. Allende, D. Altbir, D. Leitao, J. Araujo, Magnetic anisotropy in CoNi nanowire arrays: analytical calculations and experiments, *Phys. Rev. B*, 85 (2012) 035439.

[65] V. Vega, T. Böhnert, S. Martens, M. Waleczek, J.M. Montero-Moreno, D. Görlitz, V. Prida, K. Nielsch, Tuning the magnetic anisotropy of Co–Ni nanowires: comparison between single nanowires and nanowire arrays in hard-anodic aluminum oxide membranes, *Nanotechnology*, 23 (2012) 465709.

[66] C. Bran, E. Palmero, Z.-A. Li, R. del Real, M. Spasova, M. Farle, M. Vázquez, Correlation between structure and magnetic properties in Co_xFe_{100-x} nanowires: the roles of composition and wire diameter, *J. Phys. D Appl. Phys.,* 48 (2015) 145304.

[67] M. Yan, A. Kákay, S. Gliga, R. Hertel, Beating the Walker limit with massless domain walls in cylindrical nanowires, *Phys. Rev. Lett.,* 104 (2010) 057201.

[68] J.-G.J. Zhu, C. Park, Magnetic tunnel junctions, *Mater. Today*, 9 (2006) 36-45.

[69] M.H. Kryder, Magnetic thin films for data storage, *Thin Solid Films*, 216 (1992) 174-180.

[70] E. Svoukis, C. Mihailescu, V. Mai, O. Schneegans, K. Breza, C. Lioutas, J. Giapintzakis, Data storage applications based on $LiCoO_2$ thin films grown on Al_2O_3 and Si substrates, *Appl. Surf. Sci*., 381 (2016) 22-27.

[71] M. Yamanouchi, A. Jander, P. Dhagat, S. Ikeda, F. Matsukura, H. Ohno, Domain structure in CoFeB thin films with perpendicular magnetic anisotropy*, IEEE Magn. Lett.*, 2 (2011) 3000304-3000304.

[72] D. Navas, C. Redondo, G.A.B. Confalonieri, F. Batallan, A. Devishvili, O. Iglesias-Freire, A. Asenjo, C.A. Ross, B.P. Toperverg, Domain-wall structure in thin films with perpendicular anisotropy: Magnetic force microscopy and polarized neutron reflectometry study, *Phys. Rev. B*, 90 (2014) 054425.

[73] N. Sun, Y. Zhang, H. Fu, W. Che, C. You, R. Shan, Perpendicular magnetic anisotropy in Mn_2CoAl thin film, *AIP Adv*., 6 (2016) 015006.

[74] A.P. Guimarães, Principles of nanomagnetism, Springer Science & Business Media, 2009.

Chapter 2

Experimental Techniques

2.1. Anodic aluminum oxide templates fabrication

2.1.1. Anodization

The electrodeposition into anodic aluminum oxide (AAO) templates has been proposed as a straightforward route for fabrication of nanostructures with tailored and well-controlled geometries and as an alternative to the nanolithography [1-4]. The fabrication of highly ordered nanostructures such as nanowires, nanotubes, nanodots or antidots using the AAO templates as patterns offers a low-cost route for nanodevices production [5]. These advanced nanoscale systems are strong candidates for a broad range of applications such as high-density magnetic storage, semiconductors, permanent magnets, logic circuits, biomedicine or sensing [6-10]. In particular, highly ordered nanowire arrays have been proposed in a broad spectrum of technological applications as to enhance the high-density magnetic data storage or for specific functionalization in energy and environmental developments [11-15].

The anodization is the passivation or the formation of an oxide layer on the surface of a metal, by electrochemical methods, under controlled conditions, as electrolyte composition and pH, temperature or applied voltage. Several metals can be anodized (e.g. aluminum, titanium, niobium, tantalum, tungsten or zirconium) [16] but in this work, only the anodization of aluminum will be explained in detail as this metal is the used to fabricate all the studied nanowires. The anodization of Al presents some peculiarities in comparison to the other metals, such as the possibility to grow a thick oxide layer (alumina, Al_2O_3), with high pore density. Moreover, under particular

anodization conditions such as electrolyte composition or electrochemical parameters, during the nanopores growing, a self-ordering process takes place giving as a result a honeycomb structure consisting of a close-packed array of columnar alumina units, called cells, containing a central hole (Figure 2.1) [1, 17-19].

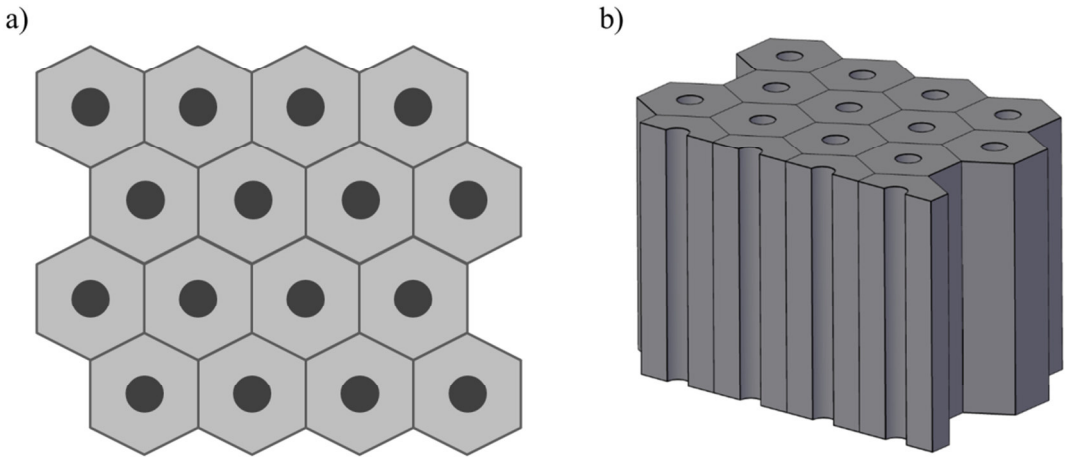

Figure 2.1 Schematic representation of (a) top and (b) 3D view of an AAO template.

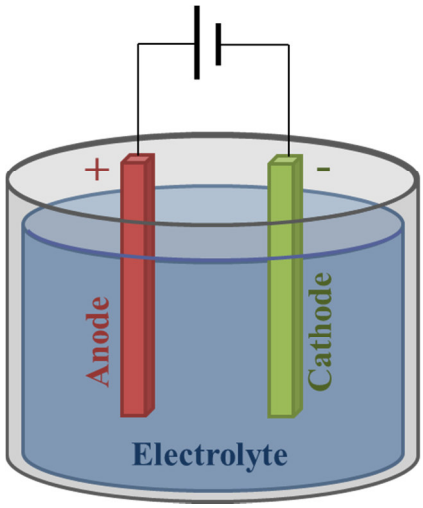

Figure 2.2 Anodization cell.

The anodization is performed in an electrochemical cell where two electrodes (the anode and the cathode) are submerged into the electrolyte. The anode is the metal that will be anodized (in our case, aluminum) and the cathode is made of a chemically resistant metal (in our case, platinum) (see Figure 2.2). Both electrodes are connected by

a power supply that applies a constant voltage, a voltage ramp or voltage pulses, depending on the type of anodization [1, 20-22].

The anodization process consists mainly of two electrochemical reactions: i) the electrical-field-driven oxide formation at the metal/oxide interface; and ii) the oxide dissolution at the electrolyte/oxide interface (Figure 2.3) [5]. The AAO growth relies on the balance between these two reactions. The electrochemical processes which take place can be simplified to [23]:

$$2Al(s) + 3H_2O(l) \rightarrow Al_2O_3(s) + 6H^+(aq) + 6e^- \quad (2.1)$$

and

$$Al_2O_3(s) + 6H^+(aq) \rightarrow 2Al^{3+}(aq) + 3H_2O(l) \quad (2.2)$$

corresponding to the oxide formation (Eq.(2.1)) and dissolution (Eq.(2.2)) at the anode, while hydrogen is released at the cathode by means of the following reaction:

$$2H^+(aq) + 2e^- \rightarrow H_2(g) \quad (2.3)$$

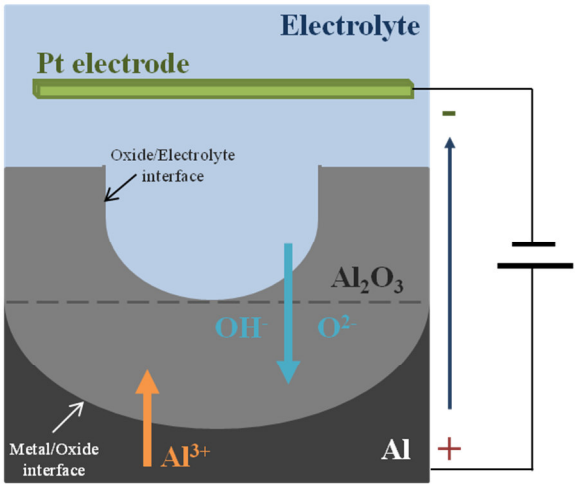

Figure 2.3 Electrochemical processes at the anode (adapted from [5]).

The previously mentioned balance between the oxide formation and its field-assisted dissolution determines the barrier layer thickness, which is the distance between the dashed line and Al substrate in Figure 2.3, and the geometrical parameters of the nanopore array (i.e. pore size and lattice parameter or distance between pore centers).

The long-range ordering of the nanopore array naturally occurs when the anodization conditions are suitable. The anodizing conditions for long-range ordering are characterized by a long-period anodization under the appropriate applied voltage which depends on the electrolyte composition [24]. At the initial stage of the anodization, the nanopore ordering degree is low because they start to develop randomly. In this sense, different anodization processes have been developed to improve the nanopore ordering, such as the two-step anodization [1], suitable pre-texturing [25-27] or pre-anodization and voltage ramp in the case of hard anodization [2, 20]. The two-step and hard anodization processes will be explained in detail in the Sections 2.1.3.1. and 2.1.3.2., respectively.

During the anodization process we have to consider different electrochemical parameters, such as the acidic solution to be used as electrolyte and its concentration, the applied voltage, temperature and time of the experiment. The choice of these parameters allows us to tailor the AAO template geometry and, in consequence, the nanowires geometry grown into the template [2].

The most important parameters to consider for the anodization of Al are the type of electrolyte, applied voltage and temperature. Firstly, the type of electrolyte should be chosen according to desired nanopores geometry, i.e. the diameter and the distance between nanopore centers that finally will be obtained. Usually, acidic aqueous solutions are used as electrolytes [24, 28], such as oxalic ($C_2H_2O_4$), sulfuric (H_2SO_4) or phosphoric (H_3PO_4), these being the most employed acids, but some others are used like glycolic, malonic, tartaric or citric acid [24, 29, 30]. The voltage applied during the anodization between the anode and the cathode also influences the geometrical parameters of the AAO template. Using the proper electrolyte and applied voltage, the nanopore diameter and distance between pore centers can be tuned.

2.1.2. Cleaning and electropolishing of Al foils

Previously to the anodization process (each process is described in detail in the following sections), several steps were needed to prepare a smooth and clean Al foil surface to reduce the inhomogeneities in the sample. In all the preparation processes aqueous solutions were prepared using high purity water (resistivity of 18.2 MΩ·cm at 25 ºC).

Firstly, the Al foils were ultrasonically cleaned in acetone for 10 min followed by 10 min in ethanol. The degreased Al foils were electropolished in a mixed solution of perchloric acid ($HClO_4$: 4.16 M) and ethanol (C_2H_5OH : 12.85 M), under a constant voltage of 20 V for 5 min. Once the surface is polished, we proceed to the anodization (see Section 2.1.3).

2.1.3. Anodization techniques

In order to fabricate hexagonally ordered AAO templates with various geometries, different anodization processes were employed to obtain the desired geometrical characteristics [1, 20-22]. The AAO templates that were used to fabricate the different nanowire arrays presented in this research work were fabricated by three different anodization processes on high purity (99.999%) Al foils:

i) Two-step anodization

ii) Hard anodization

iii) Pulsed anodization

The different anodization processes were carried out using a similar experimental setup (see Figure 2.4(a)), consisting of a Teflon cell in contact with the cooling system through a Cu plate to keep the temperature constant. In this electrochemical process, the Al foil was the anode and the cathode was a Pt mesh. The acidic electrolyte was mechanically stirred to have a constant temperature and pH of the solution during the entire process (see Figure 2.4(b)).

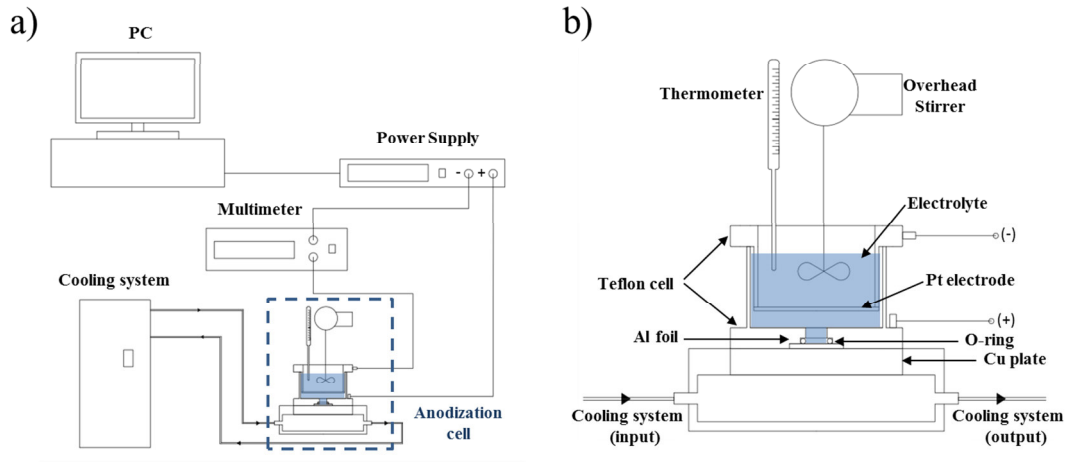

Figure 2.4 (a) Anodization setup and (b) detailed anodization cell.

2.1.3.1. Two-step anodization

The alumina templates with nanopore diameter, d_{NW}, ranging between 20 and 80 nm and with a distance between nanopore centers, D_{int}, of 55 and 105 nm were fabricated using the two-steps anodization process [1].

For alumina membranes with d_{NW} = 20 nm and D_{int} = 55 nm, a sulfuric acid aqueous solution (H_2SO_4 : 2.15 M) was used under an applied constant voltage of 20 V at a temperature of 0-1 ºC for 16 h. The resulting alumina layer was chemically removed using a mixed aqueous solution of chromium oxide (CrO_3 : 0.18 M) and phosphoric acid (H_3PO_4 : 0.72 M). The surface was re-anodized under the same voltage and temperature as in the first anodization, for 3 h.

In the case of templates with d_{NW} ranging between 35 and 80 nm and D_{int} = 105 nm, the anodization was carried out using a oxalic acid aqueous solution ($C_2H_2O_4$: 0.30 M) under a constant applied voltage of 40 V at a temperature of 3 ºC for 24 h and 20 h, first and second anodization step duration, respectively. The alumina layer formed after the first anodization was chemically etched by the CrO_3 : H_3PO_4 solution. To obtain the nanopore diameter in the range of 35 nm < $d_{NW} \leq$ 80 nm, the membranes were immersed in the H_3PO_4 aqueous solution for the time collected in Table 2.1.

Table 2.1 Immersion time and pore diameter obtained for the anodized samples.

Time (min)	40	50	60
d_{NW} (nm)	60	70	80

2.1.3.2. Hard anodization

The alumina templates with d_{NW} ranging between 100 and 150 nm and D_{int} = 320 nm were fabricated by hard anodization process, where a high voltage was used [2, 20]. Prior to the anodization, a pre-anodization using a lower voltage (80 V for 5 min) was performed to create an alumina protective surface to avoid burning the Al foil. After that, the voltage was increased using a voltage ramp (0.08 V/s) until the hard anodization voltage (140 V) was reached and kept constant for 1 h. The different voltages applied during this process are shown in Figure 2.5(a). The hard anodization process was carried out using a mixture of 0.30 M oxalic acid and 0.86 M ethanol aqueous solution at 0-1 ºC. The alumina barrier layer was dissolved and the pores were enlarged submerging the templates in the H_3PO_4 aqueous solution.

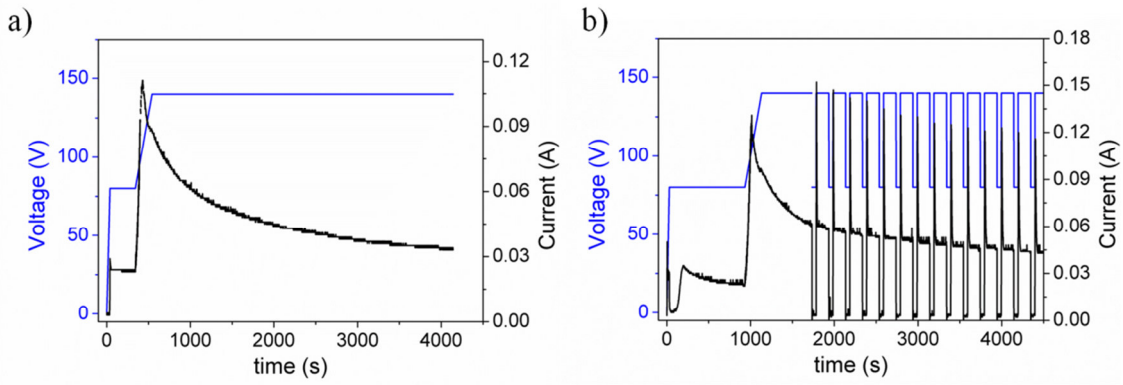

Figure 2.5 (a) Hard and (b) pulsed anodization process.

2.1.3.3. Pulsed anodization

The pulsed anodization was used to fabricate the nanopores with modulated diameter [21, 22]. The solution used for this anodization was a mixture of 0.30 M oxalic acid and 0.86 M ethanol aqueous solution at 0-1 ºC.

The pulsed anodization was performed in two different ways to obtain two different types of modulations. For both types, firstly was carried out a pre-anodization (for the first type, constant voltage of 80 V for 15 min, followed by 5 min at 140 V; and 80 V for 10 min and after that 6 min at 100 V for the second type) and then pulses with different durations in time (pulses of 10 s at 80 V and 30 s at 140 V for the first type; and pulses at 130 V for 5 s and 150 s at 100 V for the second type) were applied. The modulations of the pores are obtained by controlling the duration and the amplitude of the hard anodization pulses. An example of the process is shown in Figure 2.5(b). The alumina barrier layer was removed and the pores were enlarged submerging the templates in the H_3PO_4 aqueous solution at 32 ºC for 150 min.

2.1.4. Removal of alumina barrier layer

For the nanowire electrodeposition, we need the alumina template open at both sides. One of the sides is open due to the anodization, but the other one is covered by residual Al and the alumina barrier layer that we need to remove. Both were chemically etched using different acidic solutions. The remaining Al substrate was removed by a mixed aqueous solution of copper (II) chloride dihydrate ($CuCl_2 \cdot 2H_2O$: 0.10 M) and hydrochloric acid (HCl : 1.64 M). The alumina barrier layer was etched by a phosphoric acid aqueous solution (H_3PO_4 : 0.60 M) at room temperature. For the arrays with pore diameter bigger than 35 nm, the templates were immersed in the same H_3PO_4 aqueous solution at 35 ºC for a period of time that was previously calibrated according to the final pore diameter to obtain.

2.2. Nanowires fabrication

2.2.1. Electrodeposition

The nanowire array fabrication into AAO templates by electrodeposition is an efficient and low-cost technique that allows us the fabrication of high-density magnetic nanowire arrays with high aspect ratio and different composition, crystallographic structures and geometries.

The electrodeposition can be carried out by different modes: constant voltage (potentiostatic mode), constant current (galvanostatic mode) and by alternating voltage or current pulses [5, 10, 31, 32].

For this research work, the nanowire growth was carried out by electrodeposition of the different materials into the alumina nanopores from a sulfate bath in a three-electrode cell under potentiostatic mode at room temperature (Figure 2.6). As the potential was fixed in all the cases, the nanowire lengths and the layer/segment thickness/length were controlled by the electrodeposition time. In this process a Ag/AgCl reference electrode and a Pt mesh as the counter electrode were used.

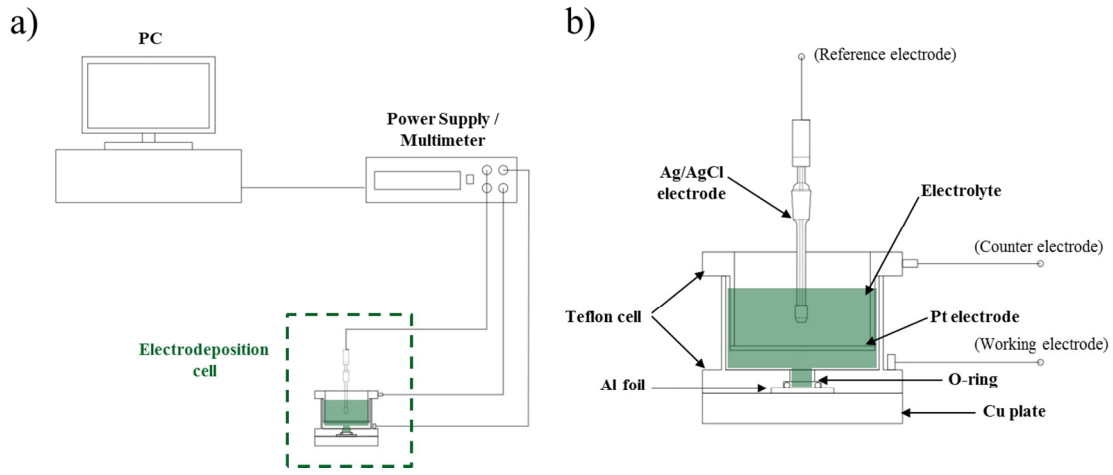

Figure 2.6 (a) Electrodeposition setup and (b) three-electrode cell.

For the electroplating an electrical contact is necessary to act as the working electrode of the cell. This electrode was created by sputtering of a thin Au layer on one side of the template. To ensure the full coverage of the pores, Au was also grown inside the pores by electrodeposition, using a commercial orosene solution as the electrolyte, in potentiostatic mode by applying a constant voltage of -2.4 V for 10 min.

2.2.2. Single element and alloy nanowires

Once the working electrode was created, the electrodeposition was performed using Watts-type baths containing the sulfates and chlorides salts of the different materials that were grown (Ni, Fe and Co as single elements, and FeCo, FeCoCu and NiCu as alloys), under a constant potential. Also, the electrolyte contains boric acid (H_3BO_3) and ascorbic acid ($C_6H_8O_6$), to act as pH buffer and prevent the oxidation, respectively. The pH of the electrolytes was kept constant during the electroplating and, if necessary (e.g. in the case of Co), adjusted using 0.30 M H_2SO_4 or 0.30 M sodium hydroxide (NaOH) aqueous solutions, for decreasing or increasing the pH value, respectively. The bath composition, pH and applied voltage (versus Ag/AgCl reference electrode) used for the electrodeposition of the different single elements and alloys nanowires are collected in Table 2.2.

2.2.3. Multilayer nanowires

The multilayer nanowires studied in this research work were grown by pulsed electrodeposition using a single Watts-type bath. The composition of the bath was the same as for the $Fe_{30}Co_{65}Cu_5$ (labeled FeCoCu in the following) continuous nanowires (see Table 2.2).

The pulsed electrodeposition consisted in applying two different potentials to grow two different compositions from the same electrolytic bath: FeCoCu alloy as the ferromagnetic (FM) segment and Cu as the non-ferromagnetic (NFM) layer. The applied voltages were −1.5 V for FeCoCu segments and −0.3 V for Cu layers, both versus Ag/AgCl reference electrode.

Table 2.2 Bath composition, pH and voltage applied during the electrodeposition.

Composition	Voltage (V vs. Ag/AgCl)	pH	Bath composition
Fe	-1.2	3.0	$FeSO_4 \cdot 7H_2O$ (0.22 M) + H_3BO_3 (0.16 M) + $C_6H_8O_6$ (0.06 M)
Co	-1.5	3.0	$CoSO_4 \cdot 7H_2O$ (0.36 M) + H_3BO_3 (0.16 M)
Ni	-1.0	2.5	0.76 M $NiSO_4 \cdot 6H_2O$ + 0.17 M $NiCl_2 \cdot 6H_2O$ + 0.65 M H_3BO_3
Co_xFe_{100-x} ($0 \leq x \leq 100$)	-1.8	3.0	$CoSO_4 \cdot 7H_2O$ (0.02-0.16 M) + $FeSO_4 \cdot 7H_2O$ (0.02-0.16 M) + H_3BO_3 (0.16 M) + $C_6H_8O_6$ (0.06 M)
$Co_xFe_{95-x}Cu_5$ ($30 \leq x \leq 90$)	-1.8	3.0	$CoSO_4 \cdot 7H_2O$ (0.05-0.16 M) + $FeSO_4 \cdot 7H_2O$ (0.02-0.09 M) + $CuSO_4 \cdot 5H_2O$ (0.01 M) + H_3BO_3 (0.16 M) + $C_6H_8O_6$ (0.06 M)
$Fe_{30}Co_{65}Cu_5$	-1.8	3.0	$CoSO_4 \cdot 7H_2O$ (0.12 M) + $FeSO_4 \cdot 7H_2O$ (0.05 M) + $CuSO_4 \cdot 5H_2O$ (0.01 M) + H_3BO_3 (0.16 M) + $C_6H_8O_6$ (0.06 M)
Ni_xCu_{100-x} ($0 \leq x \leq 75$)	-1.0	2.5	$NiSO_4 \cdot 6H_2O$ (0.35 M) + $CuSO_4 \cdot 5H_2O$ (0-0.06 M) + H_3BO_3 (0.30 M)

Two sets of multilayer nanowire arrays were prepared keeping constant the FeCoCu alloy segment or Cu layer thickness, respectively. In the first series, with constant FeCoCu segments length (25 s electroplating time), the duration of the pulses of Cu deposition varied between 5 and 60 s. In the second series, with constant Cu layer thickness (15 s electroplating time), the duration of the pulses of FeCoCu deposition was varied between 10 and 60 s. In both cases, FeCoCu/Cu bilayers were repeated ten times.

2.2.4. Single nanowires release from AAO template

To obtain single and isolated nanowires, firstly the Au layer was chemically removed from the back side of the samples by a mixed solution of iodine (I_2 : 0.12 M) and potassium iodide (KI : 0.54 M), followed by the dissolution of the alumina template

(Section 2.1.3.1). Once the template was dissolved, the released nanowires were cleaned using high purity water and, finally, they were immersed in ethanol and dispersed on silicon substrate.

2.3. Characterization techniques

2.3.1. Geometrical, structural and compositional characterization

2.3.1.1. Scanning Electron Microscopy (SEM) and Energy Dispersive X-Ray Spectroscopy (EDS)

A Scanning Electron Microscope (SEM), Nova Nano 230, was used to determine the geometry of the nanowires studied in this research work (i.e. nanowire diameter and length, distance between nanowire centers and segment length in modulated nanowires). Also, SEM technique was used to determine the distribution of the nanowires on Si substrate for the following magnetic characterization of single nanowires.

Energy Dispersive X-ray Spectroscopy (EDS) allows the elemental analysis of the sample by the detection and measurement of the X-ray radiation emitted by the sample, which is characterized by specific wavelengths and energies depending on the nature of the atoms in the specimen.

For more detailed information about SEM and EDS techniques, the reader is referred to Refs. [33-35].

2.3.1.2. X-Ray Diffraction (XRD)

The crystallographic structure of the nanowires studied in this thesis was established by means of an X-ray Diffractometer (XRD), PANalytical X'pert Pro, in Bragg-Brentano geometry and with Cu-Kα_1 radiation.

When an incident beam of monochromatic X-rays interacts with a material, those X-rays are scattered from atoms within the material. If the material presents a regular structure (i.e. crystalline materials), the scattered X-rays undergo constructive

and destructive interferences. When the interaction between the incident beam and the crystalline material originates constructive interference, the diffraction condition is satisfied and X-ray diffraction process is described by Bragg's law.

Bragg's law relates the wavelength of the electromagnetic radiation to the diffraction angle and the lattice parameter in a crystalline material:

$$2d \sin\theta = n\lambda \tag{2.4}$$

where d is the distance between crystallographic planes, θ is the diffraction angle, n is a positive integer and λ is the wavelength of the incident wave (in our case, for CuK_{α}, $\lambda = 1.54060$ Å).

Moreover, the lattice parameter of a particular crystallographic system, a, can be obtained using the following equation:

$$d = \frac{a}{\sqrt{h^2 + k^2 + l^2}} \tag{2.5}$$

where h, k and l are the Miller indices for planes in crystal lattices.

Polycrystalline materials are composed of many tiny crystallites randomly oriented in all possible orientations. In this case, all possible diffraction peaks can be detected by scanning the sample in configuration θ - 2θ angle.

From an XRD spectra several parameters can be obtained, which provide information about the crystalline structure and grain size of the material: peak positions, intensities, widths and shapes. The obtained peaks usually are compared to standard reference patterns to determine the crystallographic structure of the studied sample.

2.3.1.3. Transmission Electron Microscopy (TEM)

The compositional and structural characterization of FeCo nanowires was performed by High Resolution Transmission Electron Microscopy (HRTEM) using a FEI Tecnai F20 microscope (200 kV), equipped with an EDS spectrometer, located at the University of Duisburg – Essen, Duisburg (Germany).

The morphological and microstructure characterization of the multilayer nanowires and the NiCu nanowires was carried out by HRTEM and Selected Area Electron Diffraction (SAED) in an image-corrected FEI Titan Cube 60-300, at the Advanced Microscopy Laboratory (LMA) of the Institute of Nanoscience of Aragón (INA) - ARAID, Zaragoza (Spain).

2.3.2. Magnetic characterization

2.3.2.1. Vibrating Sample Magnetometry (VSM)

The measurement of the magnetic moment of a nanowire array depending on the applied magnetic field has been performed by a Vibrating Sample Magnetometer (VSM). The working principle of the VSM is based on Faraday's law of electromagnetic induction. The measurement is performed by attaching the sample to a non-ferromagnetic rod which vibrates and placing it between an electromagnet that applies a magnetic field. The plot of the applied magnetic field together with the corresponding magnetization of the sample results in a hysteresis loop from which we can obtain different magnetic properties to compare between samples, as coercive field (H_c), magnetic moment at saturation (m_s) or at remanence (m_r), among others.

With a VSM it is also possible to obtain information about the magnetic interactions that take place in a magnetic nanowire array by the First-Order Reversal Curve (FORC) technique. The FORC method was based on the classical Preisach model [36], a mathematical model where hysteresis can be modeled as a set of elementary processes called hysterons and characterized by two mathematical parameters: the coercive field ($\mu_0 H_c$) and the interaction field ($\mu_0 H_u$) (Figure 2.7).

For the FORC technique, firstly the major hysteresis loops were measured to determine the saturation field ($\mu_0 H_{sat}$), required to magnetically saturate the nanowire arrays in the positive direction which will be taken as the starting point for the FORC measurement. The FORC minor hysteresis loops were obtained inside the hysteresis area, under a maximum applied magnetic field ($\mu_0 H_{max}$). The hysteresis loops are recorded using a specific field step ($\mu_0 \Delta H$) and reversal field step ($\mu_0 \Delta H_r$).

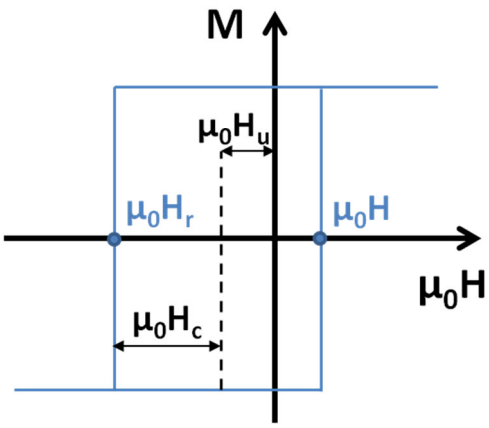

Figure 2.7 Mathematical hysteron from the classical Preisach model (adapted from [37]).

The FORC distribution (ρ_{FORC}) is calculated as the second-order mixed derivative of $M(H, H_r)$ with respect to H and H_r [38]:

$$\rho_{FORC}(H, H_r) = -\frac{1}{2}\frac{\partial^2 M(H, H_r)}{\partial H \partial H_r} \quad (H > H_r) \tag{2.6}$$

The FORC distribution can be represented graphically by a contour plot with a color scale ranging between $\rho_{FORC,\ min}$ and $\rho_{FORC,\ max}$, indicating the statistical distribution of the mathematical hysterons. In this graph, the x-axis and the y-axis correspond to $\mu_0 H$ and $\mu_0 H_r$, respectively. In order to extract directly the coercive field ($\mu_0 H_c$) and the interaction field ($\mu_0 H_u$) mathematical hysteron parameters from the graph, a new set of coordinates are included, defined as follow [39]:

$$\mu_0 H_c = \mu_0 \left(\frac{H - H_r}{2}\right), \qquad H_u = -\mu_0 \left(\frac{H + H_r}{2}\right) \tag{2.7}$$

For the process to obtain the FORCs, the sample is firstly saturated in the positive direction, then the magnetic field ($\mu_0 H$) is reduced to the minimum reversal field ($\mu_0 H_{min}$ = - $\mu_0 H_{max}$). Then, the field is increased again according to $\mu_0 \Delta H$ and the magnetization (M) is measured. To cover all the hysteresis area, the reversal field ($\mu_0 H_r$) is taken from $\mu_0 H_{min}$ to $\mu_0 H_{max}$, using the step $\mu_0 \Delta H_r$. After the measurement, the FORC

distribution is plotted and analyzed according to the influence of the studied parameters. A typical FORC curve and FORC distribution plot is shown in Figure 2.8.

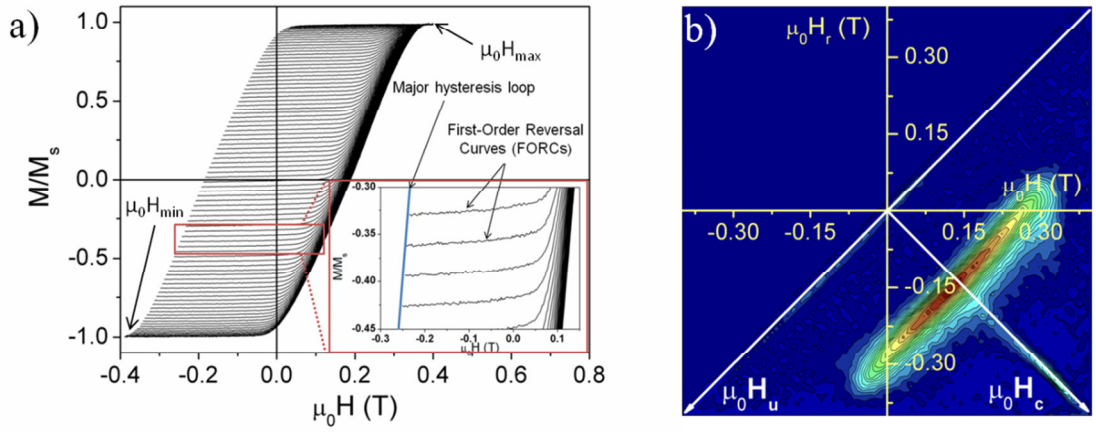

Figure 2.8 (a) VSM measurement on magnetic nanowire array. The inset corresponds to a zoom in of the measurement, where the blue line is the major hysteresis loop and the black ones are the FORC curves; and (b) corresponding FORC distribution plot (adapted from [40]).

All the hysteresis loops measured to study the samples for this thesis has been obtained in a VSM ADE system EV7 KLA-Tencor, where it is possible to apply a maximum magnetic field of ± 1.8 T.

2.3.2.2. Magneto-Optical Kerr Effect (MOKE)

The study of the magnetic behavior of single nanowires with constant diameter and with diameter modulations has been carried out by Magneto-Optical Kerr Effect (MOKE).

The Kerr effect consist in the change of the polarization and the intensity of the light reflected from a magnetized surface. There are three types of MOKE depending of the direction of the magnetization vector with respect to the reflecting surface and the plane of incidence (Figure 2.9). If the magnetization vector is perpendicular to the reflection surface and parallel to the plane of incidence of the light, it is called *polar* MOKE. When the magnetization is parallel to the reflection surface and also to the plane of incidence of the light, the effect is called *longitudinal* MOKE. And the *transversal* MOKE takes place when the magnetization lies parallel to the surface and perpendicular to the plane of incidence of the light.

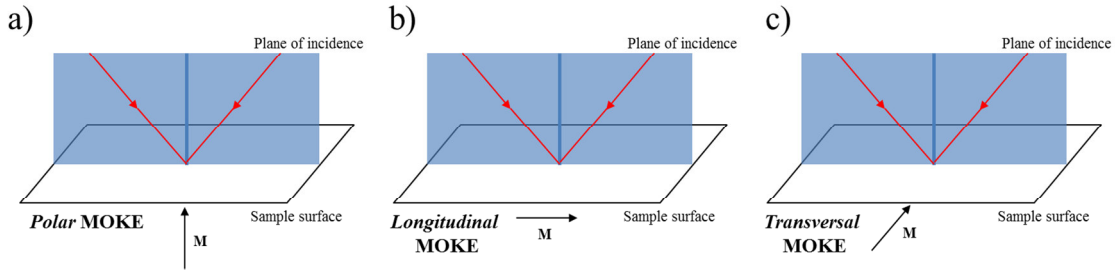

Figure 2.9 Types of Magneto-Optical Kerr effect (adapted from [41]).

The single nanowires have been measured by a Kerr effect magnetometer NanoMOKE^{TM} 2 from Durham Magneto Optics Ltd. The experimental setup consists on a laser diode (nominal laser spot of 3 µm, wavelength of 658 nm and power 7.5 mW) that emits laser light which is polarized and then goes through the light splitter. The system has also objective lens to focus the light coming from the laser on the sample surface. In this case, the magnetic surface is an isolated nanowire on a Si substrate. After the laser reaches the surface, the light is reflected and focused again by the receiving lens to the *longitudinal* Kerr detector. Before reaching the detector the light passes a quarter-wave plate which removes the circular component of the light and an analyzer that filters the component perpendicular to the filter direction. In this way, the intensity of the light that reaches the detector is directly related to the magnetization of the nanowire. The magnetic field is applied using a quadrupole electromagnet, being the maximum applied field of ± 500 Oe.

2.3.2.3. Ferromagnetic Resonance (FMR)

Ferromagnetic Resonance (FMR) has been proved to be an effective technique to quantitatively determine the magnetic anisotropy in ferromagnetic systems, particularly in ferromagnetic nanowire arrays [42-44].

FMR measurements were performed using a conventional X-band FMR spectrometer, Bruker BioSpin ELEXSYS E 500 (Figure 2.10(a)). The equipment belongs to the research group of Prof. Michael Farle at the University of Duisburg - Essen, Germany. The spectrometer is composed mainly by four parts: (i) a microwave bridge, where we find the electromagnetic radiation source and the detector; (ii) a

microwave cavity, a metal box where the sample is placed and used to amplify the signal of the sample; (iii) a electromagnet for applying the magnetic field; (iv) a console, containing the signal processing and control electronics; and (v) a computer, for controlling all the units to acquire the FMR spectrum and analyzing the data.

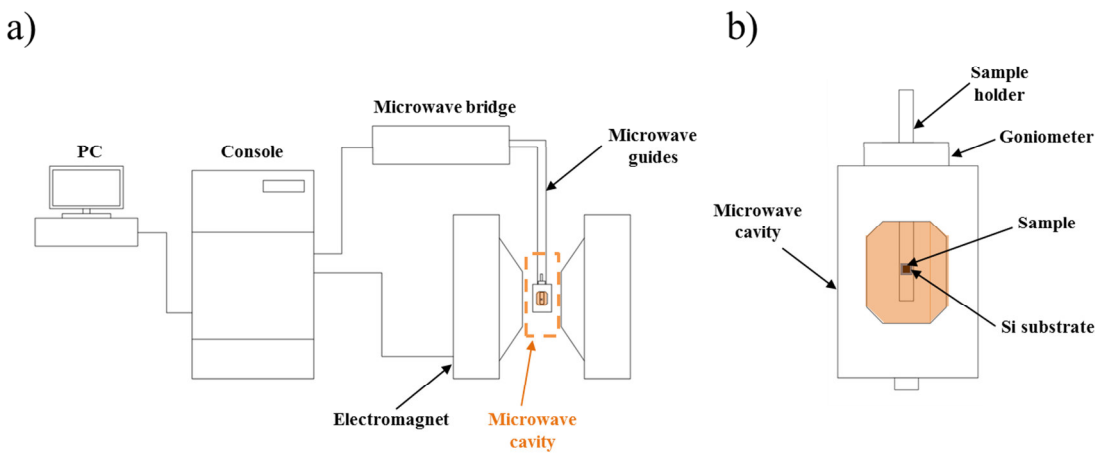

Figure 2.10 (a) Sketch showing the FMR equipment and (b) microwave cavity.

The microwave signal generated by the electromagnetic radiation source can be adjusted by the attenuator in the microwave bridge to control the power that the sample sees in the cavity. The microwave cavity is a metal box (with a rectangular shape in our case) that resonates with the microwaves (Figure 2.10(b)), i.e. stores the microwaves, which remain in the cavity not being reflected back at its resonance frequency. The quality factor of the cavity, Q, indicates how efficiently the cavity stores the microwave energy. The sensitivity of the spectrometer increases with Q. For all our measurements the quality factor had a value ranging between 3000 and 4000.

When the microwaves go through the cavity, a part of the radiation is reflected back from the microwave cavity containing the sample. The reflected microwaves are directed to the detector in the bridge, that consists on a Schottky barrier diode which converts the microwave power to an electrical current. Then, the spectrometer, by this current, measures the changes in the amount of radiation that is reflected. By sweeping the magnetic field that is applied to the sample, we obtain the first derivative of the FMR absorption power (W) as a function of the applied magnetic field, dW/dH. A

typical FMR spectra is shown in Figure 2.11. The parameters to be considered for the studies included in this thesis are the resonance field (H_r) and the linewidth (ΔH). H_r corresponds to the field value which equals dW/dH to zero and ΔH to the difference between the field values for the maxima and the minima of the FMR spectra.

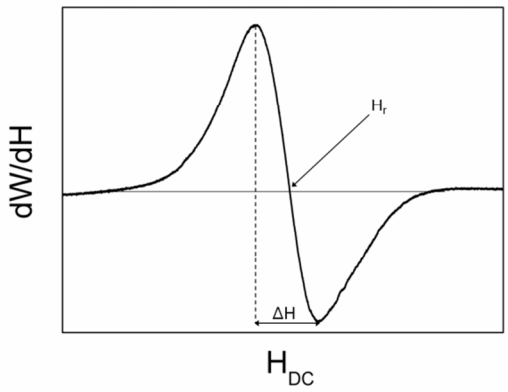

Figure 2.11 Typical FMR spectra for a nanowire array.

For the FMR characterization of the nanowire arrays, the microwave frequency, f, was adjusted to 9.49 GHz and kept fixed for all the measurements. The FMR spectra were recorded by sweeping the applied magnetic field, H_{DC}, from $\mu_0 H_{DC}$ = 1.2 T down to zero, using two different configurations: (i) in the first one (Figure 2.12(a)), the magnetic field, H_{DC}, was applied varying the angle between the magnetic field and the nanowire axis (θ_H) from parallel (θ_H = 0º) to perpendicular (θ_H = 90º), while the microwave field, h_{rf}, was applied perpendicular to the nanowire axis; and (ii) in the second one (Figure 2.12(b)), H_{DC} and h_{rf} were applied perpendicular and parallel to the nanowire axis, respectively.

For the measurements, a piece of each sample containing the nanowire array was cut into squared shape, 2 mm x 2 mm, and glued on a Si substrate. The sample was attached to a rod connected to a goniometer which allowed rotating the sample 360º.

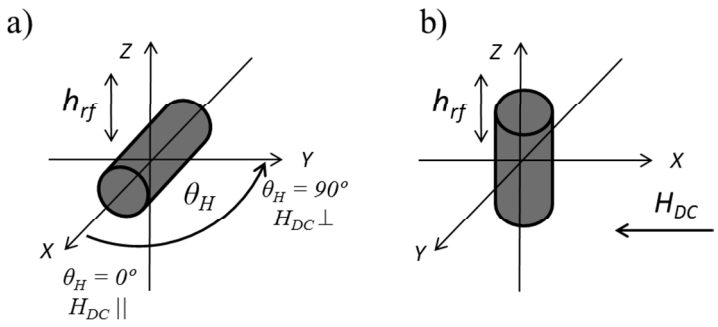

Figure 2.12 Sketch showing the FMR configurations for one nanowire, including the orientation of the applied magnetic field, H_{DC}, and the microwave field, h_{rf}.

2.3.2.4. X-Ray Magnetic Circular Dichroism - Photoemission Electron Microscopy (XMCD - PEEM)

The XMCD-PEEM measurements were performed at the CIRCE beamline at the ALBA Synchrotron Light Facility (Barcelona, Spain). The beamline is based on a collimated-light plane-grating monochromator [45], which provides soft X-ray high energy resolution and intensity photons covering the energy range from 100 to 2000 eV. The source of CIRCE is a pure permanent magnet APPLE II helical undulator which allows the light full polarization control (linearly polarized light in any directions, as well as circularly polarized light) [46]. The microscope can be operated as Low Energy Electron Microscope (LEEM), Low Energy Electron Diffraction (LEED) and Photoemission Electron Microscope (PEEM, X or UV).

The end station used for our experiments is based on a Elmitec LEEM/PEEM III microscope with electron imaging energy analyzer, and provided with a LaB_6 electron gun for LEEM [47]. The station is formed by five separable ultrahigh-vacuum (10^{-6} mbar) sections: load lock, entrance, preparation and main chambers, and electron optics. During the measurements, the samples, placed in the main chamber, are illuminated with circularly polarized X-rays at a 16º near-grazing incidence angle with respect to the surface (in our case, single nanowires dispersed on a Si substrate) (Figure 2.13). In PEEM mode, in order to form the image, the electrons emitted after excitation with the photon source are collected [48]. A micro channel plate intensifies the image formed by the electron-optical lens system and then, it is detected on a phosphor screen by an in-air CCD camera [47].

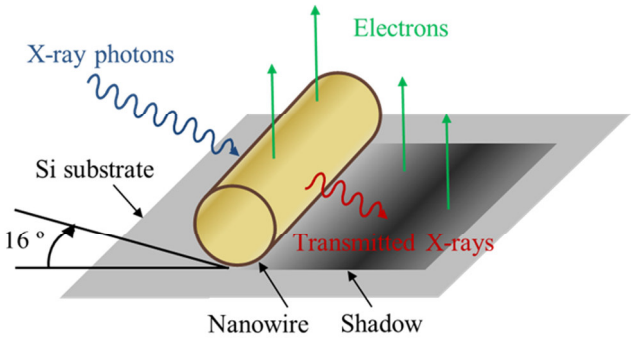

Figure 2.13 Principle of the dual sensitivity of PEEM to detect direct photoemission and transmission data using XMCD as a contrast mechanism (adapted from [49]).

The fully variable light polarization allows magnetic imaging by the X-ray magnetic circular and linear dichroism effects (XMCD and XMLD, respectively). The ferromagnetic or anti-ferromagnetic contrast can be revealed using the appropriate resonant L_3 absorption edges [50]. For our nanowires, we used the absorption edges of Fe (708 eV) and Co (778 eV). The emitted photoelectrons used to form the surface image are proportional to the X-ray absorption coefficient. In this way, after recording sequentially two PEEM images with left- and right-handed circular polarization and considering the pixel-wise asymmetry between them, the element-specific magnetic domain configuration is obtained [51]. In the XMCD image, ferromagnetic domains with magnetic moments parallel or antiparallel to the X-ray polarization vector appear bright or dark, while domains with magnetic moments at a different angle have an intermediate gray contrast. The photo-electron escape depth is around 5 nm limiting the information to the sample surface. On the other hand, the X-ray penetration depth is much larger, being the X-ray photons transmitted through the nanowire and generating photoemission from the Si substrate (shadow in the sketch in Figure 2.13). The circular dichroic or pseudo-magnetic contrast formed in transmission in the nanowire shadow can be analyzed and it is possible to obtain information about the spin configuration in the bulk of the nanowire [52]. In the study of the obtained images, we need to consider that the absorbed and transmitted X-rays are complementary. Consequently, the dark contrast in transmission is equivalent to bright contrast in photoemission.

Bibliography

[1] H. Masuda, K. Fukuda, Ordered metal nanohole arrays made by a two-step replication of honeycomb structures of anodic alumina, *Science*, 268 (1995) 1466-1468.

[2] W. Lee, R. Ji, U. Gösele, K. Nielsch, Fast fabrication of long-range ordered porous alumina membranes by hard anodization, *Nat. Mater*., 5 (2006) 741-747.

[3] D. Losic, D. Losic Jr, Preparation of porous anodic alumina with periodically perforated pores, *Langmuir*, 25 (2009) 5426-5431.

[4] B. Platschek, A. Keilbach, T. Bein, Mesoporous structures confined in anodic alumina membranes, *Adv. Mater.,* 23 (2011) 2395-2412.

[5] C. Sousa, D. Leitao, M. Proenca, J. Ventura, A. Pereira, J. Araujo, Nanoporous alumina as templates for multifunctional applications, *Appl. Phys. Rev.,* 1 (2014) 031102.

[6] T. Maurer, F. Ott, G. Chaboussant, Y. Soumare, J.-Y. Piquemal, G. Viau, Magnetic nanowires as permanent magnet materials, *Appl. Phys. Lett*., 91 (2007) 172501.

[7] T. Song, H. Cheng, H. Choi, J.-H. Lee, H. Han, D.H. Lee, D.S. Yoo, M.-S. Kwon, J.-M. Choi, S.G. Doo, Si/Ge double-layered nanotube array as a lithium ion battery anode, *ACS Nano*, 6 (2011) 303-309.

[8] X. Chen, C.K. Wong, C.A. Yuan, G. Zhang, Nanowire-based gas sensors, *Sensor Actuat. B-Chem.,* 177 (2013) 178-195.

[9] R. Lavrijsen, J.-H. Lee, A. Fernández-Pacheco, D.C. Petit, R. Mansell, R.P. Cowburn, Magnetic ratchet for three-dimensional spintronic memory and logic, *Nature*, 493 (2013) 647-650.

[10] G. Ma, X. Wang, Synthesis and Applications of One-Dimensional Porous Nanowire Arrays: A Review, *Nano*, 10 (2015) 1530001.

[11] S.S. Parkin, M. Hayashi, L. Thomas, Magnetic domain-wall racetrack memory, *Science*, 320 (2008) 190-194.

[12] A. Mourachkine, O. Yazyev, C. Ducati, J.-P. Ansermet, Template nanowires for spintronics applications: nanomagnet microwave resonators functioning in zero applied magnetic field, *Nano Lett.,* 8 (2008) 3683-3687.

[13] E. Ferain, R. Legras, Templates for engineered nano-objects for use in microwave, electronic devices and biomedical sensing application, *Nucl. Instrum. Meth. B*, 267 (2009) 1028-1031.

[14] N. Gao, H. Wang, E.-H. Yang, An experimental study on ferromagnetic nickel nanowires functionalized with antibodies for cell separation, *Nanotechnology*, 21 (2010) 105107.

[15] X. Kou, X. Fan, R.K. Dumas, Q. Lu, Y. Zhang, H. Zhu, X. Zhang, K. Liu, J.Q. Xiao, Memory effect in magnetic nanowire arrays, *Adv. Mater.,* 23 (2011) 1393-1397.

[16] P. Schmuki, Self-organized oxide nanotube layers on titanium and other transition metals, in: Electrochemistry at the Nanoscale, Springer, 2009, pp. 435-466.

[17] F. Keller, M. Hunter, D. Robinson, Structural features of oxide coatings on aluminum, *J. Electrochem. Soc.,* 100 (1953) 411-419.

[18] G. Thompson, R. Furneaux, G. Wood, J. Richardson, J. Goode, Nucleation and growth of porous anodic films on aluminium*, Nature*, 272 (1978) 433-435.

[19] K. Nielsch, J. Choi, K. Schwirn, R.B. Wehrspohn, U. Gösele, Self-ordering regimes of porous alumina: the 10 porosity rule, *Nano Lett.,* 2 (2002) 677-680.

[20] V. Vega, T. Böhnert, S. Martens, M. Waleczek, J.M. Montero-Moreno, D. Görlitz, V. Prida, K. Nielsch, Tuning the magnetic anisotropy of Co–Ni nanowires: comparison between single nanowires and nanowire arrays in hard-anodic aluminum oxide membranes, *Nanotechnology,* 23 (2012) 465709.

[21] M.S. Salem, P. Sergelius, R.M. Corona, J. Escrig, D. Görlitz, K. Nielsch, Magnetic properties of cylindrical diameter modulated Ni 80 Fe 20 nanowires: interaction and coercive fields, *Nanoscale*, 5 (2013) 3941-3947.

[22] I. Minguez-Bacho, S. Rodriguez-López, M. Vázquez, M. Hernández-Vélez, K. Nielsch, Electrochemical synthesis and magnetic characterization of periodically modulated Co nanowires, *Nanotechnology*, 25 (2014) 145301.

[23] J.W. Diggle, T.C. Downie, C. Goulding, Anodic oxide films on aluminum, *Chem. Rev*., 69 (1969) 365-405.

[24] H. Masuda, Highly Ordered Nanohole Arrays in Anodic Porous Alumina, in: R.B. Wehrspohn (Ed.) Ordered Porous Nanostructures and Applications, Springer, 2005, pp. 37-55.

[25] H. Masuda, H. Yamada, M. Satoh, H. Asoh, M. Nakao, T. Tamamura, Highly ordered nanochannel-array architecture in anodic alumina, *Appl. Phys. Lett.,* 71 (1997) 2770-2772.

[26] H. Asoh, K. Nishio, M. Nakao, A. Yokoo, T. Tamamura, H. Masuda, Fabrication of ideally ordered anodic porous alumina with 63 nm hole periodicity using sulfuric acid, *J. Vac. Sci. Technol*., 19 (2001) 569-572.

[27] K.-L. Lai, M.-H. Hon, C. Leu, Fabrication of ordered nanoporous anodic alumina prepatterned by mold-assisted chemical etching, *Nanoscale Res. Lett.,* 6 (2011) 1-6.

[28] F. Li, L. Zhang, R.M. Metzger, On the growth of highly ordered pores in anodized aluminum oxide, *Chem. Mater.,* 10 (1998) 2470-2480.

[29] S. Ono, M. Saito, H. Asoh, Self-ordering of anodic porous alumina formed in organic acid electrolytes, *Electrochim. Acta*, 51 (2005) 827-833.

[30] S. Chu, K. Wada, S. Inoue, M. Isogai, Y. Katsuta, A. Yasumori, Large-scale fabrication of ordered nanoporous alumina films with arbitrary pore intervals by critical-potential anodization, *J. Electrochem. Soc*., 153 (2006) B384-B391.

[31] G. Kartopu, O. Yalçın, Fabrication and applications of metal nanowire arrays electrodeposited in ordered porous templates, INTECH Open Access Publisher, 2010.

[32] E. Matei, I. Enculescu, M.E. Toimil-Molares, A. Leca, C. Ghica, V. Kuncser, Magnetic configurations of Ni–Cu alloy nanowires obtained by the template method, *J. Nanopart. Res.,* 15 (2013) 1-9.

[33] W. Nixon, The general principles of scanning electron microscopy, *Philos. T. Roy. Soc. B*, 261 (1971) 45-50.

[34] I.M. Watt, The principles and practice of electron microscopy, Cambridge University Press, 1997.

[35] P.J. Goodhew, J. Humphreys, R. Beanland, The Scanning electron microscope, in: Electron microscopy and analysis, Taylor & Francis, London, 2001.

[36] F. Preisach, Über die magnetische Nachwirkung, Zeitschrift für physik, 94 (1935) 277-302.

[37] F. Béron, A. Yelon, D. Ménard, L.-P. Carignan, Extracting individual properties from global behaviour: first-order reversal curve method applied to magnetic nanowire arrays, INTECH Open Access Publisher, 2010.

[38] I.D. Mayergoyz, Mathematical models of hysteresis, *Phys. Rev. Lett.,* 56 (1986) 1518-1521.

[39] F. Béron, L. Clime, M. Ciureanu, D. Ménard, R. Cochrane, A. Yelon, Magnetostatic interactions and coercivities of ferromagnetic soft nanowires in uniform length arrays, *J. Nanosci. Nanotechno*., 8 (2008) 2944-2954.

[40] E.M. Palmero, F. Béron, C. Bran, R.P. del Real, M. Vázquez, Magnetic interactions in compositionally modulated nanowire arrays, *Nanotechnology*, 27 (2016) 435705.

[41] T.C. Oakberg, Photoelastic Modulators. Magneto-optic Kerr Effect, (2013).

[42] A. Encinas-Oropesa, M. Demand, L. Piraux, I. Huynen, U. Ebels, Dipolar interactions in arrays of nickel nanowires studied by ferromagnetic resonance, *Phys. Rev. B*, 63 (2001) 104415.

[43] U. Ebels, J.-L. Duvail, P. Wigen, L. Piraux, L. Buda, K. Ounadjela, Ferromagnetic resonance studies of Ni nanowire arrays, *Phys. Rev. B*, 64 (2001) 144421.

[44] M. Darques, A. Encinas, L. Vila, L. Piraux, Tailoring of the c-axis orientation and magnetic anisotropy in electrodeposited Co nanowires, *J. Phys.-Condens. Mat.*, 16 (2004) S2279.

[45] R. Follath, F. Senf, New plane-grating monochromators for third generation synchrotron radiation light sources, *Nucl. Instrum. Meth. A*, 390 (1997) 388-394.

[46] S. Sasaki, Analyses for a planar variably-polarizing undulator, *Nucl. Instrum. Meth. A*, 347 (1994) 83-86.

[47] L. Aballe, M. Foerster, E. Pellegrin, J. Nicolas, S. Ferrer, The ALBA spectroscopic LEEM-PEEM experimental station: layout and performance, *J. Synchrotron Rad.*, 22 (2015) 745-752.

[48] B.P. Tonner, G. Harp, Photoelectron microscopy with synchrotron radiation, *Rev. Sci. Instrum.,* 59 (1988) 853-858.

[49] J. Kimling, F. Kronast, S. Martens, T. Böhnert, M. Martens, J. Herrero-Albillos, L. Tati-Bismaths, U. Merkt, K. Nielsch, G. Meier, Photoemission electron microscopy of three-dimensional magnetization configurations in core-shell nanostructures, *Phys. Rev. B*, 84 (2011) 174406.

[50] S. Anders, H.A. Padmore, R.M. Duarte, T. Renner, T. Stammler, A. Scholl, M.R. Scheinfein, J. Stöhr, L. Séve, B. Sinkovic, Photoemission electron microscope for the study of magnetic materials, *Rev. Sci. Instrum.*, 70 (1999) 3973-3981.

[51] A. Scholl, H. Ohldag, F. Nolting, J. Stöhr, H.A. Padmore, X-ray photoemission electron microscopy, a tool for the investigation of complex magnetic structures, *Rev. Sci. Instrum.*, 73 (2002) 1362-1366.

[52] S. Da Col, S. Jamet, N. Rougemaille, A. Locatelli, T. Mentes, B.S. Burgos, R. Afid, M. Darques, L. Cagnon, J.-C. Toussaint, Observation of Bloch-point domain walls in cylindrical magnetic nanowires, *Phys. Rev. B*, 89 (2014) 180405.

Chapter 3

Magnetically Hard Alloy: FeCo-based Nanowires

$Fe_{100-x}Co_x$ cylindrical nanowire arrays ranging in composition $0 \leq x \leq 100$, with diameter of 20 and 40 nm have been grown by electrochemical route into self-ordered anodic aluminum oxide templates. The crystallographic structure and the magnetic properties dependences on nanowire composition and diameter have been studied. Furthermore, the research herein reported describes the effect of the addition of a non-ferromagnetic element such as Cu into the FeCo alloy and the subsequent thermal treatment on the magnetic and structural properties of the nanowire arrays.

3.1. Introduction

For applications as permanent magnets (PMs) [1, 2], nanowire arrays need to be axially magnetized to obtain the highest energy product, $(BH)_{max}$, which requires a high remanence (B_r) and a large coercive field ($\mu_0 H_c$). In this regard, *3d* transition metal-based magnetic nanowires with a large aspect ratio (i.e. nanowire length-to-diameter, $L_{NW} / d_{NW} > 10$), have been proposed as suitable candidates [1]. These alloys usually have high Curie temperatures (which makes them appropriate for technological applications at elevated temperatures) and large saturation magnetization ($\mu_0 M_s$) due to the large magnetic moment of *3d* atoms, which leads to a strong magnetic shape anisotropy in nanowires with high aspect ratio. Consequently, nanowire arrays will show a high remanent magnetization and large coercive field. However, the demagnetizing dipolar interactions between neighboring nanowires in highly packed nanowire arrays reduce the maximum energy product [3]. To overcome this effect, an

enhanced axial magnetocrystalline anisotropy energy (MAE) is needed to favor the magnetic easy axis parallel to the nanowire [4, 5]. The magnetic anisotropy of nanowires is determined by the composition and the balance between shape, magnetocrystalline and magnetoelastic anisotropy terms. Among the *3d* metals, according to the Slater-Pauling curve [6], FeCo binary alloys have the largest saturation magnetization yielding the largest shape anisotropy, and, in this sense, they have been proposed as a novel group of alternative rare-earth free PMs [7, 8].

The magnetization reversal in cylindrical nanowires with uniaxial anisotropy parallel to the nanowire axis is driven by the nucleation of domain walls at their ends which subsequently propagate along the entire nanowires upon application of a critical switching field [9, 10]. For nanowires with strong perpendicular anisotropy, the magnetization reversal takes place in two steps: a nearly reversible rotation in the shell and a vortex in the core [10]. The contribution of both modes is affected by the nanowire crystalline structure and geometry (i.e. nanowire diameter and length) [11-13]. Tuning these parameters, we could tailor the magnetic properties of FeCo nanowire arrays in order to get the highest values of coercive field and remanent magnetization.

Furthermore, it is well known that the addition of a small amount of elements such as C, Cr, Cu, Mn, P, or V, can modify the mechanical properties (i.e. formability, strength, hardness or cryogenic toughness), the electrical and thermal characteristics, the corrosion resistance, or the magnetic properties of the alloy [14-16]. Several studies have proved that the addition of elements like B, Cu, P, or Pd, enhances the NW array coercive field (in some cases after suitable thermal treatment) [17-20].

3.2. FeCo nanowire arrays

3.2.1. Geometrical and compositional characterization

Two series of FeCo cylindrical nanowire arrays were fabricated by electrodeposition into AAO templates. The templates with the two different pore diameters, d_{NW} = 20 and 40 nm, were fabricated by two-step anodization process using sulfuric and oxalic aqueous solutions, respectively (as described in Section 2.1.3.1). The different composition of the nanowires was obtained by modifying the composition of the electrochemical bath (see Table 2.2), while the applied voltage was fixed to -1.8 V

vs. Ag/AgCl for all the samples (see Section 2.2.2 for more details about the electrodeposition process).

The geometry of the nanowire arrays (nanowire diameter (d_{NW}) and length (L_{NW}) and the distance between nanowires centers (D_{int})) was characterized by Scanning Electron Microscopy (SEM). The geometrical parameters of the two series of samples are collected in Table 3.1. Figure 3.1(a) shows the top view of an AAO template with 40 nm pore diameter and Figure 3.1(b) and (c) show the cross section view of selected FeCo nanowire arrays with d_{NW} = 20 and 40 nm, respectively, embedded into AAO templates.

Table 3.1 Geometrical parameters of the nanowire arrays fabricated with sulfuric (H_2SO_4) and oxalic ($C_2H_2O_4$) acid solutions: nanowire diameter (d_{NW}) and length (L_{NW}) and distance between nanowires centers (D_{int}).

Acid solution	d_{NW} (nm)	D_{int} (nm)	L_{NW} (μm)
H_2SO_4	20	55	4
$C_2H_2O_4$	40	105	3

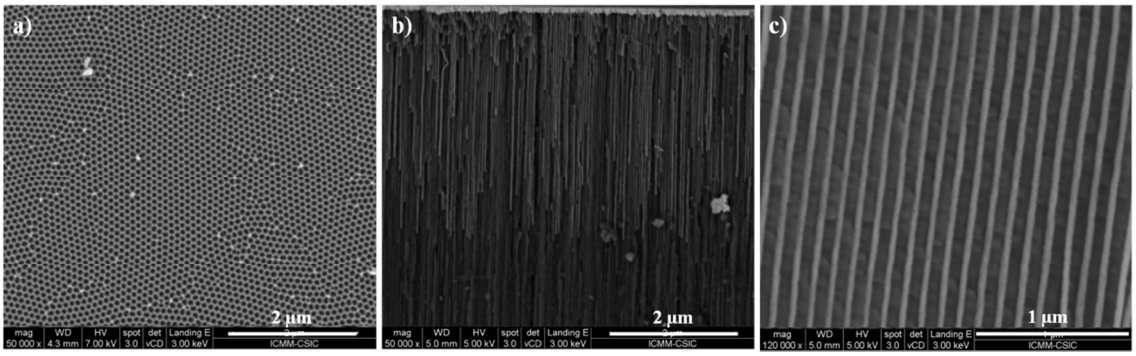

Figure 3.1 (a) Top view SEM images of an AAO template with 40 nm pore diameter; cross section view of (b) 20 nm diameter nanowires and (d) 40 nm diameter nanowires embedded in AAO templates.

The composition of the $Fe_{100-x}Co_x$ nanowires was obtained by Energy Dispersive X-Ray Spectroscopy (EDS) measurements. The composition varied in the whole range of $0 \leq x \leq 100$, from pure Fe ($x = 0$) to pure Co ($x = 100$) nanowires.

3.2.2. Crystallographic structure

The crystallographic structure of FeCo nanowires was determined by X-Ray Diffraction (XRD) measurements. XRD spectra for FeCo nanowire arrays embedded into AAO templates with different chemical composition and nanowire diameter of 20 and 40 nm are shown in Figure 3.2(a) and (b), respectively. The indexing of the patterns has been performed according to the Fe body-centered cubic (*bcc*) crystalline structure (Space group Im3m and lattice parameter a = 2.866 Å) where the peaks at 2θ values of 44.72º, 65.09º and 82.43º correspond to the (110), (200) and (211) reflections; Co face-centered cubic (*fcc*) crystalline structure (Space group Fm3m and a = 3.545 Å), where the peaks at 2θ values of 44.22º, 51.52º and 75.85º correspond to the (111), (200) and (220) reflections; and Co hexagonal close-packed (*hcp*) crystalline structure (Space group P63/mmc (194) and $a = b$ = 2.507 Å and c = 4.070 Å), where the peaks at 2θ values of 41.55º and 44.48º correspond to the (100) and (002) reflections. The positions are marked in Figure 3.2 with dashed lines: *bcc* phase (blue color), *fcc* phase (red color) and *hcp* phase (green color).

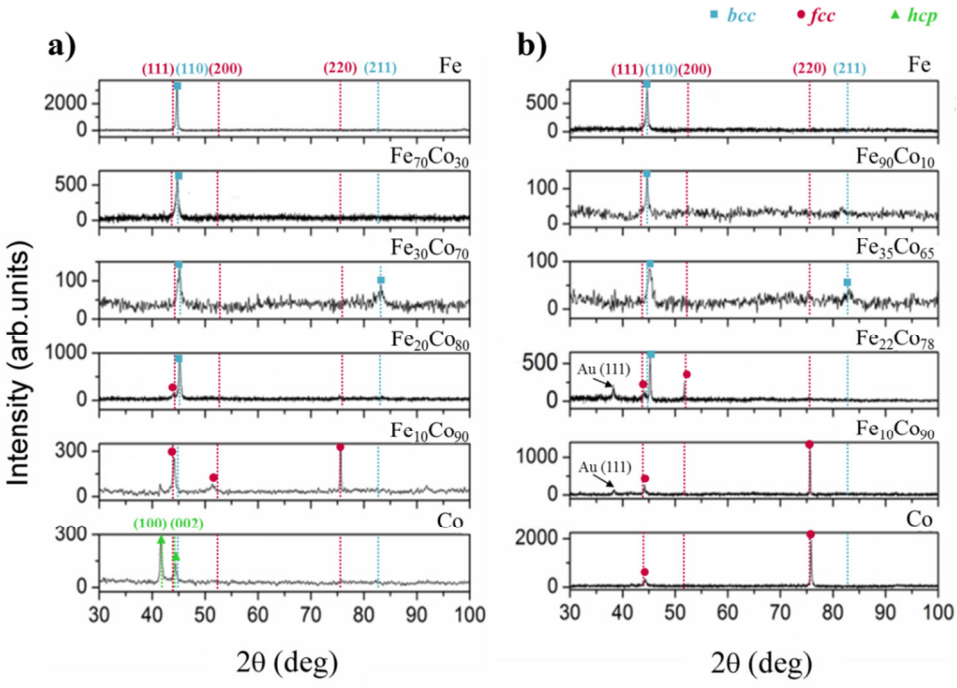

Figure 3.2 XRD spectra of FeCo nanowire arrays for selected alloy compositions: (a) d_{NW} = 20 nm, and (b) d_{NW} = 40 nm. The composition of the nanowires for each sample is labeled in the top-right part of each pattern.

Fe nanowires and those with Co content lower than 90 % with 20 nm in diameter (Figure 3.2(a)) show a *bcc* symmetry with a (110) texture. For x = 90, the nanowires present a *fcc* structure with (220) texture. For pure Co nanowires, the crystallographic structure changes to *hcp* with a (100) texture.

The 40 nm $Fe_{100-x}Co_x$ nanowires XRD spectra (Figure 3.2(b)) reveal a cubic symmetry in the whole range of compositions. The cubic structure evolves form *bcc* for pure Fe nanowires and for low and intermediate Co content ($0 < x \leq 65$) towards *fcc* as the amount of Co increases. For high Co content ($x \geq 90$) and pure Co nanowires, the only stable phase is the *fcc* structure with a (220) preferred orientation.

From the comparison between Figure 3.2(a) and (b), the most important difference which is deduced is the crystallographic structure for Co nanowires: *hcp* phase for 20 nm nanowires and *fcc* for 40 nm nanowires.

More detailed information about the composition and crystallographic structure of FeCo nanowires was obtained by High-Resolution Transmission Electron Microsopy (HRTEM), equipped with an EDS spectrometer. Figure 3.3 shows high resolution lattice images together with Selected Area Electron Diffraction (SAED) patterns of selected nanowires. These patterns show the nanowire crystallographic characteristics and atomic lattice features. From SAED patterns in the insets in Figure 3.3, the crystalline structure of FeCo nanowires is confirmed to be *bcc* for intermediate and high Fe content (Figure 3.3(a) and (b) for d_{NW} = 20 and 40 nm, respectively) and *fcc* for high Co content (Figure 3.3(c) and (d) for d_{NW} = 20 and 40 nm, respectively), being in agreement with the XRD spectra in Figure 3.2. The nanowires crystallographic structure as a function of the composition has a similar dependence as the one for bulk FeCo alloy [21]. Most of the nanowires exhibit a polycrystalline nature with a minimum grain size of 5 nm (Figure 3.3(a), (b) and (c)). Few single crystal $Fe_{10}Co_{90}$ 40 nm nanowires were found, as shown in Figure 3.3(d). The lattice image of the single crystal nanowire was oriented along its [1-10] zone axis in the *fcc* structure, as revealed by its corresponding electron diffraction. From this diffraction pattern and its image, one can further deduce the long axis, i.e. the preferential growth direction is along the <110> zone axis.

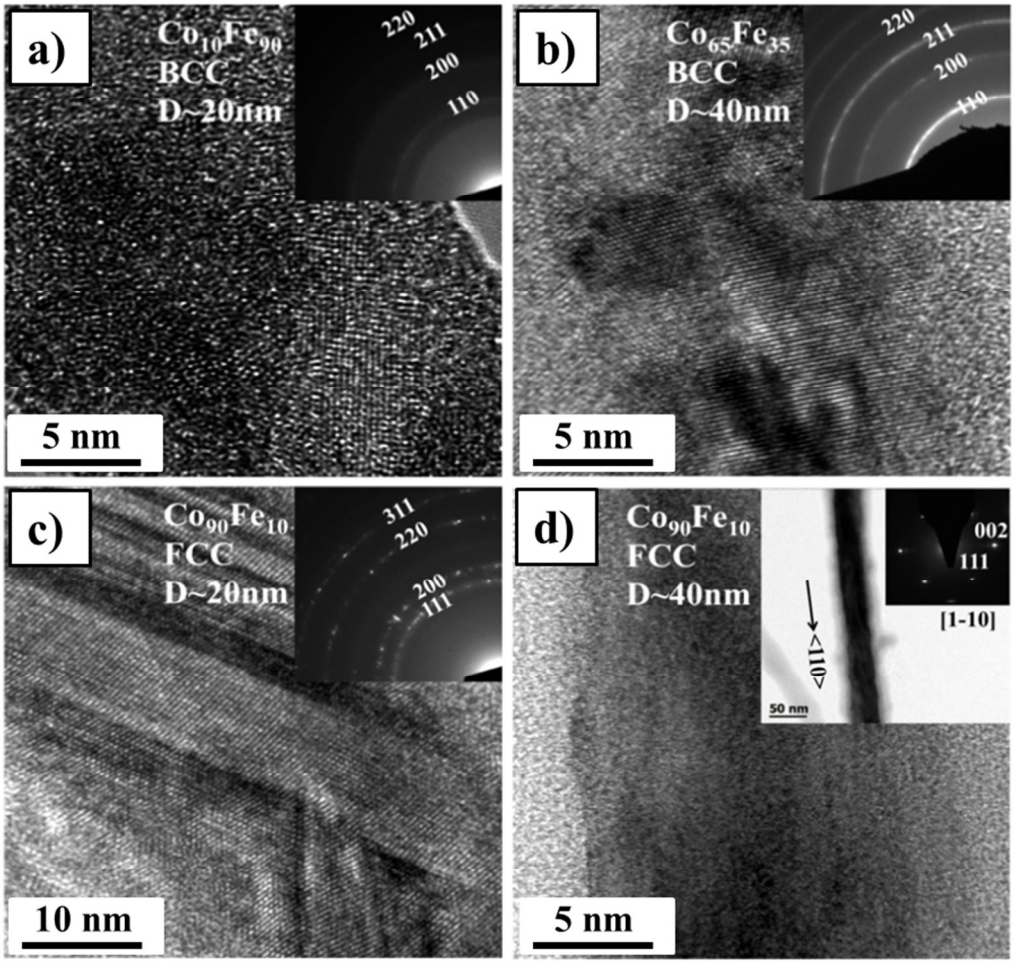

Figure 3.3 HRTEM images of FeCo alloy nanowires: (a) Body-centered cubic (*bcc*) $Co_{10}Fe_{90}$ 20 nm diameter nanowires; (b) *bcc* $Co_{65}Fe_{35}$ 40 nm diameter nanowires; (c) Face-centered cubic (*fcc*) $Co_{90}Fe_{10}$ 20 nm diameter nanowires; and (d) *fcc* $Co_{90}Fe_{10}$ 40 nm diameter nanowires. Insets in (a), (b) and (c) show SAED patterns recorded for a collection of nanowires while inset in (d) shows the SAED pattern of a part of a single nanowire.

3.2.3. Magnetic characterization

The hysteresis loops were obtained by Vibrating Sample Magnetometer (VSM) at room temperature to study the influence of the nanowire composition and, furthermore, additional measurements at a temperature range between 10 K and 290 K were performed to determine the temperature dependence of coercive field.

3.2.3.1. Compositional and temperature dependence of magnetic properties

Firstly, the influence of the nanowire composition was studied measuring the hysteresis loops of nanowire arrays and comparing the values of coercive field ($\mu_0 H_c$)

and fractional remanence (M_r/M_s) for both configuration of applied magnetic field. For all nanowire arrays, the high values of $\mu_0 H_c$ and M_r/M_s in parallel configuration of applied field compared to the vanishing values in perpendicular configuration evidence that the magnetization easy axis is parallel to the nanowire axis.

Figure 3.4 shows the evolution of $\mu_0 H_c$ and M_r/M_s for the parallel configuration of applied field as function of the amount of Co into the FeCo alloy. In this figure, it is observed a similar trend for both 20 and 40 nm nanowire arrays: a minimum value of $\mu_0 H_c$ at low % Co, and a continuous increase with increasing the Co content. For $70 \leq x \leq 90$, the highest values of $\mu_0 H_c$ and M_r/M_s are obtained, above 0.27 T and 0.90, respectively. For pure Co nanowires a decrease in both magnitudes is observed. Overall larger values of coercive field and fractional remanence are observed for nanowires with d_{NW} = 20 nm for low and intermediate Co content, while similar values are obtained for high Co content and pure Co nanowires.

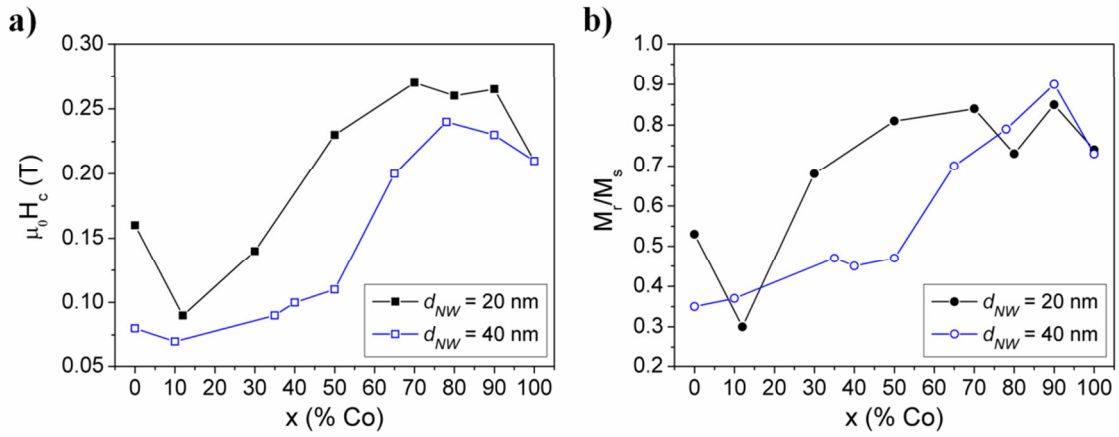

Figure 3.4 Coercive field ($\mu_0 H_c$) and fractional remanence (M_r/M_s) for the $Fe_{100-x}Co_x$ nanowire arrays as function of the Co content (x), under a magnetic field applied parallel to the nanowire axis.

Additionally, hysteresis loops were measured at temperatures between 10 K and 290 K. The values of coercive field for parallel applied field configuration were determined from the hysteresis loops and plotted in Figure 3.5(a) and (b) for selected samples ($65 \leq x \leq 100$) and nanowire diameter of 20 and 40 nm, respectively. It is observed that the coercive field of FeCo alloy nanowires decreases with increasing temperature, while for pure Co nanowires the trend is opposite (i.e. H_c increases with

temperature). Figure 3.6 shows that for 20 nm nanowires, the temperature dependence of H_c is more significant.

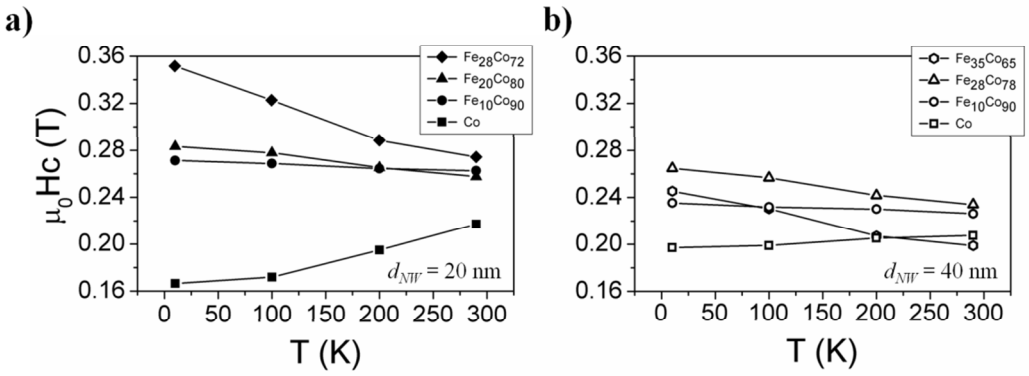

Figure 3.5 Temperature dependence of coercive field (H_c) for FeCo nanowire arrays with different nanowire composition (see the legend in each graph) and nanowire diameter of (a) 20 nm and (b) 40 nm.

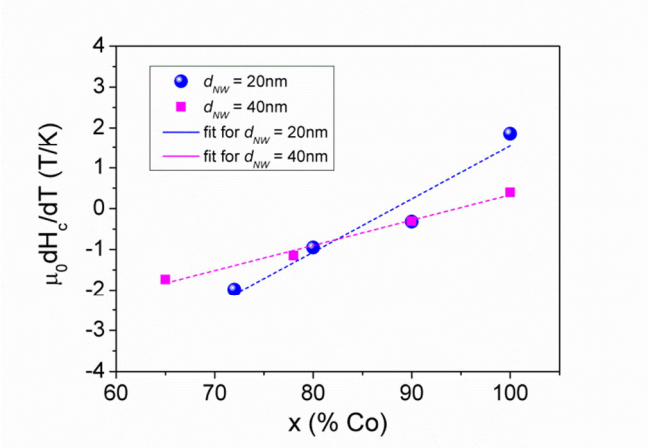

Figure 3.6 Compositional dependence of the temperature derivative of the coercive field (dH_c/dT) for nanowire arrays with d_{NW} = 20 and 40 nm.

Assuming a nucleation mechanism as the dominant for the coercive field and being x the amount of Co into the alloy, d_{NW} the nanowire diameter, and T the measurement temperature, we can consider the following general expression [22]:

$$H_c(x, d_{NW}, T) \approx \frac{K_{cryst}(x, d_{NW}, T)}{M_s(x, T)} + N(d_{NW}) M_s^2(x, T) \qquad (3.1)$$

where K_{crys} is the magnetocrystalline anisotropy energy density and N is the longitudinal demagnetizing factor.

At room temperature (Figure 3.4), a general trend of increasing coercive field with Co content (x) is observed, but for pure Fe and Co nanowires. In order to interpret the data, it is necessary to consider the increase of saturation magnetization (M_s) with x [23], which contributes to a moderate increase of the second term on the right hand side of Eq.(3.1). Additionally, and even if both phases show polycrystalline structure, the magnetocrystalline anisotropy constant is stronger for the *fcc* structure so that the continuous increase of the *fcc* crystallographic phase at the expense of the *bcc* phase should moderately increase the resulting crystalline anisotropy in the first term of Eq.(3.1). In this case, both the magnetocrystalline and the shape anisotropies contribute to the observed coercive field increase.

For pure Co nanowires, and especially for 20 nm diameter nanowires, the decrease in coercive field is ascribed to their *hcp* crystallographic structure with the magnetization easy axis oriented almost perpendicular to the nanowire axis. The different crystallography modifies the magnetization reversal process according to micromagnetic analysis [24]. The lower coercive field observed for 40 nm diameter nanowires is explained by their slightly reduced shape anisotropy (second term in Eq. (3.1)). Furthermore, micromagnetic calculations have predicted an increase in coercive field for smaller nanowire diameters [10, 20].

In dense nanowire arrays the magnetostatic interactions between nanowires influence the magnetic response of the array. They depend on the array configuration (i.e. nanowire diameter (d_{NW}) and distance between nanowire centers (D_{int})) and are more relevant when the ratio d_{NW} / D_{int} increases. The interactions also are stronger for higher value of saturation magnetization. When the magnetostatic interactions are significant the susceptibility and the remanence decrease, while a low influence on the coercive field is expected as the magnetostatic field at coercive field averages out. The parameter which characterizes the AAO template considering the ratio d_{NW} / D_{int} is the template porosity (P). The porosity factor of the AAO templates with d_{NW} = 20 and 40 nm and D_{int} = 55 and 105 nm was calculated using the equation for a hexagonal structure [25]:

$$P = \frac{\pi}{2\sqrt{3}}\left(\frac{d_{NW}}{D_{int}}\right)^2 \tag{3.2}$$

The porosity for 20 and 40 nm diameter nanowire arrays was 0.12 and 0.13, respectively. As the porosity is similar for the two different nanowire arrays, geometrical effects are not expected to play a relevant role for the magnetostatic interactions. In turn, the saturation magnetization increases continuously with Co content from pure Fe to $Fe_{60}Co_{40}$ (M_s = 2.4 T for bulk alloy), and it decreases till pure Co [23]. The inverse evolution of M_s with Co content could contribute to the squareness in Figure 3.4(b).

Figure 3.5(a) and (b) shows two different behavior in the temperature dependence of coercive field for FeCo alloy and Co nanowires, for samples with d_{NW} = 20 and 40 nm, respectively. For FeCo nanowires both the magnetocrystalline and shape anisotropies increase for a decrease in the temperature. For Co nanowires, especially for d_{NW} = 20 nm, there is a balance between nearly transverse magnetocrystalline and longitudinal shape anisotropy terms. The observed coercive field decrease for lower temperatures confirms a faster temperature dependence of crystalline anisotropy than that of saturation magnetization. The increase in the effective magnetocrystalline anisotropy at lower temperatures together with that of the magnetoelastic term arising from the induced stresses through the coupling between the ceramic alumina matrix and the metallic nanowires also contribute to a higher value of coercive field [26, 27].

The experimental data indicate a different compositional and diameter dependence of the coercive field on temperature (see the difference between Figure 3.5(a) and (b). Figure 3.6 shows the compositional dependence of the temperature derivative of coercive field (dH_c/dT). For both nanowire diameters, dH_c/dT increases with increasing the Co content, starting with a negative value and becoming positive for pure Co nanowires. Assuming a linear dependence for $dH_c(T)/dT$, the temperature derivative of Eq. (3.1). leads to the following expression:

$$\frac{\partial H_c}{\partial T} \approx \frac{K_{crys}}{M_s^2}\left|\frac{\partial M_s}{\partial T}\right| - \left(\frac{1}{M_s}\left|\frac{\partial K_{crys}}{\partial T}\right| + N\left|\frac{\partial M_s}{\partial T}\right|\right) \tag{3.3}$$

From the qualitative analysis of Eq. (3.3) together with Figure 3.6, it is concluded that $dH_c(T)/dT$ is mostly determined by the third term (shape anisotropy) on

the right hand for low values of Co content. For Co-rich nanowires, the increase in $dH_c(T)/dT$, reaching positive values for pure Co nanowires, is ascribed to a dominant increase of magnetocrystalline anisotropy.

3.3. Cu doping and thermal treatments

In the introductory part of this chapter, it was mentioned that the addition of non-ferromagnetic elements to the alloy has been proved to modify the magnetic properties of nanowire arrays. Particularly, the addition of small amounts of Cu to the FeCo alloy and the following annealing steps have been studied [20, 28, 29]. In the following Sections in this chapter, a systematic study to determine the FeCoCu ternary alloy nanowire arrays which shows the hardest magnetic behavior after annealing treatment, is presented. Furthermore, Ferromagnetic Resonance (FMR) technique has been used to quantify the magnetic hardening and together with X-Ray Spectroscopy measurements on the nanowire arrays, the reason for the hardening has been established.

3.3.1. FeCoCu alloy composition and annealing optimization

Two series of nanowire compositions were fabricated by electrodeposition, $Fe_{100-x}Co_x$ and $Fe_{95-x}Co_xCu_5$, with $30 < x < 90$ (see Section 2.2.2 for more experimental details). The small amount of Cu was set to 5 % in order not to decrease significantly the nanowire saturation magnetization.

The geometry of the nanowires were obtained by SEM, obtaining a nanowire diameter of 20 nm and length of 5 μm and 55 nm distance between nanowire centers. Figure 3.7(a) shows the top view of AAO template and Figure 3.7(b) shows a cross sectional view of a selected $Fe_{28}Co_{67}Cu_5$ nanowire array.

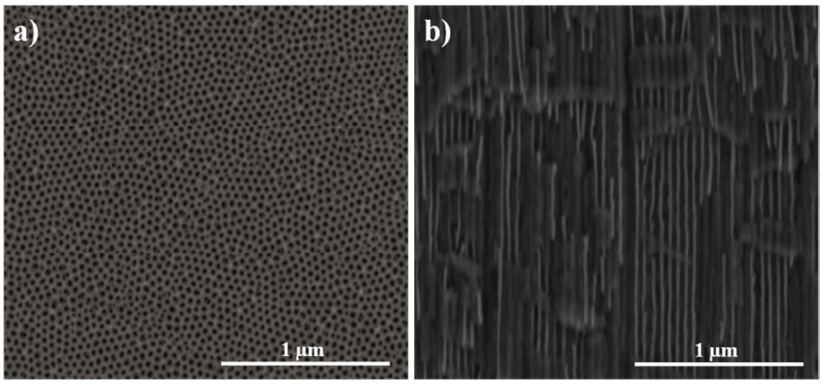

Figure 3.7 (a) Top view of AAO template with 20 nm nanopore diameter, and (b) cross section view of $Fe_{28}Co_{67}Cu_5$ nanowires embedded in the AAO template.

The nanowire arrays were structurally characterized by XRD measurements, confirming a polycrystalline *bcc* structure with (110) preferential growing direction for most of FeCo alloy nanowires. However, for high Co content, x ≈ 90, the XRD patterns show peaks ascribed to (110) *fcc* structure (see Section 3.2.2).

The incorporation of a small amount of Cu into the alloy does not modify essentially the crystallographic structure of FeCo nanowires. Figure 3.8 shows the crystallographic structure of $Fe_{28}Co_{67}Cu_5$ nanowire array in the as-prepared state and annealed sample at two different temperatures. The XRD pattern for the as-prepared state (Figure 3.8(a)) shows that the $Fe_{28}Co_{67}Cu_5$ nanowires crystallize in a *bcc* structure with a (110) preferential growing direction. Notice that no additional peaks corresponding to any Fe, Co or Cu oxides are observed in the as-prepared sample.

The influence of the thermal treatment on the nanowires crystallographic structure is shown in Figure 3.8(b) and (c). Annealing at a temperature of 723 K (Figure 3.8(b)) does not modify strongly the crystallographic structure in comparison to the as-prepared state (Figure 3.8(a)). This thermal treatment results in a better texture definition with an increase of the (110) peak intensity. This pattern also shows a small peak at $2\theta = 44.4^{\circ}$ corresponding to the Au *fcc* (200) reflection, originated from remaining Au at the backside of the template (Au working electrode for nanowires electrodeposition). If the annealing is carried out at higher temperature, in this case 748 K (Figure 3.8(c)), additional peaks corresponding to Co and Fe oxides (CoO (200) and Fe_2O_3 (200) reflections) are observed together with a degradation of the (100)

reflection. At more elevated temperatures, further crystalline deterioration of the sample is observed, together with nanowires and template bending.

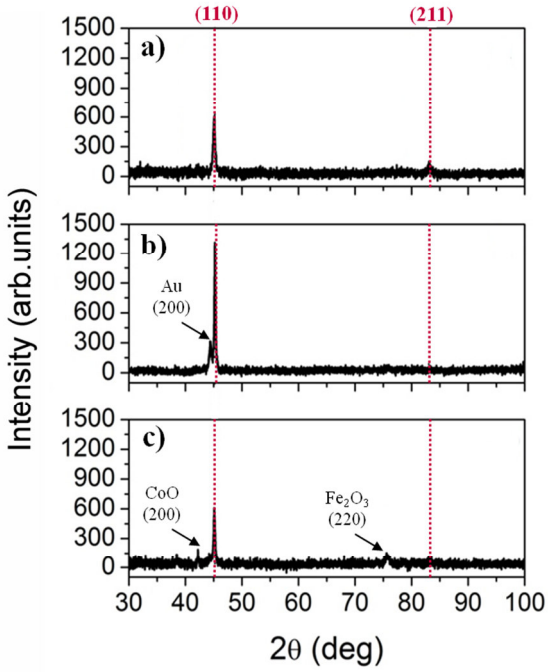

Figure 3.8 XRD spectra of a selected $Fe_{28}Co_{67}Cu_5$ nanowire array sample with d_{NW} = 20 nm measured in the (a) as-prepared state, and annealed at (b) 723 K and (c) 748 K.

The hysteresis loops of the $Fe_{95-x}Co_xCu_5$ nanowire arrays with $30 < x < 90$ were measured by VSM in the temperature range from 10 to 300 K. From the measured hysteresis loops the coercive field ($\mu_0 H_c$) and the fractional remanence (M_r/M_s) were obtained and plotted in Figure 3.9(a) and (b), respectively, as function of the Co content. The values of the magnetic properties of $Fe_{100-x}Co_x$ nanowire arrays were re-plotted for comparison. An increase in the coercive field and remanence with Co content is observed for $Fe_{95-x}Co_xCu_5$ nanowire array (as was previously observed in for $Fe_{100-x}Co_x$ nanowire arrays, see Section 4.2.3.1). However, in this case a deterioration in both magnitudes is obtained comparing with $Fe_{100-x}Co_x$ samples. Furthermore, the presence of small amount of Cu is not effective in promoting a hardening of the magnetic properties. Actually, it slightly reduces $\mu_0 H_c$ and M_r/M_s for most compositions. The lower M_r/M_s is likely an indication of the reduction of the effective longitudinal magnetic anisotropy with the presence of Cu [10, 20]. Additionally, the saturation

magnetization ($\mu_0 M_s$) for the studied FeCo alloys reaches a value of 2.1 T, decreasing to 1.9 T for Cu-doped samples.

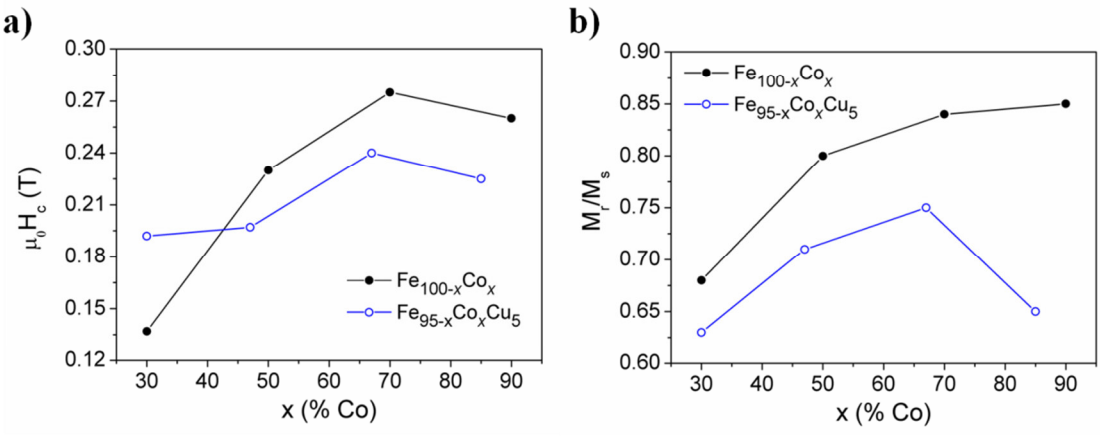

Figure 3.9 Coercive field (H_c) and fractional remanence (M_r/M_s) for the two series of nanowire arrays in as-prepared state.

As observed in Figure 3.8(c), performing the annealing at a temperature of 748 K generates a deterioration of the crystalline structure of the nanowires and even macroscopic defects as template bending. Considering this and the XRD pattern in Figure 3.8(b), annealing at a temperature of 723 K was carried out for all the samples in the two series. It is important to mention that the optimal annealing temperature depends on the geometry of the nanowire array, particularly on the nanowire diameter and distance between nanowire centers. As reported elsewhere, the optimal annealing temperature increases up to 970 K for d_{NW} = 35 nm and D_{int} = 105 nm [29].

After annealing at optimal temperature conditions (T = 723 K), magnetic hardening is observed for all the FeCo and FeCoCu samples, but the hardening is more effective for the Cu-doped nanowire arrays. Figure 3.10 shows the coercive field dependence on the measurement temperature. At room temperature (T = 300 K), for $Fe_{35}Co_{65}$ and $Fe_{22}Co_{78}$ nanowire arrays, the anneling induces an increase of coercive field by 7 % in both cases. With optimal annealing, for $Fe_{28}Co_{67}Cu_5$ and $Fe_{20}Co_{75}Cu_5$ the coercive field increases by 42 % and 24 %, respectively (full scatters in Figure 3.10). As shown in Figure 3.8(b), optimal annealing refines the textured *bcc*

crystallographic structure, which is in the origin of an enhancement of magnetocrystalline anisotropy promoted by the presence of Cu.

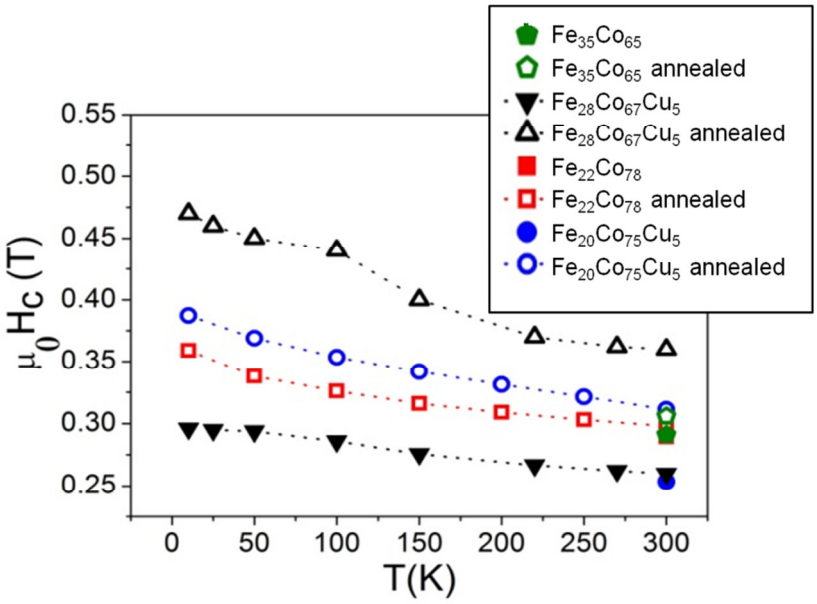

Figure 3.10 Temperature dependence of coercive field for selected FeCo and FeCoCu nanowire arrays in their as-prepared state and after annealing.

Figure 3.10 also shows the dependence of coercive field on measurement temperature. It is observed that the slope of the experimental data is higher for FeCoCu samples than for FeCo nanowire arrays. A higher slope is also obtained for annealed samples compared to as-prepared ones. Such temperature dependence, can be interpreted by the increase in the effective anisotropy energy density (K) which for lower temperatures it contains several contributions: (i) magnetocrystalline (K_{crys}), (ii) induced by annealing (K_{ind}), and (iii) magnetoelastic (K_{elas}), owing to the stress generated by decreasing the measurement temperature due to the different thermal expansion coefficients of metallic nanowires and anodic alumina [27].

3.3.2. Enhancement of magnetocrystalline anisotropy energy

The origin of the increase in coercive field has been proposed to be a result of increased magnetocrystalline anisotropy energy (MAE) in the FeCoCu nanowires with the easy axis parallel to the nanowire axis [20], but the experimental proof and quantification of the increased MAE in these systems, however, remained open. In this

sense, Ferromagnetic Resonance (FMR) is an effective technique to quantitatively determine the magnetic anisotropy in ferromagnetic systems, particularly in ferromagnetic nanowire arrays [3, 5, 30-34].

In order to determine the influence of adding Cu to the FeCo alloy nanowires and the subsequent annealing, a systematic study of the magnetic and structural properties of FeCo and FeCoCu nanowire arrays with different nanowire diameters, before and after annealing was performed.

3.3.2.1. Geometrical, compositional and structural characterization

Hexagonally ordered FeCo and FeCoCu nanowire arrays with different nanowire diameters ranging from 20 nm to 150 nm were grown into AAO templates fabricated by two-step anodization and hard anodization (for more experimental details about the anodization processes, see Section 2.1.3.1 and Section 2.1.3.2, respectively). FeCo and FeCoCu nanowires were grown by electrodeposition in a three-electrode cell using a Watts-type bath as electrolyte (more experimental details about electrodeposition technique and the electrochemical parameters can be found in Section 2.2.2).

The geometrical parameters of the nanowires such as nanowire diameter, d_{NW}, length, L_{NW}, and distance between nanowire centers, D_{int}, were determined by SEM. Figure 3.11 shows cross section SEM images of selected nanowire arrays. The porosity factor, P, of each AAO template was calculated using Eq. (3.2).

The nanowire composition was obtained by EDS, yielding a composition of $Fe_{30}Co_{70}$ and $Fe_{30}Co_{65}Cu_5$ for each series of samples. In the following, the samples will be labeled FeCo and FeCoCu, respectively, and followed by the value of the nanowire diameter. The magnetic properties obtained in the study on FeCo nanowire arrays show that the largest coercive field and a high fractional remanence are obtained for a $Fe_{30}Co_{70}$ alloy composition. The geometrical parameters of the FeCo and FeCoCu nanowire arrays are collected in Table 3.2. Notice that the samples with d_{NW} = 20, 35 and 110 nm were fabricated using electrochemical parameters to obtain similar values of P, to determine the influence of the nanowire diameter on their magnetic behavior.

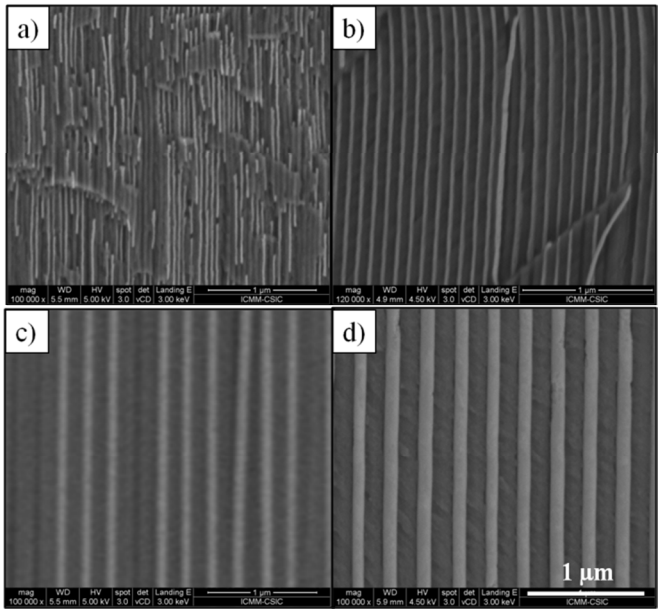

Figure 3.11 SEM images of FeCoCu nanowires embedded into AAO templates with different pore diameters: (a) 20 nm, (b) 35 nm, (c) 110 nm, and (d) 150 nm.

The crystallographic structure of the nanowires was determined by XRD measurements. For all the samples, a polycrystalline *bcc* structure was determined. Below, in Section 3.3.2.3, a detailed study of the changes in the crystalline structure after annealing and considering the different nanowire diameters is presented.

Table 3.2 Geometrical parameters of the electroplated $Fe_{30}Co_{70}$ and $Fe_{30}Co_{65}Cu_5$ nanowire arrays with different nanowire diameter (20, 35, 110, and 150 nm): nanowire diameter, d_{NW}, distance between nanowire centers, D_{int}, nanowire length, L_{NW}, and alumina membrane porosity, P.

Sample name	d_{NW} (nm)	D_{int} (nm)	L_{NW} (µm)	P	Aspect ratio L_{NW} / d_{NW}
FeCo20	20	55	7.3	0.12	365
FeCo35	35	105	7.5	0.10	214
FeCo110	110	320	15	0.11	136
FeCoCu20	20	55	7.1	0.12	355
FeCoCu35	35	105	7.4	0.10	211
FeCoCu110	110	320	29	0.11	263
FeCoCu150	150	320	13	0.20	86

3.3.2.2. Magnetic characterization

Firstly, the hysteresis loops for FeCo and FeCoCu nanowire arrays were measured by VSM in the as-prepared state for parallel and perpendicular configurations of the applied magnetic field with respect to the nanowire axis. Figure 3.12 shows the hysteresis loops of FeCoCu nanowire arrays with the four different nanowire diameters. For the arrays with d_{NW} = 20 and 35 nm (Figure 3.12 (a) and (b), respectively), high values of the coercive field ($\mu_0 H_c$) and fractional remanence (M_r/M_s) in parallel configuration and vanishing values in perpendicular configuration are observed. This evidences that the magnetization easy axis lies parallel to the nanowire axis. In the case of nanowire arrays with d_{NW} = 110 and 150 nm, which is bigger than the characteristic critical single domain size [35], a drastic decrease in $\mu_0 H_c$ and M_r/M_s in parallel configuration is observed (Figure 3.12 (c) and (d)). The decrease in $\mu_0 H_c$ and M_r/M_s with increasing d_{NW} from 20 to 35 nm can be attributed to a magnetization reversal mode change as deduced from micromagnetic simulations, where a magnetization reversal process by the propagation of a transverse domain wall is predicted for nanowires with small diameter, while for larger diameter the reversal takes place by a vortex domain wall [10]. The more pronounced decrease of these magnitudes for the larger diameters (d_{NW} = 110 and 150 nm) can be ascribed to big diameter compare to the critical single domain size and the increase in the magnetostatic interaction within the array. However, Figure 3.12 (c) and (d) also show that the saturation field ($\mu_0 H_{sat}$) for the parallel configuration is smaller than for the perpendicular one indicating that the magnetization easy axis remains along the nanowire axis. Similar hysteresis loop shapes were obtained for FeCo nanowire arrays for the different diameter.

The annealing of these samples was performed in vacuum atmosphere using a Physical Properties Measurement System (PPMS), and the hysteresis loops were measured *in-situ* before and after annealing using the same equipment. The hysteresis loops for FeCo and FeCoCu nanowire arrays with d_{NW} = 35 nm and 110 nm diameter in the as-prepared state and after annealing are shown in Figure 3.13(a) to (d). The thermal treatment leads to an increase in $\mu_0 H_c$ but has no influence on the total magnetic moment of the samples at saturation (m_s). According to the results, m_s has the same value after the annealing in vacuum atmosphere and this fact is independent of the nanowire diameter and composition.

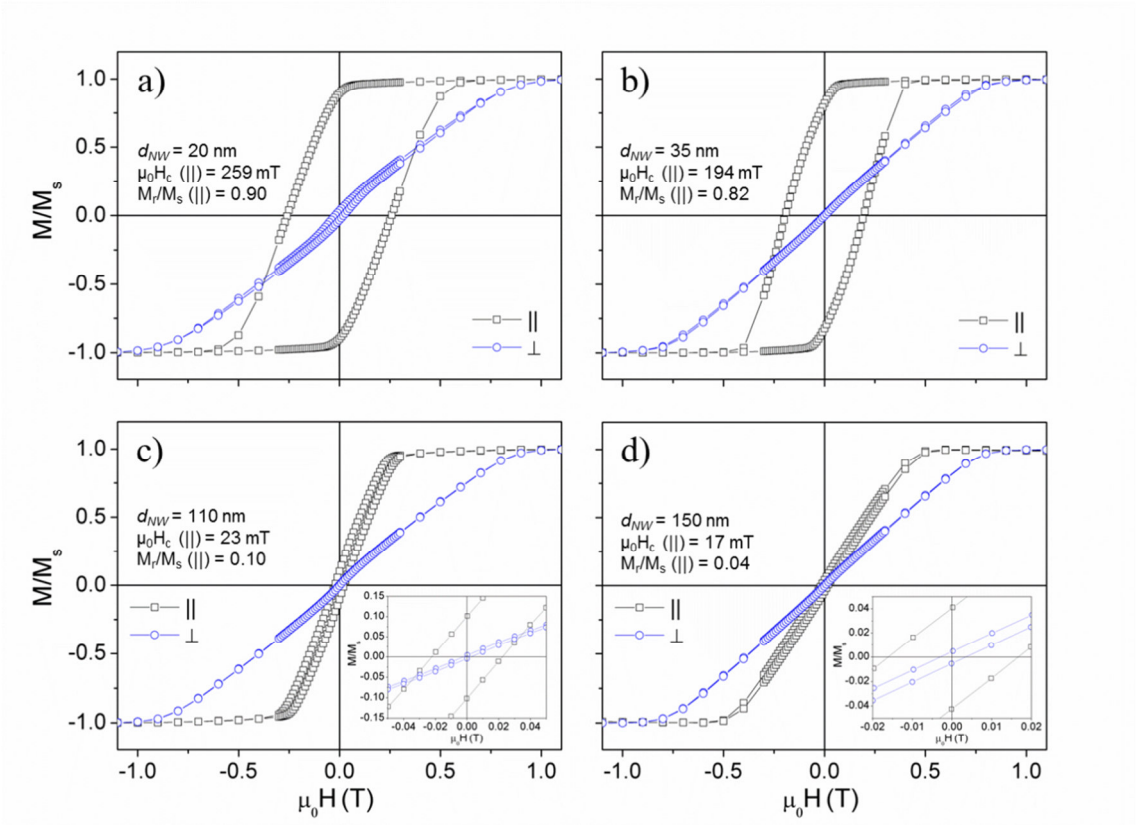

Figure 3.12 Hysteresis loops measured by VSM, with the applied field parallel (||) and perpendicular (⊥) to the NW axis, of the as-prepared FeCoCu NW arrays with d_{NW}: (a) 20 nm, (b) 35 nm, (c) 110 nm, and (d) 150 nm. Insets in (c) and (d) show a magnification of the hysteresis loops around the origin. In each graph, the coercive field and normalized remanent magnetization for parallel configuration, $\mu_0 H_c$ (||) and M_r/M_s (||), are listed.

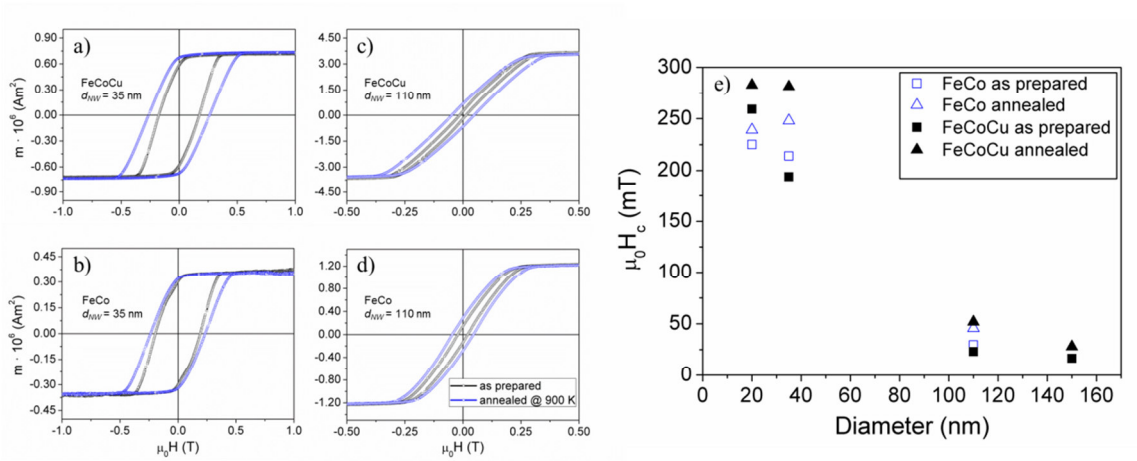

Figure 3.13 Hysteresis loops measured under parallel magnetic field for FeCoCu and FeCo nanowire array with 35 nm (a and b, respectively) and 110 nm diameter (c and d, respectively), before and after annealing; (e) Coercive field (H_c) of FeCo (blue and empty symbols) and FeCoCu (black and filled symbols) nanowire arrays before (squares) and after annealing (triangles), measured using VSM and SQUID with the applied field parallel to the nanowire axis.

Figure 3.13(e) shows the coercive field for all FeCo and FeCoCu nanowire arrays before and after annealing, extracted from the hysteresis loops measured in parallel configuration. After annealing, an increase in H_c $(||)$ is observed, but the increase is higher for the Cu-doped alloy, as was observed before [20, 28, 29].

Ferromagnetic Resonance (FMR) measurement were performed on the as-prepared and annealed FeCo and FeCoCu samples, in order to determine the origin of the higher increase in the coercive field in Cu-doped alloy nanowire arrays. FMR measurements were done using the configuration in Figure 2.13(a), where the FMR spectra were recorded at different angles of the applied magnetic field, θ_H, and for all the samples, a maximum resonance field, H_r, was found when the magnetic field, H_{DC}, was applied perpendicular to the nanowire axis (θ_H = 90º). For θ_H < 90º, H_r rapidly decreased and the FMR line vanished completely when θ_H approached zero. An example of the FMR angular measurement is shown in Figure 3.14(a), where it is observed that, for this particular sample, a small change in θ_H of 10 - 12º, originates a drastic decrease in H_r. Figure 3.14(b) shows the grey-scale plot of the angular dependence of FMR measurements for FeCoCu35 sample in the as-prepared state for a range of θ_H = 0 - 180º, where θ_H = 0º when the applied field is parallel to the nanowire axis and θ_H = 90º when the field is applied perpendicularly. The light grey color in the figure indicates the position of the resonance field for each θ_H. The maximum intensity of the signal is obtained for θ_H = 90º, indicating the maximum resonance field.

The resonance conditions for the recorded spectra have been derived using a general analytic solution of the full tensor representation of the high frequency susceptibility based on the Landau-Lifshitz equation [36, 37]. For the angular dependence of the resonance field, the free energy density given in Eq. (3.4) is used:

$$\mathrm{F} = \mu_0 M H_{eff} \sin^2\theta_M - \mu_0 M_s H_{DC} \left(cos\,\theta_M\, cos\,\theta_H + sin\,\theta_M\, sin\,\theta_H\right) \qquad (3.4)$$

where θ_M is the angle between the magnetization (M) and nanowire axis. The equilibrium values of θ_M for each H_{DC} and θ_H can be determined from the first derivative of the free energy density with respect to θ_M. H_{eff} is the effective magnetic anisotropy field with a uniaxial symmetry parallel to the nanowire axis.

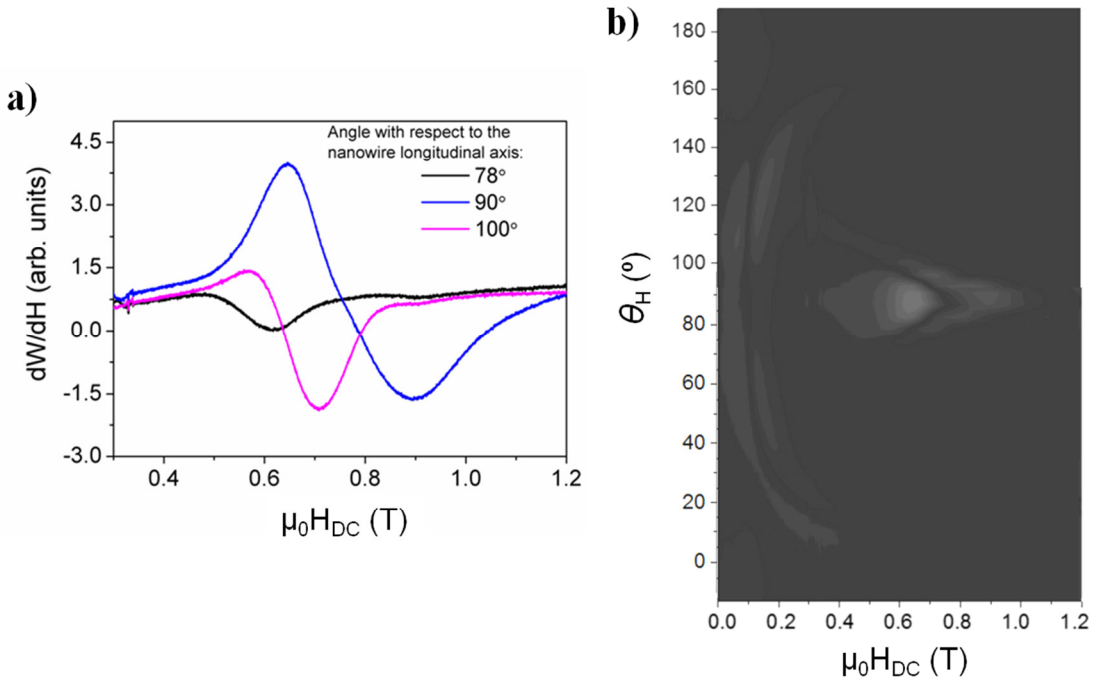

Figure 3.14 (a) FMR angular measurements around θ_H = 90º for FeCoCu nanowire array with d_{NW} = 35 nm in as-prepared state, and (b) grey-scale plot of the angular dependence of FMR measurements for the same sample for an angle of applied field in a range of θ_H = 0 - 180º, where θ_H = 0º when the applied field is parallel to the nanowire axis and θ_H = 90º when the field is applied perpendicularly.

The effective anisotropy field for a nanowire array has two contributions: i) the shape anisotropy field including the dipolar coupling between nanowires in the array (H_D); and ii) the magnetocrystalline anisotropy field (H_{MC}) [3, 5, 31, 32, 34]. Thus, H_{eff} can be estimated using the following expression:

$$\mu_0 H_{eff} = \mu_0 (H_D + H_{MC}) = \frac{1}{2}\mu_0 M_s (1 - 3P) + \frac{2K_2}{M_s} \tag{3.5}$$

where P is the AAO template porosity and K_2 is the second-order term of the magnetocrystalline anisotropy energy density for uniaxial symmetry [37]. From the H_r angular dependence, in the perpendicular configuration it is determined that $\theta_M = \theta_H =$ 90º, and the H_{eff} can be derived from the following equation [3, 5, 30, 33]:

$$\left(\frac{2\pi f}{\gamma}\right)^2 = \mu_0^2 H_r (H_r - H_{eff}), \tag{3.6}$$

where $\gamma = g\mu_B/\hbar$ is the electron gyromagnetic ratio, g is the spectroscopic splitting factor, μ_B is Bohr's magneton, and $\hbar = h/2\pi$ is the reduced Planck constant.

Figure 3.15 shows the derivative of FMR absorption power (W) as a function of the applied magnetic field for the as-prepared and annealed FeCo35 (Figure 3.15(a)) and FeCoCu35 (Figure 3.15(b)) samples at $\theta_H = 90^o$. The FMR linewidth for all studied samples presents a value of about 280 mT, which is a typical value according to previous studies on NW arrays [30]. In Figure 3.15, it is observed that the FMR line is shifted to higher magnetic fields after the annealing. The shift is larger if a small amount of Cu is added to the alloy, as it is observed comparing Figure 3.15(a) and (b).

For higher resonance fields, higher values of H_{eff} are obtained. For FeCo and FeCoCu NW arrays with different diameters in the as-prepared state and after annealing, H_{eff} was calculated using Eq. (3.6). The data obtained for all the samples in both states are collected in Table 3.3. In the as-prepared state the effective anisotropy field for FeCoCu35 is smaller than H_{eff} for FeCo35. However, after annealing, H_{eff} in FeCoCu35 increases significantly and becomes noticeably larger than in annealed FeCo35 (Table 3.3). Considering that larger magnetic anisotropy of a nanowire leads to a larger coercive field, similar behavior is expected for H_c, what is indeed seen in Figure 3.13(e) for the 35 nm diameter nanowire array.

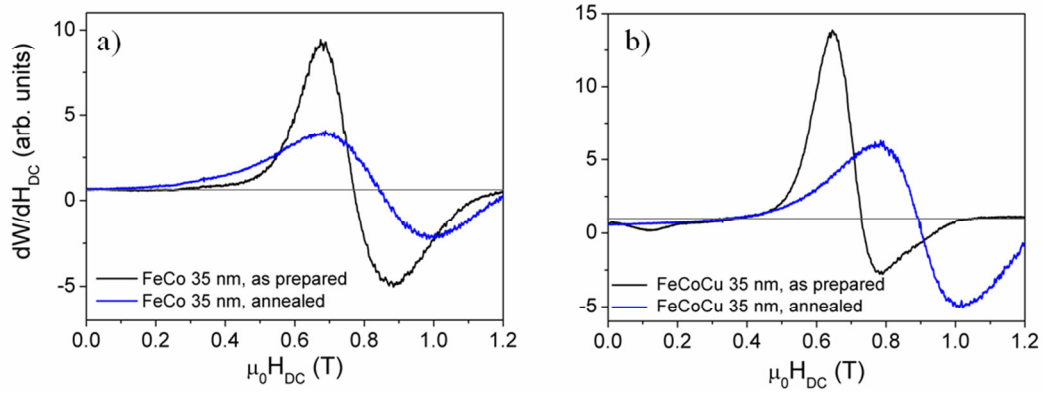

Figure 3.15 Derivative of FMR absorption power (W) as a function of the applied magnetic field (perpendicular to the NWs) for 35 nm nanowire arrays in the as-prepared state and after annealing at 900 K for 1 h: (a) FeCo and (b) FeCoCu nanowires.

Table 3.3 Resonance field, H_r, and effective magnetic anisotropy field, H_{eff}, for FeCo and FeCoCu nanowire arrays in the as-prepared and annealed state, and variation of the magnetic anisotropy constant, ΔK_2. The error bar for the H_r and H_{eff} for all the samples does not exceed 10 mT.

Sample label	*As-prepared*		*Annealed*		ΔK_2 (kJ m^{-3})
	$\mu_0 H_r$ (mT)	$\mu_0 H_{eff}$ (mT)	$\mu_0 H_r$ (mT)	$\mu_0 H_{eff}$ (mT)	
FeCo35	760	620	830	710	70 ± 4
FeCo110	880	760	890	770	14 ± 4
FeCoCu35	730	590	900	780	124 ± 6
FeCoCu110	810	690	850	730	30 ± 6
FeCoCu150	560	380	700	550	125 ± 6

The values of saturation magnetization ($\mu_0 M_s$) of the studied nanowires are 2.1 ± 0.1 T for FeCo alloy [5] and 1.8 ± 0.1 T for FeCoCu alloy [38]. The given error bar of 0.1 T is larger than the H_{MC} for *bcc* FeCo and hinders the exact determination of the MAE density in nanowire arrays. However, considering that the saturation magnetization (Figure 3.13(a) to (d)) and membrane porosity, P, after the annealing treatment in vacuum atmosphere do not change, according to Eq. (3.5) the relative increase in the magnetic anisotropy constant (ΔK_2) can be estimated from the difference in the effective fields before and after the annealing (ΔH_{eff}):

$$\mu_0 \Delta H_{eff} = \frac{2\Delta K_2}{M_s} \tag{3.7}$$

In the last column of Table 3.3 the calculated values of ΔK_2 for all the samples are summarized. It is observed that the annealing leads to a significant increase in the MAE density, and the increase is almost two times larger for the Cu-doped FeCo alloy nanowire array than for the FeCo samples. ΔK_2 is similar for FeCoCu35 and FeCoCu150 indicating that the nanowire diameter and the interface with the AAO template do not have a significant influence on the enhancement of MAE. We also note that the observed enhancement by 125 kJ/m^3 of the MAE is four times larger than the MAE reported for single crystalline *bcc* $Fe_{30}Co_{70}$ [39, 40] and is comparable with the gain in MAE due to induced strain in the bulk *bcc* FeCo lattice [41-43].

3.3.2.3. Structural characterization

In order to determine the origin of enhanced MAE after the addition of Cu to the FeCo alloy and the subsequent annealing, XRD measurements have been performed. The XRD spectra of the studied samples are shown in Figure 3.16. The spectra confirm a polycrystalline *bcc* structure for all the samples. The indexing of the XRD patterns has been performed according to the $Fe_{30}Co_{70}$ *bcc* crystalline structure where the peaks at 2θ values of 45.08º, 65.65º and 83.20º correspond to the (110), (200) and (211) reflections (these positions are marked with dashed lines in Figure 3.16) [44]. For clarity, only the 2θ ranges with the peaks corresponding to FeCo are shown in Figure 3.16, avoiding the peaks originated from the Si substrate and the cement used for the FMR measurements. Nevertheless, in Figure 3.16(b) a cement (thermostable cement used to glue the samples on the Si substrate for the thermal treatments) peak near 2θ = 66.5º appears. The patterns for FeCo and FeCoCu samples with a nanowire diameter of 35 and 150 nm (Figure 3.16(a) and (c)) show that the preferential growing directions are (110) and (211), while for the samples with 110 nm nanowire diameter, the peak intensity in the XRD spectra reveals that the preferred orientations are (200) and (110) (Figure 3.16(b)). The different preferential growth direction can be ascribed to differences in the sample preparation conditions that lead to different nanowire textures, fact that has been previously reported [29, 45].

The different growth directions can be correlated with the variations in the magnetic anisotropy constant (ΔK_2) calculated for the nanowire arrays, where the (200) preferred direction gives the lowest values of ΔK_2 for the FeCo and FeCoCu nanowire arrays with 110 nm nanowire diameter (Table 3.3). As stated in the previous section, the ΔK_2 for the FeCoCu nanowires does not depend on the nanowire diameter, as similar values are found for the samples with 35 nm and 150 nm nanowire diameter. Accordingly, the crystalline structure has the strongest influence on the variation in the magnetic anisotropy.

The thermal treatment leads to three noticeable changes in XRD spectra for all the samples (Figure 3.16): (i) sharpening of the XRD peaks; (ii) an increase of the (211) peak intensities with respect to the intensity of the (110) reflection; and (iii) a shift of XRD peaks towards lower 2θ angles, which corresponds to an increase in the lattice parameter, *a* [46].

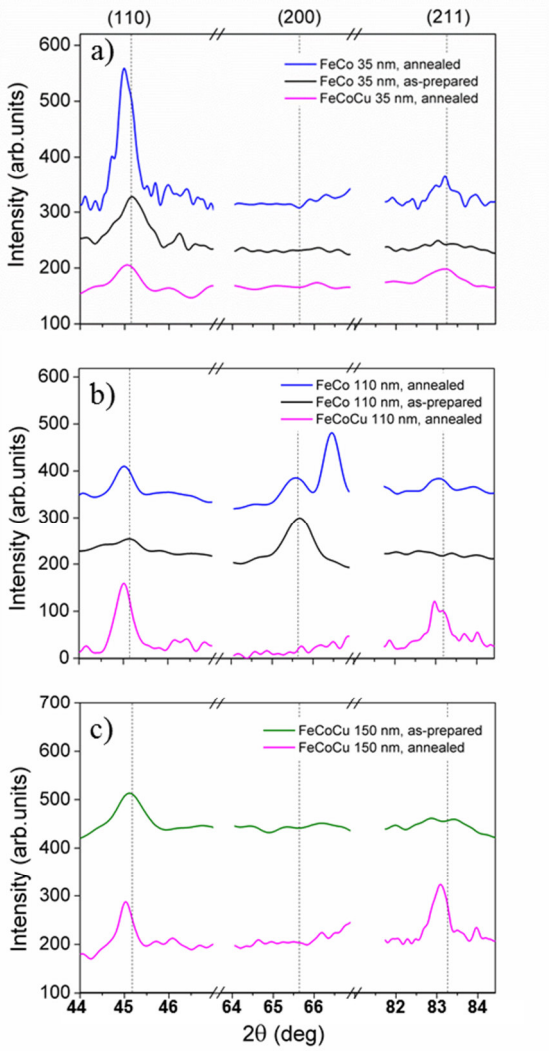

Figure 3.16 XRD pattern for different nanowire arrays: (a) annealed and as-prepared FeCo35 together with annealed FeCoCu35; (b) annealed and as-prepared FeCo110 together with annealed FeCoCu110; and (c) annealed and as-prepared FeCoCu150. The patterns in each graph are shifted vertically for clarity. The dashed lines indicate the positions of (110), (200) and (211) peaks.

The sharper peaks indicate that annealing leads to an increase of the crystallite size in polycrystalline FeCo and FeCoCu nanowires. The grain growth upon annealing may have influence on the coercive field of the nanowire array, but MAE as intrinsic property should be independent on grain size. In the present experiments, the change of the grain size itself cannot explain the increased MAE in FeCoCu nanowires, since ΔK_2 = 125 kJ/m^3 is significantly larger than the MAE in single crystalline *bcc* $Fe_{30}Co_{70}$ [39, 40]. Furthermore, annealing also supports grain growth in binary FeCo nanowires, which show two times smaller ΔK_2 compared to the value for annealed FeCoCu nanowires. The remarkable difference between XRD spectra of FeCo and FeCoCu NWs

is that annealing leads to a larger increase of (211) peak intensities in FeCoCu, so that the intensities of the (110) and (211) reflections for these nanowires become comparable (Figure 3.16). Partial reorientation of the crystallographic directions from (110) to (211) is accompanied with a crystal lattice distortion, since the lattice constant (*a*) increases after annealing. This distortion of the *bcc* lattice in ternary FeCoCu alloys after annealing has been reported before [47] and the distorted crystal lattice is the most plausible reason for the significantly enhanced MAE in FeCoCu nanowires.

According to the phase-diagrams of binary FeCo [6] and the ternary FeCoCu alloy [48], the crystalline structure of the FeCo nanowires is the (chemically ordered *bcc*) α phase, while for FeCoCu nanowires, the Cu is segregated from the FeCo phase, due to its low solubility into the Fe and Co matrix [49]. Annealing leads to a distortion of the *bcc* lattice and Cu forms a solid solution inside the FeCo matrix [47].

Previous reports on Cu-doped nanostructures suggest that the incorporation of Cu into the host matrix and the corresponding change of the microstructure, modify the magnetic properties of the nanostructures (i.e. magnetic anisotropy, coercive field and remanent magnetization) [20, 28, 29]. According to the obtained results, for nanowires with a growth direction along (110), the significantly increased MAE by adding Cu and after suitable annealing can be the result of the *bcc* lattice strain in combination with the change of the nanowire microstructure.

3.4. Conclusions

$Fe_{100-x}Co_x$ nanowire arrays with different nanowire diameters and compositions ($0 \leq x \leq 100$) have been grown by electrodeposition into the alumina templates pores of alumina membranes. FeCo nanowires present a *bcc* crystallographic structure for Fe-rich nanowires, evolving to *fcc* with increasing Co content. For pure Co nanowires, a change of the crystalline structure form *fcc* to *hcp* is found by reducing the nanowire diameter.

An increase in coercive field and fractional remanence was observed for Co-rich nanowires. The results show that for FeCo nanowires the shape anisotropy dominates and the magnetization easy axis is oriented along the nanowire axis. For Co

nanowires the magnetocrystalline anisotropy, which tends to align the magnetization perpendicularly to the nanowire axis, nearly compensate the nanowire shape anisotropy.

Adding a small amount of non-ferromagnetic material as Cu to the FeCo alloy nanowires gives rise only to modest changes in the nanowires crystallographic structure and magnetic properties. A much larger effect is produced if a thermal treatment is performed on the samples. The addition of a small amount of Cu together with optimal annealing induces a better crystalline texture and a significant magnetic hardening of the FeCo nanowire arrays. The optimal annealing temperature depends on the nanowire array geometrical parameters. At higher annealing temperatures, a partial oxidation of the metallic nanowires has been observed.

The magnetic hardening induced by Cu-doping and annealing has been found to be a consequence of enhanced magnetocrystalline anisotropy energy (MAE). Ferromagnetic Resonance together with detailed study of the crystallographic structure has been used to confirm and quantify this effect. Annealing leads to an increase in crystallite size together with a partial reorientation of the growth directions with respect to the nanowire axis. This reorientation is accompanied by a crystal lattice strain. It was determined that the maximum increase in MAE for Cu-doped nanowires is almost twice larger than that for FeCo alloy nanowires, which allow us to conclude that Cu supports the crystal reorientation upon annealing causing a larger lattice strain. This significant increase in the MAE is independent of the nanowire diameter, but was influenced by the preferential initial growth direction. The addition of Cu to the FeCo nanowires allows tailoring of their microstructure and thus the MAE, which promotes a magnetic hardening.

Bibliography

[1] T. Maurer, F. Ott, G. Chaboussant, Y. Soumare, J.-Y. Piquemal, G. Viau, Magnetic nanowires as permanent magnet materials, *Appl. Phys. Lett.*, 91 (2007) 172501.

[2] D. Niarchos, G. Giannopoulos, M. Gjoka, C. Sarafidis, V. Psycharis, J. Rusz, A. Edström, O. Eriksson, P. Toson, J. Fidler, Toward Rare-Earth-Free Permanent Magnets: A Combinatorial Approach Exploiting the Possibilities of Modeling, Shape Anisotropy in Elongated Nanoparticles, and Combinatorial Thin-Film Approach*, JOM*, 67 (2015) 1318-1328.

[3] A. Encinas-Oropesa, M. Demand, L. Piraux, I. Huynen, U. Ebels, Dipolar interactions in arrays of nickel nanowires studied by ferromagnetic resonance, *Phys. Rev. B*, 63 (2001) 104415.

[4] K. Gandha, K. Elkins, N. Poudyal, X. Liu, J.P. Liu, High energy product developed from cobalt nanowires, *Sci. Rep.,* 4 (2014) 5345.

[5] S. Liébana-Viñas, R. Salikhov, C. Bran, E.M. Palmero, M. Vazquez, B. Arvan, X. Yao, P. Toson, J. Fidler, M. Spasova, Magnetic hardening of $Fe_{30}Co_{70}$ nanowires, *Nanotechnology*, 26 (2015) 415704.

[6] R.M. Bozorth, Factors affecting magnetic quality, in: Ferromagnetism, John Wiley & Sons, Inc., Hoboken, New Jersey, 2003, pp. 14-47.

[7] J. Coey, Hard magnetic materials: A perspective, *IEEE Trans. Magn.,* 47 (2011) 4671-4681.

[8] L.H. Lewis, F. Jiménez-Villacorta, Perspectives on permanent magnetic materials for energy conversion and power generation, *Metall. Mater. Trans. A*, 44 (2013) 2-20.

[9] R. Hertel, J. Kirschner, Magnetization reversal dynamics in nickel nanowires, *Physica B*, 343 (2004) 206-210.

[10] Y.P. Ivanov, M. Vázquez, O. Chubykalo-Fesenko, Magnetic reversal modes in cylindrical nanowires, *J. Phys. D.-Appl. Phys.,* 46 (2013) 485001.

[11] Q. Zhan, Z. Chen, D. Xue, F. Li, H. Kunkel, X. Zhou, R. Roshko, G. Williams, Structure and magnetic properties of Fe-Co nanowires in self-assembled arrays, *Phys. Rev. B*, 66 (2002) 134436.

[12] J. Sánchez-Barriga, M. Lucas, F. Radu, E. Martin, M. Multigner, P. Marin, A. Hernando, G. Rivero, Interplay between the magnetic anisotropy contributions of cobalt nanowires, *Phys. Rev. B*, 80 (2009) 184424.

[13] L. Vivas, Y.P. Ivanov, D. Trabada, M. Proenca, O. Chubykalo-Fesenko, M. Vázquez, Magnetic properties of Co nanopillar arrays prepared from alumina templates, *Nanotechnology*, 24 (2013) 105703.

[14] Y. Chen, H. Tzeng, L. Wei, L. Wang, J. Oung, H. Shih, Corrosion resistance and mechanical properties of low-alloy steels under atmospheric conditions, *Corros. Sci.,* 47 (2005) 1001-1021.

[15] T. Baker, Processes, microstructure and properties of vanadium microalloyed steels, *Mater. Sci. Tech*., 25 (2009) 1083-1107.

[16] M.A. Hussein, A.S. Mohammed, N. Al-Aqeeli, Wear Characteristics of Metallic Biomaterials: A Review, *Materials*, 8 (2015) 2749-2768.

[17] J. Fu, Z. Yan, Y. Xu, X. Fan, D. Xue, Effects of annealing temperature on structure and magnetic properties of amorphous $Fe_{61}Co_{27}P_{12}$ nanowire arrays, *J. Phys. Chem. Solids,* 68 (2007) 2221-2226.

[18] V. Vega, J. García, W.d.O.d. Rosa, L. Vivas, V. Prida, B. Hernando, M. Vázquez, Magnetic Properties of (Fe, Co)–Pd Nanowire Arrays, *J. Nanosci. Nanotechno.*, 12 (2012) 7501-7504.

[19] Z. Liu, W. Li, P. Jin, W. Fei, Magnetic anisotropy transformation of Co–Fe–B nanowire arrays synthesized under the magnetic field, *J. Magn. Magn. Mater.,* 345 (2013) 96-99.

[20] C. Bran, Y.P. Ivanov, J. García, R. del Real, V. Prida, O. Chubykalo-Fesenko, M. Vazquez, Tuning the magnetization reversal process of FeCoCu nanowire arrays by thermal annealing, *J. Appl. Phys.,* 114 (2013) 043908.

[21] T. Nishizawa, K. Ishida, Binary alloy phase diagrams, ASM International, OH, 2 (1990).

[22] H. Kronmüller, M. Fähnle, Micromagnetism and the microstructure of ferromagnetic solids. 2003, in, Cambridge: Cambridge University Press.

[23] R.C. O'handley, Modern magnetic materials, Wiley, 2000.

[24] Y.P. Ivanov, D.G. Trabada, A. Chuvilin, J. Kosel, O. Chubykalo-Fesenko, M. Vázquez, Crystallographically driven magnetic behaviour of arrays of monocrystalline Co nanowires, *Nanotechnology*, 25 (2014) 475702.

[25] K. Nielsch, J. Choi, K. Schwirn, R.B. Wehrspohn, U. Gösele, Self-ordering regimes of porous alumina: the 10 porosity rule, *Nano Lett.,* 2 (2002) 677-680.

[26] S. Tang, W. Chen, M. Lu, S. Yang, F. Zhang, Y. Du, Nanostructure and magnetic properties of $Fe_{69}Co_{31}$ nanowire arrays, *Chem. Phys. Lett.,* 384 (2004) 1-4.

[27] K.R. Pirota, E.L. Silva, D. Zanchet, D. Navas, M. Vázquez, M. Hernández-Vélez, M. Knobel, Size effect and surface tension measurements in Ni and Co nanowires, *Phys. Rev. B,* 76 (2007) 233410.

[28] C. Bran, E.M. Palmero, R.P. del Real, M. Vazquez, CoFeCu electroplated nanowire arrays: Role of composition and annealing on structure and magnetic properties, *Phys. Status Solidi A*, 211 (2014) 1076-1082.

[29] B. Rodríguez-González, C. Bran, T. Warnatz, J. Rivas, M. Vazquez, Structural and magnetic characterization of as-prepared and annealed FeCoCu nanowire arrays in ordered anodic aluminum oxide templates, *J. Appl. Phys.,* 115 (2014) 133904.

[30] U. Ebels, J.-L. Duvail, P. Wigen, L. Piraux, L. Buda, K. Ounadjela, Ferromagnetic resonance studies of Ni nanowire arrays, *Phys. Rev. B,* 64 (2001) 144421.

[31] M. Darques, A. Encinas, L. Vila, L. Piraux, Tailoring of the c-axis orientation and magnetic anisotropy in electrodeposited Co nanowires, *J. Phys.-Condens. Mat.,* 16 (2004) S2279.

[32] G. Ababei, A. Popa, N. Lupu, L. Giurgiu, H. Chiriac, Ferromagnetic resonance of NiFe/Cu multilayered nanowires, *J. Optoelectron. Adv. M.,* 13 (2011) 405-408.

[33] M. Chipara, R. Skomski, R. Kirby, D.J. Sellmyer, Ferromagnetic resonance on Ni nanowire arrays, *J. Mater. Res.,* 26 (2011) 2169-2174.

[34] M. Sharma, S. Pathak, M. Sharma, FMR Measurements of Magnetic Nanostructures, Ferromagnetic Resonance–Theory and Applications, 93 (2013).

[35] X. Liu, H. Kanda, A. Morisako, The effect of underlayers on FeCo thin films, *J. Phys. Conf. Ser.,* 266 (2011), 012037.

[36] D. Polder, VIII. On the theory of ferromagnetic resonance, The London, Edinburgh, and Dublin Philosophical Magazine and Journal of Science, 40 (1949) 99-115.

[37] M. Farle, Ferromagnetic resonance of ultrathin metallic layers, *Rep. Prog. Phys.,* 61 (1998) 755.

[38] E.M. Palmero, C. Bran, R.P. del Real, M. Vázquez, Vortex domain wall propagation in periodically modulated diameter FeCoCu nanowire as determined by the magneto-optical Kerr effect, *Nanotechnology*, 26 (2015) 461001.

[39] T. Mühge, T. Zeidler, Q. Wang, C. Morawe, N. Metoki, H. Zabel, Structural and magnetic studies of Fe_xCo_{1-x} (001) alloy films on MgO (001) substrates, *J. Appl. Phys.,* 77 (1995) 1055-1060.

[40] J. Pelzl, R. Meckenstock, D. Spoddig, F. Schreiber, J. Pflaum, Z. Frait, Spin–orbit-coupling effects on g-value and damping factor of the ferromagnetic resonance in Co and Fe films, *J. Phys.-Condens. Mat.,* 15 (2003) S451.

[41] L. Reichel, G. Giannopoulos, S. Kauffmann-Weiss, M. Hoffmann, D. Pohl, A. Edström, S. Oswald, D. Niarchos, J. Rusz, L. Schultz, Increased magnetocrystalline anisotropy in epitaxial Fe-Co-C thin films with spontaneous strain, *J. Appl. Phys*., 116 (2014) 213901.

[42] G. Giannopoulos, R. Salikhov, B. Zingsem, A. Markou, I. Panagiotopoulos, V. Psycharis, M. Farle, D. Niarchos, Large magnetic anisotropy in strained Fe/Co multilayers on AuCu and the effect of carbon doping, *APL Materials*, 3 (2015) 041103.

[43] L. Reichel, L. Schultz, D. Pohl, S. Oswald, S. Fähler, M. Werwiński, A. Edström, E.K. Delczeg-Czirjak, J. Rusz, From soft to hard magnetic Fe–Co–B by spontaneous strain: a combined first principles and thin film study, *J. Phys.-Condens. Mat*., 27 (2015) 476002.

[44] G. Pourroy, S. Läkamp, S. Vilminot, Stabilization of iron-cobalt alloy isomorphous of α-Mn in a metal ferrite composite*, J. Alloy. Compd*., 244 (1996) 90-93.

[45] J.M. Baik, M. Schierhorn, M. Moskovits, Fe nanowires in nanoporous alumina: geometric effect versus influence of pore walls, *J. Phys. Chem. C*, 112 (2008) 2252-2255.

[46] B.D. Cullity, Diffraction I: The directions of diffracted beams, in: Elements of X-ray diffraction, Addison-Wesley Publishing Company, Inc., Reading, Massachusetts, 1956, pp. 78-103.

[47] N. Hosseinabadi, R.S. Mamoory, B. Kaleji, Synthesis, phase study and magnetic characterisation of $Co_{50}Fe_{40}Cu_{10}$ ternary alloy nanopowders prepared by mechanochemical alloying process, *Powder Metall*., 53 (2010) 260-264.

[48] M.V. Turchanin, T., Cobalt - Copper - Iron, in: S.I. Günter Effenberg (Ed.) Landolt-Börnstein - Group IV Physical Chemistry, SpringerMaterials, Stuttgart, Germany, 2008.

[49] H. Baker, Alloy phase diagrams, in: ASM Handbook, Materials Park, ASM publication, Ohio, 1993.

Chapter 4

Multilayer Nanowires

Series of cylindrical FeCoCu/Cu nanowires with different ferromagnetic segments (FeCoCu) lengths and non-ferromagnetic layers (Cu) thickness and keeping constant the nanowire diameter have been fabricated by electrodeposition into anodic alumina templates. A detailed geometrical and crystallographic characterization has been performed. The influence of the segments/layers length/thickness on the magnetic properties of the nanowire array has been studied. Furthermore, the effects of the magnetic interactions between neighbor nanowires have been quantified and correlated to the segments/layers length/thickness.

4.1. Introduction

As described in the previous chapter, FeCo-based nanowires are being investigated due to their large saturation magnetization and coercive field, implying a high energy product that make them appropriate for specific technological applications (e.g. alternative rare-earth-free permanent magnets) [1, 2]. Different options to enhance these magnetic properties have been proposed, like doping with non-magnetic elements [3-5], enhancing the nanowires coercive field by pinning [6], diameter modulation along the nanowire [7, 8], or compositional modulation along the nanowire (i.e. multilayer nanowires) [9, 10]. In the case of multilayer nanowires, apart from the possibility of further magnetically hardening, they show interesting properties for functionalization [11-13].

The magnetic behavior of ferromagnetic/non-ferromagnetic (FM/NFM) multilayer nanowires is affected by the Cu thickness since depending on it, magnetostatic coupling between FeCoCu segments can be originated through the Cu layers along the nanowire. The presence of Cu layers creates a complex interacting system inside the array, as the interactions between FeCoCu segments along each nanowire are accompanied by interactions among FeCoCu segments from neighbor nanowires [14-16]. Therefore, the interactions between magnetic elements in this kind of nanostructured systems critically affect the magnetic properties of the whole array.

A powerful technique to study the magnetic interactions and quantify the effects on the magnetic properties is the First-Order Reversal Curve (FORC) technique. This method has been successfully used to study different many-body interacting systems, such as magnetic nanowire, nanopillar or nanotube arrays, as well as to antidot and multilayer films [17-24].

4.2. Geometrical, compositional and structural characterization

Two series of multilayer nanowire arrays were fabricated by: (i) keeping constant the non-ferromagnetic layer thickness (x) and varying the ferromagnetic segments length (y); or (ii) keeping constant y and varying x. As FM material was used FeCoCu alloy and Cu as NFM one. The nanowire arrays were fabricated by electrodeposition into high hexagonally ordered pores of AAO templates in a three-electrode cell using a single Watts-type bath. The applied voltage was constant but different for each material, and the different layers/segments thicknesses were obtained by modifying the electrodeposition time. In all the samples, FeCoCu/Cu bilayers were repeated ten times. Along this chapter, the samples are labeled as $[\mathrm{FeCoCu}(y)/\mathrm{Cu}(x)]_{10}$. More details about the fabrication process of multilayer nanowire arrays can be found in Section 2.2.3. To complement the study a continuous FeCoCu alloy nanowire array was fabricated (see Section 2.2 for more details).

The geometrical characterization was performed by High-Resolution Scanning Electron Microscopy (SEM). For all the multilayer nanowires, the individual Cu layer thickness (x), FeCoCu segment length (y), nanowire diameter (d_{NW}), distance between nanowire centers (D_{int}) and nanowire total length (L_{NW}) were determined. For all the

nanowires d_{NW} and D_{int} were constant with a value of 35 nm and 105 nm, respectively (Figure 4.1(a)). Figure 4.1(b) to (d) show representative cross section views of multilayer nanowire arrays with different x and y. For the [FeCoCu/Cu(x)]$_{10}$ nanowires, the FeCoCu segment length was 300 nm, and x ranged between 7 and 40 nm. For the [FeCoCu(y)/Cu]$_{10}$ nanowires, the Cu layer thickness was about 15 nm and y varied between 120 and 900 nm. The values for the different layer/segment thickness/length with the corresponding growing time for each layer/segment (t_{Cu} for the NFM layers and t_{FeCoCu} for the FM segments) are collected in Table 4.1. The continuous nanowires were 35 nm in diameter and 6.5 μm in length. A composition of $Fe_{30}Co_{64}Cu_6$ for the continuous nanowires was determined by Energy Dispersive X-ray Spectrometer (EDS), assumed to be the same for FeCoCu segments in the multilayer nanowires.

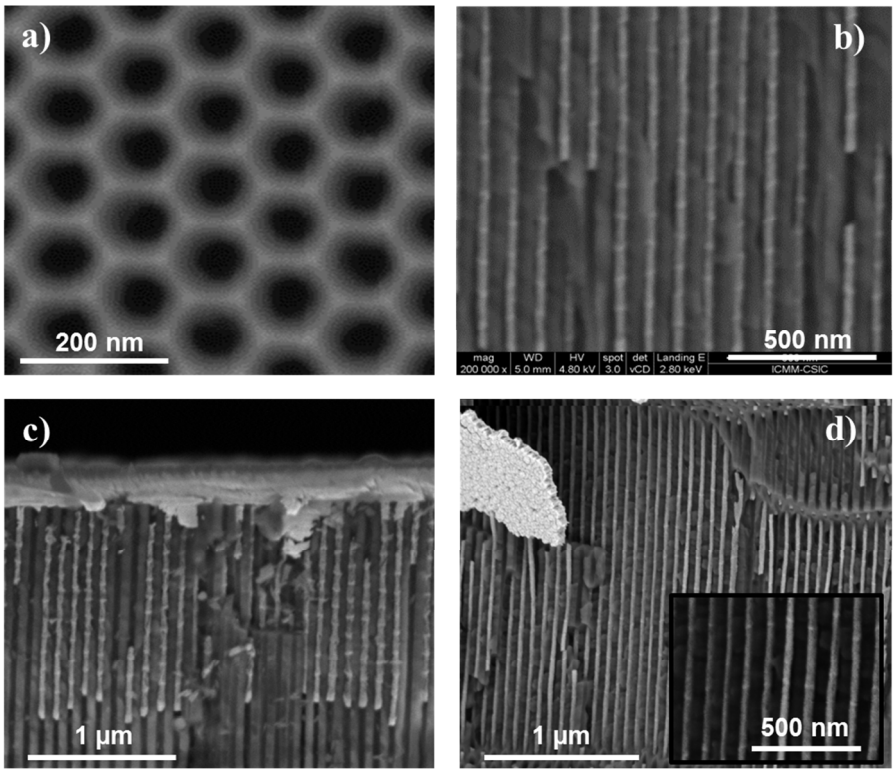

Figure 4.1 SEM images: (a) Top view of an AAO template with 35 nm pore diameter; multilayer nanowire arrays cross-section for (b) [FeCoCu(160 nm)/Cu(15 nm)]$_{10}$, (c) [FeCoCu(120 nm)/Cu(15 nm)]$_{10}$ and (d) [FeCoCu(300 nm)/Cu(15 nm)]$_{10}$ (inset: nanowires closer view).

Table 4.1 Duration of the electrodeposition pulses and corresponding segment/layer thickness for fixed Cu layer and FeCoCu segment thickness.

Fixed Cu layer thickness (15 nm)		Fixed FeCoCu segment length (300 nm)	
Electrodeposition time, t_{FeCoCu} (s)	FeCoCu segment length, y (nm)	Electrodeposition time, t_{Cu} (s)	Cu layer thickness, x (nm)
10	120	5	7
15	160	15	15
25	300	35	25
35	400	50	35
60	900	60	40

The morphology and the microstructure of the nanowires was characterized by High Resolution Transmission Electron Microscopy (HRTEM) and Selected Area Electron Diffraction (SAED) (Figure 4.2). The multilayer nanowires show polycrystalline nature, which can be identified by the granular-like contrast in the bright field image (Figure 4.2(a)). A HRTEM image with a closer view of a Cu layer is shown in Figure 4.2(b). In that image multiple sets of fringes are found in different regions related to the presence of grains with different crystal orientations. The crystal structure of the FeCoCu segments and the Cu layer was determined by local Fourier analysis of the images. Both parts of the multilayer nanowires (i.e. the FM segment and the NFM layer) show polycrystalline structure. The Fast Fourier Transform (FFT) in the Cu area (Figure 4.2(c)) presents reflections at approximately 2.08 Å and 1.80 Å corresponding to the (111) and (200) planes of a face-centered cubic (*fcc*) structure. FFT for FeCoCu presents the typical reflections associated to a body-centered cubic (*bcc*) symmetry, such as the (110) set at around 2 Å marked with white lines (Figure 4.2(d)).

The chemical composition of the multilayer nanowires was analysed by Scanning Transmission Electron Microscopy (STEM). High-Angle Annular Dark Field (HAADF) combined with Electron Energy Loss Spectroscopy (EELS) was used to acquire Spectrum Images (SI) of the different regions. An example of chemical map is depicted in Figure 4.3 for the sample with x = 300 nm and y = 7 nm. It is observed that Cu layers are perfectly segregated from the FeCoCu segments. They appear to be irregular and rough, probably due to the polycrystalline nature of the nanowires, the large grain size and inhomogeneities in the growth (see Figure 4.3(a)). The blue color at

the surface in the chemical maps of the multilayer nanowire suggests the presence of an oxidation layer all around the nanowire, evidenced by the high oxygen content in the outer surface of the nanowire. These features are confirmed by a higher magnification STEM-EELS map (Figure 4.3(b) and (c)) showing that the nanowire presents a high degree of oxidation around 9 nm near the surface. In the Cu layers, the oxidation decreases with respect to the FeCoCu segments to less than 4 nm.

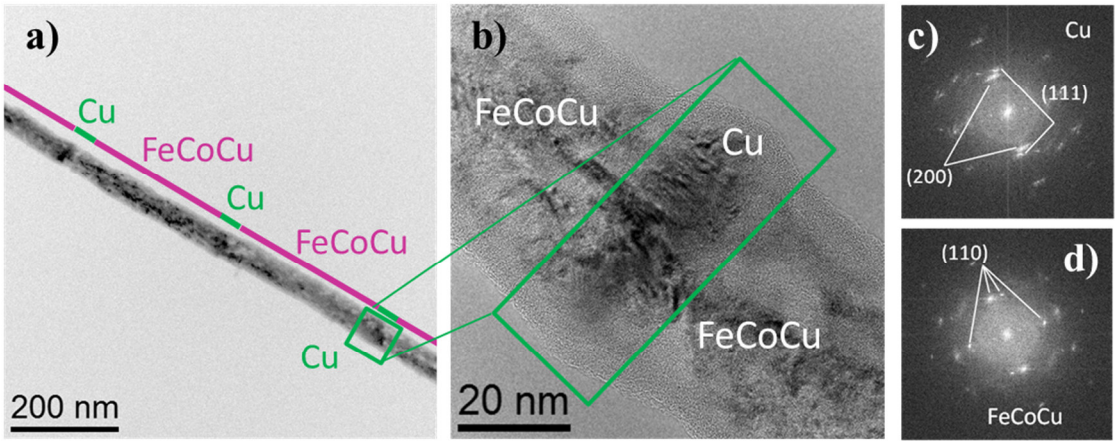

Figure 4.2 TEM images of [FeCoCu(300 nm)/Cu(15 nm)]$_{10}$ nanowires: (a) Bright field image of an individual nanowire, (b) HRTEM image of a Cu spacer, (c) and d) Fast Fourier Transform at Cu and FeCoCu regions of the HRTEM image, respectively.

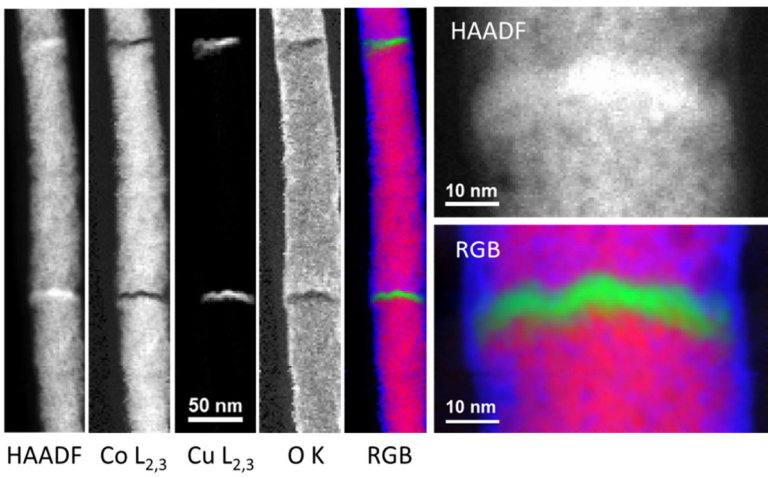

Figure 4.3 STEM-EELS chemical mapping of [FeCoCu(300 nm)/Cu(7 nm)]$_{10}$ nanowires: (a) low magnification SI of one of the nanowires, including the HAADF and the RGB composition of the Co $L_{2,3}$ (red), Cu $L_{2,3}$ (green) and O K (blue) integrated intensities; high magnification SI around a Cu spacer showing (b) the simultaneously acquired HAADF signal and (c) the RGB image composition with the same color code as in (a).

4.3. Magnetic characterization of nanowire arrays

The magnetic characterization of the multilayer nanowire arrays was performed by Vibrating Sample Magnetometer (VSM). The hysteresis loops were obtained for parallel (||) and perpendicular (⊥) applied magnetic field. Figure 4.4 shows the hysteresis loops of two of the samples measured in both configuration of the applied field. All the multilayer nanowire arrays present the same magnetic behavior in both configurations. For comparison, the hysteresis loops in || field configuration for all the samples, including the continuous nanowire array, are shown in Figure 4.5.

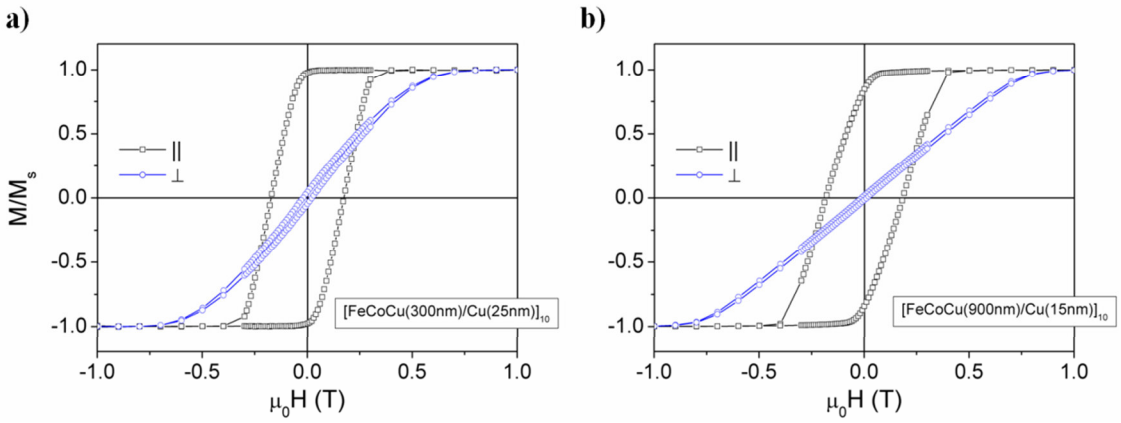

Figure 4.4 Hysteresis loops of multilayer nanowire arrays in parallel (||) and perpendicular (⊥) configurations of the applied magnetic field for: (a) x = 25 nm, y = 300 nm; and (b) x = 15 nm, y = 900 nm.

For each sample, the values of coercive field (H_c) and fractional remanence (M_r/M_s) from the hysteresis loop in || and ⊥ configuration were determined. The magnetic parameters for both configurations were plotted as a function of the Cu layer thickness (x) and FeCoCu segment length (y), Figure 4.6(a) and (b), respectively. Data for continuous FeCoCu nanowire array are also included for comparison (single scatters in the graphs). For all the samples, the high values of M_r/M_s under parallel field configuration together with the vanishing values under perpendicular field configuration suggest that the magnetization easy axis lies along the nanowires axis. The saturation magnetization for FeCoCu alloy nanowires takes a value of $\mu_0 M_s$ = 1.82 T. For FeCoCu/Cu multilayer nanowires the saturation magnetization depends on the ratio between the Cu layers and FeCoCu segments length. For both series of multilayer nanowires, it was calculated a maximum reduction of saturation magnetization of 11% in comparison to continuous FeCoCu alloy nanowire array. Figure 4.7(a) and (b) show

the differential magnetic susceptibility around the coercivity ($\chi = dM/dH$, for magnetic field applied parallel to the nanowires) for both series of multilayer nanowire arrays as a function of the Cu layer thickness and FeCoCu segments length, respectively. In these graphs the value of χ for continuous FeCoCu nanowire array is included as single scatter for comparison.

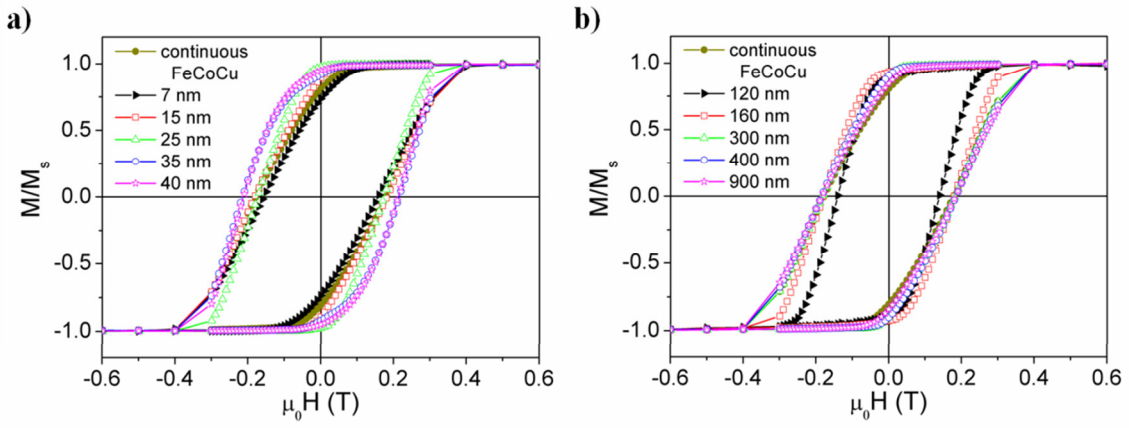

Figure 4.5 Hysteresis loops measured in parallel field configuration: (a) $[FeCoCu(300\ nm)/Cu(x)]_{10}$ series for different Cu layer thickness, and (b) $[FeCoCu(y)/Cu(15\ nm)]_{10}$ series for different FeCoCu segment length.

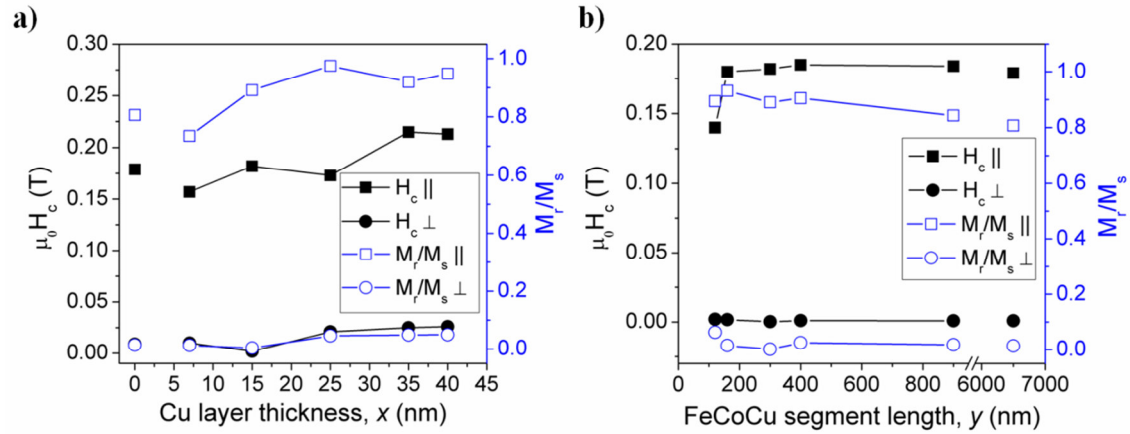

Figure 4.6 Coercive field ($\mu_0 H_c$) and fractional remanence (M_r/M_s) dependence on: (a) Cu layer thickness ($[FeCoCu(300\ nm)/Cu(x)]_{10}$), and (b) FeCoCu segment length ($[FeCoCu(y)/Cu(15\ nm)]_{10}$). Data for continuous FeCoCu alloy nanowires are represented by single scatters.

For magnetic field applied parallel to the nanowire axis, all magnitudes, the coercive field, the fractional remanence and, particularly, the susceptibility, show a general trend to increase with the Cu layer thickness for constant FeCoCu segments (y = 300 nm) (Figure 4.6(a) and Figure 4.7(a)). For perpendicular field configuration, both $\mu_0 H_c$ and M_r/M_s show small values. Figure 4.6(b) shows that for constant Cu layer thickness (x=15nm) and increasing FeCoCu segments length up to y = 160 nm, $\mu_0 H_c$ for || configuration increases significantly, being almost constant for longer FM segments. M_r/M_s for || configuration does not vary significantly for y ≤ 400 nm, while for increasing FM segments length M_r/M_s decreases slightly due the stronger demagnetizing interactions between longer nanowires. However, Figure 4.7(b) shows that the susceptibility presents a significant reduction when the FeCoCu segment length increases up to around 300 nm while it remains nearly constant for larger lengths.

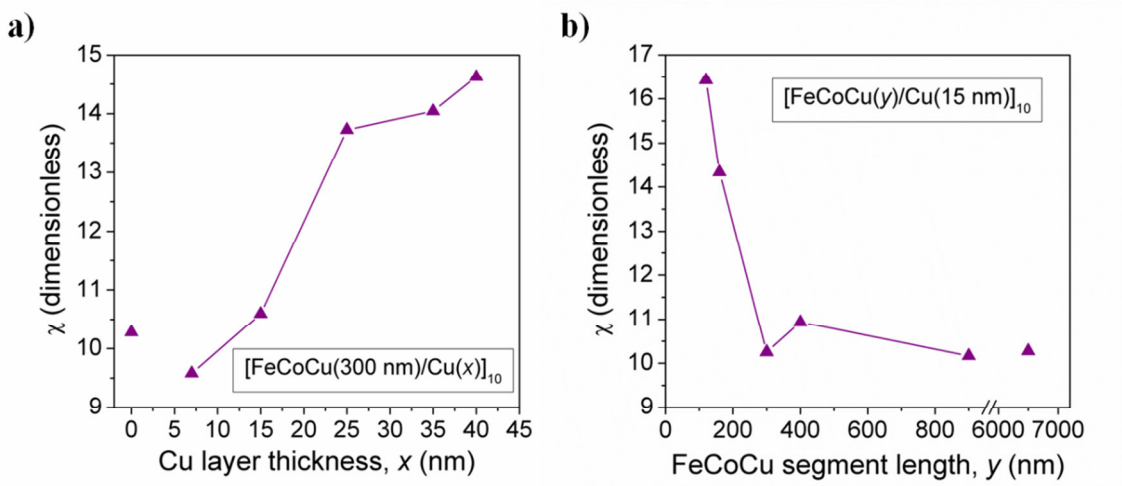

Figure 4.7 Differential susceptibility, χ, dependence on: (a) Cu layer thickness, x, and (b) FeCoCu segment length, y. Single scatters represent the data for continuous FeCoCu alloy nanowires.

4.4. Magnetic interactions in the nanowire arrays

The study of the magnetic interactions that take place into a multilayer nanowire array is a really important task as they affect substantially the magnetic behaviour of the nanowire array. The interactions in a magnetic system can be determined by qualitative or quantitative methods. In this work, firstly Henkel plots have been used as qualitative technique to determine in which of the multilayer

nanowire array a stronger interactions are obtained, while First-Order Reversal Curve (FORC) has been used to quantify the influence of the Cu layer thickness and the FeCoCu segment length on the coercivity and interaction field of the system.

Henkel plots consist on the simultaneous graphical representation of two experimental measurements: the dc-demagnetization (DCM) and the isothermal remanent magnetization (IRM) experiments. For the DCM experiment, the nanowire array is initially in a saturated state and then, at a constant temperature, a magnetic field is applied in the direction opposite to the magnetization. After this, the field is switched off and the remanent magnetization is measured. This process is repeated again, increasing the magnetic field until the nanowire array is saturated in the opposite direction. For the IRM experiment, an AC demagnetization process was performed. Subsequently, a magnetic field is applied, then switched off and the remanent magnetization is measured. This process is repeated, increasing the applied magnetic field until the nanowire array reaches the saturation magnetization [25].

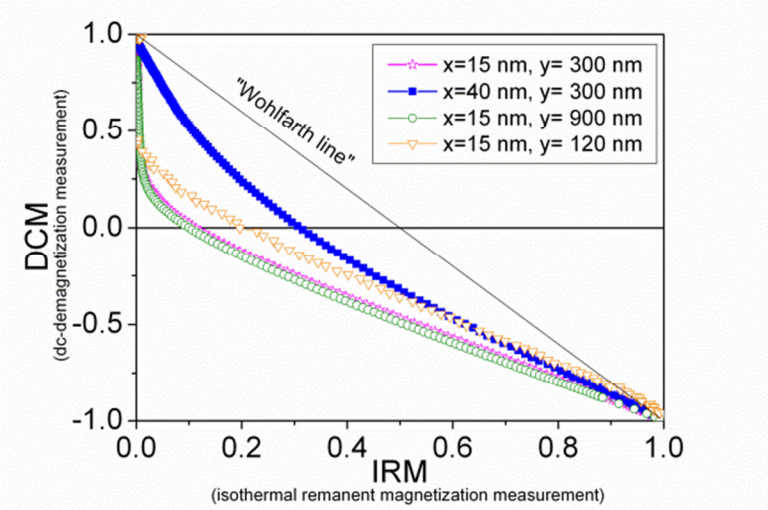

Figure 4.8 Henkel plots for [FeCoCu(y)/Cu(x)]$_{10}$ multilayer nanowires. The black line shows the behavior of non-interacting nanocylinders.

Figure 4.8 shows the Henkel plots for several [FeCoCu(y)/Cu(x)]$_{10}$ nanowire arrays with different Cu layer thickness (x) and FeCoCu segment length (y). In the graph, the black line represens the linear behaviour of a theoretical system of non-interacting nanoparticles (Wohlfarth model) [26, 27], which is given by:

$$DCM(\mu H) = 1 - 2\,IRM(\mu H) \tag{4.1}$$

The Henkel plots show that all the curves fit below the line corresponding to the Wohlfarth model, indicating that the net magnetostatic interactions in the multilayer nanowire array always favour the nanowire demagnetization. In the plots for nanowires with the same FeCoCu segment length (y = 300 nm), the one for the thickest Cu layer (*x* = 40 nm) is closer to the non-interacting line. However, for nanowires with constant Cu layer thickness (*x* = 15 nm), the data obtained for shortest FeCoCu segments is closer to the Wohlfarth line. According to the results, the qualitative analysis shows that thicker Cu layers and shorter FeCoCu segments promote a decrease of the dipolar interaction field in the multilayer nanowire array.

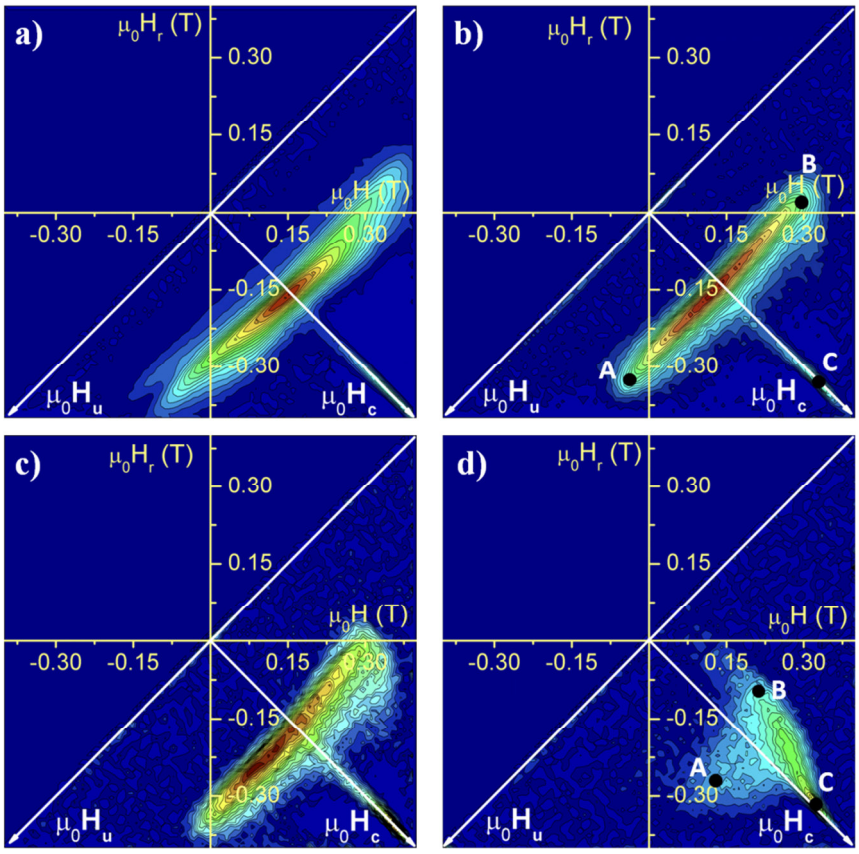

Figure 4.9 FORC distributions for: (a) continuous FeCoCu nanowire array; and multilayer nanowire arrays with different Cu layer thicknesses (*x*) and the same FeCoCu segment length ([FeCoCu(300 nm)/Cu(*x*)]$_{10}$): (b) *x* = 7 nm, (c) *x* = 15 nm and (d) *x* = 40 nm.

The magnetic behaviour of the [FeCoCu(y)/Cu(x)]$_{10}$ multilayer nanowire arrays was measured using the procedure described in Section 2.3.2.1 to obtain the FORC distributions. The distributions calculated for continuous FeCoCu alloy and multilayer nanowire arrays with constant Cu layer thickness (i.e. [FeCoCu(y)/Cu(15 nm)]$_{10}$) are shown in Figure 4.9, and the distributions for multilayer nanowire arrays with constant FeCoCu segment length (i.e. [FeCoCu(300 nm)/Cu(x)]$_{10}$) are plotted in Figure 4.10.

According to Figure 4.9 and Figure 4.10, the experimental FORC diagrams can be classified in roughly two different types, based on the number of branches and the angle made between the first branch (closest to $\mu_0 H_u$ axis, from point A to B in Figure 4.9(b) and (d)) and the $\mu_0 H_u$ axis. However, all measured multilayer nanowire arrays FORC distributions represent a system where the interactions are demagnetizing (interaction field opposite to the magnetization).

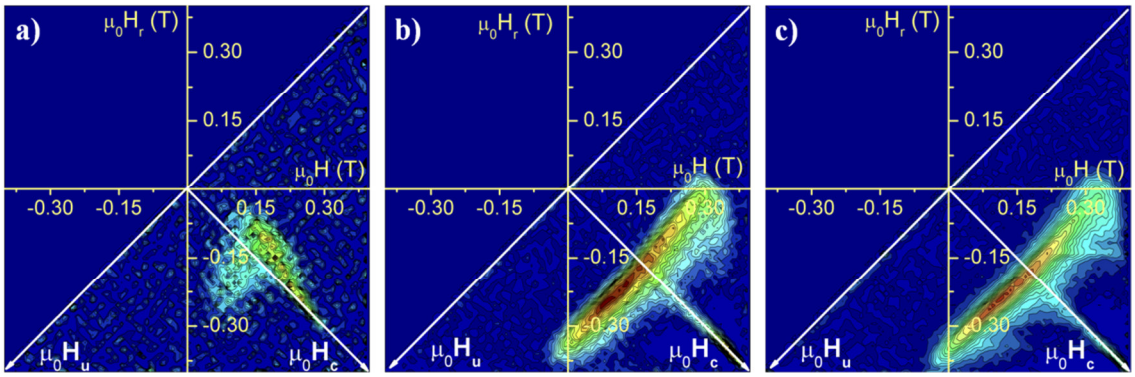

Figure 4.10 FORC distributions for multilayer nanowire arrays with the same Cu layer thickness and different FeCoCu segment length ([FeCoCu(y)/Cu(15nm)]$_{10}$): (a) y = 120 nm, (b) y = 300 nm and (c) y = 900 nm.

The diagram shape exhibited by the FORC distribution of continuous FeCoCu alloy nanowires (Figure 4.9(a)) and the multilayer nanowire arrays with thin Cu layers ($x \leq 15$ nm) (see Figure 4.9(b) and (c)) or thick FeCoCu segments ($y \geq 300$ nm) (see Figure 4.10(b) and (c)) is the shape generally associated to a magnetic nanowire array [28-31]. This diagram is characterized by a single branch, widely spread along $\mu_0 H_u$ axis (branch from point A to B in Figure 4.9(b)). It has already been reported that symmetrical and nearly identical irreversible processes (same coercive field) under a mean demagnetizing interaction field ($\mu_0 H_{int} = \mu_0 H_i\ (M/M_s)$, with $\mu_0 H_i < 0$), would

exhibit a single narrow FORC distribution parallel to the $\mu_0 H_u$ axis [32]. In this case, the value of coercive field at $\mu_0 H_u = 0$ is called the FORC coercivity ($\mu_0 H_c^{FORC}$) and can be taken as an estimation of the average coercive field of individual nanowires [28, 33]. The value of $\mu_0 H_c^{FORC}$ is determined as the coercive field where the maximum value of ρ_{FORC} is obtained in the coercive field distribution (Figure 4.11(a)). The cross-section of the FORC distribution parallel to $\mu_0 H_u$ axis and crossing the $\mu_0 H_c$ axis at $\mu_0 H_c^{FORC}$, is related to the interaction field distribution. The interaction field (ΔH_u) is obtained by taking the half-width at half-maximum of the uniform part of the interaction field distribution (see Figure 4.11(b)), and represents the interaction field maximum value (at saturation) between nanowires [19]. In these graphs, we also observe a tail along the $\mu_0 H_c$ axis, which can reach high $\mu_0 H_c$ values (point C in Figure 4.9(b) and relative maximum in Figure 4.11(a) enclosed in red color). This feature has not been considered in the present study since it comes from the spatial non-homogeneity of the interaction field at the lateral edges of the macroscopic sample [34].

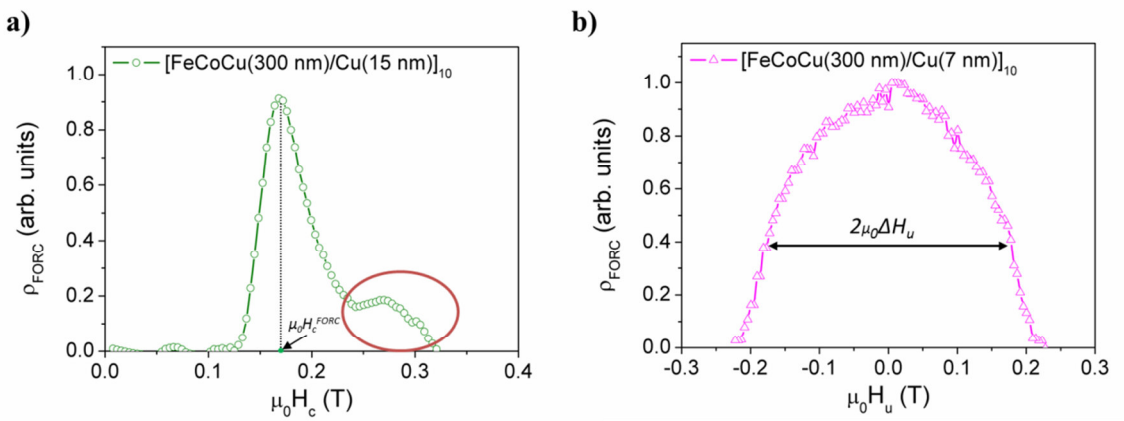

Figure 4.11 Selected examples of (a) coercive field and (b) interaction field distributions.

On the other hand, the multilayer nanowire array with thicker Cu layers (NFM layer) (i.e., y = 300 nm and x = 40 nm) (Figure 4.9(d)), and the one with shorter FM segments (i.e., y = 120 nm and x = 15 nm) (Figure 4.10(a)) show a different FORC diagram, whose distribution is similar to the so-called wishbone shape, observed in other interacting systems [18, 19, 23, 35, 36], with a demagnetizing mean interaction field but with a non-negligible coercive field distribution [18]. For the systems with wishbone shape FORC distribution, data about the nanowires coercivity and interaction field cannot be straightforward extracted as for the single elongated FORC distribution.

The parametrization of this specific configuration has been performed according to Refs. [19, 23], which has allowed us to obtain the following parameters: $\mu_0\overline{H_c}$ and $\mu_0 H_\sigma$ are the local coercivity average and its standard deviation, and $\mu_0 H_i$ and $\mu_0 H_{\sigma i}$ are the interaction field constant and the corresponding standard deviation, respectively. When performing the parametrization, it was observed that the experimental data are not auto-consistent for $\mu_0\overline{H_c}$. In order to verify the accuracy of the parametrization for the multilayer nanowire arrays, the FORC diagrams resulting from the values for the different parameters obtained using the wishbone model were simulated (Figure 4.12).

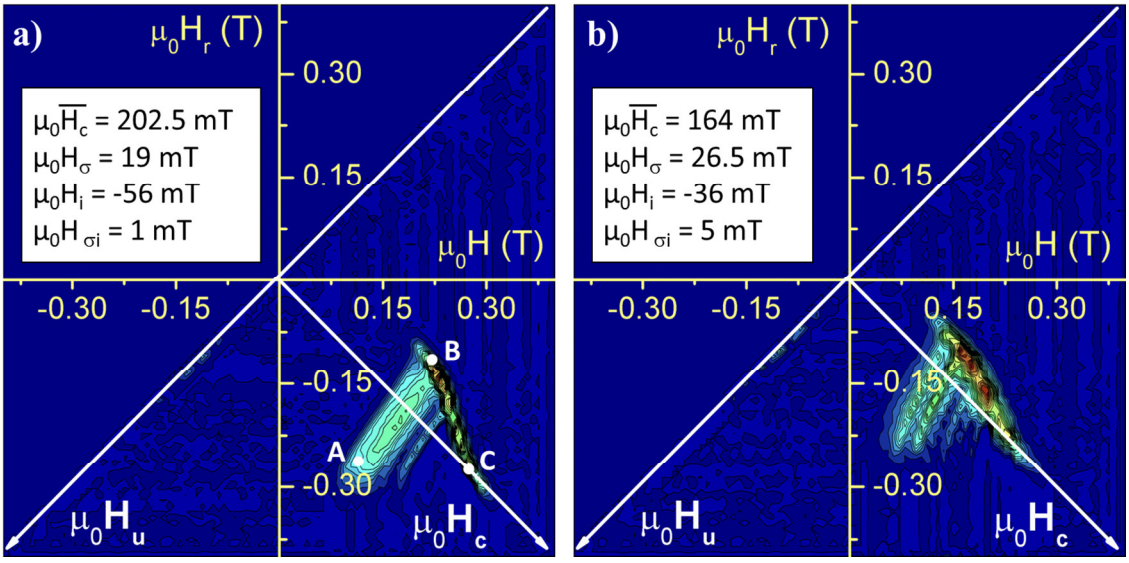

Figure 4.12 Simulated FORC distributions for: (a) [FeCoCu(300 nm)/Cu(40 nm)]$_{10}$ and (b) [FeCoCu(120 nm)/Cu(15 nm)]$_{10}$ multilayer nanowires.

Comparing the experimental FORC distributions in Figure 4.9(d) and Figure 4.10(a) with the simulated distributions in Figure 4.12(a) and (b), respectively, an overall good agreement among the FORC distribution shapes is observed, however, they present several differences. Firstly, the maximum in the left end of the simulated upper branch (point B in Figure 4.12(a)) presents a higher intensity than in the experimental distribution, which is ascribed to the possible inhomogeneities in the sample. Here it is assumed that the main difference between the experimental FORC diagram and a pure wishbone shape comes from the fact that the interaction in the arrays is not a uniform mean one. That is more relevant in terms of the interaction field

direction, as each FeCoCu segment of the multilayer nanowires in the array is subjected to intra-wire and inter-wire magnetostatic interactions (Figure 4.13): i) intra-wire (positive) interactions between adjacent FeCoCu segments along each nanowire which favour the parallel alignment of magnetization within the nanowire; and ii) inter-wire (negative) magnetostatic interactions among FeCoCu segments at different levels from neighboring nanowires which add to increase its effective demagnetization factor ([14, 15]. This fact modifies the magnitude and direction of the resulting interaction field, which is observed in the FORC graph. Considering these observations, this distribution can be defined as a *non-real wishbone* FORC distribution.

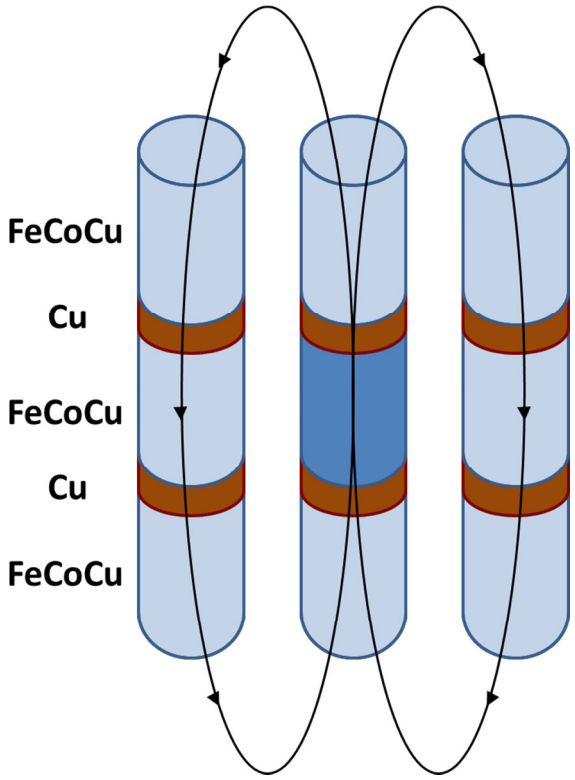

Figure 4.13 Schematic diagram of the magnetostatic interactions between neighbor nanowires in the array.

For determining the dependence of the magnetic parameters on the NFM layer and FM segment thicknesses, the $\mu_0\overline{H_c}$ and $\mu_0 H_i$ values obtained for the wishbone shape distribution have been associated to the FORC coercivity ($\mu_0 H_c^{FORC}$) and the interaction field ($\mu_0 \Delta H_u$), respectively, obtained from the single branch FORC distribution (Figure 4.14). This approximation has been done due the reasonable agreement between the simulated and experimental FORC diagrams. In this context, $\mu_0 H_c^{FORC}$ should be taken

as the average coercivity and $\mu_0 \Delta H_u$ as the demagnetizing interaction field felt at saturation, respectively, of the reversing FeCoCu segments (when the FeCoCu segments are decoupled between them along the nanowire) or of the whole nanowire (for continuous nanowires and multilayer nanowires with the FeCoCu segments coupled through the Cu layers). Data for continuous FeCoCu alloy nanowires are included in the graphs as single scatters.

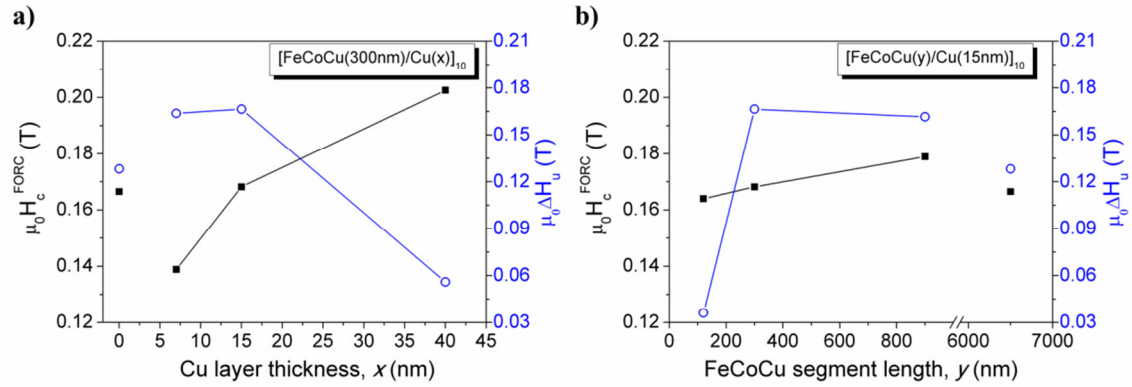

Figure 4.14 (a) Cu layer thickness and (b) FeCoCu segment length dependence of FORC coercive field (H_c^{FORC}) (filled symbols) and interaction field (ΔH_u) (empty symbols). Data for continuous FeCoCu alloy nanowires are represented with single scatters.

For both series of samples, the coercive field increases with the Cu layer and the FeCoCu thicknesses, but for different reasons. A change in the nanowire architecture, from continuous to multilayer, leads to a decrease in $\mu_0 H_c^{FORC}$. As the Cu layer becomes thicker, the coercive field increases and even overcomes the value for continuous nanowire array (Figure 4.14(a)). Such an evolution can be understood to be a consequence of the weakening of the coupling between FeCoCu segments along the nanowire through thicker Cu layers, so hardening the magnetization process. On the other hand, the increase in coercivity with the FeCoCu segment thickness (Figure 4.14(b)) can be correlated with its increasing shape anisotropy.

The interaction field of the systems presenting similar hysterons (single branch FORC distribution) remains between 160 and 170 mT, while it drastically decreases for wishbone FORC distributions (between 36-56 mT) (Figure 4.14). This strong reduction occurs for thick Cu layers or thin FeCoCu segments and can be explained by the decoupling of the FeCoCu segments along the nanowire, favored by a thicker spacer or

due to their small magnetic volume. Both multilayer nanowires exhibiting a wishbone shape presents a similar ratio between the Cu layer and the FeCoCu segment thicknesses (x / y), suggesting a similar degree of magnetic decoupling [37-39]. In both cases, the wishbone FORC distribution suggests that the magnetization reversal of the nanowires takes place in steps, i.e. the magnetization direction of all the FeCoCu segments of one nanowire does not remain pointing in the same direction. Since the reversing magnetic segments are shorter as compared to the whole nanowire, the demagnetizing interaction field values decreases. The FeCoCu segments are not completely decoupled one from each other, since these systems are also characterized by a large coercivity variation (leading to the wishbone feature). Therefore, the reversing FeCoCu segment extremities, in addition to not be aligned in the same plane, may change the magnetization reversal process. This kind of behavior directly affects the FORC diagram, and leads to a distribution not arising from a mean and uniform interaction field.

4.5. Conclusions

Two series of multilayer nanowire arrays have been fabricated by means of pulsed electrodeposition into alumina templates using a single electrolytic bath: $[FeCoCu(y)/Cu(x)]_{10}$ nanowire arrays for ranges of Cu layer thickness ($7 \leq x \leq 40$ nm) and FeCoCu segments length ($120 \leq x \leq 900$ nm), with a constant nanowire diameter of 35 nm. The structural and compositional analysis has revealed that the Cu layers with *fcc* crystal structure are segregated from the *bcc* FeCoCu segments.

For all the samples, a magnetization easy axis parallel to the nanowire axis is confirmed after comparison of the magnetic parameters extracted from the hysteresis loops measured under magnetic field applied parallel and perpendicular to the nanowire axis. The changes in coercive field and fractional remanence are modest for increasing Cu layer and FeCoCu segment thicknesses. However, a significant increase in the susceptibility around the coercive field is observed with increasing Cu layer thickness and decreasing FeCoCu segment length, suggesting a reduction of magnetostatic interactions in the array.

The preliminary study of the magnetostatic interactions in the multilayer nanowire array by Henkel plots confirm a decrease in the effective interactions for those samples with thicker Cu layers and shorter FeCoCu segments arising from stray fields at the surface of magnetic segments along the nanowire and from neighbour nanowires.

FORC technique has been used to quantitatively determine the influence of the Cu layer and FeCoCu segment thicknesses on the magnetic properties of the nanowire arrays. For all the multilayer nanowire arrays, the FORC diagrams show magnetic systems characterized by demagnetizing interactions. However, two alternative FORC distribution shapes have been identified indicating two different magnetic behaviors. Continuous nanowire and multilayer nanowire arrays with thin Cu layers ($x \leq 15$ nm) or thick FeCoCu segments ($y \geq 300$ nm) present the FORC distribution usually associated to a magnetic nanowire array. On the other hand, for thicker Cu layers and shorter FeCoCu segments, the FORC distributions exhibit the wishbone shape. The parametrization of these distributions and their corresponding simulations have been performed in order to verify the accuracy of the obtained values.

The FORC coercivity and interaction field have been obtained for all the FORC distributions. An increasing coercive field with the Cu layer and FeCoCu segment thicknesses has been determined. Thick Cu layers promote the weakening of the coupling between FeCoCu segments along the nanowire, making more difficult the magnetization reversal. The enhanced shape anisotropy promotes the higher value of coercive field observed for long FeCoCu segments. Furthermore, for thick Cu layers and thin FeCoCu segments a strong reduction in the interaction field is observed, originated by the decoupling of the FeCoCu segments along the nanowire. The value of the interaction field is similar in both cases, suggesting a similar degree of decoupling, seemingly a consequence of their similar NFM/FM thickness ratio.

Bibliography

[1] J. Coey, Hard magnetic materials: A perspective, *IEEE Trans. Magn.,* 47 (2011) 4671-4681.

[2] L.H. Lewis, F. Jiménez-Villacorta, Perspectives on permanent magnetic materials for energy conversion and power generation, *Metall. Mater. Trans. A,* 44 (2013) 2-20.

[3] J. Fu, Z. Yan, Y. Xu, X. Fan, D. Xue, Effects of annealing temperature on structure and magnetic properties of amorphous $Fe_{61}Co_{27}P_{12}$ nanowire arrays, *J. Phys. Chem. Solids,* 68 (2007) 2221-2226.

[4] Z. Liu, W. Li, P. Jin, W. Fei, Magnetic anisotropy transformation of Co–Fe–B nanowire arrays synthesized under the magnetic field, *J. Magn. Magn. Mater*., 345 (2013) 96-99.

[5] C. Bran, E.M. Palmero, R.P. del Real, M. Vazquez, CoFeCu electroplated nanowire arrays: Role of composition and annealing on structure and magnetic properties, *Phys. Status Solidi A*, 211 (2014) 1076-1082.

[6] S. Liébana-Viñas, R. Salikhov, C. Bran, E.M. Palmero, M. Vazquez, B. Arvan, X. Yao, P. Toson, J. Fidler, M. Spasova, Magnetic hardening of Fe30Co70 nanowires, *Nanotechnology,* 26 (2015) 415704.

[7] A. Esmaeily, M. Venkatesan, A.S. Razavian, J. Coey, Diameter-modulated ferromagnetic CoFe nanowires, *J. Appl. Phys.,* 113 (2013) 17A327.

[8] M.S. Salem, P. Sergelius, R.M. Corona, J. Escrig, D. Görlitz, K. Nielsch, Magnetic properties of cylindrical diameter modulated Ni*80*Fe*20* nanowires: interaction and coercive fields, *Nanoscale*, 5 (2013) 3941-3947.

[9] K. Qi, X. Li, H. Zhang, L. Wang, D. Xue, H. Zhang, B. Zhou, N.J. Mellors, Y. Peng, Nanoscale characterization and magnetic property of NiCoCu/Cu multilayer nanowires, *Nanotechnology*, 23 (2012) 505707.

[10] W. Yang, C. Cui, Q. Liu, B. Cao, L. Liu, Y. Zhang, Fabrication and magnetic properties of Sm_2Co_{17} and Sm_2Co_{17}/Fe_7Co_3 magnetic nanowires via AAO templates, *J. Cryst. Growth*, 399 (2014) 1-6.

[11] N. Gao, H. Wang, E.-H. Yang, An experimental study on ferromagnetic nickel nanowires functionalized with antibodies for cell separation, *Nanotechnology,* 21 (2010) 105107.

[12] C. Sousa, D. Leitao, M. Proenca, J. Ventura, A. Pereira, J. Araujo, Nanoporous alumina as templates for multifunctional applications, *Appl. Phys. Rev.*, 1 (2014) 031102.

[13] B. Özkale, N. Shamsudhin, G. Chatzipirpiridis, M. Hoop, F. Gramm, X. Chen, X. Martí, J. Sort, E. Pellicer, S. Pané, Multisegmented FeCo/Cu nanowires: electrosynthesis, characterization, and magnetic control of biomolecule desorption, *ACS Appl. Mater. Interfaces*., 7 (2015) 7389-7396.

[14] L.-P. Carignan, C. Lacroix, A. Ouimet, M. Ciureanu, A. Yelon, D. Ménard, Magnetic anisotropy in arrays of Ni, CoFeB, and Ni/Cu nanowires, *J. Appl. Phys*., 102 (2007) 023905.

[15] S. Krimpalis, O.-G. Dragos, A.-E. Moga, N. Lupu, H. Chiriac, Magnetization processes in electrodeposited NiFe/Cu multilayered nanowires, *J. Mater. Res.,* 26 (2011) 1081-1090.

[16] L.-Z. He, L.-R. Qin, J.-W. Zhao, Y.-Y. Yin, Y. Yang, G.-Q. Li, Magnetostatic interaction in electrodeposited Ni/Au multilayer nanowire arrays, *Chinese Phys. B*, 25 (2016) 086101.

[17] L. Spinu, A. Stancu, C. Radu, L. Feng, J.B. Wiley, Method for magnetic characterization of nanowire structures, *IEEE Trans. Magn*., 40 (2004) 2116-2118.

[18] C. Pike, C. Ross, R. Scalettar, G. Zimanyi, First-order reversal curve diagram analysis of a perpendicular nickel nanopillar array, *Phys. Rev. B,* 71 (2005) 134407.

[19] F. Béron, L. Clime, M. Ciureanu, D. Ménard, R. Cochrane, A. Yelon, Magnetostatic interactions and coercivities of ferromagnetic soft nanowires in uniform length arrays, *J. Nanosci. Nanotechno*., 8 (2008) 2944-2954.

[20] F. Béron, L.-P. Carignan, D. Menard, A. Yelon, Magnetic behavior of Ni/Cu multilayer nanowire arrays studied by first-order reversal curve diagrams, *IEEE Trans. Magn*., 44 (2008) 2745-2748.

[21] M.S. Salem, P. Sergelius, R. Zierold, J.M. Montero Moreno, D. Görlitz, K. Nielsch, Magnetic characterization of nickel-rich NiFe nanowires grown by pulsed electrodeposition, *J. Mater. Chem.,* 22 (2012) 8549-8557.

[22] D. Navas, J. Torrejon, C. Redondo, F. Batallan, B. Toperverg, A. Devishvili, B. Sierra, K. Pirota, C. Ross, Magnetization reversal and exchange bias effects in hard/soft ferromagnetic bilayers with orthogonal anisotropies, *New J. Phys*., 14 (2012) 113001.

[23] F. Béron, L.A. De Oliveira, M. Knobel, K.R. Pirota, A novel method for identifying the local magnetic viscosity process of heterogeneous magnetic nanostructures, *J. Phys. D-Appl. Phys*., 46 (2013) 045003.

[24] M. Proenca, C. Sousa, J. Escrig, J. Ventura, M. Vazquez, J. Araujo, Magnetic interactions and reversal mechanisms in Co nanowire and nanotube arrays, *J. Appl. Phys.,* 113 (2013) 093907.

[25] J. Garcıa-Otero, M. Porto, J. Rivas, Henkel plots of single-domain ferromagnetic particles, *J. Appl. Phys*., 87 (2000) 7376-7381.

[26] E. Wohlfarth, Relations between different modes of acquisition of the remanent magnetization of ferromagnetic particles, *J. Appl. Phys.*, 29 (1958) 595-596.

[27] E. Samwel, P. Bissell, J. Lodder, Remanent magnetic measurements on perpendicular recording materials with compensation for demagnetizing fields, *J. Appl. Phys.*, 73 (1993) 1353-1359.

[28] F. Béron, A. Yelon, D. Ménard, L.-P. Carignan, Extracting individual properties from global behaviour: first-order reversal curve method applied to magnetic nanowire arrays, INTECH Open Access Publisher, 2010.

[29] A. Rotaru, J.-H. Lim, D. Lenormand, A. Diaconu, J.B. Wiley, P. Postolache, A. Stancu, L. Spinu, Interactions and reversal-field memory in complex magnetic nanowire arrays, *Phys. Rev. B*, 84 (2011) 134431.

[30] M. Proenca, K. Merazzo, L. Vivas, D. Leitao, C. Sousa, J. Ventura, J. Araujo, M. Vazquez, Co nanostructures in ordered templates: comparative FORC analysis, *Nanotechnology,* 24 (2013) 475703.

[31] S. Samanifar, M. Almasi Kashi, A. Ramazani, M. Alikhani, Reversal modes in FeCoNi nanowire arrays: Correlation between magnetostatic interactions and nanowires length, *J. Magn. Magn. Mater*., 378 (2015) 73-83.

[32] F. Béron, D. Ménard, A. Yelon, First-order reversal curve diagrams of magnetic entities with mean interaction field: A physical analysis perspective, *J. Appl. Phys*., 103 (2008) 07D908.

[33] S. Alikhanzadeh-Arani, M. Almasi-Kashi, A. Ramazani, Magnetic characterization of FeCo nanowire arrays by first-order reversal curves, *Curr. Appl. Phys*., 13 (2013) 664-669.

[34] C.-I. Dobrotă, A. Stancu, Tracking the individual magnetic wires' switchings in ferromagnetic nanowire arrays using the first-order reversal curves (FORC) diagram method, Physica B, 457 (2015) 280-286.

[35] C.-I. Dobrotă, A. Stancu, What does a first-order reversal curve diagram really mean? A study case: Array of ferromagnetic nanowires, *J. Appl. Phys*., 113 (2013) 043928.

[36] E. Jafari-Khamse, M. Almasi Kashi, A. Ramazani, Angular dependence of interactions in polycrystalline Co nanowire arrays, *Mater. Chem. Phys*., 159 (2015) 128-138.

[37] M. Chen, P. Searson, C. Chien, Micromagnetic behavior of electrodeposited Ni/Cu multilayer nanowires, *J. Appl. Phys.,* 93 (2003) 8253-8255.

[38] J. Medina, M. Darques, A. Encinas, L. Piraux, Dipolar interactions in multilayered $Co_{0.96}Cu_{0.04}$/Cu nanowire arrays, *Phys. Status Solidi A,* 205 (2008) 1813-1816.

[39] D.A. Gilbert, G.T. Zimanyi, R.K. Dumas, M. Winklhofer, A. Gomez, N. Eibagi, J. Vicent, K. Liu, Quantitative decoding of interactions in tunable nanomagnet arrays using first order reversal curves, *Sci. Rep.,* 4 (2014) 4204.

Chapter 5

Magnetic Nanowires with Modulated Diameter

Cylindrical FeCoCu and Co nanowires with tailored diameter modulations have been grown by electroplating into anodic alumina templates, which were fabricated by pulsed anodization. The nanowires were fabricated with different geometrical parameters (i.e. segments diameters and lengths) and the influence of the geometry and the crystallographic structure on the magnetization reversal of individual nanowires has been studied.

5.1. Introduction

A promising route to tailor the magnetic properties of cylindrical nanowires is the imprinting of periodic diameter modulations along the nanowire length. The fabrication of nanowires with this specific geometry is possible due to the combination of mild and hard anodization [1-4]. Apart from tailoring of the magnetic properties, the modulation in diameter offers the possibility of controlling the domain wall movement along the nanowire [5-7].

While the magnetic properties of a nanowire array are significantly determined by the magnetostatic interaction among neighboring nanowires, the final magnetic response is determined by the intrinsic magnetization of individual nanowires. In this sense, together with the diameter modulation, another alternative to control the magnetization reversal of cylindrical nanowires is tuning their magnetocrystalline anisotropy. FeCo based nanowires, with face-centered cubic (*fcc*) or body-centered

cubic (*bcc*) crystallographic structures, present reduced magnetocrystalline anisotropy. In this case, the magnetization reversal is determined by an effective longitudinal magnetic anisotropy, which main source is the axial shape anisotropy [8, 9]. On the other hand, Co nanowires with hexagonal close-packed (*hcp*) crystalline structure exhibit strong magnetocrystalline anisotropy. In these magnetic structures, the competition between shape and magnetocrystalline anisotropy may originate a system with specific magnetic properties [10].

Micromagnetic calculations of demagnetization processes conclude that the reversal process can take place by the propagation of transverse or vortex-like domain wall, apart from coherent and incoherent spin rotation mechanisms [11]. Recent micromagnetic simulations, together with Magnetic Force Microscopy (MFM) studies, of the demagnetization process of isolated nanowires with axial magnetic anisotropy suggest that the process occurs by the nucleation of domain walls at the ends of the nanowires followed by their depinning and subsequent propagation along the wire [12, 13]. The suggested reversal process takes place by the spin rotation at the shell region and the propagation of a vortex at the core [14, 15].

An advanced technique that has shown promising results on the experimentally determination and study of the magnetization reversal process of cylindrical nanowires is the Magneto-Optical Kerr Effect (MOKE), which has been proved to be a useful technique to provide information about the magnetic state of such samples [16-18].

The determination of the spin configuration of cylindrical nanowires is a challenging task due to their nanometer scale dimensions and cylindrical geometry. An advanced surface technique to provide information about the magnetic properties of such individual magnetic structures is the Photoemission Electron Microscopy (PEEM) combined with X-ray Magnetic Circular Dichroism (XMCD) [19-22].

5.2. Geometrical, compositional and structural characterization

FeCoCu and Co nanowire arrays with modulations in diameter along the length were fabricated by electrodeposition into hexagonally ordered AAO templates. The templates were fabricated by pulsed anodization process to obtain the modulations in diameter (see Section 2.1.3.3 for more experimental details). The growth of the

nanowires into the templates was performed by electroplating of the metallic elements using specific electrochemical parameters (see Table 2.2). For the MOKE measurements, four types of FeCoCu nanowires with different geometry were fabricated, and for the XMCD-PEEM study, two types of nanowires were grown, with the same geometry but with different composition (i.e. FeCoCu and Co nanowires).

The nanowires geometry was characterized by Scanning Electron Microscopy (SEM) and the composition was determined by Energy Dispersive X-ray Spectrometer (EDS). The samples prepared for MOKE characterization were:

- one sample with constant nanowire diameter (sample S1);
- *Modulated type I* (samples S2 and S3): wide segments ($d_{mod,\ 1}$ in diameter and $L_{mod,\ 1}$ in length) shorter than the narrow ones ($d_{mod,\ 2}$ in diameter and $L_{mod,\ 2}$ in length);
- and *Modulated type II* (sample S4), with the narrow segments shorter than the wide ones.

The schemes with the two different geometries of the modulated nanowires are shown in Figure 5.1. The geometrical parameters, including the nanowire total length (L_{NW}) are collected in Table 5.1. Figure 5.2 shows the SEM images of the four nanowire arrays (Figure 5.2(a) to (d)) and the single nanowires (released after chemically dissolution of the AAO template) on silicon substrate (Figure 5.2(e) to (h)). The nanowire composition was $Fe_{30}Co_{63}Cu_7$ (hereafter referred to as FeCoCuMOKE).

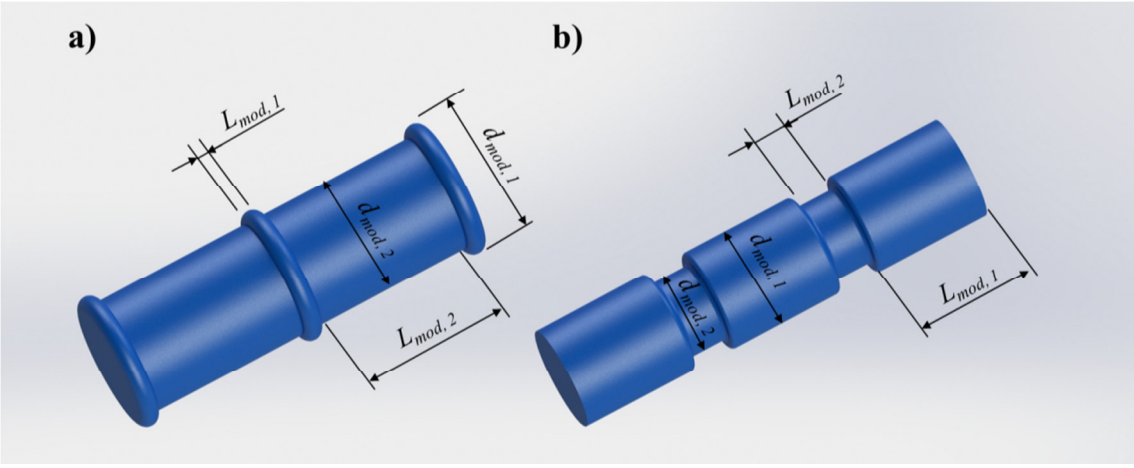

Figure 5.1 Schematic view of the two types of modulated nanowires: (a) type I, and (b) type II.

The composition of the nanowires fabricated for XMCD-PEEM measurements was Co and $Fe_{28}Co_{67}Cu_5$ (in the following these samples are named Co and FeCoCuPEEM, respectively). The geometry of these nanowires corresponds to *Modulated type I* and the values of the geometrical parameters were: $d_{mod,\ 1}$ = 140 nm, $L_{mod,\ 1}$ = 50 nm, $d_{mod,\ 2}$ = 130 nm, and $L_{mod,\ 2}$ = 400 nm. The geometry is the same as the shown in Figure 5.2(b) and (f), but with slightly smaller diameters.

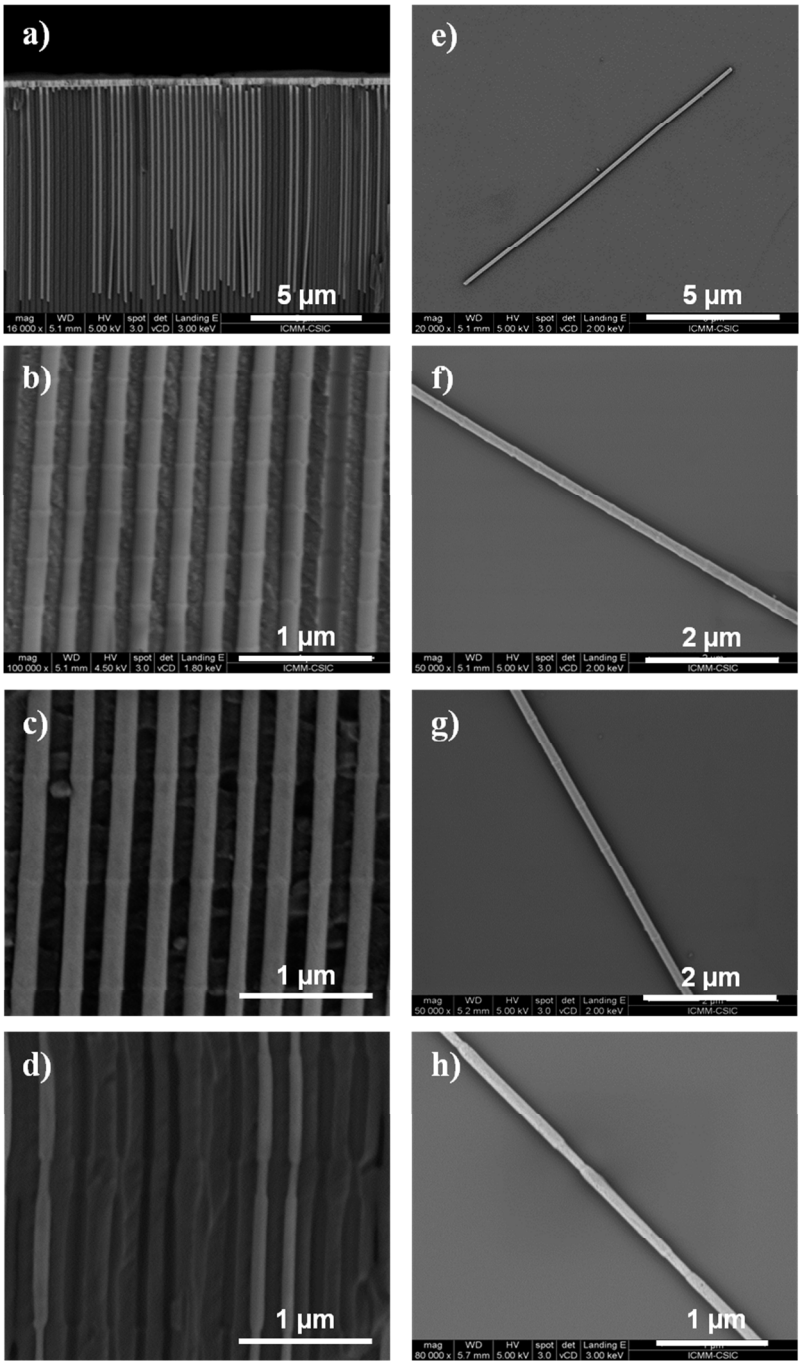

Figure 5.2 Cross section SEM images of nanowire arrays: (a) constant diameter, sample S1; (b), (c) and (d) modulated diameter nanowires, samples S2, S3 and S4, respectively. SEM images of isolated nanowires on silicon substrate with: (e) S1; (f) S2, (g) S3, and (h) S4.

Table 5.1 Geometrical parameters of the FeCoCu nanowires, for MOKE measurements: $D_{mod,\ 1}$ and $L_{mod,\ 1}$ are the diameter and length of the wide segments, respectively, in the modulated nanowires; $D_{mod,\ 2}$ and $L_{mod,\ 2}$ are the diameter and length of the narrow segments, respectively; and L_{NW} is the nanowire total length.

Sample	Type	$d_{mod,\ 1}$ (nm)	$L_{mod,\ 1}$ (nm)	$d_{mod,\ 2}$ (nm)	$L_{mod,\ 2}$ (nm)	L_{NW} (µm)
S1	Constant diameter	150	-	-	-	10
S2	Modulated Type I (a)	170	50	150	400	14
S3	Modulated Type I (b)	170	50	150	800	13
S4	Modulated Type II	130	1000	100	300	17

The crystallographic structure was determined by X-Ray Diffraction (XRD) experiments. Figure 5.3(a) and (b) show the XRD spectra of FeCoCuPEEM and Co nanowire arrays, respectively. FeCoCu nanowires grow in a polycrystalline *bcc* structure with a (110) preferred orientation, presenting also reflections along the (200) and (211) directions (Figure 5.3(a)). The XRD pattern for Co nanowires shows a *hcp* structure where the (110) peak strongly dominates the crystallographic structure (Figure 5.3(b)).

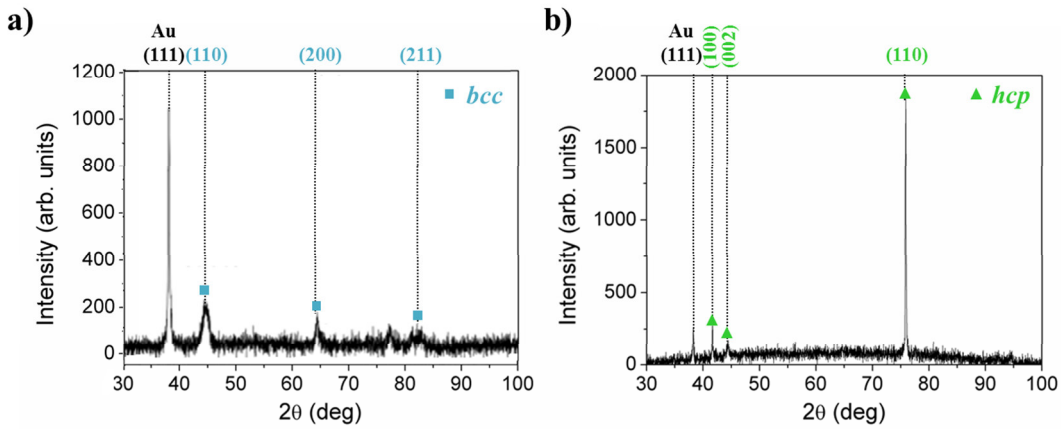

Figure 5.3 XRD patterns of modulated nanowire arrays: (a) FeCoCu and (b) Co.

5.3. Magnetic measurements on single nanowires

5.3.1. Magnetization reversal of modulated FeCoCu nanowires: influence of geometry

The magnetic characterization of isolated nanowires was performed by Magneto-Optic Kerr Effect (MOKE) magnetometer. MOKE hysteresis loops were recorded under applied field parallel to the nanowire axis. Each MOKE hysteresis loop shown in this thesis is the result of 1000 averaged loops, in order to reduce the noise to signal ratio. Furthermore, to obtain representative MOKE hysteresis loops from each type of nanowires, different nanowires from the same sample were measured, confirming that they present the same behavior. Note that, due to the laser spot size, in the case of modulated nanowires several modulations are contributing to the hysteresis loops.

Figure 5.4 shows the hysteresis loops for the different nanowires (with constant and modulated diameter). These measurements were performed with the laser spot focused on the center of the nanowire. In all cases, the normalized longitudinal Kerr effect signal at remanence is close to 1 which suggests the existence of a nearly single domain structure with longitudinal magnetization easy axis. For the nanowire with constant diameter (Figure 5.4(a)), it is observed a square hysteresis loop with sharp transition through a single giant Barkhausen jump between two stable magnetic states at remanence [17, 18]. Similarly, the hysteresis loop in Figure 5.4(b) presents one sharp transition for the *Modulated type I* nanowire with the shorter thin segments (S2). However, for the *Modulated type I* nanowire with the longer narrow segments (S3), two abrupt and symmetric magnetization jumps are observed in each branch of the hysteresis loop in Figure 5.4(c). Finally, for *Modulated type II* nanowire (S4), a main Barkhausen jump is observed in the hysteresis loop (Figure 5.4(d)) together with several additional ones of less amplitude. The presence of several magnetization jumps in *Modulated I (b)* and *Modulated II* nanowires suggests the existence of metastable magnetic states during the magnetization reversal that should be correlated to their particular diameter modulation [5].

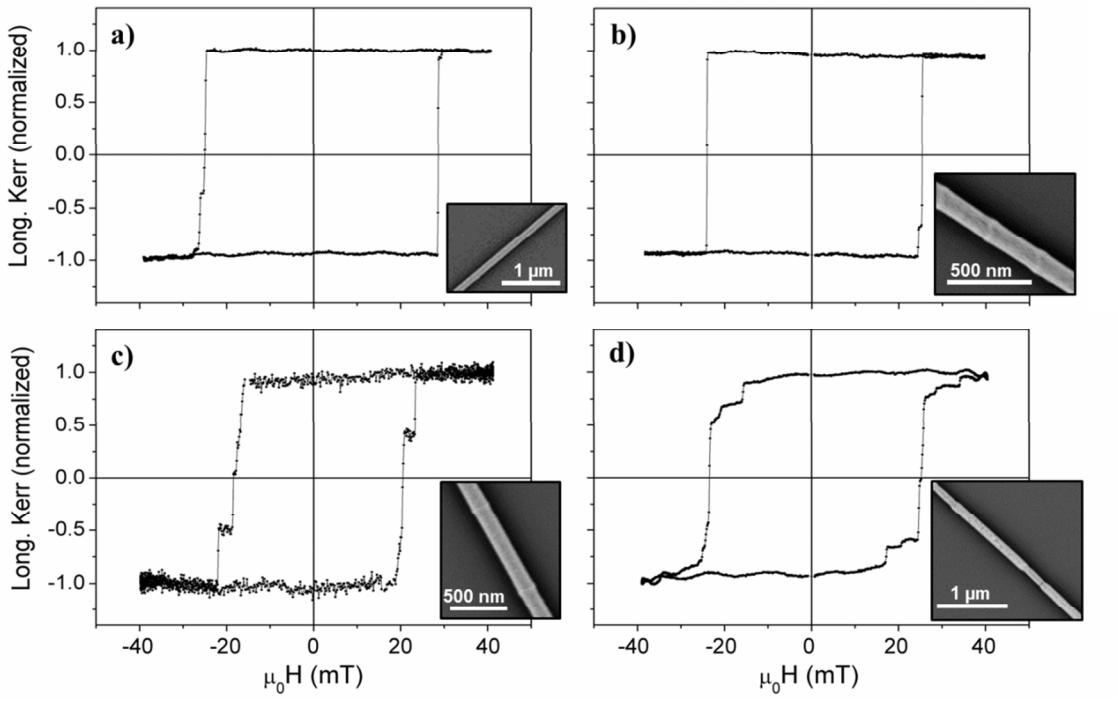

Figure 5.4 MOKE hysteresis loops for constant diameter S1 (a) and modulated diameter S2 (b), S3 (c) and S4 (d) nanowires. Insets in each graph correspond to SEM images of the modulation close view for each type of nanowire.

The profile of the magnetic response along the nanowires has been quantified through the MOKE hysteresis loops taken at different positions along the nanowires length. These measurements supply deeper information on the influence of diameter modulations at a submicron scale. The measurements were taken from one end of the nanowire to the other one using steps of 1 µm. Figure 5.5 shows selected hysteresis loops measured along a single *Modulated type II* nanowire. For all the hysteresis loops shown in this Section, the MOKE electrical signal obtained through the longitudinal Kerr detector is normalized to the received under maximum applied field at each position. However, it is important to mention that the absolute value of that signal is several times smaller when the laser spot is focused on the end of the nanowire (Figure 5.5(a) and (c)) than when focused on its central part (Figure 5.5(b), (d) and (e)). This is a consequence of the size of the laser spot: the magnetic area enclosed when focused on the wire ends, and consequently the magnetic response, is smaller than when focused on the center. Moreover, differences between local hysteresis loops at different positions are observed in Figure 5.5. While the main magnetization jump takes place at around 25

mT, usually smaller jumps are detected either before or after that main jump. According to this fact, it is assumed that the magnetization reversal process is damped locally before completion. The existence of such steps denotes again the presence of metastable states in the magnetization reversal that could be correlated to pinning centers at local modulations inside the size of the laser spot of similar but slightly different energy barrier.

As well as for modulated nanowires, local MOKE measurements were performed also on a nanowire with constant diameter (S1). In this case, the hysteresis loops present square shape along the nanowire with a single giant Barkhausen jump and constant coercivity, similarly as in Figure 5.4(a) but for the commented reduced MOKE signal close to the ends. That indicates that the magnetization process takes place with uniformity along the nanowire with constant diameter [6]. The similar and completely square shape of the hysteresis loops obtained for constant diameter nanowire, in comparison to the hysteresis loops in Figure 5.5 for modulated diameter nanowire indicates that the small Barkhausen jumps can be ascribed to diameter modulations in *Modulated type I b and II* nanowires.

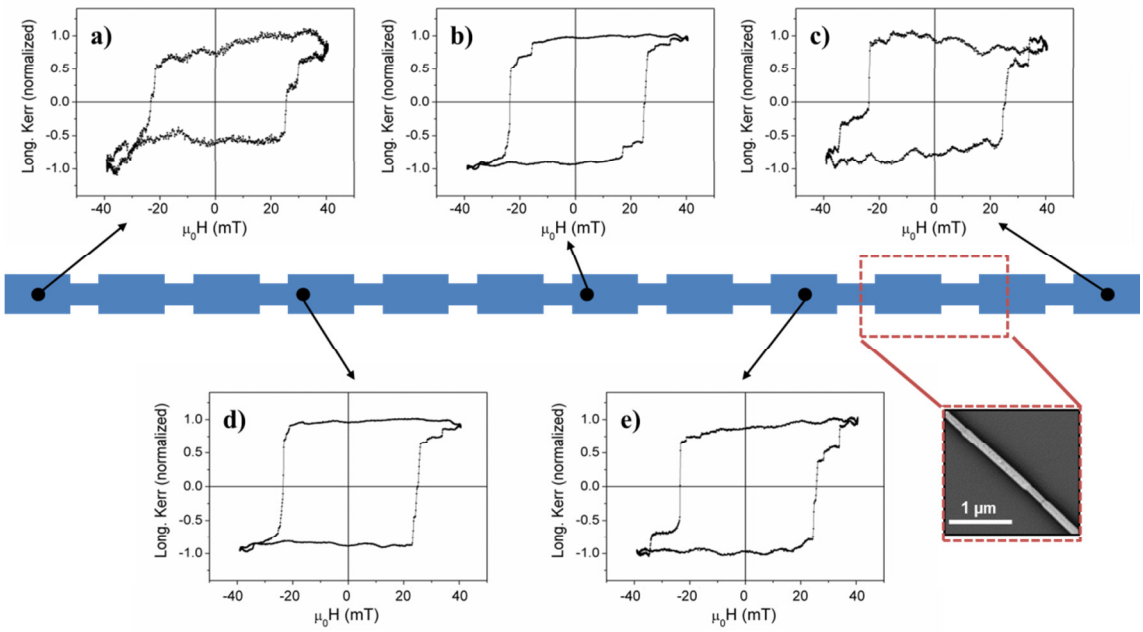

Figure 5.5 MOKE hysteresis loops profile along a single *Modulated type II* nanowire from sample S4, with the magnetic field applied parallel to the nanowire axis.

Micromagnetic simulations of the demagnetization process in nanowires with constant diameter and effective longitudinal axial anisotropy has been proposed to take place by the depinning of a domain wall from one end and its subsequent propagation along the wire [12, 13, 23]. A classical method to determine the proper coercivity mechanism is the quantification of angular dependence of the magnetization process [24]. With this objective, MOKE hysteresis loops have been recorded under applied field making an angle (θ_H) with respect to the nanowire axis ranging from θ_H = 0º (parallel) to θ_H = 90º (perpendicular to the nanowire axis) every 15º.

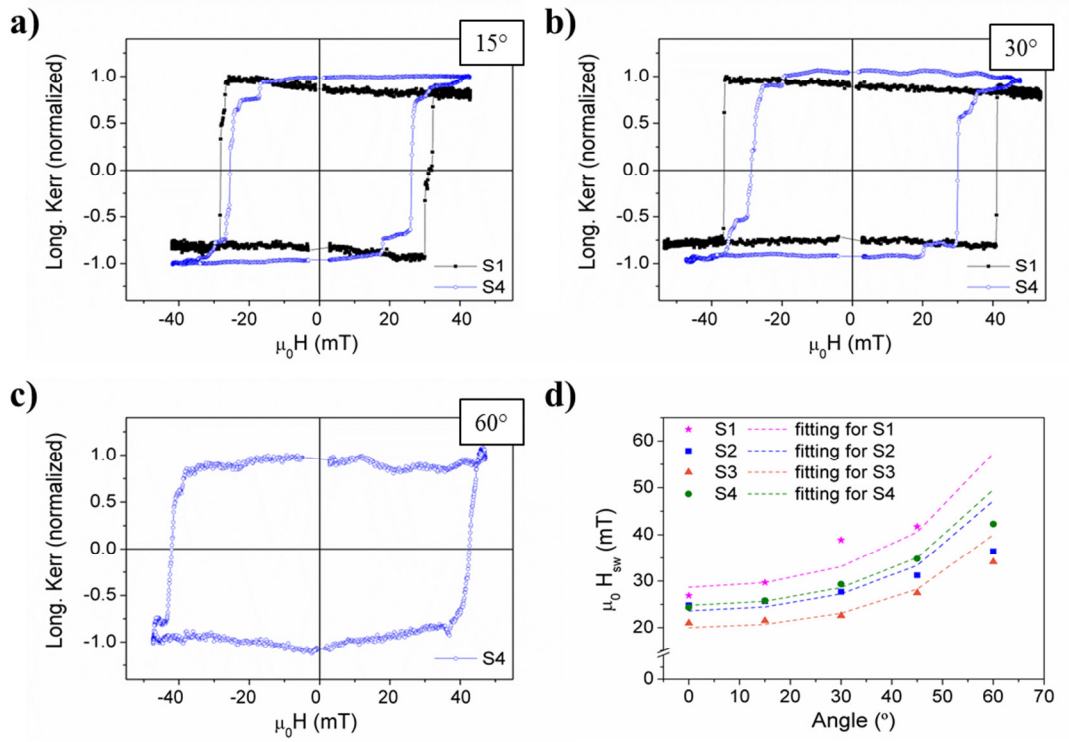

Figure 5.6 Hysteresis loops of an individual constant diameter (S1) and *Modulated type II* nanowire (S4) under an applied field with: (a) θ_H = 15º, (a) θ_H = 30º, and (c) θ_H = 60º (note that for θ_H = 60º, only the hysteresis loop for S4 is shown as the longitudinal component of the applied field is not enough to obtain the loop for the nanowire from sample S1); and experimental and fitted (see text) angular dependence of the switching field (H_{sw}) for the different nanowires.

Selected hysteresis loops for the constant diameter (S1) and *Modulated type II* nanowire (S4) under different angle θ_H between applied field and the nanowire axis are shown in Figure 5.6(a) to (c). A similar behavior with increasing angle is observed for all the investigated samples, where the switching field (H_{sw}) to complete main reversal increases with the angle. However, for θ_H > 60º, the parallel component of the available

magnetic field is not high enough to give rise to the reversal process. Figure 5.6(d) shows the experimental angular dependence of the switching field for the different nanowires. The angular evolution and even the absolute switching field take similar values.

The observed angular dependence where coercivity increases with the angle denotes clearly that the reversal process can be ascribed to the propagation of a vortex domain wall [25]. For a vortex magnetization reversal mode, the angular dependence of coercive field for an isolated nanowire with high aspect ratio is given by the expression [26]:

$$H_{sw} = \frac{\frac{8q^2 A_{exc}}{M_S d_{NW}^2}\left(2\pi - \frac{4q^2 A_{exc}}{\pi M_S^2 d_{NW}^2}\right)}{\sqrt{\frac{16q^4 A_{exc}^2}{\pi^2 M_S^4 d_{NW}^4}\sin^2\theta_H + \left(2\pi - \frac{4q^2 A_{exc}}{\pi M_S^2 d_{NW}^2}\right)^2 \cos^2\theta_H}} \tag{5.1}$$

where $q^2 = 1.08\pi$ for a cylindrical geometry [27], A_{exc} is the exchange stiffness constant, M_s is the saturation magnetization and d_{NW} is the nanowire diameter.

Table 5.2 Fitted values of the exchange stiffness constant (A_{exc}) for the different nanowires.

Sample	S1	S2	S3	S4
A_{exc} 10^{12} (J/m)	34.5	36.5	30.9	22.4

Considering a saturation magnetization $\mu_0 M_s = 1.8 \pm 0.1$ T for FeCoCu alloy, the experimental values of $\mu_0 H_{sw}$ for the different samples and θ_H have been fitted using Eq. (5.1) (dashed lines in Figure 5.6(d)). For modulated nanowires, the fitting was performed giving to d_{NW} the values of the different diameter for each sample, $d_{mod,\,1}$ and $d_{mod,\,2}$. For all the modulated nanowire samples, the best fitting was achieved taking $d_{NW} = d_{mod,\,1}$, the diameter of the wide segments. The best fitting values of A_{exc} with the experimental data are collected in Table 5.2 that are reasonable according to previous data for the nanowire alloy [28].

According to the results obtained by MOKE measurements, it is possible to state that: i) MOKE signals involving several diameter modulations show a giant Barkhausen jump preceded or followed by smaller jumps; ii) this behavior occurs at different sites along the modulated nanowires in opposition to nanowires with constant diameter; iii) the experimental angular dependence of the switching field and its analytical calculations denotes that the coercivity mechanism is ascribed to the propagation of a vortex domain wall.

5.3.2. Spin configuration of individual nanowires: influence of magnetocrystalline anisotropy

The spin configuration of two types of cylindrical nanowires with designed magnetization easy axis (i.e. FeCoCuPEEM nanowire with longitudinal easy axis and Co nanowire with perpendicular easy axis) and periodical modulations in diameter has been determined by XMCD–PEEM measurements, which were performed at the CIRCE beamline of the ALBA Synchrotron Facility (Barcelona, Spain) (see Section 2.3.2.4. for experimental details).

Figure 5.7 shows two XMCD-PEEM images of two FeCoCuPEEM nanowires with different magnetic configurations. In Figure 5.7(a) the XMCD intensity is homogeneous, both in the surface (light gray) and in the shadow (dark gray), along the whole length of the nanowires, suggesting a single domain configuration. However, a different contrast is observed in Figure 5.7(b). The periodic modulation in the contrast matches the modulated geometry along the length of the wire. The overall homogeneous bright contrast at the surface suggests a main longitudinal magnetization of the nanowire as is expected from a magnetization easy axis along the nanowires and a resultant single domain configuration at remanence (which is in agreement with the hysteresis loop measured for a similar nanowire geometry by MOKE, see Figure 5.4(b)). The contrast in the shadow is nearly vanishing except at the upper end corresponding to the shadow of the top surface of the nanowire, where a modulated line complimentary to the surface is visible. The strong dark feature at right end of the wire (appearing as bright in the respective shadow end) indicates an accumulation of spins opposite to the X-ray propagation vector, which forms an angle of about 45^{o} with the

nanowire axis (as can be indicated from the orientation of the mentioned bright spot at the shadow end).

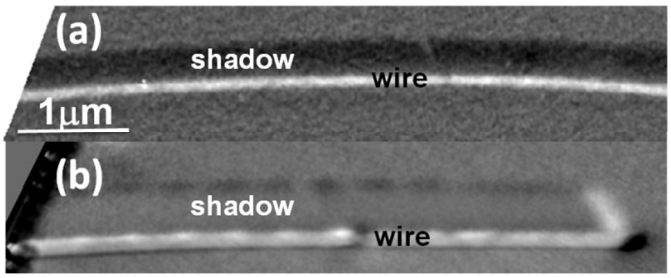

Figure 5.7 XMCD-PEEM images of magnetic configurations observed in modulated FeCoCu nanowires: (a) nanowire in a single domain state; and (b) nanowire with modulated magnetic contrast.

Several nanowires under different orientations with respect to the X-ray propagation vector were studied, revealing a variety of images with different amplitude and brightness of the shadow region. For an appropriate interpretation of the magnetic images, an angular scanning of the relative orientation of the nanowire and the X-ray incidence is essential. Figure 5.8 shows the XMCD-PEEM image of the same nanowire in Figure 5.7(b), but in this case the nanowire axis and the X-ray propagation vector make an angle of about 90^{o}. The XMCD image reveals a modulated profile along the whole nanowire length. The intensity profile in the surface region contains bright/dark local contrasts matching the position of each modulation along the length. Between those local regions, the surface shows a reduced contrast characteristic of an overall longitudinal magnetization in agreement with the interpretation of Figure 5.7(b).

Higher contrast is observed at the end of the nanowire and at given modulations, as shown in the insets of Figure 5.8. This behavior can be ascribed to a vortex-like structure at the modulation positions.

The shadow in transmission in Figure 5.8 supplies information about spin orientation inside the nanowire. A uniform gray contrast is observed in the main region of the shadow along the whole nanowire length. The vanishing contrast of the main region of the shadow reveals a longitudinal orientation of the spins inside the nanowire. In addition, bright/dark contrast can be identified also in the shadow of both the upper end (i) and along the nanowire (iii). That is identified as the vortex-like spins closure structure both at the surface and inside the nanowire. The bright/dark contrast observed in Figure 5.8(ii), which cannot be seen in the shadow might indicate a large

accumulation of stray fields. At the left edge of the shadow there are some zones with darker contrast that fit with the modulation and are related with the vortex-like structure above mentioned. Considering the width of these regions compared with the total width of the shadow, a thickness of around 30 nm for vortex-like shell at the modulations can be estimated.

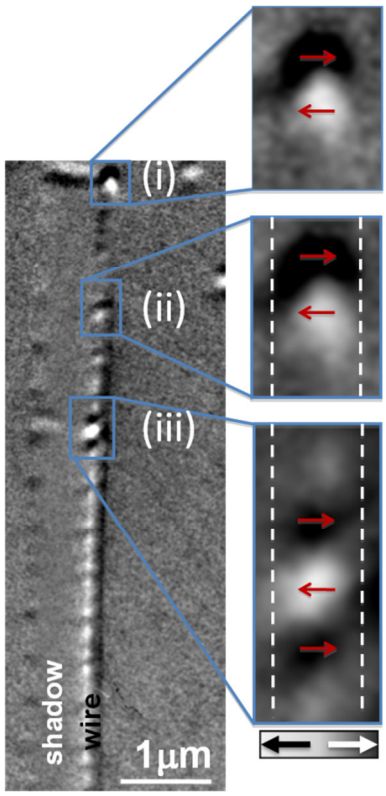

Figure 5.8 XMCD-PEEM image of a single FeCoCuPEEM nanowire oriented perpendicular to the incident X-rays. The arrows indicate the local spin configuration.

On the other hand, Co nanowires with dominant *hcp* (110) crystallographic phase, which originates uniaxial magnetocrystalline anisotropy with magnetization easy axis oriented nearly perpendicular to the nanowire axis have been studied. The magnetocrystalline anisotropy for these nanowire present a high enough value (4.5×10^5 J/m^3) to compete with the large shape anisotropy [29].

Figure 5.9(a) shows the XMCD image of a Co nanowire with the X-ray propagation vector making an angle of nearly 90º with respect to the nanowire axis.

The surface XMCD consists of a sequence of segments with azimuthal spin configuration of opposite contrast. That suggests also the presence of a vortex-like structure with alternating chirality. The shadow region shows a much weaker contrast. Along the nanowire length, the contrast in each segment of the shadow region vanishes only in about half of its area while the remaining shadow area shows a uniform XMCD contrast. This suggests a domain structure consisting of uniformly magnetized core surrounded by a shell of curling spins of opposite chiralities around the wire axis. The fact that the uniform contrast in transmission presents an opposite orientation to that of the direct photoemission confirms that this is not an artifact of the data analysis. The contrast observed in Figure 5.9(a) is interpreted by the sketch in Figure 5.9(b). The bright/dark contrast on the right is related with the nanowire surface magnetization. However, owing to the cylindrical geometry of the nanowire and the grazing angle of the X-ray with respect to the sample surface (angle of 16º, see Figure 2.14 and Figure 5.9(b)) only a certain region of the nanowire surface (the bright contrast region) is directly exposed to the X-rays while the rest is only sensitive to the transmitted beam (the dark contrast region).

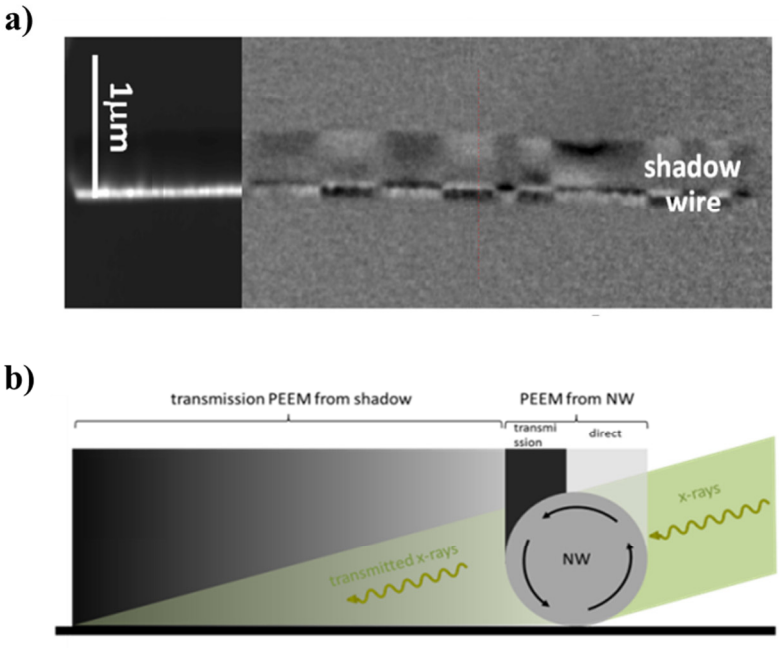

Figure 5.9 (a) XMCD contrast of a representative individual Co nanowire measured at about 90° between the incident X-rays and the nanowire; and (b) Schematic view of the contrast observed for direct photoemission and transmission, dual in the case of a nanowire with circular spin configuration.

The second type of contrast is found in the shadow area due to the transmitted X-rays through the nanowire. A complex contrast profile is observed due to the nanowire geometry, X-rays transmission and circular configuration of the magnetization. The gray contrast in the middle of the shadow (corresponding to the core of the wire) can be an indication of the magnetization pointing perpendicular to the beam (i.e. along the nanowire axis). While a precise determination of the core and shell sizes in the nanowires is hard to quantify, the comparable widths of the dark and bright contrast regions in the shadow indicate a much reduced diameter of the core. This is consistent with a strong perpendicular anisotropy of the Co nanowire.

For Co nanowires, the spin configuration observed in the XMCD-PEEM experiments indicates that the magnetocrystalline anisotropy dominates over the uniaxial longitudinal shape anisotropy. This experimental result is consistent with recent micromagnetic simulations of the spin configurations in nanowires with strong uniaxial perpendicular magnetocrystalline anisotropy [14]. The longitudinal extent of each vortex typically varies along the wire, not matching the periodicity of the diameter modulation, and it also varies from wire to wire. Both facts indicate that the local spin configuration can be also influenced by the nanowire morphology and/or microstructure.

5.4. Conclusions

According to MOKE measurements, the magnetization reversal of FeCoCu nanowires with specific tailored modulations in diameter has been determined to take place through the motion of a single vortex domain wall which is eventually pinned at local modulations of the nanowire resulting in metastable magnetic states during its whole propagation. The relatively smooth homogeneity of the modulations leads us to observe a main Barkhausen jump but for small jumps at modulations with slightly enhanced energy barrier to the wall propagation.

The combination of direct photoemission and transmission information from XMCD–PEEM allowed determining the spin configuration at the surface and the core of cylindrical nanowires with periodically modulated diameter. For FeCoCu nanowires, the spin configuration is dominated by shape anisotropy and the remanent spin

configuration consists of a main longitudinal domain with vortex structures at the ends as well as around the diameter modulations. In agreement with MOKE experiments, the magnetization reversal is expected to take place through the propagation of a vortex domain wall that can be pinned at the position of certain modulations. For Co nanowires, which present nearly perpendicular magnetocrystalline anisotropy, the spin configuration is characterized by a series of vortices with alternating chirality which appears not to be connected with the position of the modulations.

Magnetic nanowires with tailored geometry, in the form of periodically diameter modulations, and magnetocrystalline anisotropy show tunable magnetic properties and the opportunity to further control the magnetization reversal process by controlling the domain wall motion.

Bibliography

[1] K. Pitzschel, J.M.M. Moreno, J. Escrig, O. Albrecht, K. Nielsch, J. Bachmann, Controlled introduction of diameter modulations in arrayed magnetic iron oxide nanotubes, *ACS Nano*, 3 (2009) 3463-3468.

[2] M.S. Salem, P. Sergelius, R.M. Corona, J. Escrig, D. Görlitz, K. Nielsch, Magnetic properties of cylindrical diameter modulated Ni 80 Fe 20 nanowires: interaction and coercive fields, *Nanoscale*, 5 (2013) 3941-3947.

[3] A. Esmaeily, M. Venkatesan, A.S. Razavian, J. Coey, Diameter-modulated ferromagnetic CoFe nanowires, *J. Appl. Phys*., 113 (2013) 17A327.

[4] I. Minguez-Bacho, S. Rodriguez-López, M. Vázquez, M. Hernández-Vélez, K. Nielsch, Electrochemical synthesis and magnetic characterization of periodically modulated Co nanowires, *Nanotechnology,* 25 (2014) 145301.

[5] K. Pitzschel, J. Bachmann, S. Martens, J.M. Montero-Moreno, J. Kimling, G. Meier, J. Escrig, K. Nielsch, D. Görlitz, Magnetic reversal of cylindrical nickel nanowires with modulated diameters*, J. Appl. Phys.,* 109 (2011) 033907.

[6] D.M. Burn, E. Arac, D. Atkinson, Magnetization switching and domain-wall propagation behavior in edge-modulated ferromagnetic nanowire structures, *Phys. Rev. B*, 88 (2013) 104422.

[7] T.-C. Chen, C.-Y. Kuo, A.K. Mishra, B. Das, J.-C. Wu, Magnetic domain wall motion in notch patterned permalloy nanowire devices, *Physica B*, 476 (2015) 161-166.

[8] D.J. Sellmyer, M. Zheng, R. Skomski, Magnetism of Fe, Co and Ni nanowires in self-assembled arrays, *J. Phys.-Condens. Mat*., 13 (2001) R433.

[9] L.H. Lewis, F. Jiménez-Villacorta, Perspectives on permanent magnetic materials for energy conversion and power generation, *Metall. Mater. Trans. A*, 44 (2013) 2-20.

[10] L. Vivas, J. Escrig, D. Trabada, G. Badini-Confalonieri, M. Vázquez, Magnetic anisotropy in ordered textured Co nanowires, *Appl. Phys. Lett.,* 100 (2012) 252405.

[11] A. Aharoni, Introduction to the Theory of Ferromagnetism, Clarendon Press, 2000.

[12] C. Bran, Y.P. Ivanov, J. García, R. del Real, V. Prida, O. Chubykalo-Fesenko, M. Vazquez, Tuning the magnetization reversal process of FeCoCu nanowire arrays by thermal annealing, *J. Appl. Phys*., 114 (2013) 043908.

[13] S. Vock, C. Hengst, M. Wolf, K. Tschulik, M. Uhlemann, Z. Sasvári, D. Makarov, O. Schmidt, L. Schultz, V. Neu, Magnetic vortex observation in FeCo nanowires by quantitative magnetic force microscopy, *Appl. Phys. Lett.*, 105 (2014) 172409.

[14] Y.P. Ivanov, L. Vivas, A. Asenjo, A. Chuvilin, O. Chubykalo-Fesenko, M. Vázquez, Magnetic structure of a single-crystal hcp electrodeposited cobalt nanowire, *EPL Europhys. Lett.,* 102 (2013) 17009.

[15] Y.P. Ivanov, M. Vázquez, O. Chubykalo-Fesenko, Magnetic reversal modes in cylindrical nanowires, *J. Phys. D-Appl. Phys.,* 46 (2013) 485001.

[16] M. Sultan, B. Das, P. Sen, K. Mandal, D. Atkinson, Template released ferromagnetic nanowires: morphology and magnetic properties, *J. Spintron. Magn. Nanomater.*, 1 (2012) 113-121.

[17] V. Vega, T. Böhnert, S. Martens, M. Waleczek, J.M. Montero-Moreno, D. Görlitz, V. Prida, K. Nielsch, Tuning the magnetic anisotropy of Co–Ni nanowires: comparison between single nanowires and nanowire arrays in hard-anodic aluminum oxide membranes, *Nanotechnology,* 23 (2012) 465709.

[18] E.V. Vidal, Y.P. Ivanov, H. Mohammed, J. Kosel, A detailed study of magnetization reversal in individual Ni nanowires, *Appl. Phys. Lett.,* 106 (2015) 032403.

[19] J. Kimling, F. Kronast, S. Martens, T. Böhnert, M. Martens, J. Herrero-Albillos, L. Tati-Bismaths, U. Merkt, K. Nielsch, G. Meier, Photoemission electron microscopy of three-dimensional magnetization configurations in core-shell nanostructures, *Phys. Rev. B*, 84 (2011) 174406.

[20] S. Da Col, S. Jamet, N. Rougemaille, A. Locatelli, T. Mentes, B.S. Burgos, R. Afid, M. Darques, L. Cagnon, J.-C. Toussaint, Observation of Bloch-point domain walls in cylindrical magnetic nanowires, *Phys. Rev. B*, 89 (2014) 180405.

[21] S. Jamet, S. Da Col, N. Rougemaille, A. Wartelle, A. Locatelli, T. Menteş, B.S. Burgos, R. Afid, L. Cagnon, S. Bochmann, Quantitative analysis of shadow x-ray magnetic circular dichroism photoemission electron microscopy, *Phys. Rev. B*, 92 (2015) 144428.

[22] A. Wartelle, C. Thirion, R. Afid, S. Jamet, S. Da Col, L. Cagnon, J.-C. Toussaint, J. Bachmann, S. Bochmann, A. Locatelli, Broadband Setup for Magnetic-Field-Induced Domain Wall Motion in Cylindrical Nanowires, *IEEE Trans. Magn.*, 51 (2015) 1-4.

[23] Y.P. Ivanov, O. Chubykalo-Fesenko, R. Hertel, C. Andreas, S. Jamet, N. Rougemaille, J.C. Toussaint, O. Fruchart, Magnetic Nano- and Microwires, Chapters 14, 22, 25, Manuel Vázquez (ed.) (2015).

[24] H. Kronmüller, M. Fähnle, Micromagnetism and the microstructure of ferromagnetic solids. 2003, in, Cambridge: Cambridge University Press.

[25] F. Tejo, N. Vidal-Silva, A. Espejo, J. Escrig, Angular dependence of the magnetic properties of cylindrical diameter modulated Ni80Fe20 nanowires, *J. Appl. Phys*., 115 (2014) 17D136.

[26] A. Aharoni, Angular dependence of nucleation by curling in a prolate spheroid, *J. Appl. Phys.*, 82 (1997) 1281-1287.

[27] S. Shtrikman, D. Treves, Magnetism, vol. III, v. GT Rado und H. Suhl. Academic Press, New York, (1963) 395-414.

[28] X. Liu, R. Sooryakumar, C. Gutierrez, G. Prinz, Exchange stiffness and magnetic anisotropies in bcc Fe1− xCox alloys, *J. Appl. Phys.*, 75 (1994) 7021-7023.

[29] Y.P. Ivanov, D.G. Trabada, A. Chuvilin, J. Kosel, O. Chubykalo-Fesenko, M. Vázquez, Crystallographically driven magnetic behaviour of arrays of monocrystalline Co nanowires, *Nanotechnology*, 25 (2014) 475702.

Chapter 6

Magnetic Nanowires based Sensors

6.1 Introduction

The detection of the position and/or speed of a moving object usually is performed by different techniques making use of optical, inductive, capacitive, magnetic or magnetoelectric means [1-5]. Optical-based sensing devices which use a light emitter and receiver, an encoder or a laser are widely used methods to determine the rotational speed or the distance between objects [6, 7], but they present some disadvantages as they require active emitters and receptors and usually it is necessary to modify substantially the object where the sensing device is coupled.

Pick-up sensors are alternative magnetic sensing devices where the working principle is the relative displacement of a magnetic component with respect to the detector. The displacement creates a change in the detected magnetic field which can be correlated to the speed of the moving object [8-10]. The most convenient way to generate the magnetic field for these sensors is using a magnetized material instead of a coil, as in this case this element does not need to be energized for operating (i.e. passive element). Magnetic nanoparticles have been proposed as an approach for generating a magnetic field [11, 12] due to the need of a drastic reduction in the device size [13-15]. However, the use of magnetic nanoparticles presents some challenges such as the relatively complex fabrication process and the low magnetic field that can be generated, implying the need of a highly-sensitive detector to acquire the magnetic response.

Metallic magnetic nanowires have been proposed as an alternative rare-earth-free family of permanent magnets [16]. Particularly, FeCo based nanowires are characterized by their high saturation magnetization (which implies a strong shape anisotropy that tends to align the magnetization parallel to the nanowire axis, i.e. perpendicular to the film plane) and Curie temperature (which makes them appropriate for high temperature applications) [17, 18].

6.2 Nanowires fabrication and characterization

In the study described in Chapter 3 of this work, it was determined that $Fe_{30}Co_{70}$ nanowires exhibited the highest coercive field from the whole range of FeCo alloy compositions (i.e. $Fe_{100-x}Co_x$ nanowire arrays, with $0 \leq x \leq 100$) [19, 20]. For the fabrication of this specific type of nanowires an anodic aluminum oxide (AAO) template was fabricated by two-step anodization (see Section 2.1.3.1 for experimental details). The nanowires were grown inside the alumina template by electrodeposition in a three-electrode cell using a Watts-type bath, with a composition of 0.05 M $FeSO_4 \cdot 7H_2O$, 0.12 M $CoSO_4 \cdot 7H_2O$, 0.16 M H_3BO_3 and 0.06 M $C_6H_8O_6$, under a constant applied voltage of -1.8 V versus Ag/AgCl reference electrode. More detailed description of the nanowires fabrication process can be found in Section 2.2.

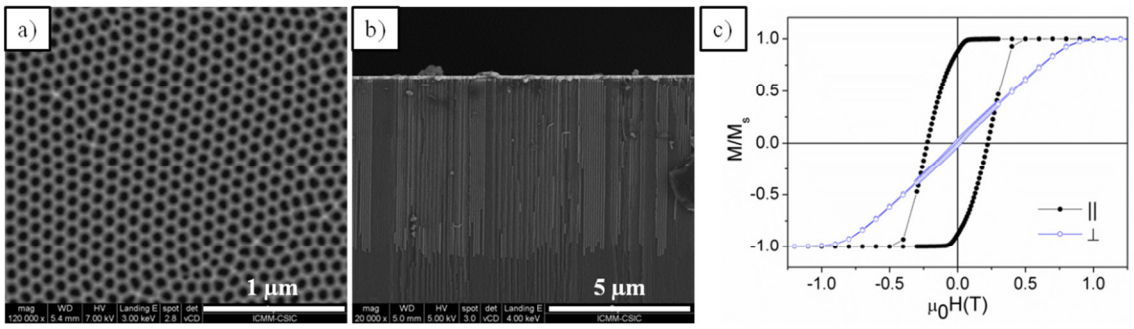

Figure 6.1 SEM images: (a) top view of the alumina template and (b) cross section of the $Fe_{30}Co_{70}$ nanowires embedded into the alumina template. (c) Hysteresis loops of the nanowire array measured under the magnetic field applied in parallel (||) and perpendicular (⊥) configurations.

The template and nanowires geometry was determined by a Scanning Electron Microscope (SEM). The alumina template thickness was 40 µm, the distance between pore centers (D_{int}) was 105 nm and the nanowires were 40 nm in diameter (d_{NW}) and 7.5

μm in length (L_{NW}). The composition of the nanowires was determined by means of Energy Dispersive X-ray Spectroscopy (EDS) and was $Fe_{30}Co_{70}$. Figure 6.1(a) and (b) show the top view of the AAO template and the cross section of the nanowires embedded into the template, respectively.

The magnetic characterization of the nanowire array was carried out by Vibrating Sample Magnetometry (VSM) under maximum magnetic field of ±1.8 T applied parallel (||) and perpendicular (⊥) to the nanowires. The hysteresis loops in both configurations are plotted in Figure 6.1(c). The values of coercive field ($\mu_0 H_c$), saturation field ($\mu_0 H_{sat}$) and fractional remanence (M_r/M_s) obtained from the hysteresis loops are collected in Table 6.1.

Table 6.1 Coercive field (H_c), saturation field (H_{sat}) and fractional remanence (M_r/M_s) of $Fe_{30}Co_{70}$ nanowire array with d_{NW} = 40 nm and L_{NW} = 7.5 μm, for applied magnetic field in parallel (||) and perpendicular (⊥) configuration.

Magnetic field configuration	$\mu_0 H_c$ (mT)	$\mu_0 H_{sat}$ (mT)	M_r/M_s
||	233	500	0.88
⊥	12	1250	0.02

According to the higher values of $\mu_0 H_c$ and M_r/M_s for || magnetic field compared to the vanishing values for ⊥ configuration, together with the large value of $\mu_0 H_{sat}$ (⊥), it is deduced a magnetization easy axis of the nanowire array parallel to the nanowire longitudinal axis. The samples which were used as magnetic field generators were fully magnetized at 1.8 T using the VSM in || configuration and then the magnetic field was switch off to reach the remanent state.

6.3 Mechanical and electronic system

A simple electronic system was implemented to develop the two different magnetic nanowire based sensors: the position sensor and the rotational speed sensor or tachometer. The Hall effect sensor used to acquire the magnetic field generated by the nanowire array was the solid state sensor SS94A1F from Honeywell. The surface of the template containing the nanowire array used for each sensor 4 mm^2.

Figure 6.2(a) and (b) show the mechanism used as the magnetic nanowires based position sensor. It was composed of a brass rod where the sample was glued (Figure 6.2(a)). The metallic rod moves along its axis which is perpendicular to the Hall sensor (movement indicated by the bidirectional orange arrow in Figure 6.2(a)). The position of the rod was accurately determined by a micrometer, with a precision of 10 µm. The rotational speed sensor is shown in Figure 6.2(c) and (d). The nanowire array sample was pasted on a polytetrafluoroethylene (PTFE) wheel (see detail in Figure 6.2(d)) connected to the rotational shaft of the motor (rotational direction indicated by the orange arrow in Figure 6.2(c)).

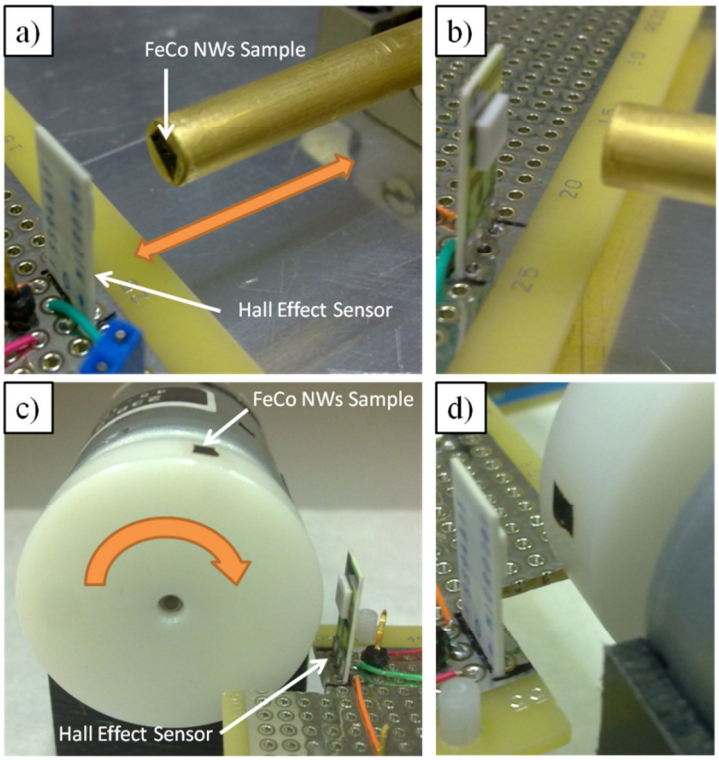

Figure 6.2 Position sensor mechanism: (a) metallic rod with the nanowire (NW) array sample and its movement direction given by the orange arrow and (b) detail of the sensing area of the Hall Effect sensor. Rotational speed sensor mechanism: (c) rotational direction of the motor given by the orange arrow and (d) wheel with the nanowire array sample opposite the Hall Effect sensor.

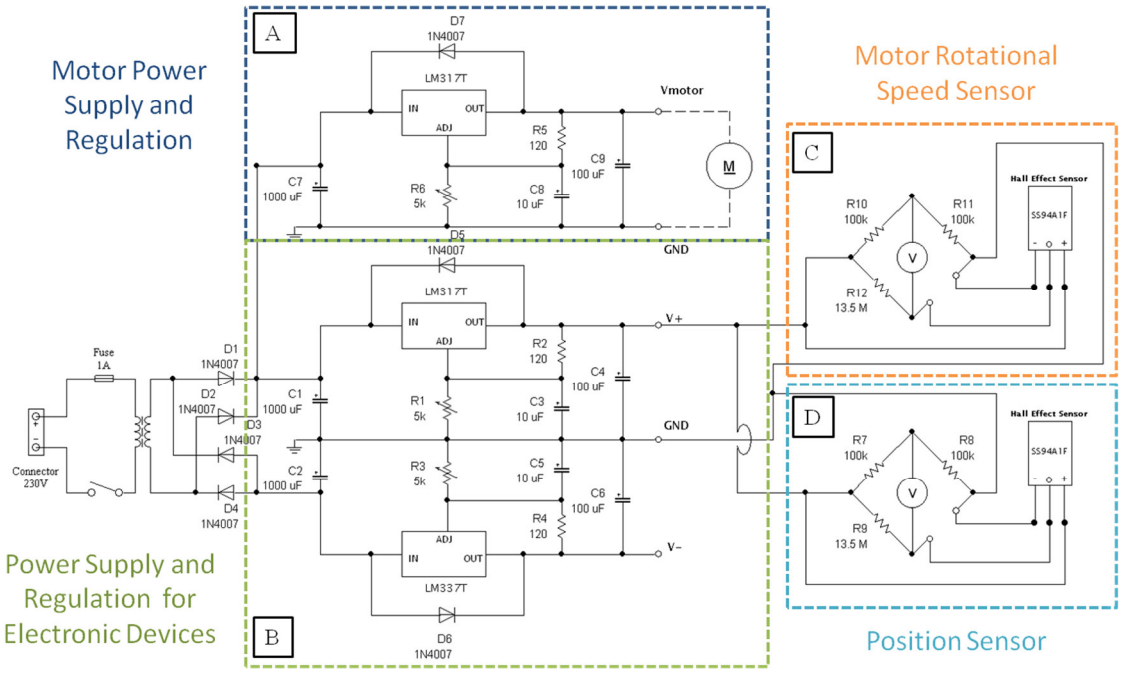

Figure 6.3 Electronic circuit for the two sensing systems.

The electronic system is composed of power supplies and electronic circuits for the signal processing. The electronic system is divided into four main parts (Figure 6.3):

i) An independent power supply for the motor (A). As it is based on a voltage regulator LM317T, it is possible to modify the voltage applied to the motor to control the rotation speed;

ii) A power supply for the electronic components (B), symmetric and with variable output voltage, which main components are the voltage regulators LM317T and LM337T;

iii) Two electronic circuits (one for the rotation speed sensor (C) and the other one for the position sensor (D)), each of them composed of two main parts: a Hall effect sensor and a Wheatstone bridge. Using this circuit, it is possible to eliminate the offset of the Hall effect sensor and obtain the magnetic field generated by the nanowire array with respect to the sample position.

6.4 Sensors response

The position sensor output (Figure 6.4) was obtained placing the nanowire array opposite and parallel to the Hall sensor (AAO template parallel and NWs perpendicular). To obtain the output signal, the distance between them was modified using the micrometer. The signal decreases with the distance, as expected from the reduction of the magnetic flux density detected by the Hall sensor. The inset in Figure 6.4 shows that the output signal presents a linear behavior for a distance up to 1 mm.

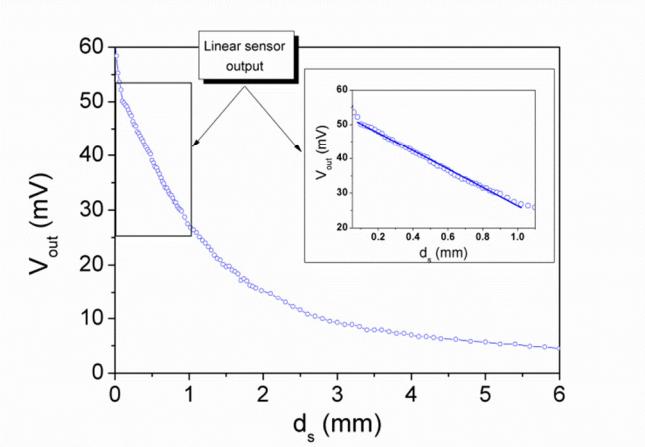

Figure 6.4 Distance sensor output: voltage generated according to the magnetic field from the nanowire sample vs. distance between the sample and the Hall sensor. The inset shows a closer view of the linear part.

The output signal (V_{out}) was linearly fitted according to the distance between the nanowire array and the Hall sensor (d_s) obtaining the Equation 1. It is worth mentioning how a small variation in the distance (i.e. order of magnitude of μm) can be macroscopically detected accurately (see inset in Figure 6.4 and consider the slope of the Eq. 1, 26.45 mV/mm).

$$V_{out}(mV) = 52.82 - 26.45\, d_s(mm) \quad (1)$$

Selected tachometer outputs (V_{sensor}) for different applied voltages to the motor (V_{motor}) are shown in Figure 6.5(a) to (c). The peaks in the different graphs correspond to the moment when the nanowire array sample is opposite to the Hall Effect sensor. A detail of one peak is shown in Figure 6.5(d) for V_{motor} = 8 V, presenting a symmetric shape of significant amplitude. This means that the magnetic field generated by the

nanowire array is measurable and strong enough to be used as the magnitude to be detected by the sensing system.

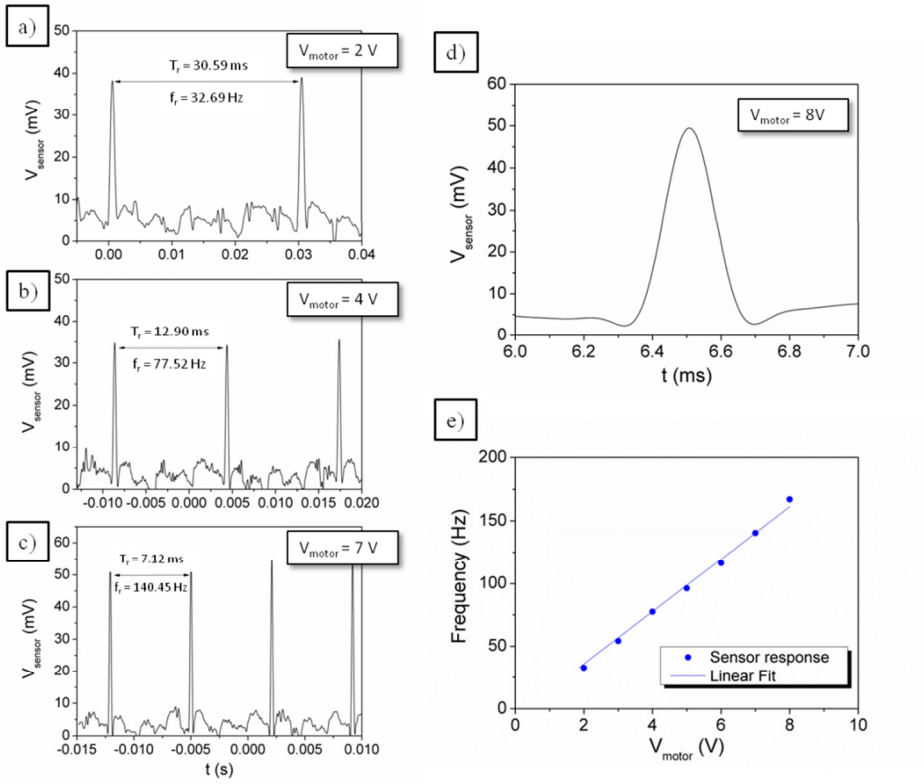

Figure 6.5 Sensor output, V_{sensor}, and rotation frequency, f_r, for different applied voltages to the motor, V_{motor}: (a) 2 V, (b) 4 V and (c) 7 V; (d) Detail of the sensor output for a V_{motor} = 8 V; and (e) Motor speed obtained using the nanowires based sensor and the data linear fit.

The rotational frequency of the motor (f_r) is determined from the time interval between two symmetric peaks (T_r). The obtained values of the motor speed for the different applied voltage to the motor are plotted in Figure 6.5(e).

6.5 Conclusions

In summary, with this work has been proved that magnetic nanowire arrays are a good alternative as magnetic field generators in pick-up sensors. The magnetic field generated by $Fe_{30}Co_{70}$ nanowire array was high enough to be easily and accurately detected in both sensors (i.e. a position sensor and a tachometer). The use of magnetic nanowires based sensors presents the advantages of low cost devices, high working temperature and the non-necessity of modifying substantially the system where is coupled. This system is adaptable to the device and the accuracy that is needed, being possible to choose the electronic components to give to the system more accuracy and the capability of a faster signal acquiring and processing.

Bibliography

[1] Y.-X. Guo, Z.-B. Shao, T. Li, An Analog-Digital Mixed Measurement Method of Inductive Proximity Sensor, *Sensors*, 16 (2015) 30.

[2] Q. Yang, S. Sun, R. Han, W. Sima, T. Liu, Intense transient electric field sensor based on the electro-optic effect of LiNbO3, *AIP Adv*., 5 (2015) 107130.

[3] B. Yang, Y. Yang, A new angular velocity sensor with ultrahigh resolution using magnetoelectric effect under the principle of Coriolis force, *Sensor. Actuat. A-Phys.,* 238 (2015) 234-239.

[4] T. Li, Y. Tan, Z. Zhou, K. Zheng, A non-contact FBG vibration sensor with double differential temperature compensation, *Opt. Rev*., 23 (2016) 26.

[5] A.A. Potdar, S. Fletcher, A.P. Longstaff, Performance characterisation of a new photo-microsensor based sensing head for displacement measurement, *Sensor. Actuat. A-Phys.*, 238 (2016) 60-70.

[6] I.I. Incze, A. Negrea, M. Imecs, C. Szabó, Incremental encoder based position and speed identification: modeling and simulation, *Acta Univ. Sapientiae Matem.*, 2 (2010) 27-39.

[7] G. Berkovic, E. Shafir, Optical methods for distance and displacement measurements, *Adv. Opt. Photonics*, 4 (2012) 441-471.

[8] R. Myers, R.A. Islam, M. Karmarkar, S. Priya, Magnetoelectric laminate composite based tachometer for harsh environment applications, *Appl. Phys. Lett.,* 91 (2007) 122904-122904.

[9] S. F Hasany, N. H Abdurahman, A. R Sunarti, R. Jose, Magnetic iron oxide nanoparticles: chemical synthesis and applications review, *Curr. Nanosci*., 9 (2013) 561-575.

[10] S.A. Harmon, M.J. Hall, S. Turner, N. Hillier, Characterization of Magnetic Sensors at the Operational Temperatures of Industrial Applications, *IEEE Trans. Magn.,* 51 (2015) 1-4.

[11] V. Khanna, Nanoparticle-based sensors, *Defence Sci. J.,* 58 (2008) 608.

[12] I. Koh, L. Josephson, Magnetic nanoparticle sensors, *Sensors*, 9 (2009) 8130-8145.

[13] M. Barbic, A. Scherer, Stray field magnetic resonance tomography using ferromagnetic spheres, *J. Magn. Reson*., 181 (2006) 223-228.

[14] T. Eichner, F. Grüner, S. Becker, M. Fuchs, D. Habs, R. Weingartner, U. Schramm, H. Backe, P. Kunz, W. Lauth, Miniature magnetic devices for laser-based, table-top free-electron lasers, *Phys. Rev. Spec. Top.-Ac*., 10 (2007) 082401.

[15] W.K. Peng, L. Chen, J. Han, Development of miniaturized, portable magnetic resonance relaxometry system for point-of-care medical diagnosis, *Rev. Sci. Instrum*., 83 (2012) 095115.

[16] T. Maurer, F. Ott, G. Chaboussant, Y. Soumare, J.-Y. Piquemal, G. Viau, Magnetic nanowires as permanent magnet materials, *Appl. Phys. Lett*., 91 (2007) 172501.

[17] J. Coey, Hard magnetic materials: A perspective, *IEEE Trans. Magn*., 47 (2011) 4671-4681.

[18] L.H. Lewis, F. Jiménez-Villacorta, Perspectives on permanent magnetic materials for energy conversion and power generation, *Metall. Mater. Trans. A*, 44 (2013) 2-20.

[19] C. Bran, E.M. Palmero, R.P. del Real, M. Vazquez, CoFeCu electroplated nanowire arrays: Role of composition and annealing on structure and magnetic properties, *Phys. Status Solidi A*, 211 (2014) 1076-1082.

[20] C. Bran, E. Palmero, Z.-A. Li, R. del Real, M. Spasova, M. Farle, M. Vázquez, Correlation between structure and magnetic properties in Co_xFe_{100-x} nanowires: the roles of composition and wire diameter, *J. Phys. D.-Appl. Phys.,* 48 (2015) 145304.

Chapter 7

General Conclusions and Future Perspectives

Along the course of this thesis new 3*d* metal based nanostructures have been synthesized with tailored composition and geometry to tune their magnetic properties. The main part of this work has been focused on FeCo-based nanowires as they have been proposed as suitable candidates for rare-earth-free permanent magnets applications. All the nanowire arrays fabricated for the studies included in this work have been synthesized by electrochemical techniques, such as different anodization processes for the alumina templates fabrication and electrodeposition of several elements and alloys for the nanowires growth. The main conclusions of this research work are collected in this chapter.

A first study was carried out to determine the magnetic properties of FeCo nanowire arrays in the whole range of composition from pure Fe to pure Co nanowires with different diameters. The main conclusions are outlined:

- In FeCo nanowires, the nanowire composition strongly influences their crystallographic structure, evolving from *bcc* crystal structure to *fcc* as the Co content into the alloy increases.
- For Co nanowires, the nanowire diameter also determines the crystal structure, promoting a change from *fcc* to *hcp* structure with the reduction in diameter.
- Among the possible alloys, $Fe_{30}Co_{70}$ nanowire arrays show the largest value of saturation magnetization, as well as the highest values of coercive field and remanence.

- The shape anisotropy dominates the magnetic behavior of FeCo nanowire, originating an effective magnetization easy axis along the nanowire axis.
- For Co nanowires the nearly perpendicular magnetocrystalline anisotropy nearly balances the nanowire shape anisotropy.

An effective magnetic hardening of FeCo alloy nanowires was achieved by adding a small amount of Cu to the alloy, followed by adequate thermal treatment:

- The addition of Cu gives rise to modest changes in the nanowire crystal structure and magnetic properties for as cast samples.
- If after Cu addition a thermal treatment is performed, the crystalline texture is optimized and a significant magnetic hardening of the FeCo nanowires is obtained.
- According to FMR measurements, the magnetic hardening has been found to be a consequence of enhanced magnetocrystalline anisotropy.

A different alternative was adding Cu as non-ferromagnetic layers between ferromagnetic FeCoCu segments (FeCoCu/Cu multilayer nanowires):

- It was determined a magnetization easy axis parallel to the nanowire axis for all the nanowire arrays.
- A modest coercive field and remanence increase was obtained for thicker Cu layer and longer FeCoCu segments.
- FORC technique has been successfully applied to study the intrawire and interwires magnetostatic interactions in the array and quantitatively determine the influence of Cu layer and FeCoCu segment thicknesses on the magnetic properties of the multilayer nanowire array.
- After FORC diagrams analysis, it was observed that thick Cu layers promote the weakening of intrawire interactions between FeCoCu segments through the Cu layers, making more difficult the magnetization reversal. Furthermore, higher value of coercive field was observed for longer FeCoCu segments, which is ascribed to the increase in shape anisotropy.

- The magnetostatic coupling between ferromagnetic segments has been proved to be a consequence of the non-ferromagnetic/ferromagnetic thickness ratio.

The domain wall propagation along the nanowire can be tuned through controlled change of the nanowire geometry and magnetocrystalline anisotropy:

- FeCoCu nanowires with specific tailored modulations in diameter present a magnetization configuration dominated by shape anisotropy.
- The magnetization reversal in these modulated nanowires takes place through a vortex domain wall which eventually is pinned at local diameter modulations.
- Co nanowires with modulated diameter present nearly perpendicular magnetocrystalline anisotropy and their magnetization configuration is characterized by vortices with alternating chirality along the nanowire length.

The applicability of magnetic nanowires has also been demonstrated using them as magnetic field source in two sensing devices:

- A position sensor and a tachometer were developed.
- The magnetic field generated by the nanowire array was high enough to be easy and accurately detected.
- Clear advantages of these prototypes are observed: low cost devices, the possibility of high working temperature and the easy electronic system tuning according to the accuracy needed for the measurement.

Additionally, the magnetic properties of the magnetically soft NiCu alloy nanowires and a hybrid magnetic-polymer nanocomposite were studied:

- The magnetic properties of NiCu nanowire arrays were tailored by tuning the nanowire compositional and geometrical characteristics.

- All NiCu nanowires crystallize in a polycrystalline *fcc* structure, varying the preferential growing direction from (220) to (111) by adding Cu.
- For intermediate Cu content, a segregation of Ni-rich and Cu-rich phases was determined.
- It was deduced an evolution of the magnetization easy axis from parallel towards perpendicular to the nanowire axis when increasing the amount of Cu into the alloy.
- A core-shell magnetic-polymeric nanocomposite formed of Ni nanowires embedded into polystyrene (PS) nanotubes was easily synthesized.
- The Ni-PS nanocomposite show an effective magnetization easy axis parallel to the nanowires, due to the shape anisotropy of Ni nanowires.

The results obtained along the research work included in this investigation open a number of opportunities to develop new research studies in the future as:

(i) Addition of different non-ferromagnetic materials, such as B or C, to the FeCo alloy to further enhance the magnetic hardening.
(ii) Determination of domain wall velocity and further control of domain wall motion.
(iii) Measurements of magnetotransport properties of single FeCo-based.
(iv) Fabrication of core-shell structures by electrochemical methods: ferromagnetic-ferromagnetic or ferromagnetic-antiferromagnetic structures.

Capítulo 7

Conclusiones Generales y Líneas Futuras de Investigación

A lo largo de este trabajo de investigación se han fabricado nuevas nanoestructuras basadas en metales de transición de la serie 3*d* con un amplio rango de composiciones y geometrías de forma que se adapten sus propiedades magnéticas a determinadas aplicaciones. El bloque principal de este trabajo se centra en nanohilos magnéticos compuestos principalmente por la aleación FeCo, ya que han sido propuestos como candidatos adecuados en aplicaciones de imanes permanentes, pero sin contenido en elementos de las tierras raras. Todos los arrays de nanohilos analizados en este trabajo han sido fabricados mediante técnicas electroquímicas, como la fabricación de las plantillas de alúmina mediante diferentes procesos de anodización, y el crecimiento de nanohilos de diversos elementos o aleación de los mismos mediante electrodeposición. En este capítulo se recogen las principales conclusiones de este trabajo de investigación.

Se realizó un primer estudio para determinar las propiedades magnéticas de los arrays de nanohilos de aleación FeCo en el rango completo de composiciones desde nanohilos de Fe puro hasta nanohilos de Co con dos diámetros distintos:

- En los nanohilos de FeCo, la composición influye de forma significativa en su estructura cristalina, variando desde estructura *bcc* a *fcc* cuando la cantidad de Co en la aleación aumenta.

- En los nanohilos de Co, su diámetro también tiene influencia sobre la estructura cristalina de forma que para diámetros menores la estructura varía de tipo *fcc* a *hcp*.
- De entre las posibles combinaciones de los elementos Fe y Co, los nanohilos con una composición de $Fe_{30}Co_{70}$ muestran el valor más alto de campo coercitivo y remanencia, presentando además un valor elevado de imanación de saturación.
- Se determinó que la anisotropía de forma domina en el comportamiento magnético de los nanohilos de FeCo, originando un eje fácil de imanación a lo largo del eje del nanohilo.
- En los nanohilos de Co la anisotropía magnetocristalina prácticamente equilibra a la anisotropía de forma del nanohilo.

Una primera opción para endurecer magnéticamente los nanohilos de aleación FeCo fue añadir una pequeña cantidad de Cu, seguido de tratamiento térmico:

- Al añadir Cu se obtienen cambios pequeños en la estructura cristalina y las propiedades magnéticas de los nanohilos.
- Si tras añadir Cu se realiza un tratamiento térmico, se favorece una mejor textura cristalina y un considerable endurecimiento magnético de los nanohilos de FeCo.
- Mediante las medidas de FMR, se determinó que el endurecimiento magnético es una consecuencia de un aumento de la anisotropía magnetocristalina.

Una diferente alternativa fue añadir Cu como capas de material no ferromagnético entre segmentos ferromagnéticos de FeCoCu:

- Se determinó un eje fácil de imanación paralelo al eje del nanohilo para todos los arrays.
- Se obtuvo un incremento modesto del campo coercitivo y de la remanencia para capas de Cu más gruesas y segmentos de FeCoCu más largos.

- La técnica FORC se empleó con éxito para estudiar las interacciones magnetostáticas entre segmentos magnéticos a lo largo del nanohilo y entre los nanohilos colindantes en el array, y determinar cuantitativamente la influencia del espesor de las capas de Cu y de los segmentos de FeCoCu en las propiedades magnéticas del sistema.
- Tras el análisis de los diagramas FORC, se determinó que capas de Cu gruesas promueven el debilitamiento de las interacciones entre segmentos magnéticos de FeCoCu a lo largo del nanohilo a través de las capas de Cu, dificultando la inversión de la imanación. Además, se observaron valores de campo coercitivo más altos para segmentos de FeCoCu largos, debido al incremento en la anisotropía de forma.
- Se ha demostrado que el acoplo magnetostático entre segmentos ferromagnéticos es una consecuencia de la relación entre los espesores de capa no ferromagnética y segmento ferromágnetico.

Una opción interesante para controlar el movimiento de pared de dominio a lo largo del nanohilo es mediante el ajuste de la geometría y la anisotropía magnetocristalina del nanohilo:

- Se determinó que la configuración de spines de los nanohilos de FeCoCu con específicas modulaciones en diámetro viene determinada por la anisotropía de forma.
- La inversión de la imanación en estos nanohilos modulados tiene lugar a través de una pared de tipo vórtice que de forma eventual se ancla en las modulaciones de diámetro.
- Los nanohilos de Co modulados en diámetro muestran una anisotropía magnetocristalina prácticamente perpendicular y su configuración de spines se caracteriza por vórtices con quiralidad alterna a lo largo de la longitud del nanohilo.

La aplicación de los nanohilos magnéticos ha sido demostrada mediante su uso como generadores de campo magnético en dos sensores:

- Se han desarrollado un sensor de posición y un tacómetro.
- El campo magnético generado por el array de nanohilos es suficientemente elevado como para ser detectado fácilmente y de forma precisa.
- Se han observado evidentes ventajas: bajo costo, la posibilidad de trabajar a altas temperaturas y el uso de un sistema electrónico sencillo que es posible adaptar acorde a la precisión que necesite la medida.

Además, se han estudiado las propiedades magnéticas de la aleación de NiCu, magnéticamente blanda, y de un nanocompuesto híbrido formado por un elemento magnético y un polímero:

- Se pueden ajustar las propiedades magnéticas de los arrays de nanohilos de NiCu a través del diseño de la composición y geometría de los nanohilos.
- Se determinó que para todas las composiciones de NiCu, los nanohilos presentan una estructura policristalina tipo *fcc*, variando su dirección de crecimiento de (220) a (111) al añadir Cu.
- Para contenidos intermedios de Cu en la aleación, se observó la segregación en dos fases cristalinas, una rica en Ni y otra rica en Cu.
- Se determinó una evolución del eje fácil de imanación desde paralelo a perpendicular respecto del eje del nanohilo conforme se incrementa la cantidad de Cu en la aleación.
- Se fabricó una estructura *core-shell* formada por un material magnético y un polímero (nanohilos de Ni dentro de nanotubos de poliestireno (PS)).
- El nanocompuesto Ni-PS presenta un eje fácil de imanación paralelo al eje del nanohilo, debido principalmente a la anisotropía de forma que presentan los nanohilos de Ni.

Teniendo en cuenta los resultados obtenidos a lo largo de este trabajo de investigación, existen interesantes líneas futuras de investigación que pueden ser desarrolladas:

(i) Añadir diversos materiales no ferromagnéticos, como B o C, a la aleación de FeCo para promover un mayor endurecimiento magnético.
(ii) Determinación de la velocidad de pared de dominio y control de su desplazamiento.
(iii) Medidas de las propiedades de magnetotransporte de nanohilos basados en la aleación de FeCo.
(iv) Fabricación de estructuras *core-shell* mediante técnicas electroquímicas: estructuras compuestas por diferentes materiales ferromagnéticos o entre material ferromagnético y antiferromagnético.

Appendix I

Magnetically Soft Alloy and Nanocomposite

I.1. Introduction

Several studies on ferromagnetic/non-ferromagnetic multilayered and binary nanowire arrays, including CoCu, FePd, CoAg and NiCu [1-4], have been reported in the literature due to their interesting magnetic and magnetotransport properties. Previous works have reported studies on the NiCu binary system using different methods, but they focused on bulk materials and multilayered nanowires [5-9]. Only few works properly deal with the magnetic properties of NiCu alloy nanowires [10, 11].

Individual Ni nanowires show easy axis along the nanowire axis due to its comparatively larger shape anisotropy energy [12, 13]. However, the magnetostatic interactions between neighboring nanowires in densely packed nanowire can modify significantly the magnetic properties of the nanowire array [14]. One alternative to reduce the demagnetizing magnetostatic interactions in the array and tailor the magnetic properties of the array according to the specific application is using an alloy of a non-ferromagnetic material and a ferromagnetic material [15]. Several studied have proved that good candidates as non-magnetic elements are B, Cu, Zn or P [2, 16-18]. On the other hand, this particular alloy (NiCu) shows interesting properties, such as corrosion resistance, high strength and good giant magnetoresistance [1, 19].

Most studies on nanostructures fabricated by electrochemical deposition focus on template synthesis of metal nanowires, nanotubes, nanorods and nanoparticles [20-24]. Template-assisted methods have been proved to be useful for the fabrication of

polymer nanowires and nanotubes from a wide number of different polymer structures [25-29]. Only few works study the combination of both materials and structures (combination of metallic and polymeric materials in the structure of nanowires and nanotubes) [30-33], but most of them are focused on nanoparticles embedded into the polymer nanorods or nanotubes [26, 34, 35]. The use of polymer as the shell in core-shell nanowires introduces the possibility of the application of these composite systems in functionalization with organic compounds. In this work, the objective has been to synthesize ordered arrays of magnetic nanowires covered by polystyrene (PS) nanotubes by combining electrochemical and chemical techniques and to study the magnetic properties of the resulting arrays.

I.2. Magnetically soft alloy: NiCu nanowires

I.2.1. Geometrical, structural and compositional characterization

The set of NiCu nanowire arrays were prepared by electrodeposition into hexagonally ordered anodic aluminum oxide (AAO) templates. The templates with the different pore diameter were fabricated by two-step anodization process (see Section 2.1.3.1 for experimental details). The different composition of the nanowires was achieved by varying the composition of the electrochemical bath (see Table 2.2), while keeping constant the applied voltage for all the samples (more details about the electrodeposition process can be found in Section 2.2).

The geometrical characterization was performed by Scanning Electron Microscopy (SEM) in order to determine the nanowire diameter (d_{NW}) and length (L_{NW}) and the distance between nanowires centers (D_{int}). As one of the objectives of this work is the study of the influence of the nanowire diameter, d_{NW} was tuned between 35 and 80 nm, while D_{int} was 105 nm for all the nanowire arrays. Figure I.1 shows the top and cross section view of selected arrays of 35 and 80 nm in diameter nanowires embedded into AAO templates. To study the influence of the nanowire length on the magnetic properties of the NiCu nanowire arrays, L_{NW} ranged from 150 nm to 28 μm, being 40 μm the template thickness. Figure I.2 shows selected nanowire arrays with different nanowire lengths: 1, 8 and 28 μm.

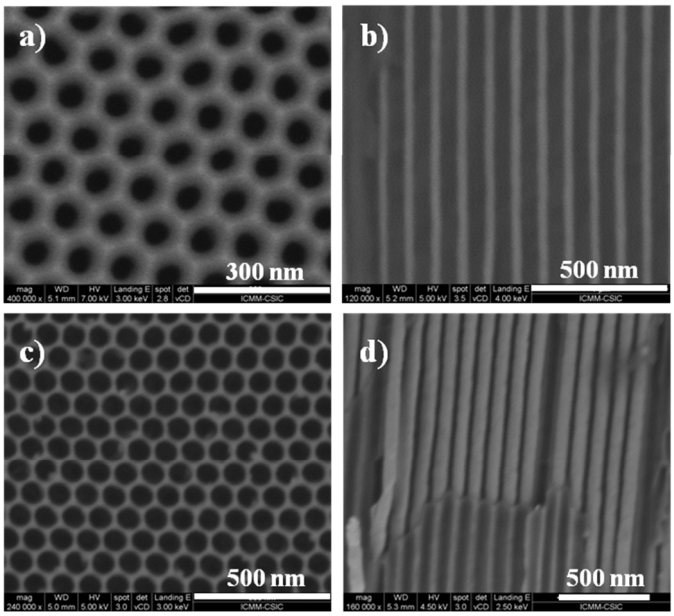

Figure I.1 Top view SEM images of an AAO template with pore diameter of (a) 35 nm and (c) 80 nm; and the cross section view of (b) 35 nm diameter nanowires and (d) 80 nm diameter nanowires embedded in AAO templates.

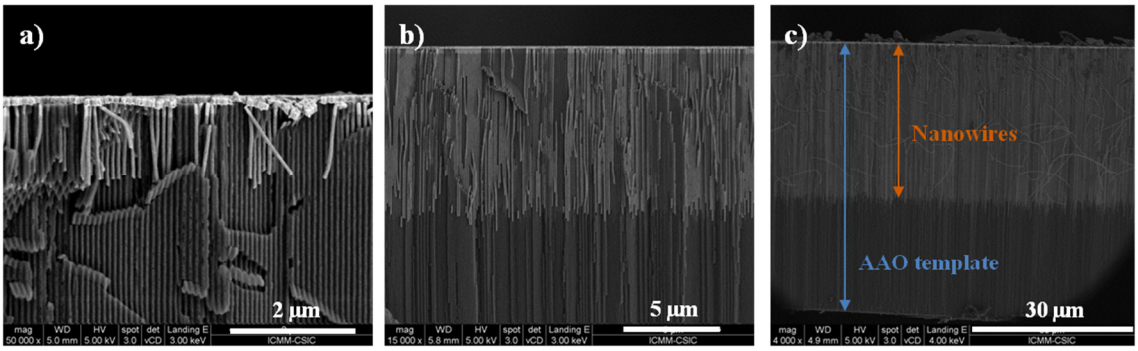

Figure I.2 Cross section images of nanowire embedded in AAO temples with different nanowire lengths: (a) 1 µm, (b) 8 µm, and (c) 28 µm.

The composition of the NiCu nanowires was obtained by Energy Dispersive X-Ray Spectroscopy (EDS) measurements, ranging from pure Ni to 75 % of Cu into the alloy (i.e. $Ni_{100-x}Cu_x$ nanowires, for $0 \leq x \leq 75$). The composition of the different nanowire arrays studied in this work is shown on the right side of the graph in Figure I.3.

The crystallographic structure of the nanowires was determined by X-Ray Diffraction (XRD) experiments. XRD spectra for nanowire arrays embedded into AAO templates with 80 nm nanowire diameter, 8 µm nanowire length and different chemical

composition are shown in Figure I.3. According to the spectra, a polycrystalline face-centered cubic (*fcc*) structure is confirmed for all the samples. The indexing of the patterns has been performed according to the Ni *fcc* crystalline structure (Space group Fm3m and lattice parameter a = 3.5239 Å) and Cu *fcc* crystalline structure (Space group Fm3m and a = 3.6150 Å), where the peaks at 2θ values of 44.55º, 51.89º, 76.45º and 93.05º correspond to the (111), (200), (220) and (311) reflections for Ni and the peaks at 2θ values of 43.35º, 50.49º, 74.20º and 89.56º correspond to the same reflections but for Cu. These positions are marked with dashed lines in Figure I.3 (blue color was used for Ni reflections and orange color for Cu ones). The XRD spectra in Figure I.3(b) shows a peak at 2θ = 41.7º, which corresponds to Cu_2O (200) reflection. The Cu oxidation in these samples took place after chemically removing the Au layer at the backside of the template for the XRD measurements [36]. To avoid Cu oxidation, the Au layer was kept and because of this in Figure I.3(d) and (e) a peak at 2θ = 38.2º appears, which corresponds to the Au *fcc* (111) reflection.

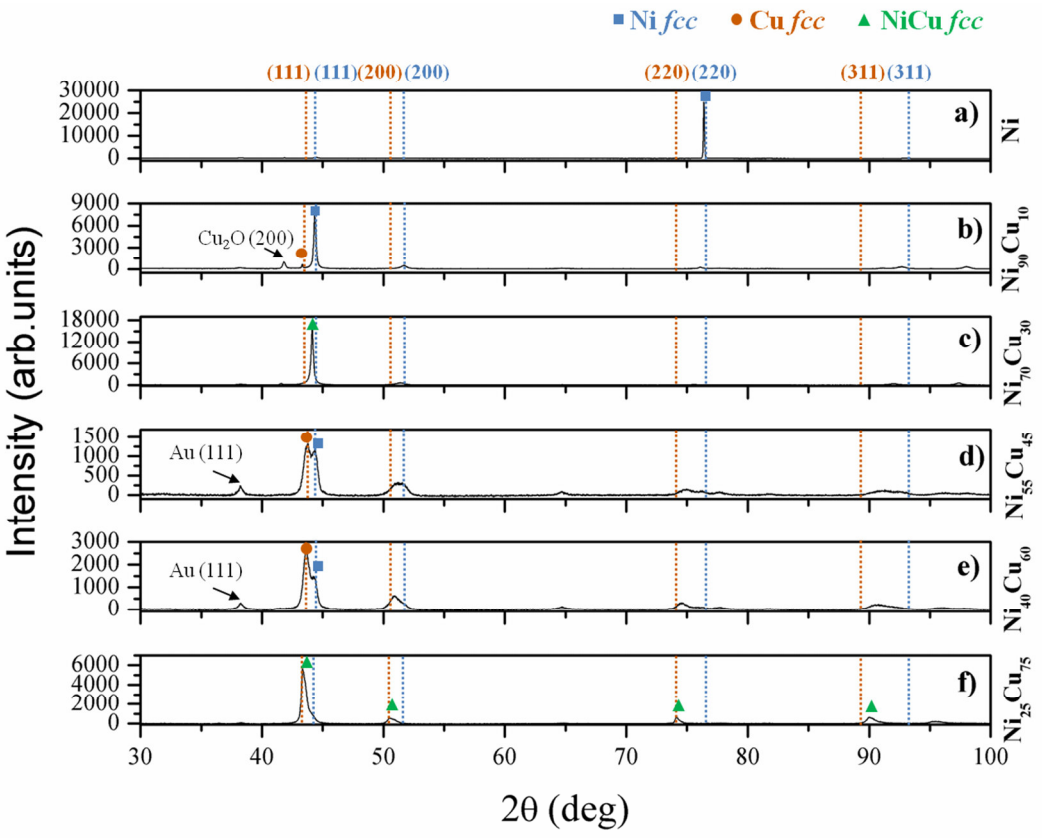

Figure I.3 XRD spectra of NiCu nanowires with different composition.

The diffraction pattern shows that the pure Ni nanowires (x = 0) grow in a *fcc* structure with a (220) preferred orientation (Figure I.3(a)). $Ni_{100-x}Cu_x$ nanowires crystallize in *fcc* structure mainly along the (111) direction but showing also (200), (220) and (311) reflections. For low Cu content, x = 10, two different (111) *fcc* phases for Ni and Cu are observed (Figure I.3(b)), which are ascribed to an inhomogeneous nanowire crystallization. For $Ni_{70}Cu_{30}$ nanowires, the higher content of Cu into the alloy promotes a shift to lower angles in the main (111) peak (Figure I.3(c)). For intermediate Cu content, $45 \leq x \leq 60$, we observe two (111) peaks that partly overlap each other which are ascribed to Ni-like and Cu-like structures, respectively (Figure I.3(d) and (e)). In these XRD spectra, it is observed that the relative amplitude of the peaks changes accordingly to the Cu content into the alloy. For the higher Cu content, x = 75, (Figure I.3(f)) only one peak is observed along the main (111) direction, ascribed to the Cu-like structure. However, a shoulder is still detected in all the peaks as remains of the presence of Ni. Comparing the spectra for x = 30 (Figure I.3(c)) and for x = 75 (Figure I.3(f)), we observe that all the *fcc* NiCu peaks are shifted to lower angles, closer to the 2θ values of Cu *fcc* used as reference for indexing, when increasing the amount of Cu into the alloy.

Morphology and microstructure of the NiCu nanowires were analyzed by High-Resolution Transmission Electron Microscopy (HRTEM). Figure I.4 shows the images obtained of selected nanowires with an intermediate composition of $Ni_{55}Cu_{45}$ and 60 nm diameter. Figure I.4(a) and (b) show a bright field TEM image and the Selected Area Electron Diffraction (SAED) pattern of a representative nanowire, respectively, which illustrate the polycrystalline nature of the nanowires. They present polycrystalline structure as demonstrated by the presence of diffraction rings indexed as (111), (200) and (220) sets of reflections of a *fcc* structure. These results are in agreement with XRD data in Figure I.3(d). Figure I.4(c) shows a HRTEM image of the selected nanowire, evidencing the good nanowire crystallinity.

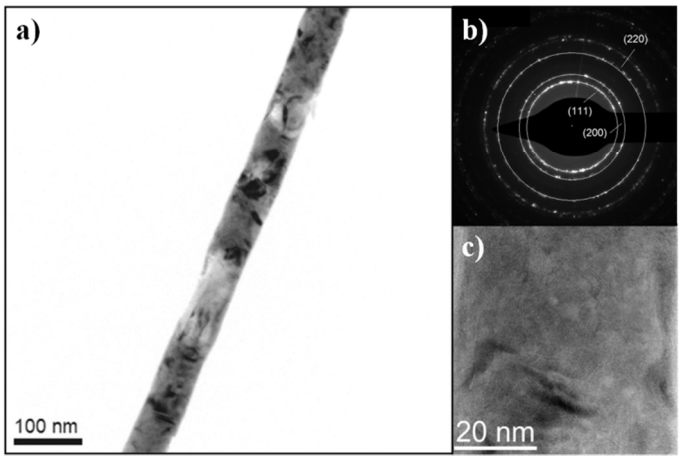

Figure I.4 HRTEM images of of one $Ni_{55}Cu_{45}$ nanowire (d_{NW} = 60 nm, L_{NW} =8 μm): (a) Bright field TEM image, (b) SAED pattern showing the polycrystalline structure of the nanowires, and (c) HRTEM image.

I.2.2. Magnetic characterization

The magnetic characterization of the NiCu nanowire arrays was performed by Vibrating Sample Magnetometry (VSM), under a maximum applied magnetic field of ± 1.0 T. For hysteresis measurements the magnetic field was applied parallel (||) and perpendicular (⊥) to the nanowire axis. The hysteresis loops were obtained at room temperature and for the study of the influence of the composition on the magnetic properties, measurements at a temperature range between 10 K and 290 K were performed.

The influence of different parameters has been considered in this work: (i) the diameter, (ii) the length, and (iii) the composition of the nanowires. From the hysteresis loops, the values of the coercive field (H_c) and the fractional remanence or squareness (M_r/M_s) have been obtained and plotted for both configuration of applied magnetic field.

I.2.2.1. Influence of nanowire geometry

In this section of the work, it has been studied how the magnetic properties of NiCu nanowire arrays can be tailored by tuning the geometrical parameters such as nanowire length and diameter.

Figure I.5 shows representative hysteresis loops of $Ni_{70}Cu_{30}$ nanowire arrays, 80 nm in diameter and different nanowire lengths, measured in both configuration of the applied magnetic field, parallel (||) and perpendicular (⊥) to the nanowire axis. For the arrays with 300 nm and 9 µm nanowire length (Figure I.5(a) and (b)), higher values of H_c and M_r/M_s in parallel configuration compared to the perpendicular one are obtained, indicating a easy magnetization axis along the nanowire longitudinal axis. Figure I.5(c) shows a drastic reduction of these magnitudes for a large aspect ratio (i.e. nanowire length-to-diameter), being in this case $L_{NW} / d_{NW} = 350$.

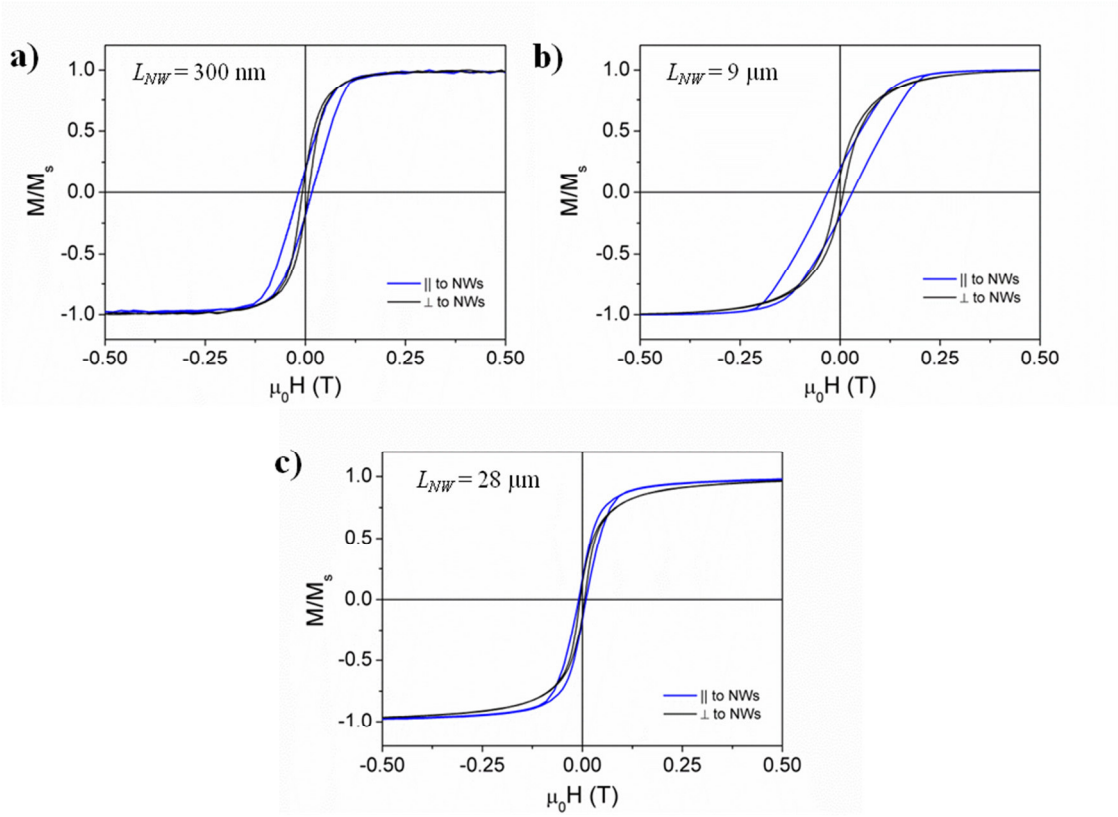

Figure I.5 Hysteresis loops of $Ni_{70}Cu_{30}$ nanowire arrays with nanowire diameter of 80nm and different nanowire lengths: (a) 300 nm, (b) 9 µm, and (c) 28 µm.

Figure I.6(a) shows the nanowire length dependence of the coercivity and squareness for $Ni_{70}Cu_{30}$ nanowire arrays with 80 nm nanowire diameter, where the length ranged from 150 nm to 28 µm. Both magnitudes, measured with the magnetic field applied parallel to the nanowire axis, increase with the nanowire length up to around 1 µm (Figure I.6(b)). This behaviour is ascribed to an increase in the shape anisotropy. For longer nanowires (L_{NW} between 1 and 8 µm) these properties decrease slightly due to magnetostatic interactions between neighbouring nanowires. The dipole

interactions increase with the nanowire length, originating a higher interaction field in the opposite direction [14, 37]. For L_{NW} > 8 µm, both coercive field and squareness show a more pronounced decrease which is attributed to enhanced magnetostatic interactions among nanowires [14, 38] and to the averaging of inhomogeneities in morphology or in composition along the length of the nanowires due to the decrease of metallic ions in the electrolyte during the electrodeposition process [37, 39, 40].

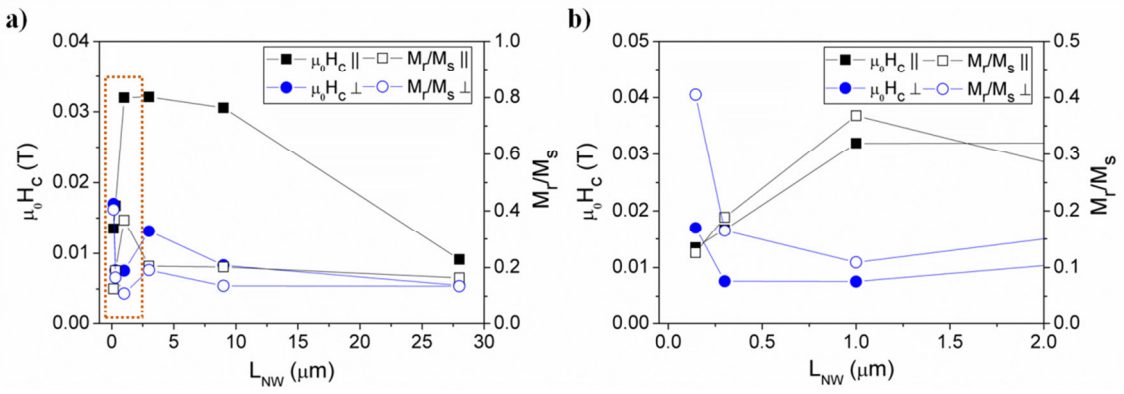

Figure I.6 Coercivity and squareness (a) as a function of the nanowire length (for $Ni_{70}Cu_{30}$ nanowires with diameter of 80nm), and (b) detail of length dependence for L_{NW} below 2 µm (zoom-in of the region included in the dashed line in (a)).

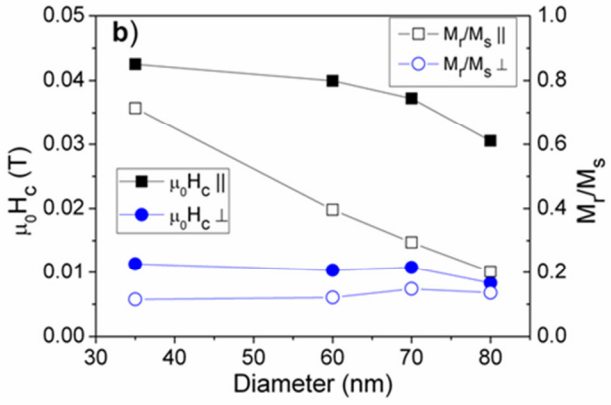

Figure I.7 Coercivity and squareness as a function of the nanowire diameter for $Ni_{70}Cu_{30}$ nanowires with a length of 8 µm.

Figure I.7 shows the influence of nanowire diameter on the coercive field and squareness of $Ni_{70}Cu_{30}$ nanowire arrays with nanowire length of 8 µm. Both magnitudes decrease with the nanowire diameter, for the parallel configuration of the applied

magnetic field. This is ascribed again to the increase in the magnetostatic interactions between nanowires. The enhanced interactions are favoured by the decrease in the distance between nanowires due to the increase in diameter while keeping constant the distance between nanowire centers.

I.2.2.2. Influence of nanowire composition

Figure I.8 shows representative hysteresis loops of $Ni_{100-x}Cu_x$ nanowire arrays, 80 nm in diameter and 8 µm nanowire length, measured with the magnetic field applied in parallel (||) and perpendicular (⊥) configurations. For pure Ni nanowires (Figure I.8(a)) and intermediate Cu content (x = 45, Figure I.8(b)), an easy magnetization axis along the nanowire is observed due the higher values of H_c and M_r/M_s in parallel configuration compared to the perpendicular one. On the other hand, for higher Cu content (x =75, Figure I.8(c)) a change in the easy axis from parallel to perpendicular to the nanowire is observed.

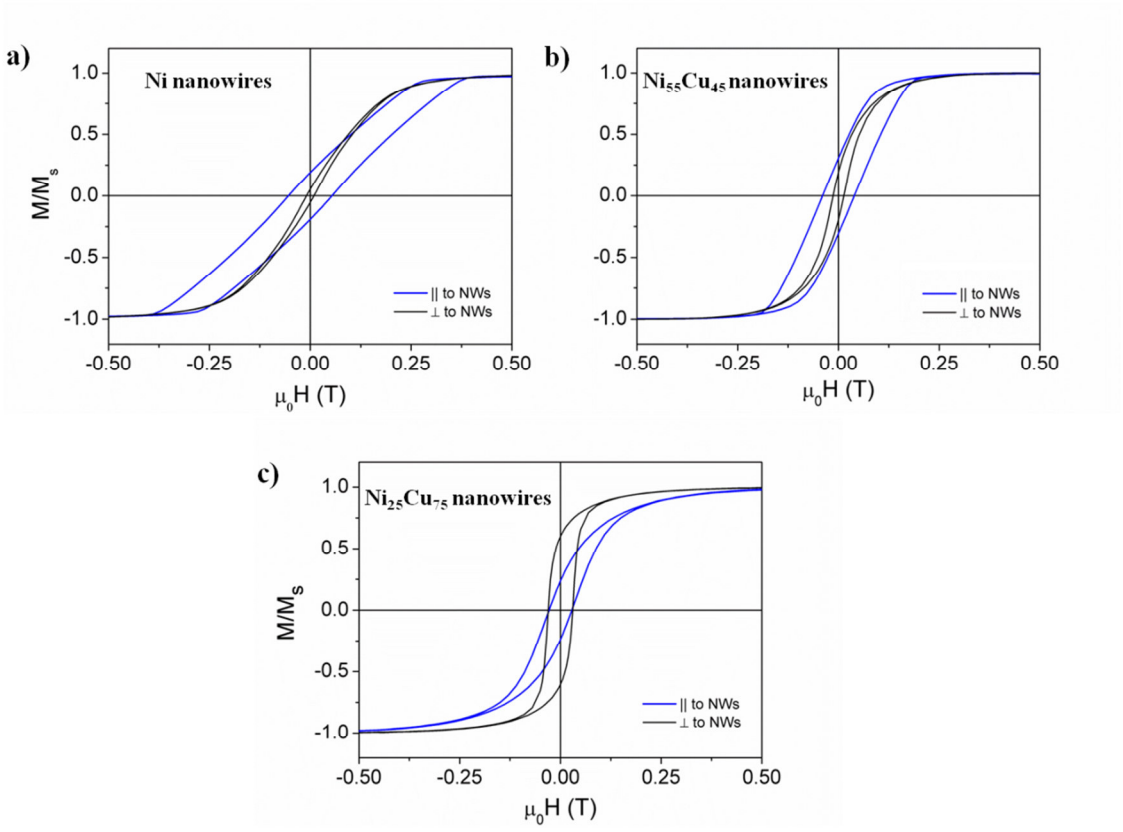

Figure I.8 Hysteresis loops of $Ni_{100-x}Cu_x$ nanowire arrays with 80 nm nanowire diameter and 8 µm nanowire length for: (a) x = 0, (b) x = 45, and (c) x = 75.

Figure I.9 shows the magnetic properties, coercive field (H_c) and squareness (M_r/M_s) of the $Ni_{100-x}Cu_x$ nanowire arrays for both configuration of applied magnetic field with respect to the amount of Cu into the alloy. The considered nanowire arrays have the same nanowire diameter (d_{NW} = 80 nm) and length (L_{NW} =8 µm).

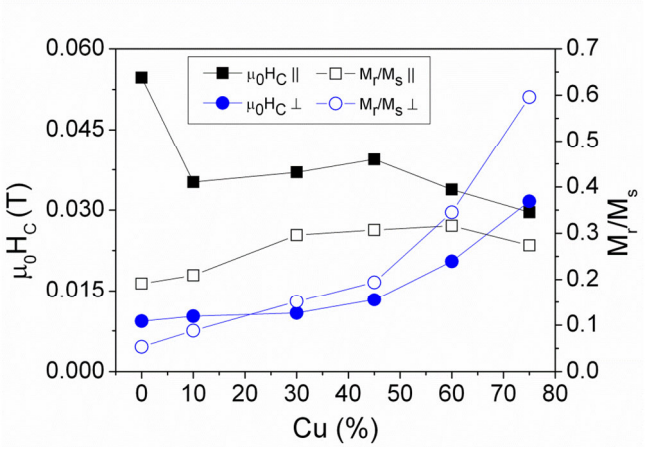

Figure I.9 Compositional dependence of coercive field and squareness of 80 nm diameter and 8 µm long nanowire array.

For the parallel field configuration, the coercivity of the nanowire array decreases with the amount of Cu in the alloy, showing a relative maximum at around 45% Cu content. In this configuration, the squareness increases with the Cu content, reaching a value of around 0.3 for $45 \leq x \leq 60$ and then decreases. A different behavior is observed for the perpendicular field configuration, where the coercive field and squareness increase continuously with Cu content. With the increasing amount of Cu in the alloy, the saturation magnetization of the nanowire array decreases and, according to the behavior shown in Figure I.9, an overall evolution of the magnetization easy axis from parallel towards perpendicular to the nanowire axis is deduced, together with a likely change in the magnetization reversal mechanism.

Magnetic measurements as function of temperature have been performed in order to obtain additional information of the magnetization reversal processes of NiCu nanowire arrays. For this purpose, the study has been carried out measuring $Ni_{100-x}Cu_x$ ($0 \leq x \leq 75$) nanowire arrays and the particular case of nanowires with 80 nm diameter and 8 µm length, under magnetic field applied in parallel and perpendicular configurations. The temperature dependence of the coercivity and squareness for the

different nanowire compositions and in both configurations are shown in Figure I.10. As observed, the variation in the nanowire composition has an overall stronger influence on the magnetic properties measured when the applied field is perpendicular to the nanowire axis (Figure I.10(b) and (d), showing $H_c(\perp)$ and $M_r/M_s(\perp)$, respectively) than in parallel configuration (see Figure I.10(a) and (c), where $H_c(||)$ and $M_r/M_s(||)$ were plotted respectively).

Figure I.10(a) shows the coercivity of the nanowire arrays when the field is applied parallel to the nanowire axis, $H_c(||)$. For low Cu content, $x \leq 30$, $H_c(||)$ increases with the temperature until a maximum is reached at around 175-200 K and then it decreases at more elevated temperature. For intermediate amount of Cu in the alloy, $45 \leq x \leq 60$, the coercive field decreases when the temperature increases up to 100 K, then it increases until reaching a maximum at about 175 K, decreasing again after this. Finally, for high Cu content, x = 75, the coercive field decreases continuously, almost linearly, with temperature.

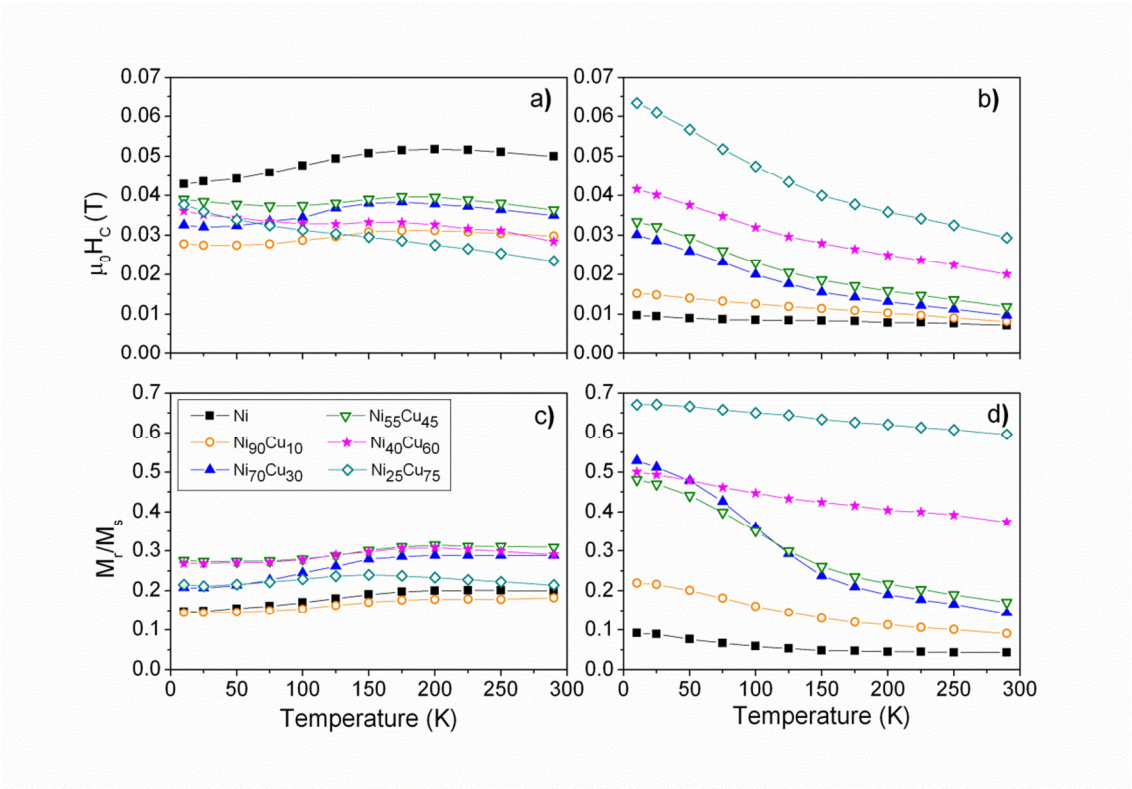

Figure I.10 Temperature dependence of coercivity and squareness of different composition NiCu nanowires (80 nm diameter and 8 µm length), when the magnetic field is applied parallel (a and c) and perpendicular (b and d) to the nanowires.

Figure I.10(c) shows that the squareness when the field is applied parallel to the nanowire axis, $M_r/M_s(||)$, presents a similar behavior for all the compositions. This magnitude increases until the temperature is around 175-200 K, and it remains constant for low and intermediate Cu content, x < 60. When the amount of Cu further increases, a small decrease in $M_r/M_s(||)$ with temperature is observed.

On the other hand, when the magnetic field is applied perpendicular to the nanowire axis, the coercivity ($H_c(\perp)$) shows a different behavior (Figure I.10(b)). For an increase in the temperature, a pronounced decrease in the coercivity is obtained, particularly for intermediate and high Cu content, x ≥ 30, when two different slopes are observed. Note that the temperature where the two slopes intersect (around 175 K) coincides with the maximum of coercive field in Figure I.10(a). A similar behavior is observed in Figure I.10(d) for the squareness when the applied field is perpendicular to the nanowire axis, $M_r/M_s(\perp)$. For all the compositions, a decrease in $M_r/M_s(\perp)$ with the temperature is observed and, for x < 60 two different slopes in the temperature dependence are obtained, intersecting both at around 175 K.

For the interpretation of the observed phenomenological behavior we have to consider the different involved magnetic energy terms as well as the changes introduced in the crystallographic structure of the nanowires by adding Cu. The relevant energy contributions to the anisotropy in this case are the magnetocrystalline, K_{crys}, the magnetoelastic, K_{elas}, and the shape, K_{sh}, anisotropy energy density terms.

On the other hand, as shown in Figure I.3, the XRD spectra suggest the presence of two main (111) *fcc* phases namely, a ferromagnetic, Ni-like, and a non-ferromagnetic, Cu-like. Additionally, from the modest and similar fractional reduction of the saturation magnetization with temperature for each composition, we deduce a similar Curie temperature for all the samples. That leads us to assume a low Cu content in the magnetic Ni-like phase, that is, increasing the Cu content gives rise to a reduction in the magnetic moment of the nanowires while keeping similar Curie temperature.

Firstly, we have considered the evolution of the magnetic anisotropy terms for Ni to explain the observed behavior with temperature: (i) the magnetocrystalline anisotropy, K_{crys}, is one order of magnitude higher at 10 K (~5.10^4 J/m^3) than at room temperature (~5.10^3 J/m^3); (ii) the magnetoelastic anisotropy, K_{elas}, perpendicular to the nanowire axis at low temperature increases significantly due to the different thermal

expansion coefficient of Ni and alumina [14, 41]; and (iii) the shape anisotropy, K_{sh}, is assumed to be nearly constant owing to the reduced change in saturation magnetization in this temperature range.

On the other hand, it is expected that the increase in the amount of Cu into the alloy gives rise to a reduction in the magnitude of the three energy terms. Particularly, for high Cu content (x > 30) the macroscopic (e.g. shape) anisotropy can be significantly altered by the structural changes induced by the dominant presence of Cu-like phase (see Figure I.3(d) to (f)).

For low amount of Cu (x < 30) at low temperatures, all the magnetic anisotropy energy densities would show similar values, although K_{sh} is the predominant [42]. As the temperature increases, K_{elas} would decrease and this brings the increase of coercivity when the magnetic field is applied parallel to the nanowire axis (Figure I.10(a)) [14, 42]. At around 175 K (temperature where the maximum coercivity is obtained), K_{crys} and K_{elas} would balance and already become small compared to K_{sh}, which determines the magnetic behavior at higher temperature.

For intermediate content of Cu ($45 \leq x \leq 60$), the XRD patterns present two phases, Ni-like and Cu-like (Figure I.3(d) and (e)). This means that magnetic Ni-like nanocrystals would be surrounded by non-magnetic Cu-like ones and, therefore, K_{sh} would significantly decrease with the Cu content. At low temperature, K_{sh} would be no more the predominant term and $H_c(||)$ decreases with increasing temperature until K_{crys} and K_{elas} are negligible and K_{sh} becomes again the most important contribution for the effective magnetic anisotropy energy. For high Cu content ($Ni_{25}Cu_{75}$), the most predominant phase is the Cu-like (see the high peak close to the Cu (111) reflection in Figure I.3(f) and the shoulder in the right part of the peak). In this case, K_{sh} for the magnetic nanocrystals could be perpendicular to the nanowire axis and the maximum for $H_c(||)$ disappears Figure I.10(a). The two different slopes in $H_c(\perp)$ (Figure I.10(b)) should be then related with the predominance of the different magnetic anisotropies, K_{crys} and K_{elas} for low and K_{sh} for high temperatures, respectively.

The dependence of Curie temperature (T_C) on the Cu content in the alloy for NiCu bulk samples is well known: T_C is around 300 K for $Ni_{70}Cu_{30}$ and goes to zero for $Ni_{44}Cu_{56}$, that is, the alloy should be paramagnetic for Cu content higher than 56% [43]. In contrast to the bulk NiCu alloy, NiCu nanowires show a different behavior with the

temperature. For nanowires with Cu content above 45%, the magnetic behavior shown in Figure I.9 at room temperature can be explained from the XRD spectra in Figure I.3(d) to (f): two phases appear, one Cu-like (paramagnetic due to the Ni atoms) and one Ni-like, ferromagnetic and with magnetic properties close to those of Ni and, therefore, with similar T_C. For $Ni_{70}Cu_{30}$ nanowires, the XRD spectrum does not indicate any Cu segregation (Figure I.3(c)), so the magnetic response should be very low due to the proximity to its Curie temperature. It could be related to the high specific surface of the nanowires compared to the bulk [44] and /or with the special magnetic behavior of these alloys [45, 46].

I.3. Magnetically soft nanocomposite: Ni nanowires embedded into polystyrene nanotubes

I.3.1. Nanocomposite fabrication and geometrical characterization

The AAO templates were prepared by two-step anodization of high purity Al foils using a phosphoric acid aqueous solution (H_3PO_4 : 0.12 M) as electrolyte under an applied voltage of 195 V at 0−1 °C for 24 h (all the parameters were the same for both anodization steps). For more details about the anodization process, the reader is referred to Section 2.1.2.

For the PS nanotubes synthesis, firstly a polymer film was prepared by pressing the PS homopolymer (with a molecular weight of M_W = 192,000 g/mol) at 240 ºC in order to get an 80 μm thick layer. The AAO template was cleaned in an oven at in vacuum atmosphere 200 °C for 2 h. The PS film was placed on the AAO template surface and the PS was infiltrated in nitrogen atmosphere at 200 ºC for 1 h [47]. Figure I.11(a) shows Scanning Electron Microscopy (SEM) cross-sectional view of the AAO template with the infiltrated PS, where it is possible to observe that the polymer goes from the top to the bottom part of the template. This is confirmed by the presence of PS nanotubes which get out from the pores at the end of the pores.

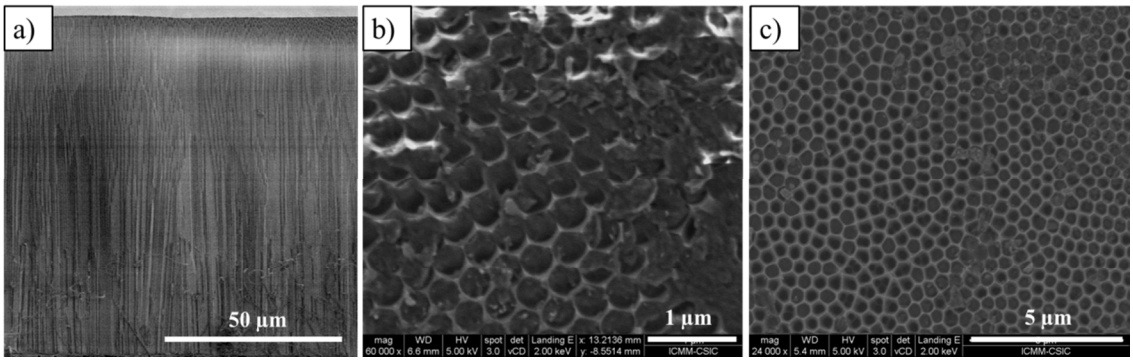

Figure I.11 (a) Cross-section view of the AAO template with the infiltrated PS nanotubes; top view of the AAO template after the PS infiltration and (b) before and (c) after the residual PS chemical etching.

The residual polystyrene layer on top of the membrane was chemically removed by tetrahydrofuran (THF) (see the difference between Figure I.11(b) and (c) which correspond to the top view the template with the infiltrated PS before and after the residual PS etching). Figure I.11(c) shows the pores (darker areas in the figure) surrounded by thin polystyrene nanotubes (gray color). Then, a thin Au layer was sputtered at the bottom of the template to cover the pores and serve as working electrode for Ni nanowire electrodeposition. The electrochemical parameters used to grow the Ni nanowires are collected in Table 2.2.

SEM was used to characterize the PS nanotubes inside the AAO templates and the nickel nanowires inside the PS nanotubes. The average alumina pore diameter was 280 nm, the distance between hexagonally ordered pores centers was 420 nm (Figure I.12(a)) and the pore length was 100 µm.

The alumina template was partially dissolved using a sodium hydroxide solution (NaOH : 0.19 M) at room temperature [48], to perform the morphological analysis of free polymer nanostructures. Figure I.12(b) shows PS nanotubes out of the AAO template, with a wall thickness of around 70 nm. Figure I.12(c) and (d) shows the Ni nanowires with a diameter of 140 nm diameter and 25 µm in length covered by the PS nanotubes, thus demonstrating the nickel electrodeposition inside polymer nanotubes.

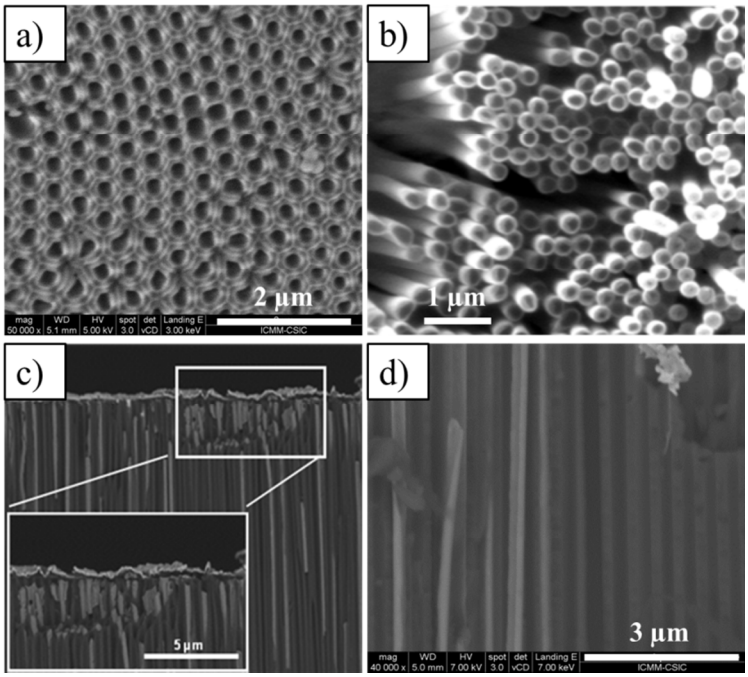

Figure I.12 (a) Top view SEM image of AAO template with an average pore diameter of 280 nm and distance between pore centers of 420 nm; (b) polystyrene (PS) nanotubes out of the AAO template; (c) and (d) cross section of SEM images of Ni nanowires inside PS nanotubes, both embedded into the AAO template.

I.3.2. Magnetic characterization

The nickel nanowire array inside PS nanotubes (magnetic nanocomposite array), both embedded into AAO templates, was magnetically characterized by Vibrating Sample Magnetometer (VSM) under a maximum magnetic field of ±1.8 T, applied in parallel (∥) and perpendicular (⊥) configuration with respect to the nanowires axis. The hysteresis loops of the nanocomposite array in both configurations are shown in Figure I.13. Coercivity (H_c) and fractional remanence (M_r/M_s) values have been obtained from the hysteresis loops for both applied magnetic field configurations. The values for the magnetic magnitudes are collected in Table I.1. The fractional remanence and the coercive field take significantly larger values for the parallel configuration than for the perpendicular one. According to this, together with the lower value of the saturation field (H_{sat}) for the parallel configuration, we can deduce an effective magnetization easy axis parallel to the nanowires characterized by a longitudinal magnetic anisotropy field of around 0.3 T. This magnetic anisotropy can be ascribed mostly to the shape anisotropy of Ni nanowires, determined by their high aspect ratio

(i.e. length-to-diameter). A similar behavior was observed for Ni nanowires not embedded in PS nanotubes as described in Ref. [49].

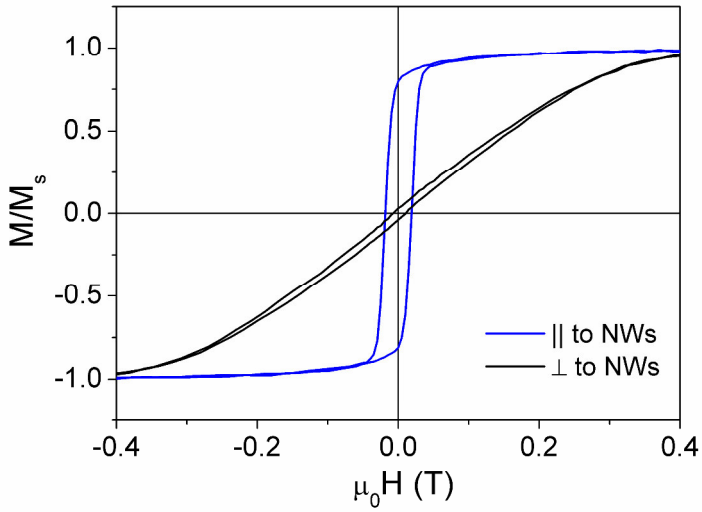

Figure I.13 Hysteresis loops measured by VSM using both configuration of the applied magnetic field, parallel (||) and perpendicular (⊥) to the nanowires (NWs).

Table I.1 Coercive field (H_c) and fractional remanence (M_r/M_s) of Ni nanowire embedded into PS nanotubes array, for applied magnetic field in parallel (||) and perpendicular (⊥) configuration.

Magnetic field configuration	$\mu_0 H_c$ (mT)	M_r/M_s
||	19	0.80
⊥	9	0.03

I.4. Conclusions

The magnetic properties of NiCu nanowire arrays can be tailored by tuning the composition and the geometry of the nanowires, i.e. nanowire diameter and length. Tailoring the magnetic properties, such as coercive field and squareness, by adjusting the compositional and geometrical parameters to obtain the needed values of the magnitudes, suggests the possibility to use NiCu nanowires for specific applications in microelectronics or sensing devices, among others.

The electrochemical routes have allowed us to fabricate $Ni_{100-x}Cu_x$ nanowires with a range of compositions of $0 \leq x \leq 75$, with nanowire diameter between 35 and 80 nm, and nanowire length ranging from 150 nm to 28 μm.

All the NiCu nanowires crystallize in a polycrystalline *fcc* structure, being for pure Ni nanowires the (220) the preferred growing direction and for NiCu nanowires the (111) direction but showing also other reflections. For Cu content below 30% and above 75%, a NiCu alloy is obtained, but for intermediate amount of Cu into the alloy, two different phases appear, one Ni-rich and another one Cu-rich.

Among the NiCu nanowire arrays, the highest values of coercive field and squareness have been obtained for arrays with a Cu content into the alloy of 45%, nanowire length of 1 μm and 35 nm nanowire diameter. This behaviour is mainly ascribed to the reduction in the magnetostatic interactions between nanowires in the array for nanowires with smaller diameter and shorter in length.

The temperature dependence of the magnetic properties of the nanowire arrays can be explained by the reduction in shape anisotropy with increasing Cu content, together with an increase in the magnetocrystalline and magnetoelastic anisotropies at low temperatures.

Furthermore, the work described here allowed us, for the first time, to easily synthesize nickel nanowires embedded into polystyrene nanotubes, as a core-shell magnetic-polymeric nanocomposite. This nanocomposite presents an effective magnetization easy axis parallel to the nanowires, mostly ascribed to the shape anisotropy of the nickel nanowires. This type of metal-polymer core-shell material could be developed for a variety of systems, therefore opening new opportunities in numerous applications. In this case, PS was selected as the shell material due to its properties which offer the advantage of the easy infiltration into the AAO templates. This material possesses interesting properties as mechanical and thermal stability, transparency, and isolation. Nickel was selected as the metallic element for the core because of its biocompatibility [50, 51], easy growing, magnetic and electrical properties. This element could be replaced by other metallic materials (Fe, Co, Cu, or alloys of these elements), according to the needed magnetic properties. Moreover, the geometry and dimensions of the nanowires (nanowire diameter and length) can be tailored.

The suitable choice of polymer nanotubes and magnetic nanowires enables, in a relatively simple, reliable, and low-cost fabrication way, the tailoring of the core-shell nanocomposite for applications such as hyperthermia, drug delivery, biodetection, or removal of water contamination.

Bibliography

[1] A. Blondel, J.P. Meier, B. Doudin, J.P. Ansermet, Giant magnetoresistance of nanowires of multilayers, *Appl. Phys. Lett*., 65 (1994) 3019-3021.

[2] Z. Yang, Z. Li, L. Liu, L. Kong, Microstructure and magnetic properties of Co–Cu nanowire arrays fabricated by galvanic displacement deposition, *J. Magn. Magn. Mater.,* 323 (2011) 2674-2677.

[3] M. Vázquez, L.G. Vivas, Magnetization reversal in Co-base nanowire arrays, *Phys. Status Solidi B*, 248 (2011) 2368-2381.

[4] V. Vega, J. García, W.d.O.d. Rosa, L. Vivas, V. Prida, B. Hernando, M. Vázquez, Magnetic Properties of (Fe, Co)–Pd Nanowire Arrays, *J. Nanosci. Nanotechno*., 12 (2012) 7501-7504.

[5] D. Lashmore, M. Dariel, Electrodeposited Cu-Ni Textured Superlattices, *J. Electrochem. Soc.*, 135 (1988) 1218-1221.

[6] R. Oberle, R. Cammarata, C. Su, M. Wuttig, Internal friction of artificially multilayered Cu–Ni (100) membranes produced by electrodeposition, *J. Mater. Res*., 14 (1999) 3837-3839.

[7] E. Tóth-Kádár, L. Péter, T. Becsei, J. Tóth, L. Pogány, T. Tarnóczi, P. Kamasa, G. Láng, Á. Cziráki, W. Schwarzacher, Preparation and magnetoresistance characteristics of electrodeposited Ni-Cu alloys and Ni-Cu/Cu multilayers, *J. Electrochem. Soc.*, 147 (2000) 3311-3318.

[8] M. Chen, P. Searson, C. Chien, Micromagnetic behavior of electrodeposited Ni/Cu multilayer nanowires*, J. Appl. Phys*., 93 (2003) 8253-8255.

[9] F. Béron, L.-P. Carignan, D. Menard, A. Yelon, Magnetic behavior of Ni/Cu multilayer nanowire arrays studied by first-order reversal curve diagrams, *IEEE Trans. Magn.*, 44 (2008) 2745-2748.

[10] C. Wang, G. Meng, Q. Fang, X. Peng, Y. Wang, Q. Fang, L. Zhang, Structure and magnetic property of Ni-Cu alloy nanowires electrodeposited into the pores of anodic alumina membranes, *J. Phys. D-Appl. Phys.,* 35 (2002) 738.

[11] E. Matei, I. Enculescu, M.E. Toimil-Molares, A. Leca, C. Ghica, V. Kuncser, Magnetic configurations of Ni–Cu alloy nanowires obtained by the template method, *J. Nanopart. Res*., 15 (2013) 1-9.

[12] K. Ounadjela, R. Ferre, L. Louail, J. George, J. Maurice, L. Piraux, S. Dubois, Magnetization reversal in cobalt and nickel electrodeposited nanowires*, J. Appl. Phys.,* 81 (1997) 5455-5457.

[13] X. Xu, G. Zangari, Microscopic structure and magnetic behavior of arrays of electrodeposited Ni and Fe nanowires, *J. Appl. Phys*., 97 (2005) 10A306.

[14] H. Schlörb, V. Haehnel, M.S. Khatri, A. Srivastav, A. Kumar, L. Schultz, S. Fähler, Magnetic nanowires by electrodeposition within templates, *Phys. Status Solidi B,* 247 (2010) 2364-2379.

[15] R.S. Liu, S.C. Chang, P.Y. Chen, S.F. Hu, C.Y. Huang, Preparation and characterization of Ni or Co/Cu multilayer nanowires, *J. Chin. Chem. Soc*., 57 (2010) 888-891.

[16] M. Ciureanu, F. Beron, L. Clime, P. Ciureanu, A. Yelon, T. Ovari, R. Cochrane, F. Normandin, T. Veres, Magnetic properties of electrodeposited CoFeB thin films and nanowire arrays, *Electrochim. Acta*, 50 (2005) 4487-4497.

[17] D. Xue, J. Fu, H. Shi, Preparation and magnetic properties of Fe 0.88− xCoxP 0.12 amorphous nanowire arrays, *J. Magn. Magn. Mater.,* 308 (2007) 1-4.

[18] C. Bran, Y.P. Ivanov, J. García, R. del Real, V. Prida, O. Chubykalo-Fesenko, M. Vazquez, Tuning the magnetization reversal process of FeCoCu nanowire arrays by thermal annealing, *J. Appl. Phys.,* 114 (2013) 043908.

[19] A. Santos, L. Vojkuvka, J. Pallarés, J. Ferré-Borrull, L. Marsal, Cobalt and nickel nanopillars on aluminium substrates by direct current electrodeposition process, *Nanoscale Res. Lett*., 4 (2009) 1021.

[20] H. Pan, B. Liu, J. Yi, C. Poh, S. Lim, J. Ding, Y. Feng, C. Huan, J. Lin, Growth of single-crystalline Ni and Co nanowires via electrochemical deposition and their magnetic properties, *J. Phys. Chem. B*, 109 (2005) 3094-3098.

[21] H.J. Fan, P. Werner, M. Zacharias, Semiconductor nanowires: from self-organization to patterned growth, *Small*, 2 (2006) 700-717.

[22] J.G. Ovejero, C. Bran, E. Vilanova, J. Kosel, M.P. Morales, M. Vazquez, Electrochemical synthesis of core–shell magnetic nanowires, *J. Magn. Magn. Mater.,* 389 (2015) 144-147.

[23] J. García, V. Prida, L.G. Vivas, B. Hernando, E. Barriga-Castro, R. Mendoza-Reséndez, C. Luna, J. Escrig, M. Vázquez, Magnetization reversal dependence on effective magnetic anisotropy in electroplated Co–Cu nanowire arrays, *J. Mater. Chem. C*, 3 (2015) 4688-4697.

[24] K.S. Repa, D. Israel, J. Alonso, M. Phan, E. Palmero, M. Vazquez, H. Srikanth, Superparamagnetic properties of carbon nanotubes filled with NiFe2O4 nanoparticles, *J. Appl. Phys*., 117 (2015) 17C723.

[25] M. Zhang, P. Dobriyal, J.-T. Chen, T.P. Russell, J. Olmo, A. Merry, Wetting transition in cylindrical alumina nanopores with polymer melts, *Nano Lett.,* 6 (2006) 1075-1079.

[26] J. Martín, J. Maiz, J. Sacristan, C. Mijangos, Tailored polymer-based nanorods and nanotubes by" template synthesis": From preparation to applications, *Polymer*, 53 (2012) 1149-1166.

[27] J.-T. Chen, T.-H. Wei, C.-W. Chang, H.-W. Ko, C.-W. Chu, M.-H. Chi, C.-C. Tsai, Fabrication of polymer nanopeapods in the nanopores of anodic aluminum oxide templates using a double-solution wetting method, *Macromolecules*, 47 (2014) 5227-5235.

[28] A. Houachtia, P. Alcouffe, G. Boiteux, G.r. Seytre, J.-F. Gérard, A. Serghei, Nanofluidics Approach to Separate between Static and Kinetic Nanoconfinement Effects on the Crystallization of Polymers, *Nano Lett.,* 15 (2015) 4311-4316.

[29] C. Mijangos, R. Hernández, J. Martín, A review on the progress of polymer nanostructures with modulated morphologies and properties, using nanoporous AAO templates, *Prog. Polym. Sci.,* 54 (2016) 148-182.

[30] K. Nielsch, F. Castano, C. Ross, R. Krishnan, Magnetic properties of template-synthesized cobalt⁄ polymer composite nanotubes, *J. Appl. Phys.*, 98 (2005) 034318.

[31] K. Nielsch, F.J. Castano, S. Matthias, W. Lee, C.A. Ross, Synthesis of cobalt/polymer multilayer nanotubes, *Adv. Eng. Mater*., 7 (2005) 217-221.

[32] M. Lahav, E.A. Weiss, Q. Xu, G.M. Whitesides, Core-shell and segmented polymer-metal composite nanostructures, *Nano Lett*., 6 (2006) 2166-2171.

[33] D.N. Kelly, R.H. Wakabayashi, A.M. Stacy, A Modified Sol–Gel Technique for Pore Size Control in Porous Aluminum Oxide Nanowire Templates, *ACS Appl. Mater. Interfaces,* 6 (2014) 20122-20129.

[34] J. Martín, M. Vázquez, M. Hernández-Vélez, C. Mijangos, Ordered arrays of magnetic polymer-based nanorods by template synthesis, *J. Nanosci. Nanotechno*., 9 (2009) 5898-5902.

[35] X. Han, J. Maiz, C. Mijangos, C. Zaldo, Nanopatterned PMMA-Yb: Er/Tm: Lu2O3 composites with visible upconversion emissions, *Nanotechnology*, 25 (2014) 205302.

[36] U. Cvelbar, Copper oxide nanowires: a review of growth, *Nanotechnology*, 23 (2012) 194001.

[37] S. Aravamudhan, J. Singleton, P.A. Goddard, S. Bhansali, Magnetic properties of Ni–Fe nanowire arrays: effect of template material and deposition conditions, *J. Phys. D-Appl. Phys.,* 42 (2009) 115008.

[38] L. Clime, P. Ciureanu, A. Yelon, Magnetostatic interactions in dense nanowire arrays, *J. Magn. Magn. Mater.,* 297 (2006) 60-70.

[39] I. Rahman, K. Razeeb, M. Kamruzzaman, M. Serantoni, Characterisation of electrodeposited nickel nanowires using NCA template*, J. Mater. Process. Technol.,* 153 (2004) 811-815.

[40] J. Azevedo, C. Sousa, J. Ventura, A. Apolinario, A. Mendes, J. Araujo, Ultra-long Fe nanowires by pulsed electrodeposition with full filling of alumina templates, *Mater. Res. Expr.,* 1 (2014) 015028.

[41] H. Zeng, S. Michalski, R.D. Kirby, D.J. Sellmyer, L. Menon, S. Bandyopadhyay, Effects of surface morphology on magnetic properties of Ni nanowire arrays in self-ordered porous alumina, *J. Phys. Condens. Mat*., 14 (2002) 715.

[42] A. Kumar, S. Fähler, H. Schlörb, K. Leistner, L. Schultz, Competition between shape anisotropy and magnetoelastic anisotropy in Ni nanowires electrodeposited within alumina templates*, Phys. Rev. B*, 73 (2006) 064421.

[43] D. Chakrabarti, D. Laughlin, S. Chen, Y. Chang, Phase Diagrams of Binary Nickel Alloys, ed, P. Nash (Materials Park, OH: ASM International, 1991).

[44] V. Leontyev, Magnetic properties of Ni and Ni–Cu nanoparticles, *Phys. Status Solidi B,* 250 (2013) 103-107.

[45] T. Hicks, B. Rainford, J. Kouvel, G. Low, J. Comly, Giant moments in Ni-Cu alloys near the critical composition, *Phys. Rev. Lett.,* 22 (1969) 531.

[46] R. Houghton, M. Sarachik, J.S. Kouvel, Anomalous Electrical Resistivity and the Existence of Giant Magnetic Moments in Ni-Cu Alloys, *Phys. Rev. Lett.,*, 25 (1970) 238.

[47] C. Sun, J. Luo, L. Wu, J. Zhang, Self-ordered anodic alumina with continuously tunable pore intervals from 410 to 530 nm, ACS Appl. Mater. Interfaces, 2 (2010) 1299-1302.

[48] H. Masuda, K. Yada, A. Osaka, Self-ordering of cell configuration of anodic porous alumina with large-size pores in phosphoric acid solution, *Jpn. J. Appl. Phys.,* 37 (1998) L1340.

[49] M. Sharma, B.K. Kuanr, V. Veerakumar, A. Basu, Z.J. Celinski, Magnetization Dynamics and Reversal Mechanisms in Ni Nanowire and Nanotube Arrays, *IEEE Trans. Magn.,* 50 (2014) 1-4.

[50] F. Byrne, A. Prina-Mello, A. Whelan, B.M. Mohamed, A. Davies, Y.K. Gun'ko, J. Coey, Y. Volkov, High content analysis of the biocompatibility of nickel nanowires, *J. Magn. Magn. Mater*., 321 (2009) 1341-1345.

[51] N. Gao, H. Wang, E.-H. Yang, An experimental study on ferromagnetic nickel nanowires functionalized with antibodies for cell separation, *Nanotechnology,* 21 (2010) 105107.

Appendix II

Template-Assisted Fabrication of Carbon Nanotubes filled with Nanoparticles

The samples studied in this appendix have been produced in collaboration with the group of Prof. Hari Srikanth at the University of South Florida in Tampa, USA. The research herein reported focuses on the fabrication of multi-walled carbon nanotubes (MWCNTs) filled with magnetic nanoparticles (NPs) using the anodic aluminum oxide (AAO) membranes as templates. Moreover, a brief study of the magnetic properties of these composed magnetic nanostructures is reported. For more detailed information about the magnetism of these nanostructures, the reader is referred to Ref. [1].

One-dimensional magnetic nanostructures composed of MWCNTs filled with magnetic NPs are very promising nanocomposite materials for a broad spectrum of application, such as electromagnetic interference shielding, water purification, and biomedical applications as hyperthermia or drug delivery [2-7]. The synthesis of MWCNTs with a diameter below 100 nm is a challenging task. MWCNTs can be fabricated using commercial templates, however it has been observed that the use of these templates originates non-uniform magnetic properties due to the low uniformity in pore size and distribution throughout the template [8]. Custom highly ordered AAO templates are a good alternative to overcame this problem.

Highly ordered AAO templates were fabricated from high purity Al foils by electrochemical route using a controlled two-step anodization process (see Section 2.1.2.1 for experimental details). These templates were later used for the synthesis of

MWCNTs embedded into the alumina pores and, subsequently, they were filled with magnetic NPs.

Nickel-ferrite ($NiFe_2O_4$) NPs were synthesized by thermal decomposition method [9] and the final product was suspended in high purity hexane to prepare a ferrofluid. MWCNTs were synthesized by a catalyst-free method via chemical vapor deposition [8]. Firstly, a heat treatment at 640 ºC was performed to the AAO template in order to avoid bending during the MWCNTs growing. Then, the MWCNTs synthesis was carried out by heating up the template under argon atmosphere until the reaction temperature was reached (620 ºC). After this and at the reaction temperature, flows of helium and ethylene gases were introduced and kept for 5.5 h. More details about this process can be found in Ref. [1].

Once the MWCNTs were fabricated, they were filled with NPs by a magnetically assisted capillary action [10]. This process consisted on placing the AAO template with the embedded MWCNTs on top of a permanent magnet (H = 5 kOe). Then, the ferrofluid was slowly dropped on the template surface so that the NPs coat the MWCNTs inner walls. In order to release the MWCNTs filled with the NPs, the alumina template was dissolved by a sodium hydroxide solution (NaOH : 8 M) and, then, the magnetic nanocomposite material was suspended in isopropanol for further structural and magnetic characterization.

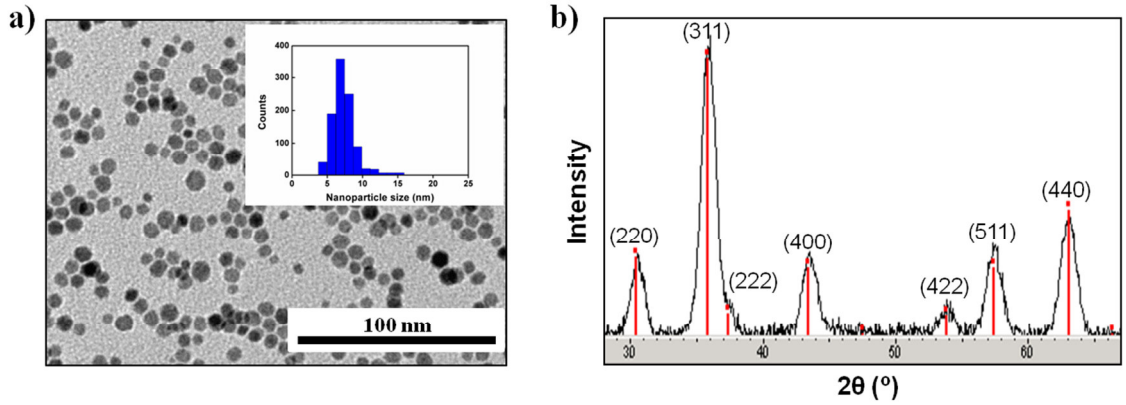

Figure II.1 (a) TEM image of nickel ferrite nanoparticles (inset shows the histogram with the nanoparticle size distribution); and (b) XRD pattern of nickel ferrite nanoparticles.

Transmission Electron Microscopy (TEM) was used to characterize the NPs geometry. Figure II.1(a) shows a TEM image together with an histogram showing the

particle size distribution. The NPs exhibit spherical shape and an average size of 7.4 ± 1.7 nm with a narrow size distribution. The X-Ray Diffraction (XRD) measurements (see pattern in Figure II.1(b)) show highly crystalline NPs, despite their small size.

Scanning Electron Microscopy (SEM) was used to determine the geometrical characteristics of the AAO template. Figure II.2(a) shows the SEM top view image of an empty AAO template with nanopore diameter of 80 nm, distance between pore centers of 105 nm and template thickness of 40 μm. TEM analysis of empty MWCNTs after dissolving the AAO template (Figure II.2(b)) shows that they are 80 nm in outer diameter and 11 μm in length. Figure II.2(c) shows a TEM image of MWCNTs filled with nickel-ferrite NPs. It is observed that no NPs remain outside of the MWCNTs and the NPs packing is quite uniform, property that is needed for to obtain reproducible magnetic behavior.

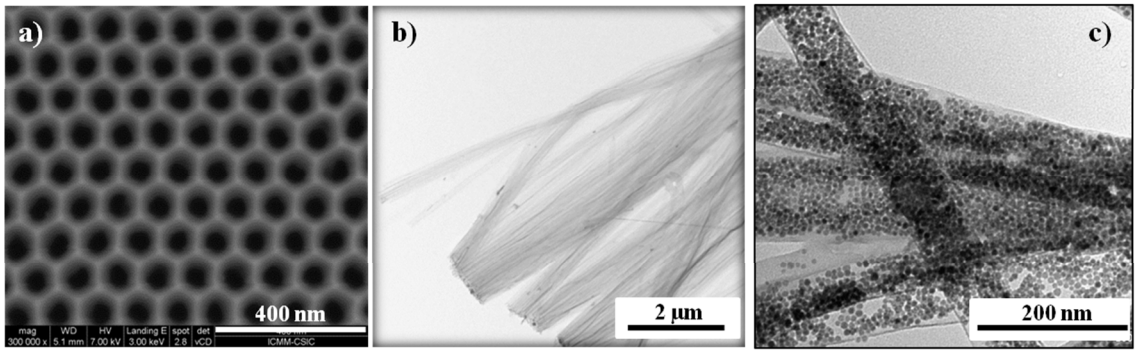

Figure II.2 (a) SEM top view image of an AAO template with nanopore diameter of 80 nm and distance between nanopore centers of 105 nm; (b) TEM image of free-standing MWCNTs out of the AAO template; and (c) TEM image of MWCNTs filled with nickel-ferrite nanoparticles.

The magnetic characterization was performed using a Physical Property Measurement System (PPMS) and obtaining the zero-field-cooled/field-cooled (ZFC-FC) curves and the hysteresis loops for different samples at different temperatures. Figure II.3 shows the ZFC-FC curves for nickel-ferrite NPs (triangles) and for MWCNTs filled with nickel-ferrite NPs (squares). The curves for both samples exhibit a similar shape, where the ZFC curves present a maximum around $T_B \sim 52$ K, which is associated to the blocking process of the nanoparticles. The value of the irreversibility temperature, where the ZFC and FC curves split, is close to T_B indicating monodispersity of the nanoparticles, as shown in Figure II.1(a). The inset in Figure II.3

shows the fitting to the Curie-Weiss Law, obtaining a good agreement with experimental results above 200 K, with a Curie temperature (T_C) of around 50 K, indicating weak ferromagnetic-like interactions.

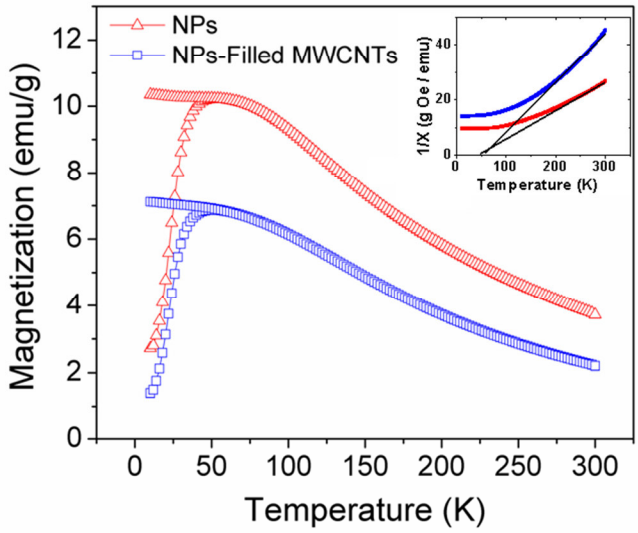

Figure II.3 Temperature dependence of the magnetization of the nickel-ferrite nanoparticles (NPs) (triangles) and the NPs-filled multi-walled carbon nanotubes (MWCNTs) (squares) obtained using the zero-field-cooled and field-cooled protocols (H = 100 Oe).

Figure II.4(a) and (b) show the normalized magnetization with respect to the applied magnetic field for the nickel-ferrite NPs and the MWCNTs filled with the NPs at 10 K and 300 K, respectively. Before the curves normalization, it was observed a decrease in the magnetization for the measured sample containing the MWCNTs filled with the NPs. This reduction is ascribed to the fact that the mass includes that of the MWCNTs in addition to the nickel-ferrite NPs. Table II.1 collects the values of coercive field (H_c) and normalized remanence (M_r/M_s) obtained from the hysteresis loops measured at 10 K (Figure II.4). Both samples exhibit relatively small coercivity. At 300 K, for any of the samples coercivity or remanence are observed, suggesting a superparamagnetic (SPM)-like behavior of the 7.4 nm nickel-ferrite NPs at room temperature. To confirm this behavior, the hysteresis loops were fitted with a standard Langevin expression. The good agreement between the experimental measurements and the fitted curves (inset in Figure II.4(b)) confirms the SPM-like behavior, although the apparent NP size obtained from the fittings is a bit bigger (8.5-9 nm), fact that is likely due to the weak but no negligible dipolar interactions [11]. The reader is referred to Ref.

[1] where a deeper study of the magnetic behavior of MWCNTs filled with nickel-ferrite NPs was performed.

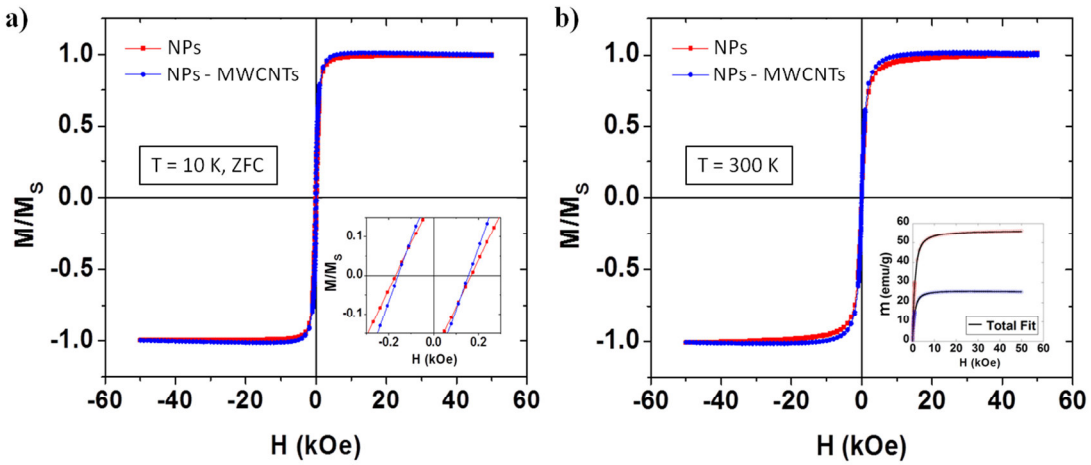

Figure II.4 Normalized magnetization vs. applied magnetic field curves for nickel-ferrite nanoparticles (NPs) and multi-walled carbon nanotubes (MWCNTs) filled with nickel-ferrite NPs: (a) at 10 K under zero-field cooled (ZFC) protocol (inset shows a closer view of the curves around the coercivity) and (b) at room temperature, T = 300 K (inset shows the Langevin-function fit of both curves).

Table II.1 Coercive field (H_c) and fractional remanence (M_r/M_s) of nickel-ferrite nanoparticles (NPs) and multi-walled carbon nanotubes (MWCNTs) filled with nickel-ferrite NPs.

Sample	H_c (Oe)	M_r/M_s
Nickel-ferrite NPs	167	0.20
MWCNTs filled with nickel-ferrite NPs	155	0.22

In summary, the study reported here allowed us to state that 7.4 nm nickel-ferrite nanoparticles were successfully synthesized embedded into multi-walled carbon nanotubes with custom dimensions due to the template-assisted fabrication method. The magnetic measurements have revealed a superparamagnetic-like behavior of this nanocomposite system with weak ferromagnetic dipolar interactions. These magnetic properties make the MWCNTs filled with nickel-ferrite NPs a very promising system for hyperthermia, sensing or microwave absorption applications.

Bibliography

[1] K. Stojak Repa, D. Israel, J. Alonso, M.H. Phan, E.M. Palmero, M. Vázquez, and H. Srikanth, Superparamagnetic properties of carbon nanotubes filled with $NiFe_2O_4$ nanoparticles, *J. Appl. Phys*., 117 (2015) 17C723.

[2] D. Sarkar, A. Bhattacharya, P. Nandy, S. Das, Enhanced broadband microwave reflection loss of carbon nanotube ensheathed Ni–Zn–Co-ferrite magnetic nanoparticles, *Mater. Lett.*, 120 (2014) 259.

[3] R.K. Srivastava, T.N. Narayanan, A.P. Reena Mary, M.R. Anantharaman, A. Srivastava, R. Vajtai, P.M. Ajayan, Ni filled flexible multi-walled carbon nanotube–polystyrene composite films as efficient microwave absorbers*, Appl. Phys. Lett.,* 99 (2011) 113116.

[4] M. Abdel Salam, M.A. Gabal, A.Y. Obaid, Preparation and characterization of magnetic multi-walled carbon nanotubes/ferrite nanocomposite and its application for the removal of aniline from aqueous solution, *Synth. Met*., 161 (2012) 2651.

[5] I. Mönch, A. Leonhardt, A. Meye, S. Hampe, R. Kozhuharova-Koseva, D Elefant, M.P. Wirth, B. Büchner, Synthesis and characteristics of Fe-filled multi-walled carbon nanotubes for biomedical application, *J. Phys.: Conf. Ser.,* 61 (2007) 820.

[6] J.H. Choi, F.T. Nguyen, P.W. Barone, D.A. Heller, A.E. Moll, D.Patel, S.A. Boppart, M.S. Strano, Multimodal Biomedical Imaging with Asymmetric Single-Walled Carbon Nanotube/Iron Oxide Nanoparticle Complexes, *Nano Lett.,* 7 (2007) 861.

[7] Y. Krupskaya , C. Mahn , A. Parameswaran , A. Taylor , K. Kramer , S. Hampel , A. Leonhardt, M. Ritschel , B. Buchner , R. Klingeler, Magnetic study of iron-containing carbon nanotubes: Feasibility for magnetic hyperthermia, *J. Magn. Magn. Mater.,* 321 (2009) 4067.

[8] S. Pal, S. Chandra, M.H. Phan, P. Mukherjee, and H. Srikanth, Carbon nanostraws: nanotubes filled with superparamagnetic nanoparticles, *Nanotechnology,* 20 (2009) 485604.

[9] J. Xie, S. Peng, N. Brower, N. Pourmand, S.X. Wang, S. Sun, One-pot synthesis of monodisperse iron oxide nanoparticles for potential biomedical applications, *Pure Appl. Chem*., 78 (2006) 1003.

[10] G. Korneva, H. Ye, Y. Gogotsi, D. Halverson, G. Friedman, J.C. Bradley, K.G. Kornev, Carbon Nanotubes Loaded with Magnetic Particles, *Nano Lett.*, 5 (2005) 879.

[11] P. Allia, M. Coisson, F. Spizzo, P. Tiberto, F. Vinai, Magnetic correlation states in cosputtered granular $Ag_{100-x}Fe_x$ films, *Phys. Rev. B*, 73 (2006) 054409.

List of publications

Directly related with the work included in the thesis:

1. E.M. Palmero, C. Bran, M. Vázquez, and R.P. del Real, "Magnetic nanowires based sensors", *submitted*.

2. E.M. Palmero, C. Bran, R.P. del Real, and M. Vázquez, "Synthesis and magnetism of modulated FeCo-based nanowires", *submitted*.

3. E.M. Palmero, F. Béron, C. Bran, R.P. del Real, and M. Vázquez, "Magnetic interactions in compositionally modulated nanowire arrays" *Nanotechnology* 27, 435705 (2016). DOI:10.1088/0957-4484/27/43/435705

4. E.M. Palmero, R. Salikhov, U. Wiedwald, C. Bran, M. Spasova, M. Vázquez, and M. Farle, "Enhanced magnetocrystalline anisotropy of $Fe_{30}Co_{70}$ nanowires by Cu additives and annealing" *Nanotechnology* 27, 365704 (2016). DOI: 10.1088/0957-4484/27/36/365704

5. C. Bran, E. Berganza, E.M. Palmero, J.A. Fernández-Roldán, R.P. del Real, L. Aballe, M. Foerster, A. Asenjo, A. Fraile Rodríguez, and M. Vázquez, "Spin configuration of cylindrical bamboo-like magnetic nanowires" *J. Mater. Chem. C* 4, 978–984 (2016). DOI: 10.1039/C5TC04194E

6. B. Sanz, E.M. Palmero, R.P. del Real, M. Vázquez, and C. Mijangos, "Arrays of magnetic Ni nanowires grown inside polystyrene nanotubes" *Ind. Eng. Chem. Res.* 54 (51), 13005–13008 (2015). DOI: 10.1021/acs.iecr.5b02860

7. E.M. Palmero, C. Bran, R.P. del Real, and M. Vázquez, "Vortex domain wall propagation in periodically modulated diameter FeCoCu nanowire as determined by the magneto-optical Kerr effect" *Nanotechnology* 26, 461001 (2015). DOI: 10.1088/0957-4484/26/46/461001

8. S. Liébana Viñas, R. Salikhov, C. Bran, E.M. Palmero, M. Vázquez, B. Arvan, X. Yao, P. Toson, J. Fidler, M. Spasova, U. Wiedwald and M. Farle, "Magnetic hardening of $Fe_{30}Co_{70}$ nanowires" *Nanotechnology* 26, 415704 (2015). DOI: 10.1088/0957-4484/26/41/415704

9. C. Bran, A.P. Espejo, E.M. Palmero, J. Escrig, and M. Vázquez, "Angular dependence of coercivity with temperature in Co-based nanowires" *J. Magn. Magn. Mater.* 396, 327–332 (2015). DOI :10.1016/j.jmmm.2015.08.056

10. K. Stojak Repa, D. Israel, J. Alonso, M.H. Phan, E.M. Palmero, M. Vázquez, and H. Srikanth, "Superparamagnetic properties of carbon nanotubes filled with $NiFe_2O_4$ nanoparticles" *J. Appl. Phys.* 117, 17C723 (2015). DOI: 10.1063/1.4914952

11. C. Bran, E.M. Palmero, Z-A. Li, R.P. del Real, M. Spasova, M. Farle, and M. Vázquez, "Correlation between structure and magnetic properties in Co_xFe_{100-x} nanowires: role of composition and wire diameter" *J. Phys. D: Appl. Phys*. 48, 145304 (2015). DOI: 10.1088/0022-3727/48/14/145304

12. E.M. Palmero, C. Bran, R.P. del Real, C. Magén, and M. Vázquez, "Structural and Magnetic Characterization of FeCoCu/Cu Multilayer Nanowire Arrays" *IEEE Magn. Lett.* 5, 6700304 (2014). DOI: 10.1109/LMAG.2014.2365151

13. E.M. Palmero, C. Bran, R.P. del Real, C. Magén, and M. Vázquez, "Magnetic behavior of NiCu nanowire arrays: Compositional, geometry and temperature dependence" *J. Appl. Phys.* 116, 033908 (2014). DOI: 10.1063/1.4890358

14. C. Bran, E.M. Palmero, R.P. del Real, and M. Vázquez, "CoFeCu electroplated nanowire arrays: Role of composition and annealing on structure and magnetic properties" *Phys. Status Solidi A* 211 (5), 1076–1082 (2014). DOI: 10.1002/pssa.201300766

Other publications during PhD period:

15. C. Bran, J. Guzmán, E.M. Palmero, E. Berganza, R.P. del Real, A. Asenjo, A. Fraile-Rodríguez, and M. Vázquez, "Magnetism of Co_xNi_{100-x} nanowires: From arrays to the internal domain structure of an individual wire" *(in preparation).*

16. A. Fardi-Ilkhchy, F. Nasirpouri, E.M. Palmero, and M. Vázquez, "On the electrochemical deposition mechanism of Fe-Pt binary system on n-Si (001) and nanoporous alumina template" *Ionics (under revision).*

17. F. Béron, A. Kaidatzis, M.F. Velo, L.C.C. Arzuza, E.M. Palmero, R.P. del Real, D. Niarchos, K.R. Pirota, and J.M. García-Martín, "Nanometer scale hard/soft bilayer magnetic antidots" *Nanoscale Res. Lett.* 11:86 (2016). DOI: 10.1186/s11671-016-1302-3

List of abbreviations

AAO	Anodic Aluminum Oxide
bcc	body-centered cubic
DCM	dc-demagnetization measurement
EDS	Energy Dispersive X-Ray Spectroscopy
FC	Field-Cooled
fcc	face-centered cubic
FM	Ferromagnetic
FMR	Ferromagnetic Resonance
hcp	hexagonal close-packed
HRTEM	High-Resolution Transmission Electron Microscopy(e)
IRM	Isothermal remanent magnetization measurement
LEED	Low Energy Electron Diffraction
LEEM	Low Energy Electron Microscopy(e)
MAE	Magnetocrystalline Anisotropy Energy
MFM	Magnetic Force Microscopy(e)
MOKE	Magneto-Optical Kerr Effect
MWCNT	Multi-Walled Carbon Nanotube
NFM	Non-ferromagnetic
NP	Nanoparticle
NT	Nanotube
NW	Nanowire
PEEM	Photoemission Electron Microscopy(e)
PM	Permanent Magnet

PPMS	Physical Properties Measurement System
PTFE	Polytetrafluoroethylene
PS	Polystyrene
RTU	Ready-To-Use
SAED	Selected Area Electron Diffraction
SEM	Scanning Electron Microscopy(e)
SQUID	Superconducting Quantum Interference Device
TEM	Transmission Electron Microscopy(e)
THF	Tetrahydrofuran
VSM	Vibrating Sample Magnetometry(er)
XMCD	X-Ray Magnetic Circular Dichroism
XMLD	X-Ray Magnetic Linear Dichroism
XRD	X-Ray Diffraction
ZFC	Zero-Field-Cooled

List of symbols

A_{exc}	Exchange stiffness constant (J/m)
a	Lattice parameter (Å)
$(BH)_{max}$	Maximum energy product (kJ/m^3)
B_r	Magnetic flux density at remanent state (G, T, Wb/m^2)
D_{int}	Distance between nanopore / nanowire centers (nm)
$d_{mod,1(2)}$	Segment diameter in modulated nanowires (nm)
d_{NW}	Nanopore / Nanowire diameter (nm)
d_s	Distance between nanowire array and Hall sensor (mm)
f	Microwave frequency (GHz)
f_r	Motor rotation frequency (Hz)
ΔH	Linewidth of the FMR spectra (A/m, Oe)
ΔH_u	Interaction field, FORC distribution (A/m, Oe)
H_c	Coercive field or coercivity (A/m, Oe)
$\overline{H_c}$	Local coercivity average, FORC distribution (A/m, Oe)
H_c^{FORC}	FORC distribution coercive field (A/m, Oe)
H_D	Shape anisotropy field (A/m, Oe)
H_{DC}	Applied magnetic field in FMR measurement (A/m, Oe)
H_{eff}	Effective magnetic anisotropy field (A/m, Oe)
H_i	Interaction field constant, FORC distribution (A/m, Oe)
H_r	Resonance field in FMR measurement (A/m, Oe)
H_{MC}	Magnetocrystalline anisotropy field (A/m, Oe)
H_{sat}	Saturation field (A/m, Oe)
H_{sw}	Switching field (A/m, Oe)

H_σ	Local coercivity standard deviation, FORC distribution (A/m, Oe)
$H_{\sigma i}$	Interaction field standard deviation, FORC distribution (A/m, Oe)
h	Planck constant ($6.63 \cdot 10^{-34}$ J·s)
K_2	Second-order term of the magnetocrystalline anisotropy energy density for uniaxial symmetry (J/m^3)
K_{crys}	Magnetocrystalline anisotropy energy density (J/m^3)
K_{elas}	Magnetoelastic anisotropy energy density (J/m^3)
K_{sh}	Shape anisotropy energy density (J/m^3)
$L_{mod,1(2)}$	Segment length in modulated nanowires (nm)
L_{NW}	Nanowire length (nm or μm)
M_r/M_s	Fractional remanence or squareness (dimensionless)
M_s	Saturation magnetization (A/m, emu/cm^3)
M_W	Molecular weight (g/mol)
m_r	Magnetic moment at remanence ($A \cdot m^2$, J/T)
m_s	Magnetic moment at saturation ($A \cdot m^2$, J/T)
n	Positive integer, Bragg's law (dimensionless)
P	Nanoporous template porosity (dimensionless or %)
Q	Microwave cavity quality factor (dimensionless)
T_B	Blocking temperature (K)
T_C	Curie temperature (K)
t_{Cu}	Electrodeposition time for Cu layer growth (s)
t_{FeCoCu}	Electrodeposition time for FeCoCu segments growth (s)
T_r	Period of tachometer signal (ms)
V_{motor}	Applied voltage to the motor, tachometer (V)
V_{out}	Distance sensor output (mV)
V_{sensor}	Tachometer output (mV)

θ	Diffraction angle, Bragg's law (º)
θ_H	Angle between the applied magnetic field and nanowire axis (º)
θ_M	Angle between the magnetization and nanowire axis (º)
λ	Wavelength of the incident wave, Bragg's law (Å)
μ_0	Magnetic permeability of free space ($4\pi \cdot 10^{-7}$ Wb/(A·m))

μ_B	Bohr's magneton ($9.27 \cdot 10^{-24}$ J/T)
$\hbar$	Reduced Planck constant or Dirac constant ($1.05 \cdot 10^{-34}$ J·s)